

AD-A078 436

GENERAL ELECTRIC CO CINCINNATI OH AIRCRAFT ENGINE GROUP F/G 17/5
ADVANCED INFRARED SIGNATURE PREDICTION PROGRAM, SPECTRAL CALCUL--ETC(U)
NOV 79 M E WILTON N00140-76-C-1072
R78AEG314 NL

UNCLASSIFIED

1 OF 3
AD
4078 436



2
Sc

Contract N00140-76-C-1072
R78AEG314

LEVEL

CD12462

ADA 078436

ADVANCED INFRARED SIGNATURE PREDICTION PROGRAM

Spectral Calculation Of Radiation from a turbine Propulsion
system as Intercepted by an Observer (SCORPIO-N)

Volume III - Analysis

DDC
RECEIVED
DEC 17 1979
RECEIVED
E

M. E. Wilton
General Electric Company

November 1979

This document has been approved
for public release and sale; its
distribution is unlimited.

NAVAL AIR PROPULSION TEST CENTER
TRENTON, NEW JERSEY 08628

DDC FILE COPY

79 12 14 075

6
ADVANCED
INFRARED SIGNATURE PREDICTION PROGRAM,
Spectral Calculation Of Radiation from a turbine Propulsion
system as Intercepted by an Observer (SCORPIO-N),

Volume III • Analysis,

12 245

14 R78AEG314

10 M.E. / Wilton

11 Nov 79

403 468

403 468

slt

TABLE OF CONTENTS

	<u>Page</u>
I. Introduction	1
A. Background	1
B. Problem Statement	1
1. Internal Engine Emissions	2
2. Flow Field Definition	3
3. Gaseous Plume Emissions/Absorption	4
4. Airframe	5
5. Totalling	5
6. Missile Characteristics	6
C. SCORPIO-N Structure	6
1. Discussion	6
2. Module Descriptions	8
D. Introduction to Analysis	10
II. Atmospheric Conditions	11
III. Flowfield Module Analysis (JETMIX)	13
A. Discussion	13
B. Analysis	13
1. Governing Equations	13
2. Transformation to Von Mises Coordinates	18
3. Numerical Technique	19
C. Turbulence Model	25
1. Discussion	25
2. Definition of Turbulence Length Scale	26
3. Swirling Jets	27
4. Coannular/Coplanar Jets	29
D. Gas Properties	31
E. Particle Injection	32
IV. Internal Exhaust Hot Parts Radiation (SIGNIR)	36
A. Discussion	36
B. Exhaust System Gas Flow (RIMAIN)	36
1. Compressible Fluid Flow (COFLOW)	36
2. Surface Boundary Layer (TURBLT)	38
C. Exhaust System Surface Cooling (LINKT)	48
1. Film Cooling (FILMCL)	48
2. Convection-Film Cooling (CNFLM)	53
3. Transpiration Cooling (TRANCL)	58
D. Exhaust System Radiation (NVIEW)	61
1. View Factor Calculations (VIEW)	61
E. Exhaust System Heat Balance (TASLB)	131
F. Special Computation Considerations	132
1. Pressure Loss Parameters	132
2. Heat Transfer Parameters	133
G. Radiation Coefficients and Source Emissions (SIRER)	135

TABLE OF CONTENTS (Concluded)

	<u>Page</u>
V. Plume Emission/Absorption (PLUMIR)	139
A. Introduction	139
B. Geometrical Considerations	139
1. Flow Field Centerline (TRAJCT)	139
2. Ray Selection (TRAJCT, ALA)	145
3. Additional Ray Intercept Points	147
4. Plume Through Plume Calculations	151
a. Critical Angle	151
b. Flow Field Axis	153
c. Method of Calculation	153
5. Plume-Ray Segments	157
C. Gaseous Emissions Model (EMIST)	159
1. Transfer Equation	160
2. Molecular Behavior of Gases	163
3. Vibrational Energy	165
4. Partially Overlapped Lines	170
5. Rotational Energy	173
6. Spectral Lines	177
7. Effect of Line Structure Along a Path	179
8. Atmospheric Absorption (ATMS)	184
9. Evaluation of Function ψ	184
10. Evaluation of Lines with Combined Doppler, Natural and Collision Broadening	185
11. Summary of Gaseous Emission Theory	189
D. Particle Attenuation	202
1. Attenuation by a Single Particle	202
2. Attenuation by a Cloud of Particles	205
VI. Total Spectral Intensity (TOTALR)	215
A. General Discussion	215
B. Blockage of Plume-Airframe Calculations (SUMA, TRANS)	216
C. Blockage of Internal Engine Emissions (ENGOBS)	217
VII. Lockon Range	221
A. Discussion	221
IX. References	222
X. Appendix A - Spectral Plots of Backgrounds	225

LIST OF FIGURES

<u>Figure</u>		<u>Page</u>
1.	Overlay Structure.	7
2.	Schematic Diagram of Jet Flowfields.	14
3.	Particle Diffusivity of Beads.	34
4.	Multiple Slot Film Cooling.	52
5.	Convection-Film Cooling Scheme.	55
6.	Transpiration Cooling, Sectioned, Porous - Wall Model.	59
7.	Geometry Parameters Used in the Definition of the View Factor.	62
8.	Frustrum Geometry Variables.	63
9.	Direction of Cosine Angles Defined.	65
10.	Geometry Used to Determine the Infinitesimal Area Expression for a Frustrum.	71
11.	Unit Vectors for Cylindrical Coordinates.	72
12.	Subdivision of Receiver Node Axial Length for Numerical Integration.	91
13.	Subdivision of Source Node Axial Length for Numerical Integration.	91
14.	Definition of the Variables Required for a Disc Node.	95
15.	Geometry Used to Determine the Expression for the Elemental Area on a Disc.	98
16.	Subdivision of Receiver Node Radial Length for Numerical Integration.	103
17.	Subsivision of Source Node Radial Length for Numerical Integration.	105
18.	Schematic of Engine Surface Frustrum.	106
19.	Geometry Involved in a Typical Visibility Determination Performed by Subroutine RING.	111

LIST OF FIGURES (Cont'd)

<u>Figure</u>		<u>Page</u>
20.	Geometry Associated with the Visibility Studies Made When $Y_{\text{source}} = Y_{\text{receiver}}$.	114
21.	Schematic of Visibility Limits.	119
22.	Range Integration for ϕ .	120
23.	Sample Situations with No Solution.	121
24.	Cone of Vision Envelopes Shadowing Body.	121
25.	Geometry Involved in a Typical Visibility Determination Performed by Subroutine BODY.	124
26.	Schematic of Flow in a Crosswind.	140
27.	Schematic Indicating Balance of Forces.	140
28.	Cross Sectional Configurations of a Jet in a Lateral Flow at Various Distances from the First Section.	143
29.	The Axis of a Jet in a Lateral Deflecting Flow.	146
30.	Projections of Exhaust Surfaces to Determine Additional Ray Intercept Points.	148
31.	Critical Elevation Angle for Plume-Through-Plume Calculation.	152
32.	Flowfield Intercept Points for Single and Dual Plumes.	152
33.	X-Y Project of Primary Exhaust System and Image Exhaust System About Plane of Symmetry.	154
34.	Image of a Single Point.	155
35.	Schematic to Determine Plume-Ray Segments.	158
36.	Schematic of a Diatomic Molecule.	164
37.	Schematic FORTRAT Diagram.	175
38.	Emissivity of H_2O , 1.38 and 1.8μ Bands.	192
39.	Emissivity of H_2O , 2.7μ Band for $T = 1000^\circ R$.	193
40.	Emissivity of H_2O , 2.7μ Band for $T = 2000^\circ R$.	194

LIST OF FIGURES (Concluded)

<u>Figure</u>		<u>Page</u>
41.	Emissivity of CO ₂ , 4.3μ Band, P = 1 Atms.	195
42.	Emissivity of CO ₂ , 4.3μ Band, P = 0.06 Atm.	196
43.	Emissivity of H ₂ O, 6.3μ Band.	197
44.	Emissivity of H ₂ O for Pure Rotation Band.	198
45.	Comparison of Spectral Radiance of Nonisothermal H ₂ O with Calculations.	199
46.	Comparison of Spectral Radiance of Nonisothermal CO ₂ with Calculations.	200
47.	Cylindrical Cloud of Aerosol Particles Which Absorbs and Scatters the Incident Beam.	201
48.	Extinction Efficiency, X _T , and Ratio of Scatter to Absorption Efficiency for a Graphite Sphere as a Function of the Size Parameter, X.	206
49.	Complex Index of Refraction of Carbonaceous Materials as a Function of Wavelength.	207
50.	Differential Element of a Cloud of Aerosol Particles.	208
51.	Schematic Demonstrating the Computational Techniques Used in PLUMIR.	211
52.	Schematic of Plume Strips with Projection of Quadrilateral onto Plane Normal to Observer.	217
53.	Projection of Quadrilateral onto X = 0 Plane.	218
54.	Projection of Nose Area onto X = 0 Plane.	218
55.	Y-Z Plane with Projections.	219
56.	Determination of Blockage of a Ring Segment.	220

Accession For	NTIC G-1111	
DTIC TAB	Unannounced	
Justification		
By		
Distribution/		
Availability Codes		
Availand/or		
Dist		

LIST OF TABLES

<u>Table</u>		<u>Page</u>
1.	Use of Data by Routes.	8
2.	Atmospheric Temperature.	12
3.	Saturated Water Vapor Pressure.	12
4.	Coefficients of Conservation Equations.	22
5.	Fundamental Frequencies of CO ₂ and H ₂ O.	165
6.	Transition Band Centers and Integrated Intensity.	167
7.	Equation and Constants for Energy Levels.	169

SECTION I

INTRODUCTION

The SCORPIO-N computer program has been developed by the General Electric Company to predict the infrared radiation emitted by turbojet-, turboshaft-, or turbofan-propelled aircraft at the source and as intercepted by the observer (whether a missile or a measuring instrument). In addition, this program can compute the lock-on ranges for specified missiles to assess the vulnerability of the aircraft at any flight condition and from any elevation or aspect angle. Infrared radiation can be evaluated for any wavelength region between 1 and 20 μ m.

A. Background

Current infrared-guided missiles can detect and destroy aircraft from relatively long distances. Future IR missiles will be even more sensitive and destructive. The engine designer must select cycles and engine configurations that present as small a target as possible to these missile threats. To accomplish this, he must know the IR emissions from the aircraft and be able to judge the success of schemes to suppress these emissions.

Measurements are invaluable in determining the IR emissions for selected aircraft situations but cannot possibly be made for all aircraft and for all situations. This is obviously true in the engine design phase. In addition, understanding of the fundamental sources of these emissions is essential to the invention or evaluation of new suppression concepts. An accurate prediction tool, therefore, is vital to the process of reducing the vulnerability of an aircraft to IR-guided missiles.

As a supplier of jet engines for military aircraft, the General Electric Company has developed a series of computer programs to predict the IR signatures and vulnerability of IR-guided missiles. The SCORPIO-N computer program presented in this report is the latest in the series. It is an outgrowth of the SCORPIO-IIIA program (Reference 1) and the SPRITE program (Reference 2) with improvements to the plume module which permit studies of truly three-dimensional flow fields.

B. Problem Statement

The evaluation of instantaneous vulnerability of a particular jet-powered aircraft to a particular missile is the problem SCORPIO-N attempts to solve. The solution conveniently divides into six separate problem areas.

1. Emissions from the internal hot parts of the jet engine.
2. Definition and distribution of the flow field parameters.

3. Evaluation of gaseous emission and transmission including atmospheric effects.
4. Airframe contributions including emissions, and installation effects.
5. Combination of the results of the preceding four areas.
6. Missile characteristics to evaluate the range at which a missile can discriminate the target from the background.

Each of these problem areas is summarized in the following paragraphs.

1. Internal Engine Emissions

The spectral IR emission, J , from a solid surface, S , is obtained at a uniform temperature T_s , using Planck's Law as:

$$J_{\lambda_s} = A_s \epsilon_{\lambda_s} \frac{C_1}{\lambda^5} \left(e^{C_2/\lambda T_s} - 1 \right) \quad (1)$$

where

$$C_1 = 76805.4 \text{ watts-}\mu^4/\text{sr/in.}^2$$

$$C_2 = 2.5884 \times 10^4 \text{ microns} - ^\circ \text{R}$$

$$\lambda = \text{wavelength (microns)}$$

$$A_s = \text{surface area (in.}^2\text{)}$$

$$J_\lambda = \text{surface spectral emissivity}$$

$$T_s = \text{surface temperature, } ^\circ \text{R}$$

$$J_{\lambda_s} = \text{spectral emission}$$

The total radiation (or radiosity) seen by an observer from a surface consists not only of the direct emissions, but also consists of the reflections of emittances from all other engine surfaces which leave the given surface.

Therefore, the ingredients entering into the evaluation of the radiant emissions from the interior engine surface are the temperatures, the emissivities and reflectivities, the projected areas, and the interchange factors between each pair of surfaces.

a. Temperatures

Temperatures can be measured, estimated, or calculated using basic heat-transfer relationships. Since radiation depends on temperature exponentially, each temperature difference of 50° F or more typically is represented by a different surface. In normal jet engine applications, this would result in at least 20 different surface temperatures.

If the temperatures are calculated, the basic modes of heat transfer to be considered are conduction, convection, radiation, and transpiration.

b. Geometry

The geometry can be represented by tabled projected areas of given temperature and emissivity located and oriented with respect to the observer. The view factors of each surface to every other surface also can be tabled into the program along with the projected areas and emissivities in order that diffuse reflections can be included in the total radiation.

A higher order of complexity is to specify axisymmetric geometries and permit the program to calculate view factors and projected areas. These capabilities are available in SCORPIO-N. The calculations for nonsymmetric configurations are not included.

c. Reflectivities

The reflection of radiant intensity at a surface can be a function of either specular or diffuse absorption and of specular or diffuse reflection, the angle of incidence, the wavelengths, and the surface temperatures. The surface of jet engines, in general, tend to be diffuse absorbers and reflectors to the first order of approximation for reflections. This is the only kind of reflection considered in SCORPIO-N. Both reflectivity and emissivity, however, are permitted to vary with wavelength.

2. Flow Field Definition

a. Calculations

Flow fields, in practice, are three-dimensional in nature, influenced by nonaxial mounting, tapered installations (boattails), nonuniform exit conditions, crosswinds, shocks, and possibly other forces such as incomplete combustion. All of these complications have not as yet been solved analytically.

The current analytical program solves a nonuniform axially symmetric flowfield with external flow. The analysis contains the usual axial momentum, energy, and diffusion conservation equations: and, in addition, the conservation of turbulent kinetic energy and conservation of tangential momentum. This results in a higher order of accuracy than the simpler viscosity model techniques.

b. Tabulated Input

SCORPIO-N accepts tabulated input for either (1) 2-dimensional axisymmetric flow with temperature and concentrations as functions of radius at each axial location or, (2) 3-dimensional flows with or without axes or symmetry where the temperature is input as a function of location and concentrations are calculated from the temperature and the fuel-air ratio.

3. Gaseous Plume Emissions/Absorption

Unlike the continuous emission-spectrum characteristics of solids, the emission and absorption from gases occurs in discrete lines that depend on the local thermodynamic and molecular properties of the gas. Band models, strengths and distributions for IR active constituents both in the plume and in the atmosphere. The band models deal only with homogeneous gases, so an additional complexity is present for the nonhomogeneous paths that occur through the plume and atmosphere to the observer.

After suitable analysis the resultant spectral transmissivity of a homogeneous gas often takes the form:

$$\tau_{\lambda} = \exp \left[- \frac{S}{d} X / \sqrt{1 + \left(\frac{S}{\gamma} \right) X} \right] \quad (2)$$

where,

S = the average line strength

d = the line spacing

γ = related half-width

X = the optical depth

For weak lines or for thin path lengths:

$$\frac{S}{\gamma} X \ll 1 \text{ and}$$

$$\tau_{\lambda} \approx \exp \left(- \frac{S}{d} X \right)$$

In this instance, the logarithms of the transmissivities of two neighboring paths of gas are additive, and the problem of a nonhomogeneous medium (or a plume as seen through the atmosphere) becomes relatively simple to evaluate. More often than not, the term SX/γ is quite large, especially for CO_2 in a plume or at long distance in the atmosphere: more elaborate methods must be devised than merely multiplying transmissivities together.

It is necessary to invoke the complete transfer equation:

$$J_{\lambda} = \int_0^L N_{b\lambda}(T) d\tau \approx \sum_{i=1}^N N_{b\lambda}(T_i) \Delta\tau_i \quad (3)$$

where,

J_{λ} = spectral radiant intensity

$N_{b\lambda}$ = blackbody spectral radiance at temperature, T

The extinction coefficients due to particles in the flow are also included in the transmissivity calculation. The transmissivity over a long path can then be evaluated from the averaged line properties along the path in a manner similar to the Curtis-Godson approximation.

CO and scattering by atmospheric particles must be included to properly assess the plume emissions. Since the hotter gases of the plume absorb over a wider band than those of the cooler atmosphere, the transmission of internal hot parts radiation must be related to the plume characteristics as well as to the atmosphere.

4. Airframe

The airframe itself emits radiation and can be a major contributor to the target signal - especially from the forward hemisphere. The emissions from the airframe are at a lower temperature but cover a much larger area than engine emissions. In addition to the direct emissions, the airframe can affect the IR by blocking the view of the plume and/or engine at certain aspect angles. In the lower wavelength bands, reflections from the sun (sun-glint) often will supersede all other contributors. When viewed from above, the earth shine may predominate, particularly in regions of atmospheric windows. Because of the large surface areas, reflections of the plume off the airframe also may be significant. Only the emissions and blockage are considered in SCORPIO-N.

5. Totalling

The totalling of all sources of radiation is complicated by the interactions of the different parts: the blockage of the plume by the airframe, the obscuration of the airframe and engine hot parts by the plume, the existence of more than one plume engine on an airframe, the obscuration of one plume by another, the mixing of two plumes, the influence of eddies or shock off the airframe on the plumes, the effects of external flows when the engine axis does not lie in the flight direction, and the nonaxial flows resulting from noncylindrical surfaces (external boattail, internal expanding flow) which promote additional mixing. SCORPIO-N considers only blockage by the airframe and obscuration by the plume at all aspect angles and plume-through-plume obscuration at near-horizontal viewing angles.

6. Missile Characteristics

When a missile receives target radiation, it must be processed internally. The resultant signal must be large enough to overcome the internal noise of the system and to discriminate such noise from background-induced signals. The sensitivity of the missile optics to the wavelength of the incoming emission also must be factored in. Knowledge of the scanning method used in the design of the missile detection systems is necessary to determine the ability of a missile to obtain and maintain target lockon. This ability also is a function of the relative velocities and direction of the missile and target. SCORPIO-N takes a simplified approach to the missile target interrelation as a first step in the problem solution. It assumes that all of the missile parameters are known input and computes a lock-on range for a minimum and maximum signal-to-noise ratio. The effective radiations for at least two distances must have been calculated for each angle at which lockon is required. The resolution of the missile optics (or measurement instrument) is not factored into the spectral results.

C. SCORPIO-N Structure

1. Discussion

The calculation of an aircraft signature and its vulnerability logically subdivides into sections according to the problem areas (or functions described above):

- The hot-parts emissions/reflections
- The flow field parameter distribution
- The plume emission/transmission properties
- The airframe emissions and obstructions
- The totalling of the many sources of emissions
- The lock-on calculation

Programs have been developed independently by various organizations to solve each of these problem areas. From these, selected programs have been modified to form modules of the SCORPIO-N system. These modules are almost independent, related only by an input/output problem file. One additional module of the SCORPIO-N system manipulates the input/output files and stores data common to more than one module.

Since the modules are independent, only one need be in memory at a time. The modules, therefore, are overlaid as shown in Figure 1.

Overlay	Module	Overlay	Title
(1, 0)	UPDATE		
(2, 0)	JETMIX	(2, 1)	INLINK
		(2, 2)	CPLINK
		(2, 3)	TBLINK
(3, 0)	FLOTAB		
(4, 0)	SIGNIR	(4, 1)	RIMAYN
		(4, 2)	LINKT
		(4, 3)	NVIEW
		(4, 4)	TMP
		(4, 5)	REDEYE
(5, 0)	PLUMIR		
(6, 0)	AMFM	(6, 1)	SHADIN
		(6, 2)	CALC
		(6, 3)	PLOT
(7, 0)	BBODY		
(10, 0)	TOTALR	(10, 1)	PLUM
		(10, 2)	ENGIN
(11, 0)	LOCKON	(11, 1)	B1
		(11, 2)	B2
		(11, 3)	B3
		(11, 4)	B4
		(11, 5)	B5
(12, 0)	CWFLO		

Figure 1. Overlay Structure.

2. Module Descriptions

A brief discussion of the modules and their functions follows. The output records are ordered by a function number (or route number). The discussions will be sequenced according to these route numbers.

Route 1 - UPDATE Module

General information necessary to more than one module is input in this overlay. Only the flow field modules can be run independently of this module. The data entered in UPDATE and the route numbers for which these data must be supplied are listed in Table 1.

Table 1. Use of Data by Routes

Data	Used by Routes
Wavelength Intervals	3, 4, 6, 7
Engine Schematic	2, 4, 6
Flight Velocity	2, 7
Atmospheric Conditions	2, 4
Elevation Angle	4, 5
Flow Field Schematic	4, 5

Route 2

The flow field is provided to the other routines via Route 2. There are three different modules performing this function, and they are specified by NTYP.

1) NTYP = 1 JETMIX Module

The flow field parameters for axisymmetric flows are calculated from the input at the nozzle exit plane to a specified downstream location.

INLINK - reads and processes the input

CPLINK - calculates the flow field parameters

TBLINK - tables the flow field for use in Route 4 and stores a schematic definition for use in Routes 4 and 5

2) NYTP = 2 FLOTAB Module

Axisymmetric flow field parameters are read in tabular form and stored for use in Route 4; a schematic definition is stores for Routes 4 and 5.

3) NYTP = 3 CWFLO Module

Three-dimensional flow field parameters are read in tabular form and stored for use in Route 4. NOTE: The plume schematic is not provided from this module. It must be obtained from Route 4 or input in Route 1 or Route 4.

Route 3 - SIGNIR Module

Internal exhaust system emissions are evaluated in this overlay. As a part of this, view factors may be input or calculated from geometry inputs; temperatures may be input or calculated from basic-heat transfer information; projected areas may be calculated or input; and, source emissions may be calculated and printed out.

Route 4 - PLUMIR Module

Plume emissions, as attenuated by the plume and atmosphere, and transmissivity of the plume/atmosphere are calculated spectrally over the previously specified wavelength bands. Calculations are performed along a number of rays emanating from specified observer locations.

Route 5

The airframe emissions and obstructions defined in Route 5 are of two types:

1) NYTP = 1 AMFM Module

The coordinates of a multifaceted model of the airframe are input. The projected areas and obstructions are tabled output for each observer angle. Alternatively, the airframe can be plotted at any aspect or elevation angle.

2) NTYP = 2 BBODY Module

The resultant area temperature tables representing the airframe may be input directly for each aspect angle.

Route 6 - TOTALR Module

The totalling in this module consists of combining the results of Routes 3, 4, and 5 and integrating over the specified wavelength bands to provide band total emissions. The totalling may be of three types:

- 1) NTYP = 1 integrate plume only
- 2) NTYP = 2 add engine hot parts to plume totals
- 3) NTYP = 3 integrate for airframe, plus plume, plus engine.

Route 7 - LOCK-ON Module

Spectral output from Route 6 is modified by missile sensitivities and background specifications. The lock-on ranges for the specified missiles then are calculated.

The particular angles and wavelengths used in the various modules may differ in order to include the variations and yet maintain maximum efficiency. For this reason, in combining the results from the different modules, linear interpolations are made freely, but extrapolations usually are prohibited.

D. Introduction to Analysis

Certain of the modules included in SCORPIO-N required intensive theoretical derivations that were beyond the scope of the presentations in Volume I - User Manual or Volume II - Programmers Manual (References 1 and 2). It is the purpose of this manual to provide this background analysis and some associated verification of the analytical techniques. The analysis will include atmospheric properties, flow-field mixing phenomena, hot parts cooling and viewfactor calculations, gaseous transmission model development and blockage considerations for the engine and plume.

SECTION II

ATMOSPHERIC CONDITIONS

During the course of calculating infrared spectral transmission values, it becomes clear that some means is needed to obtain atmospheric conditions quickly. The main factors in atmospheric infrared attenuation are absorption by water vapor, carbon dioxide, ozone, and scattering by airborne particles. The water vapor content of the atmosphere is weather-dependent. Thus, either the amount of water vapor between the target and observer (the optical thickness) must be known for a particular problem or average-weather and relative-humidity assumptions must be made. The carbon dioxide content of the atmosphere is taken to be 3.3×10^{-4} parts per unit volume of air. The ozone content of the atmosphere is neglected.

From Reference 3, the scattering coefficients of transmission is calculated as a function of wavelength, range, and visibility:

$$\tau_{s\lambda} = e^{-\frac{3.91}{V} \left(\frac{\lambda}{0.55} \right)^{-q} \cdot VR} \quad (1)$$

where,

$\tau_{s\lambda}$ = Transmissivity due to scattering at wavelength λ

V = Visibility (kilometers)

q = $0.585 V^{1/3}$

λ = Wavelength (microns)

VR = Range (kilometers)

The properties of the atmosphere are tabled as a function of distance from the target for a standard atmosphere assumed according to Table 3.

The Molal humidity then is determined from:

$$M = P_v/P_a = P_v/(P_T - P_v)$$

Table 2. Atmospheric Temperature.

	Altitude (km)	Temperature (° R)
Troposphere	0-11	$T = T_g - \frac{72h}{11}$
Stratosphere	11-25	$T = T_g - 72$
Ionosphere	25-48	$T = T_g = 72 \left(1 - \frac{h-25}{23}\right)$
	48-	

T_g = Ground temperature, ° R

h = Altitude, km

$P = \exp (1 - h/8)$ pressure, atms

The pressure of saturated vapor at dry bulb temperature can be found from the following table.

Table 3. Saturated Water Vapor Pressure.

<u>TL(° C)</u>	<u>Pd (atmos)</u>	<u>TL(° C)</u>	<u>Pd (atmos)</u>
-80	0.531E-6	0	6.107E-3
-70	2.577E-6	10	1.228E-2
-60	1.076E-5	20	2.338E-2
-50	3.947E-5	30	4.243E-2
-40	1.292E-4	40	7.377E-2
-30	3.827E-4	50	1.234E-1
-20	1.039E-3	60	1.922E-1
-10	2.865E-3	--	---

The water vapor pressure P_v , then is given by:

$$P_v = r_h * P_D$$

where r_h is the relative humidity.

SECTION III

FLOWFIELD MODULE ANALYSIS (JETMIX)

A. Discussion

The distribution of temperature, pressure, and concentration of IR active constituents in the plume flow field is needed as input to calculate plume emissions or transmissivity. Either these parameters can be calculated within the SCORPIO-N program or data obtained from measurements or estimates can be tabled indirectly.

The calculations, performed in the JETMIX module of SCORPIO-N, are axisymmetric or plane symmetric only. They do, however, consider effects of coannular flow, external flow, turbulent kinetic energy, and swirl.

SCORPIO-calculated flow fields are plane or axisymmetric turbulent jets exhausting into regions of constant or variable pressure. The constant pressure problems are referred to as "free" jets and are used to determine the parameter distributions in an external flow. The variable pressure problem is referred to as "confined mixing" and pertains to coannular flows internal to the exhaust system.

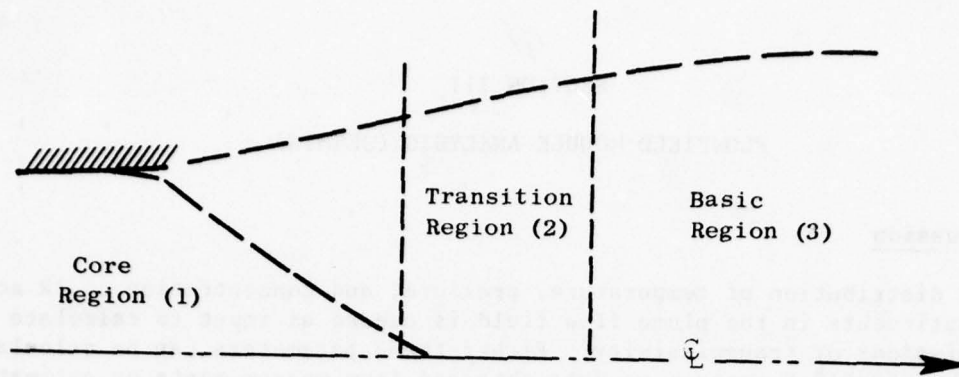
Free mixing can be calculated for a single jet, Figure 2a, with or without swirl, with uniform or nonuniform radial profiles at the exit plane, or for two coannular jets, Figure 2b, with external flow, uniform profiles, and no swirl. The confined mixing problem, Figure 2c, includes specification of a centerbody and an outer boundary. The free jet problem with a centerbody (extended plug) is approximated as a confined flow problem with a far-removed outer boundary.

The calculation model solves the conservative equations of continuity, energy, axial and tangential momentum, turbulent kinetic energy, and diffusion of species for a compressible turbulent jet. The differential equations are solved using finite difference techniques. The detailed analysis follows.

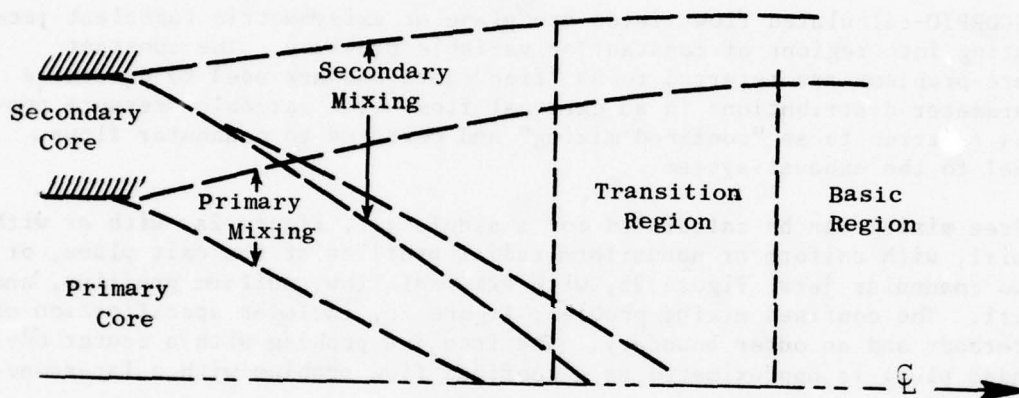
B. Analysis

1. Governing Equations

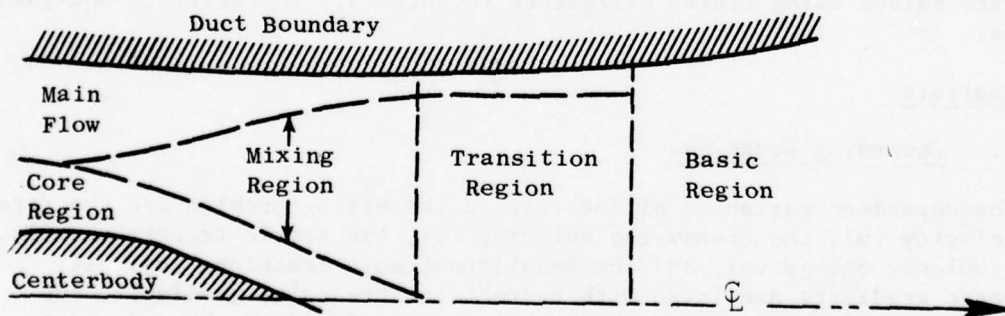
The dependent variables of interest in the mixing problem are the streamwise velocity (u), the transverse velocity (w), the static temperature (T), the turbulence energy (e), and the constituent mole fractions (α). If transverse gradients are large with respect to streamwise gradients, the equations of motion describing the turbulent flow field may be reduced to boundary layer form. The governing equations for compressible turbulent plane or axisymmetric swirling jets are:



A. Single Jet



B. Dual Jets



C. Confined Jet

Figure 2. Schematic Diagram of Jet Flowfields.

Continuity

$$\frac{\partial(\rho u y^\epsilon)}{\partial x} + \frac{\partial}{\partial y} (\rho v y^\epsilon) = 0 \quad (1)$$

Conservation of Axial Momentum

$$\rho u \frac{\partial u}{\partial x} + \rho v \frac{\partial u}{\partial y} = \frac{1}{y^\epsilon} \frac{\partial}{\partial y} \left(y^\epsilon \tau_{yx} \right) - g_c \frac{\partial p}{\partial x} \quad (2)$$

Conservation of Radial Momentum

$$\rho \frac{w^2}{r} = \frac{\partial p}{\partial r} \quad (3)$$

Conservation of Tangential Momentum

$$\rho u \frac{\partial e}{\partial x} + \rho v \frac{\partial w}{\partial r} = \frac{1}{r^2} \frac{\partial}{\partial r} \left(r^2 \tau_{r\theta} \right) - \frac{\rho v w}{r} \quad (4)$$

Conservation of Turbulent Kinetic Energy

$$\rho u \frac{\partial e}{\partial x} + \rho v \frac{\partial e}{\partial y} = \frac{1}{y^\epsilon} \frac{\partial}{\partial y} \left(\mu D y^\epsilon \frac{\partial e}{\partial y} \right) + \tau_{r\theta} \left[r \frac{\partial}{\partial r} \left(\frac{w}{r} \right) \right] - \mu \frac{c D e}{L_f^2} + \tau_{yx} \frac{\partial u}{\partial y} \quad (5)$$

Conservation of Energy

$$\rho u C_p \frac{\partial T}{\partial x} + \rho v C_p \frac{\partial T}{\partial y} = \frac{1}{y^\epsilon} \frac{\partial}{\partial y} \left[k_e y^\epsilon \frac{\partial T}{\partial y} \right] + y^\epsilon \mu D \frac{\partial e}{\partial y} + \frac{\mu e}{M} y^\epsilon \sum_{i=1}^e \frac{c_{p_i}}{s_i} \frac{\partial \alpha_i}{\partial y} \frac{\partial T}{\partial y} \quad (6)$$

$$\frac{\mu e}{g_j} \left(\frac{\partial u}{\partial y} \right)^2 + \mu \left[\frac{\partial w^2}{\partial r} + \frac{1}{r} \frac{\partial}{\partial r} \left(\frac{w}{2} \right)^2 \right] + \frac{u}{J} \frac{\partial p}{\partial x} + \frac{\rho v w^2}{r}$$

Conservation of Species

$$\rho v \frac{\partial \alpha_i}{\partial x} + \rho v \frac{\partial \alpha_i}{\partial y} = \frac{1}{y\epsilon} \frac{\partial}{\partial y} \left(\frac{\mu_e}{S_{ie}} y\epsilon \frac{\partial \alpha_i}{\partial y} \right) \quad (7)$$

The applicable boundary conditions are:

on the jet axis or $y = 0$:

$$\frac{\partial u}{\partial y} = \frac{\partial e}{\partial y} = \frac{\partial T}{\partial y} = + \frac{\partial \alpha_i}{\partial y} = w = 0 \text{ (symmetry)} \quad (8)$$

and on the boundary of the jet or $y = d_p$:

$$\begin{aligned} u &= u_e & w &= 0 \\ T &= T_e & p &= p_e \\ e &= e_e \\ \alpha_i &= \alpha_{ie} \end{aligned} \quad (9)$$

The system of equations presented above is not closed. There are 10 unknowns ($u, v, w, \tau_{rx}, \tau_{r\theta}, P, \rho, e, T$, and α_i) and 8 equations including the equation of state. Therefore, 2 more auxiliary equations relating to the shear stress τ_{rx} and $\tau_{r\theta}$ to the mean characteristics of flow are introduced.

$$\begin{aligned} \tau_{yx} &= \overline{\rho u'v'} = \mu \frac{\partial u}{\partial y} \\ \tau_{r\theta} &= -\rho v'w' = \mu \quad r \cdot \frac{\partial}{\partial r} (w/r) \end{aligned} \quad (10)$$

The molecular contribution to shear stress is so small, compared to apparent (or Reynolds) stress, it may be neglected.

Thus, we have

$$\begin{aligned} \tau_{yx} &= \overline{-\rho u'v'} = \mu_e \frac{\partial u}{\partial y} \\ \tau_{r\theta} &= \overline{-\rho u'w'} = \mu_{r\theta} \quad r \frac{\partial}{\partial y} (w/r) \end{aligned} \quad (11)$$

where μ_e and $\mu_{r\theta}$, the effective viscosities, analogous to molecular viscosity in laminar flow are defined empirically.

The governing equations (11) may be cast in a more convenient form by nondimensionalizing with respect to the primary jet diameter and the discharge flow field variables u_p , e_p , T_p . The requisite relations are:

$$\begin{aligned} X &= \frac{x}{d_p}, \quad y = \frac{2y}{d_p} = \frac{2R}{d_p} \\ U &= \frac{u}{u_p}, \quad V = \frac{v}{u_p}, \quad E = \frac{e}{e_p}, \quad \theta = \frac{T}{T_p}, \quad W = \frac{w}{u_p} \end{aligned} \quad (12)$$

Substitution into equations 1 to 7 yields:

Continuity

$$\frac{\partial(\rho U Y^e)}{\partial X} + 2 \frac{\partial}{\partial Y} (\rho V Y^e) = 0 \quad (13)$$

X-Momentum

$$\rho U \frac{\partial U}{\partial X} + 2 \rho V \frac{\partial U}{\partial Y} = \frac{\partial P}{\partial Y} \left(\frac{4}{u_p d_p Y^e} \frac{\partial}{\partial Y} \mu_e Y^e \frac{\partial U}{\partial Y} \right) - \frac{g_c}{U_p^2} \frac{\partial P_{ex}}{\partial X} \quad (14)$$

Radial Momentum

$$\rho \frac{W^2}{Y} = \frac{g_c}{u_p^2} \frac{\partial p}{\partial y} \quad (15)$$

Tangential Momentum

$$\rho U \frac{\partial W}{\partial X} + 2 \rho V \frac{\partial W}{\partial Y} = \frac{4}{Y^2 e} \frac{\partial}{\partial Y} \left[\frac{Y^3}{d_p} \frac{\mu_r}{u_p} \frac{\partial}{\partial Y} \left(\frac{W}{Y} \right) \right] - 2 \rho \frac{VW}{Y} \quad (16)$$

Turbulent Kinetic Energy

$$\begin{aligned} \rho U \frac{\partial E}{\partial X} + 2 (\rho V) \frac{\partial E}{\partial Y} &= \frac{4}{u_p d_p Y^e} \frac{\partial}{\partial Y} \mu D Y^e \frac{\partial E}{\partial Y} + \frac{4 u_p}{g_c J d_p e_p} \mu_t \left(\frac{\partial U}{\partial Y} \right)^2 \\ &+ \frac{4 u_p}{g_c J d_p e_p} \mu_\theta \left[Y \frac{\partial}{\partial Y} \left(\frac{W}{Y} \right) \right]^2 - \frac{\mu c D d_p E}{u_p L_t^2} \end{aligned} \quad (17)$$

Species Continuity

$$\rho U \frac{\partial \alpha_i}{\partial X} + 2 (\rho V) \frac{\partial \alpha_i}{\partial Y} = \frac{4}{u_p d_p Y^\epsilon} \frac{\partial}{\partial Y} \left(\frac{\mu_e Y^\epsilon}{S_{i_e}} \frac{\partial \alpha_i}{\partial Y} \right) \quad (18)$$

Energy

$$\begin{aligned} \rho U \frac{\partial \theta}{\partial X} + 2 (\rho V) \frac{\partial \theta}{\partial Y} = & \frac{4}{C_p u_p d_p Y^\epsilon} \frac{\partial}{\partial Y} \left(k_e Y^\epsilon \frac{\partial \theta}{\partial Y} \right) + \left(\frac{U}{J C_p T_p} \right) \frac{\partial P_{ex}}{\partial X} \\ & + \frac{\mu C_d p_e p_{ED}}{C_p T_p u_p L_t^2} + \frac{2 \rho U p^2}{g_c J C_p T_p} \frac{V W^2}{Y} + \frac{4 \mu_e}{u_p d_p M} \sum_i \frac{C_{p_i}}{S_{i_e}} \frac{\partial \alpha_i}{\partial Y} \frac{\partial \theta}{\partial Y} \end{aligned} \quad (19)$$

The boundary conditions become:

$$\begin{aligned} @Y = 0 \quad & \frac{\partial U}{\partial Y} = \frac{\partial E}{\partial Y} \quad \frac{\partial \theta}{\partial Y} = \frac{\partial \alpha_i}{\partial Y} = W = 0 \\ @Y = Y_{ex} \quad & U \rightarrow U_{ex} \\ & E \rightarrow E_{ex} \\ & \theta \rightarrow \theta_{ex} \\ & \alpha_i \rightarrow \alpha_{iex} \\ & W \rightarrow 0 \end{aligned} \quad (20)$$

These equations (13 to 19) are quasilinear, parabolic, and strongly coupled. A simple quick forward marching numerical technique due to Spalding and Patanker has been used to solve the system. This technique solves the system in streamline coordinates. The main novelty of this method lies in the choice of the grid, which adjusts its width automatically at each forward step so as to conform to the thickness of the mixing layer in which significant variations are occurring. This method is a fully implicit one, completely stable, accurate, and economical. This is one of the widely used techniques in the field and is well-documented.

2. Transformation to Von Mises Coordinates

The continuity equation (13) may be identically satisfied by introduction of the stream function ψ . Define a modified stream function satisfying continuity as follows.

$$\frac{\partial \psi}{\partial Y} = \frac{1}{2} \rho U Y^\epsilon \quad \frac{\partial \psi}{\partial X} = -\rho V Y^\epsilon \quad (21)$$

Introduce the following new variables

$$\zeta = \zeta(X), \quad \zeta = X$$

$$\psi = \psi(X, Y)$$

Then, using the chain rule, the following operators may be defined:

$$\frac{\partial}{\partial X} = \frac{\partial \zeta}{\partial X} \frac{\partial}{\partial \zeta} + \frac{\partial \psi}{\partial X} \frac{\partial}{\partial \psi} = \frac{\partial}{\partial \zeta} - (\rho V) Y^\epsilon \frac{\partial}{\partial \psi} \quad (22)$$

$$\frac{\partial}{\partial Y} = \frac{\partial \zeta}{\partial Y} \frac{\partial}{\partial \zeta} + \frac{\partial \psi}{\partial Y} \frac{\partial}{\partial \psi} = \frac{1}{2} \rho U Y \frac{\partial}{\partial \psi}$$

Using these relations in equations 13-19 results in the final set of differential equations:

X-Momentum

$$\frac{\partial U}{\partial X} = \left(\frac{1}{u_p d_p} \right) \frac{\partial}{\partial \psi} \left(\mu \epsilon \rho U Y^2 \frac{\partial U}{\partial \psi} \right) - \left(\frac{g_c}{\rho U_p^2} \right) \frac{\partial p_{ex}}{\partial X} \quad (23)$$

Radial Momentum

$$W^2 = \left(\frac{g_c}{2 \rho U_p^2} \right) \cdot \rho U Y^2 \frac{\partial P}{\partial \psi} \quad (24)$$

Tangential Momentum

$$\frac{\partial}{\partial X} \left(\frac{W}{Y} \right) = \frac{1}{u_p d_p} \frac{1}{Y^2} \frac{\partial}{\partial \psi} \left[\mu \theta \rho U Y^4 \frac{\partial}{\partial \psi} \left(\frac{W}{Y} \right) \right] - \left(\frac{W}{Y} \right) \frac{1}{Y} \left[\frac{\partial Y}{\partial \zeta} + 2 \frac{V}{U} \right] \quad (25)$$

Turbulent Kinetic Energy

$$\frac{\partial E}{\partial X} = \left(\frac{1}{U_p d_p} \right) \frac{\partial}{\partial \psi} \left(\mu D \rho Y^2 \epsilon \frac{\partial E}{\partial \psi} \right) + \left(\frac{\rho U Y^2 \epsilon U_p \mu_t}{g_c J e_p e_p} \right) \left(\frac{\partial U}{\partial \psi} \right)^2 - \frac{\mu_c D d_p E}{p U \mu_p L_t^2} + \quad (26)$$

$$\frac{u_p \mu \theta \rho U Y^2}{g_c J e_p d_p} \left[\frac{\partial}{\partial \psi} \left(\frac{W}{Y} \right) \right]^2$$

Species Continuity

$$\frac{\partial \alpha_i}{\partial X} = \left(\frac{1}{u_p d_p} \right) \frac{\partial}{\partial \psi} \left(\frac{\mu_e}{S_{i_e}} \rho U Y^{2\epsilon} \frac{\partial \alpha_i}{\partial \psi} \right) \quad (27)$$

Energy

$$\frac{\partial \theta}{\partial X} = \left(\frac{1}{u_p d_p C_p} \right) \frac{\partial}{\partial \psi} \left(k_e U Y^{2\epsilon} \frac{\partial \theta}{\partial \psi} \right) + \left(\frac{1}{\rho C_p J T_p} \right) \frac{\partial P_{ex}}{\partial X} + \left(\frac{\mu_e}{d_p u_p \bar{M} C_p} \right) x \quad (28)$$

$$\rho U Y^{2\epsilon} \sum \frac{C_{p_i}}{S_{i_e}} \frac{\partial \alpha_i}{\partial \psi} \left(\frac{\partial \theta}{\partial \psi} \right) + \frac{2 U_p^2}{g_c J C_p T_p} \cdot \frac{V}{U} \cdot \frac{W^2}{Y} + \frac{\partial C_{e_p}}{C_p T_p d_p} \left(\frac{1}{\rho U} \right) \frac{DE}{L_f^2}$$

Boundary Conditions

Taking the lower boundary as the zero streamline ($\psi = 0$) the boundary conditions become:

$$\begin{aligned} @ \psi=0 & \quad \frac{\partial U}{\partial \psi} = \frac{\partial E}{\partial \psi} = \frac{\partial \theta}{\partial \psi} = \frac{\partial \alpha}{\partial \psi} = W = 0 \\ @ \psi=\psi_{ex} & \quad U = U_{ex} \\ & \quad T = T_{ex} \\ & \quad \theta = \theta_{ex} \\ & \quad \alpha_i = \alpha_{iex} \\ & \quad W = 0 \end{aligned} \quad (29)$$

The physical coordinate Y may be recovered by integration of the equation for a stream function from $\psi = 0$ to a given streamline.

$$Y^{\epsilon+1} = Y_L^{\epsilon+1} + 2(1+\epsilon) \int_0^{\psi} \frac{d\psi}{\rho u} \quad (30)$$

The effective "outer edge" of the jet may be taken as the streamline where the maximum velocity difference across the jet is approached to a specific fractional degree.

The equations (23) to (24) in the Von Mises Coordinate system are all of the general diffusion equation form.

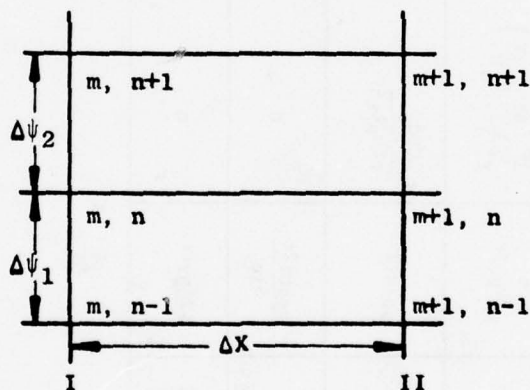
$$\epsilon \frac{\partial F}{\partial X} = \frac{\partial}{\partial \psi} \left(\beta \frac{\partial F}{\partial \psi} \right) + \eta \frac{\partial F}{\partial \psi} + \delta F + \gamma \quad (31)$$

where ϵ , α , β , η , δ and γ are distinct for each conservation equation. The coefficients in equation (31) are obtained by comparing each term in equation (31) to the corresponding one in each of equations (23 to 28). See Table 4.

3. Numerical Technique

The differential equations (23-28) are coupled principally through the normal derivative terms, and are of such a nature that a sequential solution technique may be utilized as opposed to direct simultaneous integration. The initial specific procedure is to solve the X-momentum equation for U and $\partial U / \partial \psi$. Using this, solve the tangential momentum for W . Then integrate the turbulent kinetic energy equation for E and $\partial E / \partial \psi$. Finally, the energy equation may be solved for θ using the results of the preceding solutions.

An implicit finite difference procedure employing the Thomas algorithm is utilized to effect the solution. Consider a grid network as shown in the following sketch.



x- ψ Grid

Conditions are known at station I and are to be determined at station II by solution of the following equation:

$$\epsilon \frac{\partial F}{\partial X} = \alpha \frac{\partial}{\partial \psi} \left(\beta \frac{\partial F}{\partial \psi} \right) + \delta F + \eta \frac{\partial F}{\partial \psi} + \gamma \quad (32)$$

Table 4. Coefficients of Conservation Equations.

	ϵ	α	β	δ	η	γ
Axial Momentum	1	$\frac{1}{u_p d_p}$	$\mu_e \rho u y^2 \epsilon$	0	0	$-\frac{g_c}{\rho u u_p} \frac{\partial p_e}{2 \partial x}$
Tangential Momentum	1	$\frac{1}{u_p d_p y^2}$	$\mu \theta^p u y^2 \epsilon$	$-\frac{1}{y^2} \left(\frac{\partial y}{\partial \xi} + \frac{2v}{u} \right)$	0	0
Turbulent Kinetic Energy	1	$\frac{1}{u_p d_p}$	$\mu_D \rho u y^2 \epsilon$	$-\frac{\mu C_D d_p}{\rho u u_p L_T^2}$	0	$\frac{\rho u y^2 u_p \mu_t}{g_c J d_p \epsilon} \left(\frac{\partial u}{\partial \psi} \right)^2 + \frac{u_p \mu \rho u y^2}{g_c J d_p \epsilon} \left[\frac{\partial}{\partial \psi} \frac{W}{Y} \right]^2$
Species	1	$\frac{1}{u_p d_p}$	$\frac{\mu_e \rho u y^2 \epsilon}{S_{ie}}$	0	0	0
Energy	1	$\frac{1}{u_p d_p C_p}$	$k_e \rho u y^2 \epsilon$	0	$\frac{\mu_e \rho u y^2 \epsilon}{d_p u_p M C_p} \sum \frac{C_{pi}}{S_{ie}} \frac{\partial \alpha_i}{\partial \psi}$	$\frac{1}{\rho C_p J T_p} \frac{\partial p_e}{\partial x} + \frac{\mu C_e p_e}{C_p T_p d_p \rho u L_T^2}$

For the mesh indicated in the above sketch, the X derivative may be approximated by a backward difference, and the ψ derivatives may be approximated as noncentered three-point differences in the following fashion:

$$\frac{\partial F}{\partial X} = \frac{F_{m+1, n+1} - F_{m, n}}{\Delta X} \quad (33)$$

$$\frac{\partial f}{\partial \psi} = \frac{\Delta \psi_1^2 F_{m+1, n+1} - F_{m+1, n} + \Delta \psi_2^2 F_{m+1, n} - F_{m+1, n-1}}{\Delta \psi_1^2 \Delta \psi_2 + \Delta \psi_2^2 \Delta \psi_1} \quad (34)$$

$$\frac{M2F}{\partial \psi^2} = \frac{2 \Delta \psi_1 F_{m+1, n+1} - \Delta \psi_1 + \Delta \psi_2 F_{m+1, n} + \Delta \psi_2 F_{m+1, n-1}}{\Delta \psi_1^2 \Delta \psi_2 + \Delta \psi_2^2 \Delta \psi_1} \quad (35)$$

Substituting these derivatives in (28) yields:

$$[(m+k)\Delta \psi_2^2 - \ell \Delta \psi_2] F_{m+1, n-1} + [\epsilon + \ell(\Delta \psi_1 + \Delta \psi_2) + (m+k) \Delta \psi_1^2 - \Delta \psi_1^2 - \delta \Delta X] F_{m+1, n} \quad (36)$$

$$[(m+k)\Delta \psi_1^2 - \ell \Delta \psi_1] F_{m+1, n+1} = \epsilon F_{m, n} + \gamma \Delta X$$

where:

$$\ell = \ell_{m, n} = \frac{2\alpha\beta\Delta X}{\Delta \psi_1^2 \Delta \psi_2 \Delta \psi_2 \Delta \psi_1}$$

$$m = m_{m, n} = \frac{2\alpha\beta\Delta X}{\Delta \psi_1^2 \Delta \psi_2 \Delta \psi_2 \Delta \psi_1}$$

$$k = k_{m, n} = \frac{\eta \Delta X}{\Delta \psi_1^2 \Delta \psi_2 \Delta \psi_2 \Delta \psi_1}$$

Evaluation of the quantities ϵ , α , β , γ , δ , η , and F at the known station I results in a set of linear simultaneous equations of the form:

$$a F_{n, m+1, n-1} + b F_{n, m+1, n} + g F_{n, m+1, n+1} = h_n \text{ for } n=2, N-1 \quad (37)$$

where:

$$a(\psi) = (m+k)\Delta\psi_2^2 - 2\Delta\psi_2$$

$$b(\psi) = \epsilon + 2(\Delta\psi_1 + \Delta\psi_2) + (m+k)(\Delta\psi_1^2 - \Delta\psi_2^2) - \delta\Delta X$$

$$g(\psi) = (m+k)\Delta\psi_1^2 - 2\Delta\psi_1$$

$$h(\psi) = \epsilon F_{m,n} + \gamma\Delta X$$

Inclusion of boundary conditions in finite difference form closes the system of linear algebraic equations. For most cases, the use of forward or backward differences at the boundaries is adequate. The boundary conditions then may be written in a general form as the linear combination of the dependent variable F and its ψ derivative:

$$\xi_1 F_1 + K_1 \left(\frac{dF}{d\psi} \right)_1 = \lambda_1$$

(38)

$$\xi_N F_N + K_N \left(\frac{dF}{d\psi} \right)_N = \lambda_N$$

The coefficients corresponding to a , b , g and h in the preceeding expressions are:

$$a_1 = 0$$

$$a_N = -K_N/\Delta\psi_N$$

$$b_1 = -K_1/\Delta\psi_1$$

$$b_N = \xi_N + K_N/\Delta\psi_N$$

$$g_1 = K_1/\Delta\psi_1$$

$$g_N = 0$$

$$h_1 = \lambda_1$$

$$h_N = \lambda_N$$

The resulting set of N simultaneous equations may be written in the concise matrix form as:

$$\Gamma \bar{F} = J$$

where

\bar{F} = solution vector

J = Vector of right hand sides

Since the Γ , matrix is triagonal, the solution may be obtained readily using the previously mentioned Thomas algorithm, yielding the new values of F at station II.

C. Turbulence Model

1. Discussion

The turbulence model utilized in the jet analysis is that model proposed by Prandtl/Glushko (Reference 4) and Spalding (Reference 5). As mentioned previously, the differential equations have been initially written in terms of the empirical parameters pertinent to this model. The relationship of Reynold's stress, τ_t , to the local mean flow quantities is taken as:

$$\tau_t = \mu H \alpha R_t \frac{\partial u}{\partial y} \quad (39)$$

where the suggested values are:

$$H = 1.0$$

$$\alpha = 0.2$$

The turbulence of Reynold's number in the above expression is given by:

$$R_t = \frac{\rho \sqrt{e} L_t}{\mu} \quad (40)$$

where:

e = Turbulence Kinetic Energy

L_t = Characteristic length scale of turbulence

The turbulence kinetic energy is obtained by solution of the conservation equation (Equation 26). The principal uncertainty in the turbulence model rests in the specification of the length scale, L_t , associated with turbulence. In the present analysis, the length scales are related to the geometric parameters of the jet and must be specified in terms of empirical relationships. Expressions for the length scale will be given in a subsequent section.

The turbulent or "eddy" viscosity from (39) is:

$$\mu_t = \mu H \alpha R_t \quad (41)$$

An "effective" exchange coefficient may be determined as the sum of the laminar and turbulent terms:

$$\mu_e = \mu + \mu_t = \mu(1 + \alpha H R_t) \quad (42)$$

Defining a turbulent Prandtl number as $Pr_t = \frac{C_p t}{k_t}$, the "effective" thermal conductivity is given as:

$$k_e = C_p \mu \frac{1}{Pr} + \left(\frac{\mu t}{\mu} \right) \left(\frac{1}{Pr_t} \right) \quad (43)$$

The diffusion parameter, D, appearing in equations (5) and (6) is given by Glushko and Spalding as:

$$D = 1 + \alpha \eta H R_t \quad (44)$$

where

$$\begin{aligned} \eta &= \text{Empirical constant} \\ \eta &= (0.586 \text{ after Spalding}) \end{aligned}$$

The constant C in the dissipation term of the turbulence energy equation is assigned the value 2.59 (Spalding) for application to the turbulent mixing problem.

2. Definition of Turbulence Length Scale

As mentioned previously, the principal uncertainty in the turbulence model resides in the characteristics length scale assigned to the turbulence (L_t). A partial differential equation for L_t , similar to the turbulence energy equation (5), has been derived from Rotta (Reference 6). In the present analysis, however, the characteristics scale of the jet turbulence is assumed independent of the transverse coordinate, Y, and is expressed in terms of the geometric parameters of the jet. Experimental data are used to define the constants in the model.

Single Jet

Referring to Figure 2a, the mixing region of the single jet may be divided into three distinct zones. In zone 1, the flow consists of a mixing layer which penetrates into the uniform parallel flow emanating from the jet discharge. The turbulence scale in this region is assumed proportional to the width of the mixing layer:

$$L_t(1) = C_{t1} * b * (1 + C_{t2} M_J)^{-1} \quad (45)$$

where

$$\begin{aligned} b &= \text{Width of mixing layer} \\ M &= \text{Jet discharge Mach number} \\ C_{t1}, C_{t2} &= \text{Empirical constants} \end{aligned}$$

The above relationship, along with empirical values for C_{t1}/C_{t2} , is developed in References 7 and 8, where comparisons with experimental data are given.

In zone 3, the velocity profiles are known to be similar. The turbulent scale for this fully developed region is defined, after Spalding (Reference 5) to be proportional to the local radius or half-height of the jet.

$$L_t(3) = C_{t8} Y_J \quad (46)$$

The turbulence length scale in the transition zone (Region 2) is less well-defined than those in Regions 1 and 3, in that experimental data are sparse or nonexistent. Since the scale is known to increase rapidly upon disappearance of the potential core, an exponential increase in L_t to match the exponential decrease in momentum is assumed.

$$L_t(2) = C_{t3} * (k + C_{t5} M_J)^{-1} * \left(\frac{X}{X_c}\right) C_{t4} * (C_{t6} + C_{t7} M_J) \quad (47)$$

The constants in this model must be determined from experimental data and are dependent on the downstream distance where velocity profiles become similar.

The numerical values assigned to the constants $C_{t1} - C_{t8}$, which apply for most situations are:

$C_{t1} = 0.28$	$C_{y5} = 0.38$
$C_{t2} = 0.38$	$C_{t6} = 1.4$
$C_{t3} = 0.28$	$C_{t7} = 0.43$
$C_{t4} = 0.3$	$C_{t8} = 0.22$

3. Swirling Jets

The effective viscosity $\mu_{r\theta}$ is defined by:

$$\tau_{r\theta} = \mu_{r\theta} \quad r \quad \frac{\partial}{\partial r} (w/r) \quad (48)$$

for the swirling jet.

By analogy with turbulent Prandtl and Schmidt numbers, it is assumed in the present work that $\mu_{r\theta}$ and μ_e are related to each other by:

$$\sigma_{r\theta} = \mu_e / \mu_{r\theta} \quad (49)$$

where μ_e and $\mu_{r\theta}$ are the effective viscosities analogous to those in laminar flows. Thus, the presence of swirl in the jet introduces another unknown, $\mu_{r\theta}$. The logical expectation is that all of these quantities, the effective viscosities and their ratio, have functional dependence of the degree of swirl in a jet. It was shown by Chigier and Chervinsky (Reference 9) that swirling jets are characterized by swirl parameter (often referred to as swirl strength - defined as the ratio of axial momentum to angular momentum at the exit). Often, the angular velocity component is a difficult one to measure. In this work an empirical model suggested by Chigier and Chervinsky has been used to define the swirl strength.

Explicitly, the swirl strength(s) is defined as:

$$\begin{aligned} S &= (G/2) / [1 - (G/2)] & G < 0.4 \\ &= (G/2) / [1 - (G/2)^2] & G \geq 0.4 \end{aligned} \quad (50)$$

where, $G = \frac{\text{Maximum Swirl Velocity Component}}{\text{Axial Velocity Component at Exit}}$

The constants of proportionality, α and H , are the same as suggested by Prandtl/Glushko and Spalding. In the present work it has been tacitly assumed that the same basic turbulence mechanism will hold for swirling jets. While the effects of swirl are adequately reflected in the turbulent kinetic energy (from the solution of turbulent kinetic energy equation), the length scale, L_t , is modified to reflect the influence of swirl. Care must be exercised in defining the length scales for jets, for the jet flow characteristics are markedly different in the initial region (near the exit) than those far from the exit. For swirling jets, it has been assumed that the transition regions are small and may be treated as a fully developed regime. The length scales for swirling jets than are appropriately modified as follows:

Initial Region:

$$L_t(1, \text{SWIRL}) = L_t(1, \text{NOSWIRL}) \left[1 + K_{t1} \cdot S^{K_{t2}} \right] \quad (51)$$

and, in the fully developed region:

$$L_t(3, \text{SWIRL}) = L_t(3, \text{NOSWIRL}) \left[1 + K_{t3} S^{K_{t2}} \right] \quad (52)$$

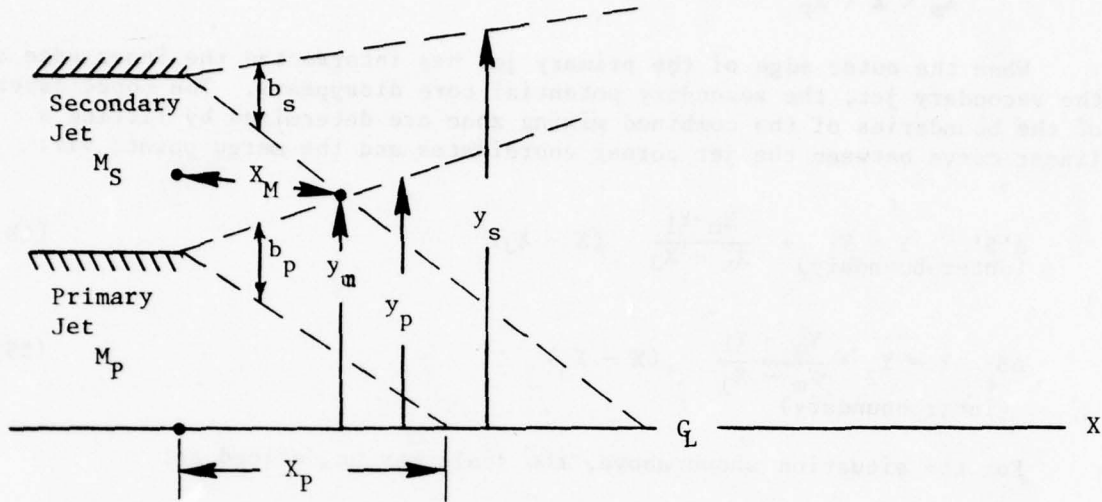
where K_{t1} , K_{t2} , K_{t3} , and K_{t4} are empirical components determined from experimental data.

In addition, Lilly's postulation (Reference 10) for $\sigma_{r\theta} = 1 + 5S^{1/3}$ is used in this work.

These definitions, along with the auxiliary equations, close the system of governing equations.

4. Coannular/Coplanar Jets

A geometric scale model, developed by General Electric is utilized for the coannular/coplanar jet. The schematic diagram of the symmetric dual jet flow field is shown in the following sketch.



Schematic Diagram of Dual Jet with Turbulence Scale Parameters.

The region upstream of the point where the secondary core disappears consists of two independent jets which mix in somewhat the same manner as the previously described single jet. The turbulence length scale is defined in terms of the scale in the two mixing regions as follows:

$$L_p = C_{tp} b_p (1 + C_{t2} M_p)^{-1} \quad (53)$$

$$L_s = C_{ts} b_s (1 + C_{t2} M_s)^{-1} \quad (54)$$

$$a.) \quad 0 \leq Y < 0.9Y_p$$

$$L = L_p \quad (55)$$

$$b.) \quad 0.9Y_p \leq Y < (Y_m - 0.9 b_s)$$

$$L = L_p + \frac{(L_s - L_p)}{Y_s - 0.9(L_p + b_s)} (Y - 0.9Y_p) \quad (56)$$

$$c.) (Y_s - 0.9b_s) \leq Y < Y_s$$

$$L = L_s \quad (57)$$

The factor 0.9 allows marginal interaction of the two mixing zones, in that the scale in the secondary core region varies linearly between the two extreme values:

$$X_m < X < X_p$$

When the outer edge of the primary jet has intersected the inner edge of the secondary jet, the secondary potential core disappears. The coordinates of the boundaries of the combined mixing zone are determined by fitting a linear curve between the jet corner coordinates and the merge point; viz:

$$\begin{array}{l} \text{A'B' (outer boundary)} \end{array} \quad Y = Y_1 + \frac{Y_m - Y_1}{X_m - X_j} (X - X_j) \quad (58)$$

$$\begin{array}{l} \text{AB (inner boundary)} \end{array} \quad Y = Y_2 + \frac{Y_m - Y_1}{X_m - X_j} (X - X_j) \quad (59)$$

For the situation shown above, the scale may be defined as:

$$a.) Y < 0.0 * (Y_s - b_s)$$

$$L = L_p \quad (60)$$

$$b.) 0.9 * (Y_s - b_s) < Y < Y_s - 0.9(Y_s - Y_p)$$

$$L = L_p + \frac{L_s - L_p}{0.9(Y_p + b_s) - 0.8Y_s} [Y - 0.9*(Y_s - b_s)] \quad (61)$$

$$c.) Y_s - 0.9(Y_s - Y_p) < Y$$

$$L = L_s \quad (62)$$

Special situations occur as follows:

If

$$b_s > Y_s' \text{ set } b_s = Y_s \quad (63)$$

$$a.) 0 < Y < [Y_s - 0.9 * (Y_s - Y_p)]$$

$$L = L_p + \frac{(L_s - L_p)}{0.9(Y_s + b_s) - 0.8Y_s} [Y - 0.8*(Y_s - b_s)] \quad (64)$$

$$b.) \quad 0.9* (Y_s - b_s) < Y \quad (65)$$

$$L = L_p + \frac{(L_s - L_p)}{0.9(Y_p + b_s) - 0.8Y_s} [Y - 0.9 (Y_s - b_s)] \quad (66)$$

In the region downstream of the point where the primary core has disappeared, the combined mixing zone scale is redefined to:

$$L_p = C_{tm} b_p (1 + C_{t2} M_p)^{-1} \quad (67)$$

D. Gas Properties

Compressible flow relationships are utilized to establish flow field conditions at the discharge plane of the jet, where the flow is assumed uniform and parallel except for a small interface region where the streams are adjacent. The stagnation enthalpy of the given stream is defined as:

$$H = h + \frac{v^2}{2g_c J} + e \quad (68)$$

The stagnation temperature then is determined using:

$$C_{pt} T_t = C_p T + \frac{v^2}{2g_c J} + e \quad (69)$$

The mean mixture heat capacity at constant pressure is determined using:

$$C_p = \frac{\gamma R}{\gamma - 1} \quad (70)$$

where the isentropic exponent varies with temperature as follows:

$$\begin{array}{ll} T \leq 800^\circ \text{ R} & \gamma = 1.4 \\ 800 < T < 3600^\circ \text{ R} & \gamma = 2.23708 T^{-0.70271} \\ T \geq 3600^\circ \text{ R} & \gamma = 1.254 \end{array} \quad (71)$$

For a given static temperature in the range 800°-3600° R,

$$T^{0.929729} = (C_p + \frac{v^2}{2g_c J} + e) / 2.23708$$

or

$$T_t = \frac{\left(\frac{C_p T}{P} + \frac{V^2}{2g_c J} + e \right)^{1.078}}{2.23708}$$

The jet streams may be defined in terms of Mach number (M), total pressure (P_t), static temperature (T), or velocity (V). The defining equations are:

$$a = \sqrt{\gamma g_c R T} \quad (73)$$

$$V = Ma \text{ or } M = V/a \quad (74)$$

$$\frac{P_t}{P} = \left(1 + \frac{\gamma - 1}{2} M^2 \right)^{\gamma/\gamma-1} \quad (75)$$

Following determination of the independent variables (u , θ , E , and α_i) at a given station, the dimensional velocity, temperature, and turbulence energy profiles may be determined by multiplication by the normalizing parameters. Local profiles of M , T_t , and P_t also may be computed using the preceding relationships. Finally, dimensionless pressure and temperature coefficients are determined using:

$$P_{TD} = \frac{(P_t - P_{ex})}{(P_t - P_{ex})} \quad (76)$$

(Jet discharge plane)

$$T_{TD} = \frac{(T_t - T_{ex})}{(T_t - T_{ex})} \quad (77)$$

(Jet discharge plane)

For supersonic flows, the location where the supersonic core disappears is of interest. The axial sonic line through the jet is determined as a function of the normal coordinate Y .

E. Particle Injection

Since JETMIX assumes that all constituents are perfect gases, certain approximations must be made in order to use this flow field model to calculate the concentrations and temperature of particles injected into a jet engine plume. In Reference 11, it is shown experimentally that, for small particles (10-50 micron diameter) in turbulent air stream, the particle velocity was equal to the velocity of the airstream within the accuracy of the measurements. In Reference 12, it is shown that soot particles will have a temperature within one degree of the gas temperature. Therefore, since the aerosol particles follow the temperature and velocity profiles of

the fluid stream closely, the flow field calculated by the JETMIX module can be used to define the velocity and temperature of the particles in the plume, if it is assumed that the basic flow field without the particles is not changed significantly when the particles are injected. This will be true when the weight flow of the particles is small compared with the total weight flow of the jet plume.

In the computer module the specific heat and the Schmidt number (which is inversely proportional to the diffusion coefficient) must be input. Since the temperature of the particles follows the fluid stream temperature and it is assumed that the basic flow field distribution will not change as a result of injection of the particles, the specific heat of air is used as input for the specific heat of the particles. The diffusion coefficient for small particles in a fluid stream is much lower than for gases. In Figure 3. from Reference 13, the ratio of the particle diffusivity to the diffusivity of a turbulent air stream is shown for various sizes of glass beads suspended in turbulent air streams of varying Reynolds number. Since the particle sizes of usual interest are less than about 2 microns in diameter, a value of $D_{\text{particle}}/D_{\text{fluid stream}} = 0.02$ is typical. a value of Schmidt number $SC = 35$ can be used to obtain a single set of data which is representative of the particle mixing rate in an engine plume. If measured engine flow field data became available, the value of the Schmidt number which provides the most favorable agreement between the predicted flow field and the measurements should be determined, and this value should be used in the program.

The plume flow field, including the velocity of the particles injected into the stream, is calculated using the nonuniform flow field option. In this option, the user provides the mole fractions of the constituents as a function of radius in the plume at a single axial station along with the static temperature, velocity, and turbulent intensity profiles. Also to be provided are the ambient pressure, temperature, and velocity of the external flow surrounding the jet. Using this option, the particles are input artificially as only a small mole fraction (M_a) at the desired locations. Since the program treats the particles as a perfect gas, the weight flow input (\dot{m}) then can be calculated as:

$$\dot{m} = \frac{P_0}{RT} A V M_a$$

where, $P_0 \equiv$ static pressure of external flow

$R \equiv$ gas constant

$A \equiv$ area over which particles are injected

$V \equiv$ velocity of the particles

$M_a \equiv$ mole fraction of the particles

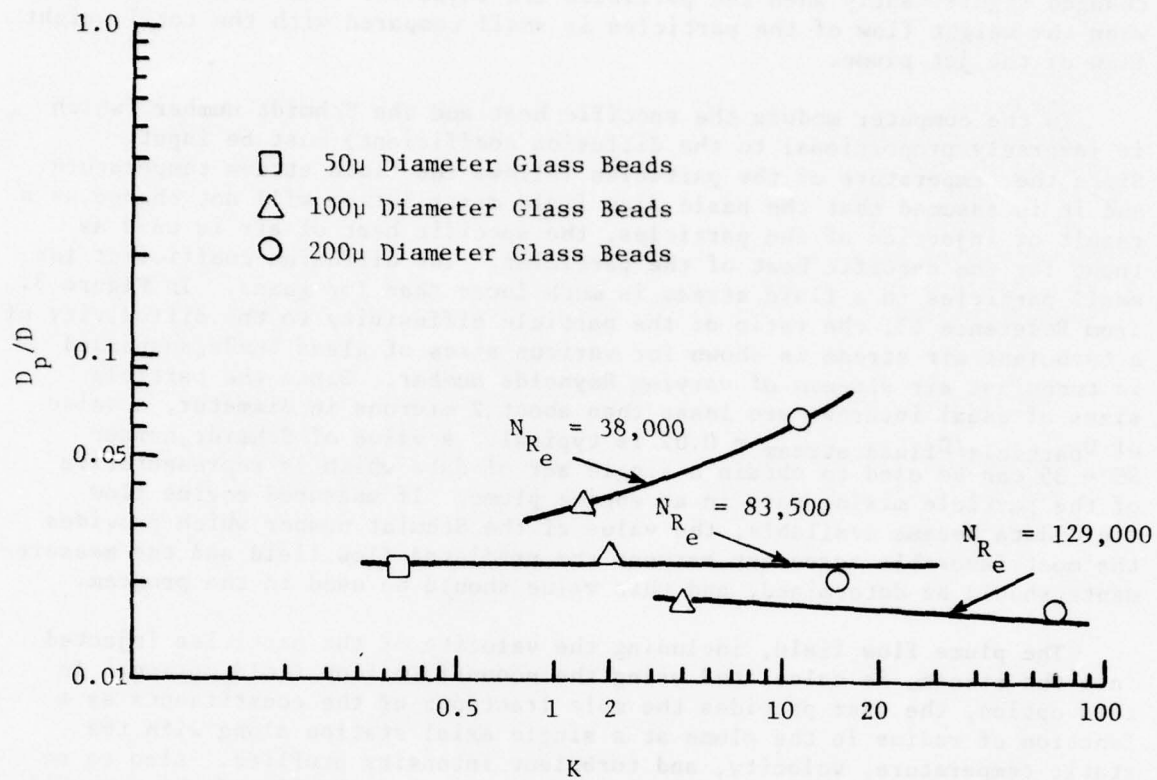


Figure 3. Particle Diffusivity of Beads.

The mass flow rate generally will be different from the actual flow desired, since a low value of the mole fraction is input to assure that the basic flow field is not changed as a result of injecting the particles.

To define the actual mass flow rate which is injected into the engine plume, a constant (WT) is input into the PLUMIR module. This constant is defined as follows:

$$WF = \frac{\text{Actual Mass Flow Rate}}{\frac{P_o}{RT} AVMa}$$

With this input, the flow field option then calculates the static temperature, velocity, and mole fraction of the particles at user-selected points in the plume flow field. Now, an equation to calculate the concentration of the particles (particles/volume) must be developed since this is the quantity required to evaluate absorption coefficients in the PLUMIR module (See Section V.D.)

SECTION IV

INTERNAL EXHAUST HOT PARTS RADIATION (SIGNIR)

A. Discussion

The internal hot surfaces of the exhaust system are primary contributors to the IR signature, especially when viewed from tail-on azimuth angles. Not only are direct emissions from the visible surfaces important, but emissions from hot hidden sources (such as the turbine) can be important if a significant portion of these emissions is reflected off the visible surfaces. The factors needed to determine the extent of internal hot parts IR radiation are surface temperatures and emissivities, view factors between the various surfaces of the system, and the visible projected areas of the surfaces at each prescribed viewing angle.

Temperature may be either read in directly or calculated using knowledge of the heat transfer parameters in the exhaust system. Emissivities are functions of tabular input of wavelength. View factors and projected areas may either be tabulated or calculated from the system geometry. The analysis associated with each calculation type is presented in the analysis sections that follow.

B. Exhaust System Gas Flow (RIMAIN)

An internal gas flow analysis is conducted by SIGNIR under the control of subprogram RIMAIN. The primary effort is to determine the distribution of gas stream properties and the surface boundary layer convection coefficients. The following sections cover the analytical procedures utilized in computing the compressible flow and surface boundary layer.

1. Compressible Fluid Flow (COFLOW)

The subprogram COFLOW establishes the flow properties within a compound stream based on a one-dimensional, isentropic flow analysis. The method employed is based on the analysis presented in Reference 14 which assumes that the primary and secondary streams of a mixed turbofan exhaust system can be handled separately. Its theory has been found to agree well with experimental findings. COFLOW provides an array of compound-flow properties associated with flow areas for a given combination of flow rates. The fluid static pressure is chosen to be constant across adjacent streams. If a single-stream configuration is employed, the same analytical procedure is employed utilizing only the single stream.

The nomenclature used within this section is as follows:

A	-	Flow area, ft ²
C _F	-	flow coefficient
g	-	acceleration of gravity, ft/sec ²
j	-	an integer (corresponding to the subscript j)
k	-	ratio of specific heats
\dot{m}	-	mass flow rate, lbm/sec
M	-	flow Mach number
n	-	number of compound streams
P	-	static pressure, lbf/ft ²
P _T	-	total pressure, lbf/ft ²
ΔP	-	increment in static pressure, lbf/ft ²
R	-	gas constant, lbf ft/lbm °R
T	-	Static temperature, °R
T _T	-	Total temperature, °R
V	-	Flow velocity, ft/sec
β	-	compound-flow indicator
ρ	-	density, lbm/ft ³

subscripts

amb	-	ambient conditions
ex	-	nozzle exit
i	-	an integer, stream number
j	-	an integer, relates physical conditions and flow properties at the same static pressure conditions

The subprogram COFLOW computes an array of fluid properties compatible with values of static pressure decremented from the total pressure provided to the ambient static pressure, i.e.;

$$P_j = P_T - j \cdot \Delta P \quad (1)$$

The stream properties for a perfect gas are computed by the following isentropic flow relationships:

$$\dot{M}_{i,j} = \sqrt{\frac{2}{(k_i - 1)}} \left[(P_T - P_j)^{(k_i - 1)/k_i} - 1 \right] \quad (2)$$

$$T_{i,j} = T_{Ti,j} \left[1 + \frac{k_i - 1}{2} M_{i,j}^2 \right]^{-1} \quad (3)$$

$$V_{i,j} = M_{i,j} \sqrt{k_i g R_i T_{i,j}} \quad (4)$$

$$\rho_{i,j} = P_j / R_i T_{i,j} \quad (5)$$

$$A_{i,j} = \dot{m}_i / (\rho_{i,j} V_{i,j}) \quad (6)$$

A compound flow indicator, β , is used to determine if choking occurs at a static pressure value which is greater than ambient pressure (choked convergent nozzle). Compound flow is subsonic when $\beta > 0$, sonic at $\beta = 0$ and supersonic when $\beta < 0$. The indicator is evaluated by the equation given in Reference 14 as

$$\beta_j = \sum_{i=1}^n \frac{A_{i,j}}{k_i} \left(\frac{1}{\dot{m}_{i,j}} - 1 \right) \quad (7)$$

This shows that, at the compound-choke condition, some streams can be supersonic while others are subsonic. For a single stream, $n = 1$, $\beta = 0$ when the stream Mach number is 1. The subprogram COFLOW is limited to two streams ($n = 2$). Once the array of stream properties is formed, the total flow area:

$$AT_j = \sum_{i=1}^n A_{i,j} \quad (8)$$

at the nozzle exit is determined from the program at:

$$\beta = 0, \text{ if } P > P_{amb} \quad (9)$$

or at:

$$P = P_{amb} \text{ of } \beta > 0 \quad (10)$$

The total flow area of the array is adjusted by a flow coefficient:

$$C_F = A_{T(ex)} / A_{ex} \quad (11)$$

which is an adjustment toward 2-dimensional flow considerations.

2. Surface Boundary Layer (TURBLT)

The conditions within the compressible turbulent boundary layer which exist along each of the exhaust system surfaces are computed by subprogram TURBLT. This is a segment of an existing computer program written by A.H. Ybarra of Vought Aeronautics Company of LTV Aerospace Cooperation. The

analytical methods employed basically are those presented by Reference 15 in which the boundary layer is expressed in terms of the momentum integral and moment-of-momentum integral, simplified by a Mager-type transformation, and solved simultaneously. Ybarra incorporated an empirical modification to the moment-of-momentum equation which improved the agreement between calculations and test data.

The following is a list of nomenclature for symbols used within this section:

$b(x)$	- transformation parameter
C_f	- local skin friction coefficient, dimensionless
$c(x)$	- transformation parameter
C_p	- specific heat at constant pressure, Btu/lbm-° R
d	- exact differential
e	- differential
F_1	- empirical factor
F_2	- empirical factor
H	- boundary layer shape factor, dimensionless (incompressible transformed denoted by subscript tr)
h	- enthalpy, Btu/lbm
h_c	- convection heat transfer coefficient, Btu/hr ft ² ° R
M	- Mach number, dimensionless
m	- power law profile exponent, dimensionless
p	- pressure, lbf/in. ²
Pr	- Prandtl number, dimensionless
R	- Radius of symmetry, feet
Re_θ	- Reynolds number based on momentum thickness, dimensionless
R_g	- gas constant, lbf ft/lbm ° R
r	- recovery factor, dimensionless
S	- enthalpy ratio factor, $S = (h_g/h_o) - 1.0$, dimensionless
T	- temperature, ° R
U	- transformed velocity along surface, ft/sec
u	- physical velocity along surface, ft/sec
V	- transformed velocity normal to surface, ft/sec
v	- physical velocity normal to surface, ft/sec
X	- transformed coordinate along surface, feet
x	- physical coordinate along surface, feet
Y	- transformed coordinate normal to surface, feet
y	- physical coordinate normal to surface, feet
q	- ratio of specific heats, dimensionless
W	- transformed boundary layer thickness, feet
W^*	- transformed boundary layer displacement thickness, feet
w	- physical boundary layer velocity thickness, feet
w^*	- physical boundary layer displacement thickness, feet
θ	- boundary layer momentum thickness, feet
μ	- absolute viscosity, lbm/sec-ft
ν	- kinematic viscosity, ft ² /sec
ρ	- density, lbm/ft ³
τ	- shear stress, lbm/ft-sec ²

- Ψ - transformed velocity potential, 1/sec
- ψ - velocity potential, 1/sec
- ∂ - partial derivative symbol

Subscripts

- e - local inviscid flow, at edge of boundary layer
- z - gravitational acceleration, ft/hr²
- i - incompressible
- o - freestream stagnation conditions
- ref - at Eckert reference enthalpy conditions
- s - local stagnation conditions
- T - total conditions (unsubscripted indicates static conditions)
- tr - transformed
- w - at the surface, wall
- 1 - current value, at end of current increment
- 2 - previous value, at start of current increment

For steady, compressible, turbulent flow, the boundary layer equations, in which the flow variables appear as time-averaged quantities, are expressed by the continuity and momentum equations for an axisymmetric system, as:

$$\frac{\partial(\rho u)}{\partial x} + \frac{\partial(\rho u)}{\partial y} - \frac{\rho u}{R} \frac{dR}{dx} = 0 \quad (12)$$

and:

$$\rho u = \frac{\partial u}{\partial x} + \rho u \frac{\partial u}{\partial y} = - \frac{d\rho}{dx} + \frac{\partial \tau}{\partial y} \quad (13)$$

These two partial differential equations, in their present form, cannot be solved simultaneously. To simplify and reduce the difficulty of integration, a Mager-type transformation is performed which transforms the physical coordinates as:

$$X = \int_0^x b(x) dx \quad (14)$$

and:

$$Y = c(x) \int_0^y \frac{\rho}{\rho_o} dy \quad (15)$$

where

$$b(x) = (T_{To}/T_{ref}) (T_e/T_{To})^{\frac{\gamma+1}{2(\gamma-1)}} \quad (16)$$

$$c(x) = (T_e/T_{To})^{1/2} \quad (17)$$

The velocities can be replaced through the definition of a stream function, as:

$$\frac{\partial \psi}{\partial y} = \frac{\rho u}{\rho_0} \quad (18)$$

$$\frac{\partial \psi}{\partial x} = - \frac{\rho v}{\rho_0}$$

and the transformed velocities by the relationships:

$$U = \frac{\partial \psi}{\partial Y} \quad (19)$$

$$V = - \frac{\partial \psi}{\partial X}$$

Applying Equations 14, 15, and 16 to the boundary layer equations (12) and (13) results in the following transformed continuity and momentum equation:

$$\frac{\partial U}{\partial X} + \frac{\partial V}{\partial Y} = 0 \quad (20)$$

$$U \frac{\partial U}{\partial X} + V \frac{\partial U}{\partial Y} = U_e \frac{\partial U_e}{\partial X} (1+S) + v_o \frac{\partial^2 U}{\partial Y^2} \quad (21)$$

where the enthalpy term is defined as:

$$S = (h_s/h_o) - 1 \quad (22)$$

where h_s is the local stagnation enthalpy.

The boundary conditions applicable to Equations 20 and 21 are:

$U(X,0) = 0$	no slip at wall
$V(X,0) = 0$	no mass added or removed from boundary layer at wall
$S(X,0) = S_w(X)$	enthalpy ratio at wall depends only on local recovery temperature
Limit $S = 0$	local stagnation temperature approaches free stream total temperature
$Y \rightarrow \infty$	
Limit $U = U_e(X)$	
$Y \rightarrow \infty$	boundary layer velocity approaches external velocity.

Some correlations between transformed and physical parameters which result from the Mager-type transformations are as follows:

$$\text{Longitudinal velocity, } U = (T_e/T_{To})^{1/2} U = [c(X)] U \quad (23)$$

$$\text{Velocity potential, } \psi \doteq \Psi \quad (24)$$

$$\text{Boundary Layer Shape Factor, } H = 1 + \frac{\gamma-1}{2} M_e^2 H_{tr} + \frac{\gamma-1}{2} M_e^2 \quad (25)$$

$$\text{Momentum Thickness, } \theta = \theta_{tr} T_{To}/T_e \frac{\gamma+1}{2(\gamma-1)} \quad (26)$$

$$\begin{aligned} \text{Displacement Thickness, } \delta^* = & \left(\theta_{tr} + \Delta^* \right) \left(T_{To}/T_e \right)^{\frac{3\gamma-1}{2(\gamma-1)}} \\ & - \theta_{tr} \left(T_{To}/T_e \right)^{\frac{\gamma+1}{2(\gamma-1)}} \end{aligned} \quad (27)$$

The combining and manipulation of Equations 20 and 21 produce the equation:

$$\begin{aligned} \frac{\partial}{\partial X} [U(U - U_e)] + \frac{\partial}{\partial Y} [V(U - U_e)] + \frac{\partial U_e}{\partial X} (U - U_e) \\ + U_e \frac{\partial U_e}{\partial X} S = - v_o \frac{\partial^2 U}{\partial Y^2} \end{aligned} \quad (28)$$

The transformed momentum thickness, θ_{tr} , and the transformed displacement thickness, Δ^* , are defined as:

$$\theta_{tr} = \int_0^{\Delta} \left(\frac{U}{U_e} \right) \left(1 - \frac{U}{U_e} \right) dY \quad (29)$$

$$\Delta^* = \int_0^{\Delta} \left(1 - \frac{U}{U_e} \right) dY \quad (30)$$

and the transformed boundary layer shape factor follows as:

$$H_{tr} = \Delta^* / \theta_{tr} \quad (31)$$

By integrating Equation 28 with respect to Y between the limits Y=0 and Y=Δ (where Δ is a distance normal to the surface sufficiently large that the conditions S=0 and U=U_e are both satisfied), applying the chain rule, and incorporating Equations 29 and 30 the following equation can be obtained:

$$\frac{d\theta_{tr}}{dX} + \frac{1}{U_e} \frac{dU_e}{dX} \left[2\theta_{tr} + \Delta^* + \int_0^{\Delta} S dY \right] = \frac{v_o}{U_e^2} \left(\frac{\partial U}{\partial Y} \right)_{Y=0} \quad (32)$$

The fundamental definition of the boundary layer shear stress is expressed by:

$$\tau_w = \mu_w \left(\frac{\partial U}{\partial Y} \right)_{Y=0} \quad (33)$$

By utilizing Equations 14, 23, 31, and 33 and a reference temperature technique, then:

$$(\mu\rho)_w = \mu_o \rho_o \left(T_{To}/T_{ref} \right) \quad (34)$$

Equation 32 becomes:

$$\frac{d\theta_{tr}}{dX} + \frac{\theta_{tr}}{U_e} \frac{dU_e}{dX} \left[2 + H_{tr} + \frac{1}{\theta_{tr}} \int_0^{\Delta} S dY \right] = \left(\frac{T_{To}}{T_e} \right) \left(\frac{T_{ref}}{T_{To}} \right) \frac{\tau_w}{\rho_e U_e} \quad (35)$$

which is the form of the transformed momentum integral equation presented in Reference 15.

The moment-of-momentum integral equation is derived in a similar manner. The differential from the momentum equation (28) is multiplied by the parameter Y, and the results, in turn, are integrated with respect to Y from Y=0 to Δ. The resulting integral equation obtained is:

$$\begin{aligned}
\frac{dH_{tr}}{dX} = & \frac{-1}{2U_e} \frac{dU_e}{dX} \left[H_{tr} (H_{tr} + 1)^2 (H_{tr} - 1) \right] \left[1 + \frac{2}{(H_{tr} + 1)\theta_{tr}} \int_0^{\Delta} S dY \right] \\
& - \frac{2 (H_{tr} - 1)}{H_{tr}^2 (H_{tr} + 1) \theta_{tr}^2} \int_0^{\Delta} SY dY \\
& + \frac{H_{tr} (H_{tr}^2 - 1)}{\theta_{tr}} \left(\frac{T_{To}}{T_e} \right) \left(\frac{T_{ref}}{T_{To}} \right) \frac{\tau_w}{\rho_e U_e^2} \\
& - \frac{(H_{tr}^2 - 1)(H_{tr} + 1)}{\theta_{tr}} \left(\frac{T_{To}}{T_e} \right) \left(\frac{T_{ref}}{T_{To}} \right) \frac{\tau_w}{\rho_e U_e^2} \int_0^1 \frac{\tau}{\tau_w} d \left(\frac{Y}{\Delta} \right) \quad (36)
\end{aligned}$$

The Ludwig-Tillman skin-friction relationships for incompressible turbulent flow, both convenient and valid over a wide range of pressure gradients, is given as:

$$C_f = \frac{\tau_w}{1/2 \rho U_e^2} = 0.246 e^{-1.561 \cdot H_i} Re_{\theta}^{-0.268} \quad (37)$$

The Reynolds number based on momentum thickness is defined as:

$$Re_{\theta} = U_e \theta / \nu \quad (38)$$

With the application of the reference enthalpy concept, Equations 23 and 26, and the relationships:

$$\frac{\rho_{ref}}{\rho} = \frac{T}{T_{ref}} \quad (39)$$

and:

$$\nu_{ref} = \nu_o \frac{\mu_{ref}}{\mu_o} \frac{\rho_o}{\rho_{ref}} \quad (40)$$

Equation 37 can be put in the form:

$$\frac{C_f}{2} = \frac{\tau_w}{\rho_e U_e^2} = \frac{0.123 (T_e/T_{ref}) (\mu_{ref}/\mu_o)^{0.268}}{e^{1.561 H_i} (U_e \theta_{tr}/\nu_o)^{0.268}} \quad (41)$$

This is the expression of skin coefficient for compressible flow in terms of the transformed velocity, momentum thickness, and reference temperature (and viscosity).

The integrals which appear in the transformed momentum and moment-of-momentum equations (35) and (36), shall be reduced to a usable form. The recovery factor is defined as:

$$r = \frac{3}{\sqrt{Pr}} \quad (42)$$

for a turbulent boundary layer. For a Prandtl number of unity, the recovery temperature will be equal to the freestream stagnation temperature. Therefore, for adiabatic flow, the value of S in Equation 22 would be zero, and the integrals would be zero. To evaluate the integrals at an arbitrary surface temperature, the Crocco relationship is employed together with a power law assumption for the velocity profiles, i.e.:

$$\frac{h_s - h_w}{h_o - h_w} = \frac{u}{u_e} = \frac{U}{U_e} \quad (43)$$

and:

$$\frac{U}{U_e} = \left(\frac{Y}{\Delta} \right)^{1/m} \quad (44)$$

Since the purpose of the Mager-type transformation is to render the boundary layer equations analogous to the incompressible form, the transformed and incompressible shape factors are near equal. Using this information, the integrals are evaluated as:

$$\int_0^{\Delta} S dY = S H_i \theta_{tr} = \left(\frac{h_w}{h_o} - 1 \right) H_i \theta_{tr} \quad (45)$$

and:

$$\int_0^{\Delta} SY dY = \left(\frac{h_w}{h_o} - 1 \right) \frac{H_i^2 (H_i + 1)^2}{2(H_i - 1)(H_i + 3)} \theta_{tr}^2 \quad (46)$$

Substituting Equations 22, 23, 37, and 45 into Equation 35, the momentum equation becomes:

$$\frac{d\theta_{tr}}{dX} = \left(\frac{T_{ref}}{T_{To}} \right) \left(\frac{C_f}{2} \right) - \frac{\theta_{tr}}{U_e} \frac{dU_e}{dX} \left(2 + \frac{h_w}{h_o} H_i \right) \quad (47)$$

By the same procedure, the term of Equation 36 containing the integration in Y reduces as:

$$\begin{aligned} & \left[1 + \frac{2}{(H_i + 1)\theta_{tr}} \int_0^\Delta S \, dY - \frac{2(H_i - 1)}{H_i^2 (H_i + 1)\theta_{tr}^2} \int_0^\Delta S \, dY \right] \\ & = 1 + \left(\frac{h_w}{h_o} - 1 \right) \frac{H_i^2 + 4H_i - 1}{(H_i + 1)(H_i + 3)} \end{aligned} \quad (48)$$

The integral contained in the last term of Equation 36 is not so easily simplified. An empirical relationship:

$$\int_0^1 \frac{\tau}{\tau_w} \, d\left(\frac{Y}{\Delta}\right) = \frac{0.003075 H_i - 0.003352}{C_f/2} \quad (49)$$

was established from the data presented in Reference 15 in terms of the variables H_i and C_f . Once the analytical model was complete, further empirical corrections in the last term of Equation 36 made it necessary to correlate with measured test data. These correlation factors took the form of:

$$F1 = C_p / \left(1 + \frac{Y - 1}{2} M_e^2 \right) \quad (50)$$

$$F2 = 1, \text{ when } \frac{dM_e}{dX} \geq 0$$

$$= 1 + \left(\frac{dM_e}{dX} \right)^2, \text{ when } \frac{dM_e}{dX} < 0 \quad (51)$$

with the further restriction that:

$$(F1)(F2) \leq 1 \quad (52)$$

By employing those methods required in establishing Equation 42 and applying the empirical parameters presented, Equation 36 reduces the form:

$$\begin{aligned} \frac{dH_i}{dX} = & - \frac{H_i(H_i + 1)^2(H_i - 1)}{2} \left[1 + \left(\frac{h_w}{h_o} - 1 \right) \frac{H_i^2 + 4H_i - 1}{(H_i + 1)(H_i + 3)} \right] \frac{1}{U_e} \frac{dU_e}{dX} \\ & + \frac{H_i(H_i + 1)^2}{\theta_{tr}} \left(\frac{T_{ref}}{T_{To}} \right) \left(\frac{C_f}{2} \right) \\ & - (F1)(F2) \frac{(H_o^2 - 1)(H_i + 1)}{\theta_{tr}} \left(\frac{T_{ref}}{T_e} \right) (0.003075 H_i - 0.003352) \end{aligned} \quad (53)$$

In subprogram TURBLT, the two transformed boundary layer equations (42) and (43) are solved simultaneously using an iterative finite difference numerical integration procedure. Specifically, the process employed divides the surface being analyzed into small increments. For each surface increment, a value for H_i and θ_{tr} is assumed at the downstream end of that increment; and then, using the average value for all pertinent parameters over the surface increment, the two equations (47) and (53) are solved. The results are compared with the initial estimates and an iteration is carried out to converge on a solution.

The program is provided with the properties of the gas stream flowing adjacent to the surface and the initial (upstream) values of momentum thickness, θ , and incompressible shape factor, H_i , (these two values must be input by the program user which requires some estimate of the boundary layer conditions entering the exhaust system). With a surface increment's upstream (2) boundary layer condition, the program makes an assumption as to the downstream (1) growth. The condition and property values over the increment are averaged; Equations 41, 50, and 52 are evaluated; and, in turn, Equations 47 and 53 are solved simultaneously utilizing the equations:

$$\theta_{tr1} = \theta_{tr2} + \frac{d\theta_{tr}}{dX} (X_1 - X_2)$$

and:

$$H_{i1} = H_{i2} + \frac{dH_i}{dX} (X_1 - X_2)$$

The initial estimate is corrected, and the solution process is continued until the parameters converge. In turn, the parameters for the following increments are solved in a systematic order.

From the solution obtained, local physical boundary layer parameters along the surface are computed by the program; these are:

- boundary layer thickness:

$$\delta = \theta_{tr} \left(\frac{T_{To}}{T_e} \right)^{\frac{\gamma+1}{2(\gamma-1)}} \left[H_i + 2 + \left(\frac{H_i+1}{H_i-1} \right) + \frac{\gamma-1}{2} M_e^2 (H_i+1) \right]$$

- local skin friction coefficient:

$$C_f = 0.246 e^{-1.56 H_i} \left(\frac{v}{U_e \theta} \right)^{0.268}$$

- local convection heat transfer coefficient:

$$h_c = \frac{C_f}{2} \sqrt{\frac{\gamma g}{R_g}} (Pr)^{2/3} \cdot C_p P_{To} (T_{To})^{-1/2} M_e \left(1 + \frac{\gamma-1}{2} M_e^2 \right)^{\frac{-(\gamma-1)}{2(\gamma+1)}} \cdot e^{1.561 [H_i - 1.3 - 0.2(3.25\gamma - 2.25)M_e^2]}$$

C. Exhaust System Surface Cooling (LINKT)

Three methods for cooling exhaust surfaces have been incorporated into the LINKT; they are film convection-film, and transpiration-cooling. These cooling methods were selected as the more efficient means of cooling surfaces. They give the program latitude in the types of systems wherein this program is applicable. The following section presents the analytical procedures employed for each of the surface cooling methods.

1. Film Cooling (FILMCL)

The gaseous film cooling method incorporated by subprogram FILMCL is an empirical correlation of various investigators' data presented in Reference 16. The cooling configuration utilized by the program is specifically for tangential injection of the coolant. The method proposed by Reference 17 was coupled with this film cooling method to be capable of handling multiple-slot configurations. The nomenclature used within this section is as follows:

- A - Area, ft²
- C_d - flow discharge, nondimensional
- C_p - specific heat at constant pressure, Btu/lb_m ° R
- f(v) - velocity mismatch factor, nondimensional
- g - gravitational acceleration, ft/hr²
- h - convective heat transfer coefficient, Btu/hr ft², ° R
- m - total number of cooling slots, nondimensional
- M - heat capacity ratio, (ρVC_p)_c/(ρVC_p)_g
- ω - mass flow rate, lb_m/hr
- n - flow exponent, nondimensional
- P - static pressure, lb_m/ft²
- P_T - total pressure, lb_m/ft²
- R - gas constant, lb_f ft/lb_m, ° R
- s - slot height, ft
- St - Stanton number (h_g/ρVC_p), nondimensional
- T - temperature or static temperature, ° R
- T_r - recovery temperature, ° R
- T_T - total temperature, ° R
- UA - overall rate of heat transfer, Btu/hr, ° R
- V - velocity, ft/hr
- x - distance downstream from slot, feet
- γ - ratio of specific heats
- Δ - the change in a property, nondimensional
- η - film effectiveness
- ρ_{std} - density at standard temperature and pressure, lb_m/ft³

Subscripts:

- c - coolant
- f - fluid film
- f' - adjacent to film
- g - mainstream gas
- s - slot
- t - total
- w - wall
- 1 - coolant source
- 2 - heat source

The empirical equation for film effectiveness proposed by Reference is:

$$\eta = 1 / \left\{ 1 + 3.6 \left[\left(\frac{St_g}{M} \right) \left(\frac{x}{s} \right) \left(\frac{T_{rg}}{T_{rc}} \right)^{2/3} f(v) \right] \right\} \quad (54)$$

where:

$$\eta = (Tr_g - Tw)/(Tr_g - Tr_c) \quad (55)$$

$$\left. \begin{aligned} f(v) &= 1 + 0.4 \arctan \left(\frac{V_g}{V_c} - 1 \right) ; \text{ when } \frac{V_g}{V_c} > 1, \\ &= \left(\frac{V_g}{V_c} \right)^{1.5(V_g/V_c - 1)} ; \text{ when } \frac{V_g}{V_c} \leq 1 \end{aligned} \right\} \quad (56)$$

These equations were converted into a form where the independent variables are those available to the program. Specific terms of Equation 141 were altered in form as shown.

$$\frac{St_g}{M} = \frac{h_g}{C_{pc}} \cdot \frac{C_d A_s}{\dot{m}_c} \quad (57)$$

$$\frac{Tr_g}{Tr_c} = \frac{T_{f'}}{T_{tc}} \quad (58)$$

Equation 142 takes the form:

$$\eta = (T_{f'} - Tw)/(T_{f'} - T_{tc}) \quad (59)$$

where $T_{f'}$ is the gas film temperature resulting from the upstream slot flow. The term:

$$\frac{V_g}{V_c} = \frac{V_g}{R_c} \cdot \frac{C_d A_s}{\dot{m}} \cdot \frac{P_g}{T_{tc}} \left(\frac{P_{tc}}{P_g} \right)^{\frac{\gamma-1}{\gamma}} \quad (60)$$

From Equation 56, is converted as shown which assumes isentropic flow from a common coolant plenum to the slot where discharge static pressure adjusts to equal the mainstream gas static pressure. Combining the foregoing equations, the equation for wall temperature becomes:

$$Tw = T_{f'} - (T_{f'} - T_{tc}) / \left\{ 1 + 3.6 \frac{h_g}{C_{pc}} \left(\frac{C_d A_s}{\dot{m}_c} \right) \left(\frac{x}{s} \right) \left(\frac{T_{f'}}{T_{tc}} \right)^{2/3} f(v) \right\} \quad (61)$$

where the term $f(v)$ is defined by Equations 56 and 60.

The computational process conducted by FILMCL starts with the upstream slot; utilizing the local gas stream recovery temperature for T_6 , compute the wall temperature from the slot to the end of the surface being cooled. This is accomplished in incremental steps using the local gas stream properties along the surface. Progressing to the next slot, the gas film temperature (T_f) along the remaining surface is assigned the values of the wall temperature (T_w) computed from the previous slot. In this manner, upstream slot coolant films affect all surface temperatures downstream. The procedure is continued progressively along the cooled surface producing the wall temperature distribution as demonstrated in Figure 4. In turn, an area-weighted average temperature is computed for each of the nodes assigned along this cooled surface.

A coolant flow balance is incorporated into this subprogram which provides the coolant flow properties required by Equations 60 and 61. the program user is provided the option of defining either the coolant flow rate or its source. The slots are assumed to be supplied from a common plenum such that the driving total pressure to each slot is identical. The coolant flow from each coolant slot is a function of both the slot flow area and the gas stream local static pressure. The coolant total pressure and individual slot coolant flow rate are computed using an iteration process. A form of the continuity equation, using isentropic considerations, is shown in terms of dependent variables, slot flow rate, and total pressure:

$$\dot{m}_c = C_d A_s P_{tc} \left(\frac{P_{tc}}{P_g} \right)^{\frac{(\gamma+1)}{\gamma}} \sqrt{\left(\frac{2\gamma}{\gamma-1} \right) \left(\frac{g}{RT_{tc}} \right) \left(\frac{P_{tc}}{P_g} \right)^{\frac{\gamma-1}{\gamma}} - 1} \quad (62)$$

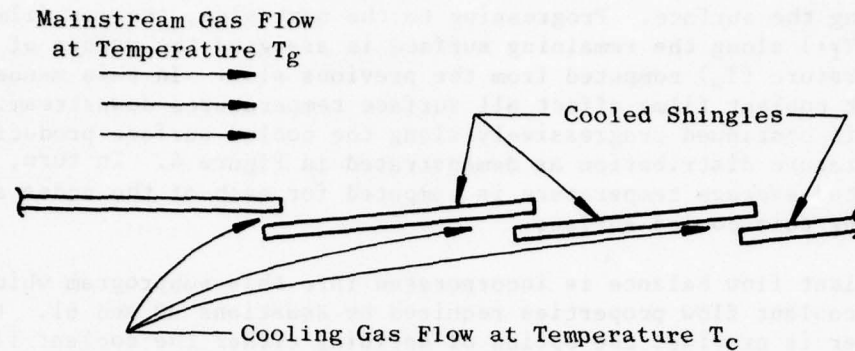
The selected total coolant flow rate is:

$$\dot{m}_{ct} = \sum_{i=1}^m \dot{m}_{ci} \quad (63)$$

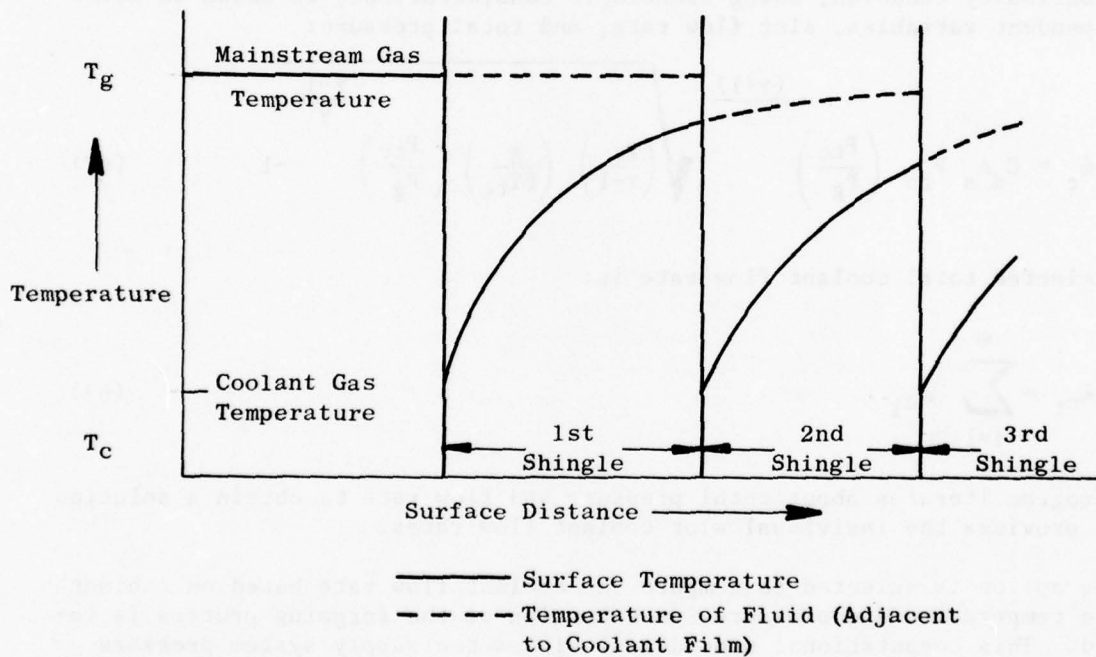
The program iterates about total pressure and flow rate to obtain a solution which provides the individual slot coolant flow rates.

If the option is selected to compute the coolant flow rate based on coolant source temperature and pressure, an extension of the forgoing process is required. This computational procedure includes the supply system pressure loss and heat transfer. The coolant supply system pressure loss is computed by the equation form:

$$\theta \Delta P_t = K (\dot{m})^n, \quad (64)$$



(a) MULTIPLE-SLOT FILM-COOLED SURFACE



(b) MULTIPLE-SLOT FILM-COOLED SURFACE TEMPERATURE DISTRIBUTION

Figure 4. Multiple-Slot Film Cooling.

where the system characteristics K and n are required input. The program solves this equation in the form:

$$\dot{m}_{ct} = \left[\rho_{std} (P_{t1}^2 - P_{t2}^2) / KR (T_{t1} + T_{tc}) \right]^{1/n} \quad (65)$$

The coolant plenum temperature is evaluated by the equation:

$$T_{tc} = T_{t2} - (T_{t2} - T_{t1}) e^{-\frac{UA}{C_{pc} \dot{m}_c}}, \quad (66)$$

where temperature of the heat source (T_{t2}) and coolant supply overall heat transfer coefficient (UA) are required input data. The combination of Equations 62, 63, 65, and 66 is solved by an iteration process which provides the resulting slot flow rates and coolant plenum temperature and pressure required in determining the wall temperature.

2. Convection-Film Cooling (CNFLM)

The convection-film cooling method computational procedure incorporated by subprogram CNFLM, developed by VAC, utilizes the empirical film-cooling correlation presented by Reference 17, and the characteristics of plate-fin heat-exchanger materials as presented in References 18 and 19.

The nomenclature used within this section is as follows:

A	- area, ft^2
C_p	- specific heat at constant pressure, $Btu/lbm, ^\circ R$
d	- the differential of a variable
d_e	- hydraulic diameter, ft
exp	- exponential (e)
ff	- Fanning friction factor, nondimensional
$f(v)$	- velocity mismatch factor, nondimensional
g	- acceleration of gravity, ft/hr^2
G	- gas mass flow velocity through the heat exchanger, $lb_m/hr\ ft^2$
h	- convective heat transfer coefficient, $Btu/hr-ft^2-^\circ R$
K	- pressure loss coefficient, lb_f/ft^2
L	- length of convection-film-cooled shingle, $feet$
\dot{m}	- mass flow rate, lb_m/hr
P	- static pressure, lb_m/ft^2
Pr	- Prandtl number, nondimensional
P_t	- total pressure, lb_m/ft^2
q	- heat flow rate, Btu/hr
R	- gas constant, $lb_f ft/lb_m, ^\circ R$
Re	- Reynolds number, nondimensional
s	- slot height, $feet$
T	- temperature or static temperature, $^\circ R$
T_t	- total temperature, $^\circ R$
UA	- overall rate of heat transfer, $Btu/hr\ ^\circ R$

- x - distance downstream of slot, ft
 ρ - density, lb_m/ft^3
 ρ_{std} - density at standard temperature and pressure, lb_m/ft^3

Subscripts:

- c - coolant
 cd - coolant discharge
 f - fluid film
 f' - adjacent to film
 g - mainstream gas
 hx - heat exchanger
 s - slot
 w - wall
 $X+\Delta x$ - incremented wall location

Figures 5a and 5b show sketches of sectioned convection-film-cooling panel configurations analysis. Referring to the element shown in Figure 5c, the heat transfer from the fluid film to the wall is equal to that transferred from the wall to the coolant when conduction along the wall is ignored, i.e.:

$$q_f = h_f A_w (T_{tf} - T_w) = (hA)_{hx} (T_w - T_{tc}) \quad (67)$$

The wall temperature can be solved as:

$$T_w = (UA) \left[T_{tf}/(hA)_{hx} + T_{tc}/(h_f A_w) \right] \quad (68)$$

where,

$$(UA) = \left[1/(hA)_{hx} + 1/(h_f A_w) \right]^{-1} \quad (69)$$

The heat flow from the heat exchanger to the plenum coolant is low because of a small difference in temperature with a relatively low plenum-side coefficient of convection. The heat gained by the heat exchanger coolant, due to the predominance of the heat flow from the film, is found to be:

$$dq_c = - \dot{m}_c C_p dT_{tc} = \left(\frac{h_f A_w}{L} \right) (T_{tf} - T_w) dx \quad (70)$$

When substituting Equation 68 into this equation and rearranging, the equation becomes:

$$\int_{(T_{tc})_x}^{(T_{tc})_{x+\Delta x}} \frac{dT_{tc}}{(T_{tc} - T_{tf})} = \frac{(UA)}{\dot{m}_c C_p L} \int_x^{x+Wx} dx \quad (71)$$

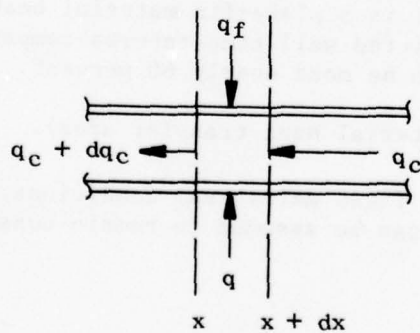
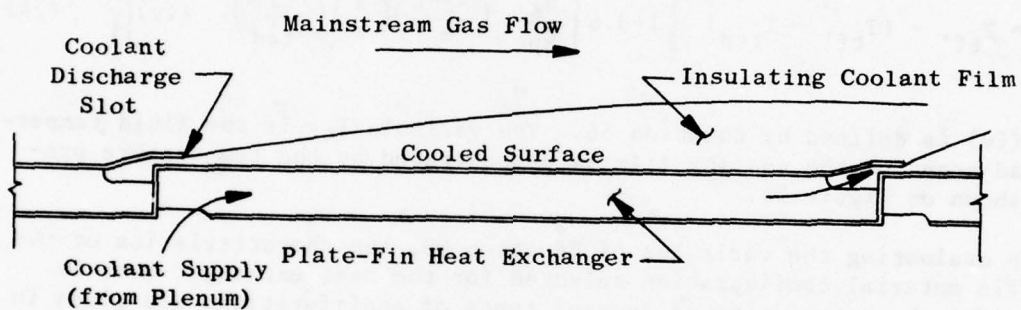
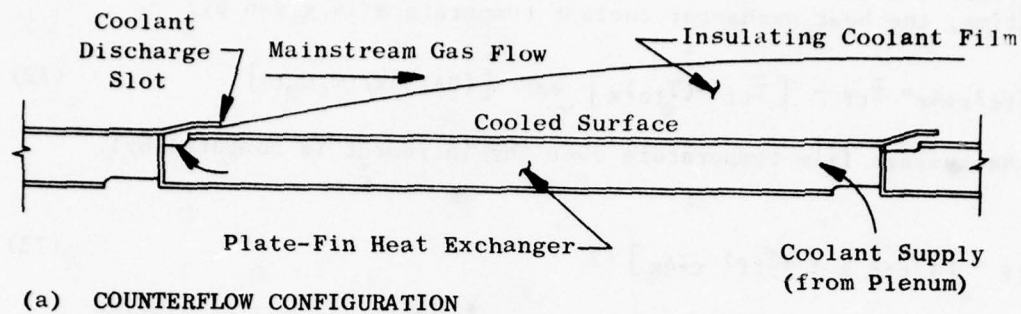


Figure 5. Convection-Film Cooling Scheme.

Holding the film temperature constant over the incremental distance Δx and integrating, the heat exchanger coolant temperature is given by:

$$(T_{tc})_{x+\Delta x} = \bar{T}_{tf} - [\bar{T}_{tf} - (T_{tc})_x] \exp [(UA) \Delta x / (\dot{m}_c C_{pL})], \quad (72)$$

where the average film temperature over the increment is computed by:

$$\bar{T}_{tf} = [(T_{tf})_x + (T_{tf})_{x+\Delta x}] / 2 \quad (73)$$

The film temperature is evaluated by methods presented in Section V.B.2.a, where, for this case, the computed wall temperature becomes the temperature of the fluid adjacent to the wall; and, the coolant temperature becomes the coolant discharge temperature. Therefore, from Equation 61, the fluid film temperature is:

$$T_{tf} = T_{tf'} - (T_{tf'} - T_{tcd}) \left\{ 1 + 3.6 \left[\frac{h_g}{C_{pc}} \left(\frac{C_d A_s}{\dot{m}_c} \right) \left(\frac{x}{s} \right) \left(\frac{T_{tf'}}{T_{tcd}} \right)^{2/3} f(v) \right] \right\}^{-1} \quad (74)$$

where $f(v)$ is defined by Equation 56. The variable T_{tf} is the fluid temperature adjacent to the cooling film as demonstrated by the temperature profiles shown on Figure 5b.

In evaluating the variables of Equation 69, the characteristics of the plate-fin material configuration selected for the heat exchanger must be known. The characteristics of several types of configurations are given in References 18 and 19. Heat transfer characteristics are presented in the form of $(h/GC_p)(Pr)^{2/3}$ versus Re . The physical characteristics, such as heat transfer and flow area, also are provided. The heat transfer data presented are for the same rate of heat transfer occurring on both walls of the heat exchanger. For the convection-film cooling method, the bulk of the heat flow occurs across only one wall. Analytically predicted, the effect of heat flow from only one wall is a plate-fin material heat transfer area reduction of 50 percent. Predicted wall temperatures compared with empirical data show this reduction to be more nearly 60 percent. Therefore,

$$A_{hx} = 0.4 \times (\text{Plate-fin material heat transfer area}). \quad (75)$$

Reference 20 shows that, under fixed mainstream conditions, the coefficient of convection along a surface can be assumed to remain constant with or without a coolant film, i.e.:

$$h_f \approx h_g \quad (76)$$

A coolant-flow-balance, pressure-loss analysis is conducted by subprogram CONFILM similar to that for film cooling in Section IV.C.1.a. With one difference between these analyses is the pressure losses which occur between the coolant plenum and the slot exit. For any reasonable design, entrance losses should be small in comparison to the losses which occur within the coolant flow passage. Plate-fin heat exchanger characteristic data include the Fanning frictional factor (fF) versus Re . The flow through this system, related to a series pressure loss, is:

$$\dot{m}_c = \left\{ (P_{tc} P_g) / \left[K_{cd} \rho_{std} R_c T_{tcd} / P_g \right] + fF \left(\frac{L}{d_e} \right) / \left(2g \rho_{hx} \Delta^2_{flow(hx)} \right) \right\}^{1/2} \quad (77)$$

The coefficient (K_{cd}) includes all the pressure losses which occur from the downstream end of the heat exchanger passage to the coolant discharge slot.

The subprogram CONFILM can either compute the total coolant flow rate or it can be a fixed input to the program. If the total flow rate is fixed, Equations 63 and 64 are solved to obtain the individual slot flow rates. Equations 63 and 66 are used to compute the overall coolant flow balance in a manner similar to that described in Section IV.C.1.a. To initiate the computational procedure, initial estimates are made of the heat exchanger fluid density and the slot discharge temperature. Initial values of flow rate are computed. The gas film temperature distribution is computed utilizing Equation 74. In turn, using Equations 72 and 73, the temperature distribution of the heat exchanger coolant is computed and based on the initial estimate of the coolant discharge temperature. The computed heat exchanger entrance coolant temperature then is compared with the coolant plenum temperature computed from Equation 66. With a mismatch in temperature, and iteration is carried out, utilizing Equations 66 through 77 for each surface by revising the estimate of coolant discharge temperature until the coolant entrance temperature converges. Once completed, the initial estimates of heat exchanger fluid density and slot discharge temperature are repeated, iterating until temperature values converge. The wall temperature distribution for each surface then is computed from Equation 68, and an area-weighted-average surface temperature is computed for each surface node involved.

The subprogram CONFILM also can handle the parallel configuration shown on Figure 5b. The basic equations are identical, with the exception that the sign of the exponential term of Equation 72 is changed. The computational procedure is carried out in a manner similar to that for the counter-flow configuration, but the iteration on coolant slot discharge temperature is not required.

3. Transpiration Cooling (TRANCL)

The cooling of a surface utilizing a transpiring gas is computed by the subprogram TRANCL. The empirical correlation for air injected through a porous wall, which was used in this program, is presented in Reference 15.

The nomenclature used within this section is as follows:

A	-	area, ft ²
C _p	-	specific heat at constant pressure, Btu/lbm, °R
F	-	injection mass flow ratio, $(\rho V)_w / (\rho V)_g$, dimensionless
h	-	convection heat transfer coefficient, Btu/hr-ft ² -°R
ii	-	number of surface increments
k'	-	porous wall loss factor, $\text{lb}_f/\text{ft}^2(\text{hr ft}^2/\text{lb}_m)^{1/n}$
\dot{m}	-	mass flow rate lb _m /hr
n	-	flow exponent to be input, nondimensional
P	-	pressure
p	-	porosity, ratio of flow area to surface area
q	-	heat flow rate, Btu/hr
R	-	gas constant, lb _f ft/lb _m , °R
St	-	Stanton number $(h_g / \rho V C_p)$
T	-	temperature or static temperature, °R
T _r	-	recovery temperature, °R
T _t	-	total temperature, °R
V	-	velocity, ft/hr
z	-	dimensionless parameter
ρ	-	density, lb _m /ft ³
ρ _{std}	-	density at standard temperature and pressure, lb _m /ft ³

Subscripts:

c	-	coolant
c'	-	coolant discharge
g	-	mainstream gas
o	-	without transpiration cooling
w	-	wall

A sectioned, transpiring, porous-wall model is shown in Figure 6 and shall be used for discussion purposes.

The heat flux by convection from a gas to an uncooled wall is determined by the equation:

$$q_o / A_w = h_o (T_r - T_w) \quad (78)$$

At steady-state conditions, heat added to the porous wall from the mainstream is removed by the coolant flow. The lateral heat transfer by conduction is assumed to be zero, i.e., no temperature gradient exists along the wall. The heat addition from the mainstream is transferred to, and carried off by, the coolant gas. This is presented by the heat balance:

$$q = hA_w (T_r - T_w) = \dot{m}_c C_{pc} (T_{tc}' - T_{tc}) \quad (79)$$

For a good design, the heat transfer efficiency between the porous wall and the coolant passing through the wall will permit the coolant discharge temperature (T_{tc}) to approach the wall's outer surface temperature (T_w)

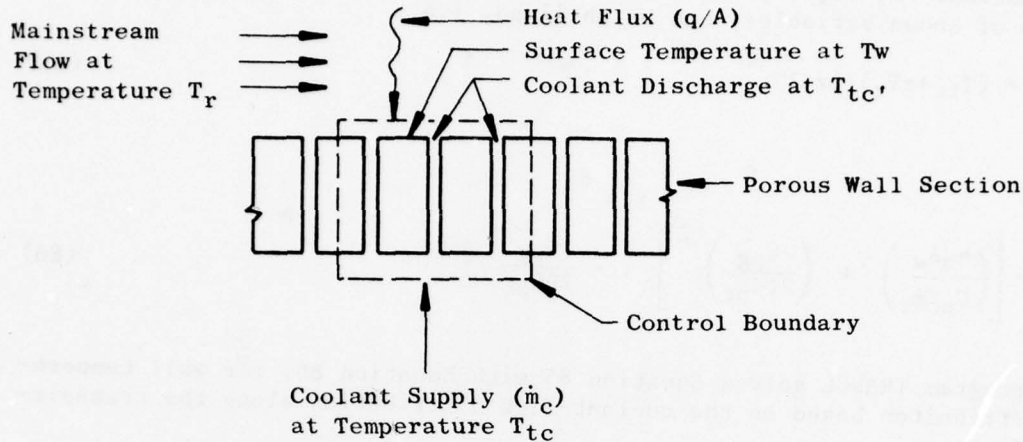


Figure 6. Transpiration Cooling, Sectioned, Porous-Wall Model.

Assuming this to be the case, then Equation 79 can be written as:

$$hA_w (T_r - T_w) = \dot{m}_c C_{pc} (T_w - T_c) \quad (80)$$

The coefficient of convection (h) on a transpiration surface is difficult to obtain. An equation derived by Reference 21, compared with the empirical data presented in Reference 22, relates the heat flow rate to a surface with and without transpiration cooling under the same imposed mainstream conditions. Correlation is provided by the relationship:

$$\frac{q}{q_0} = \sqrt{\frac{1}{2} \frac{F}{St_0} + 1} - \frac{1}{2} \frac{F}{St_0} \quad (81)$$

where:

$$F = (\rho_c/V_c)/(\rho_g V_g), \quad (82)$$

With the aid of the continuity equation and the definition of Stanton number:

$$St_0 = h_0/(C_{pg} \rho_g V_g), \quad (83)$$

the ratio:

$$F/St_0 = (C_{pg} \dot{m}_c) / pA_w h_0 \quad (84)$$

From Equations 78, 80, 81, and 84, an equation defining wall temperature, in terms of known variables, can be obtained, i.e.:

$$T_w = (T_{tc} + zT_r) / (z+1) \quad (85)$$

where,

$$z = \left[\left(\frac{h_0 A_w}{C_{pc} \dot{m}_c} \right) + \left(\frac{C_{pg}}{2PC_{pc}} \right)^2 \right]^{1/2} - \frac{C_{pg}}{2PC_{pc}} \quad (86)$$

The subprogram TRANCL solves Equation 85 with Equation 86, for wall temperature distribution based on the coolant-flow distribution along the transpiring surface.

The coolant flow conditions are established by this program in a manner similar to that discussed in Section IV.C.1.a. The same options are available (i.e., the coolant flow rate fixed or computed based on its source conditions). The pressure loss across the wall is computed from Equation 64. Since the mainstream static pressure may vary along the surface being cooled, surface increments are taken by the program which permit the coolant flow rate to vary along the surface. The flow relationship for the surface increments, assuming that the same plenum feeds the complete surface is found to be:

$$\dot{m}_{ci} = A_{ci} \left[p_g (P_{Tc} - P_g) / (k' \rho_{std} R_c T_{tc}) \right]^{1/n} \quad (87)$$

where the total coolant flow rate is:

$$\dot{m}_c = \sum_{i=1}^{ii} \dot{m}_{ci} \quad (88)$$

If the coolant flow rate is fixed by the user, Equations 87 and 88 are solved to provide flow for each surface increments. When the program is required to compute the coolant flow rate, these equations (in conjunction with Equations 65 and 66) are solved in a manner similar to that presented in Section IV.C.1.a.

D. Exhaust System Radiation (NVIEW)

Radiant energy is interchanged between the internal surfaces of the exhaust system and is emitted from the exhaust system surfaces to a remote detector. Internal radiation is required for an internal surface heat balance which produces the surface temperature distribution within the exhaust system. The irradiation incident upon the detector provides the signature of the particular exhaust system under investigation. The most difficult parameter to compute is the radiation view factor.

1. View Factor Calculations (VIEW)

Heat transfer texts define the view factor between a radiating black surface A, and a receiving black surface B, as that fraction of the radiation that leaves A and arrives at B. For bodies which are gray bodies (that is, their emissivities are constant with respect to radiation wave length), the black-body view factors can be used in combination with the emissivities of the surfaces to arrive at a parameter $F(A,B)$, which expresses the net fraction of the radiation which leaves A and is absorbed by B. The black-body view factor, therefore, is a key parameter to radiation heat transfer computations.

The defining equation for the view factor between two surfaces is given by Equation 89:

$$F_{1-2} = \frac{1}{A_1} \int_{A_2} \int_{A_1} \frac{\cos \theta_1 \cos \theta_2}{\pi r^2} dA_1 dA_2 \quad (89)$$

The nomenclature used in Equation 89, and the computer program name used for each variable, are listed below:

- F_{1-2} , $F(J,K)$ - The surface radiation view factor between the radiation source surface (J) and the radiation receiving surface (K) $J=1$, $K=2$.
- A_1 , $A(J)$ - The surface area of the radiation source surface.
- A_2 , $A(K)$ - The surface area of the radiation receiver surface.
- π , PIE - The constant 3.141592653589793
- dA_1 , dA_2 (no computer name) - infinitesimally small areas respectively on surfaces 1 and 2 (Figure 7)

- ρ - (Computer name RH ϕ) - the distance between the two areas dA_1 and dA_2 (see Figure 7).
- θ_1 - (No computer name) - the angle between the outward normal, \bar{N}_1 , on the radiating surface and the line of length, ρ , between dA_1 and dA_2 (see Figure 7).
- θ_2 - (No computer name) - the angle between the outward normal, \bar{N}_2 , on the receiving surface and the line of length, ρ , between dA_1 and dA_2 (see Figure 7).

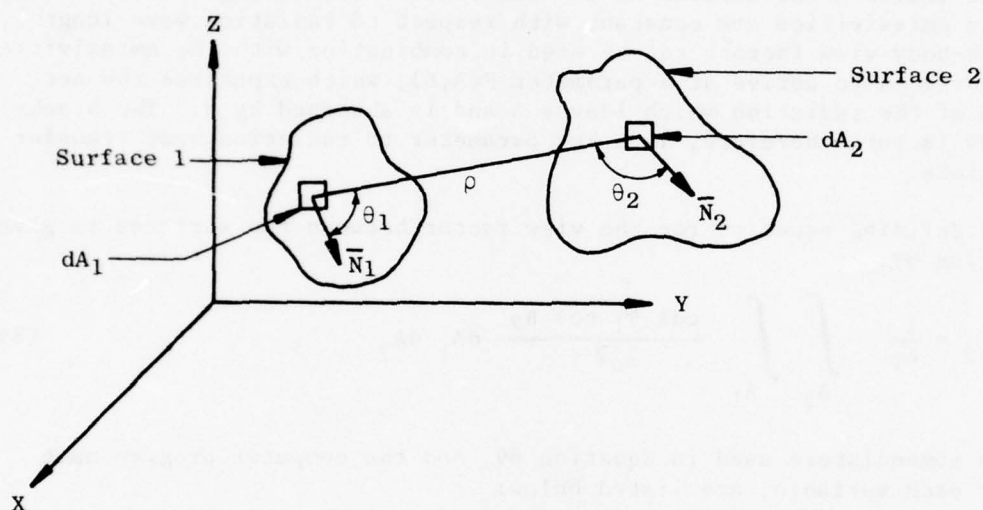


Figure 7. Geometry Parameters Used in the Definition of the View Factor.

We now seek to evaluate the quantities in the integrand of Equation 89. We do this for a typical axisymmetric subsection of the exhaust system which is either a frustrum of a cone or a disc. First we restrict our attention to frustrums.

A frustrum is shown in Figure 8 to define the variables to be used in describing the frustrum.

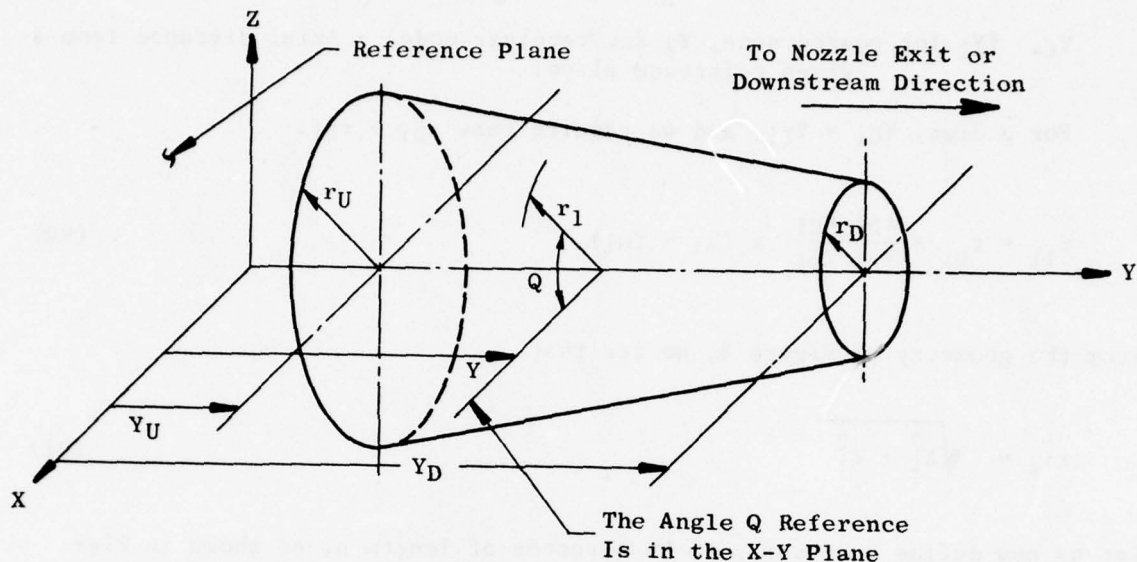


Figure 8. Frustum Geometry Variables.

The frustrum variables and their corresponding computer names are as follows:

- Y_{Ui} , $YU(I)$ - Axial distance from the reference plane to the upstream end of the frustrum. $I=1$ for the source node; $I=2$ for the receiver node.
- Y_{Di} , $YD(I)$ - Axial distance from the reference plane to the downstream end of the frustrum. $I=1$ for the source node; $I=2$ for the receiver node.
- r_{Ui} , $RU(I)$ - Radius of the frustrum at its upstream end. $I=1$ for the source node; $I=2$ for the receiver node.
- r_{Di} , $RD(I)$ - Radius of the frustrum at its downstream end. $I=1$ for the source node; $I=2$ for the receiver node.

r_{li} , (R_1 for node 1, R_2 for node 2) - Radius of the frustrum at any Y .

ϕ_i (PHI_i for the source node surface) - an angle that determines circumferential positions on the frustrum. ($I=1$ for the source node; $I=2$ for the receiver.)

Y_i , (Y_1 for source node, Y_2 for receiver node) - Axial distance from a given reference plane.

For a disc, $Y_{Ui} = Y_{Di}$, and we require that $r_{Di} > r_{Ui}$.

$$r_{li} = r_{Ui} + \frac{r_{Di} - r_{Ui}}{Y_{Di} - Y_{Ui}} \times (Y_i - Y_{Ui}) \quad (90)$$

From the geometry of Figure 8, we see that

$$r_{li} = \sqrt{x_i^2 + z_i^2} \quad (91)$$

Let us now define a vector $\bar{\rho}$ to be a vector of length ρ , as shown in Figure 8, which has the direction from differential area dA_1 to differential area dA_2 . The equation for $\bar{\rho}$ can be defined in terms of the position coordinates of the differentials dA_1 and dA_2 , and is:

$$\bar{\rho} = (X_2 - X_1) \bar{i} + (Y_2 - Y_1) \bar{j} + (Z_2 - Z_1) \bar{k} \quad (92)$$

where

X_2 (has the computer name X2 for the receiver node)
 X_1 (has the computer name X1 for the source node)
 Z_2 (has the computer name Z2 for the receiver node)
 Z_1 (has the computer name Z1 for the source node)
 i (no computer name) the unit vector along the x axis
 j (no computer name) the unit vector along the y axis
 k (no computer name) the unit vector along the z axis

The orientation of the normal vectors \bar{N}_1 and \bar{N}_2 (see Figure 7) in space must be known as well as the position the line ρ , or the vector $\bar{\rho}$, in order to determine the values for $\cos \theta$, and $\cos \theta_2$ of Equation 176. This can be done by finding the direction cosines of N_1 and N_2 with respect to the X-Y-Z axes of the problem. The angles between N_1 and the X-Y-Z axes are displayed in Figure 9. (the variables α , β , and γ have no computer program names.)

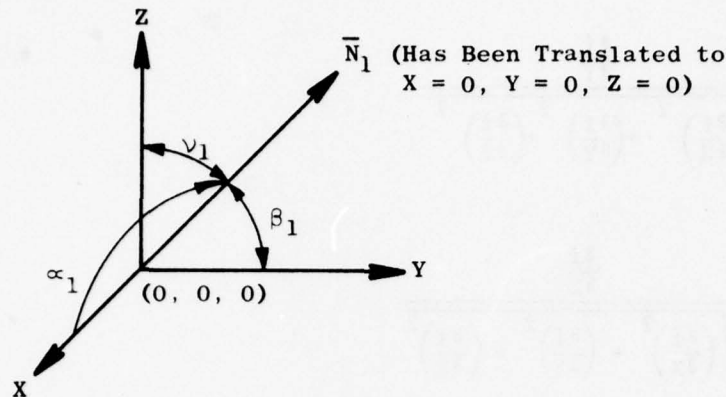


Figure 9. Direction of Cosine Angles Defined.

It can be shown that if \bar{N}_1 and \bar{N}_2 are vectors of unit length then:

$$\bar{N}_1 = \cos \alpha_1 \bar{i} + \cos \beta_1 \bar{j} + \cos \gamma_1 \bar{k} \quad (93)$$

and,

$$\bar{N}_2 = \cos \alpha_2 \bar{i} + \cos \beta_2 \bar{j} + \cos \theta_2 \bar{k}_2 \quad (94)$$

where, $\cos \alpha_1$ has the computer name CA1
 $\cos \beta_1$ has the computer name CB1
 $\cos \gamma_1$ has the computer name CG1 and
 $\cos \alpha_2$, $\cos \beta_2$, and $\cos \gamma_2$ do not have computer names

The evaluation of the direction cosine is based on information drawn from texts on calculus. This information says that, given a surface whose coordinates may be written functionally as:

$$f(X, Y, Z) = 0,$$

then, the outward normal to the surface is given by the following relationship:

$$\bar{N} = \frac{\bar{i} \frac{\partial f}{\partial X} + \bar{j} \frac{\partial f}{\partial Y} + \bar{k} \frac{\partial f}{\partial Z}}{\sqrt{\left(\frac{\partial f}{\partial X}\right)^2 + \left(\frac{\partial f}{\partial Y}\right)^2 + \left(\frac{\partial f}{\partial Z}\right)^2}}$$

It then can be shown that:

$$\cos \alpha = \frac{\frac{\partial f}{\partial X}}{\sqrt{\left(\frac{\partial f}{\partial X}\right)^2 + \left(\frac{\partial f}{\partial Y}\right)^2 + \left(\frac{\partial f}{\partial Z}\right)^2}}$$

$$\cos \beta = \frac{\frac{\partial f}{\partial Y}}{\sqrt{\left(\frac{\partial f}{\partial X}\right)^2 + \left(\frac{\partial f}{\partial Y}\right)^2 + \left(\frac{\partial f}{\partial Z}\right)^2}}$$

$$\cos \gamma = \frac{\frac{\partial f}{\partial Z}}{\sqrt{\left(\frac{\partial f}{\partial X}\right)^2 + \left(\frac{\partial f}{\partial Y}\right)^2 + \left(\frac{\partial f}{\partial Z}\right)^2}}$$

For a frustum, the equation $f(X, Y, Z) = 0$ is obtained by combining Equations 90 and 178 to get:

$$f_i = \sqrt{X_i^2 + Z_i^2} - \frac{(rU_i YD_i - rD_i YU_i)}{(YD_i - YU_i)} - Y_i \left(\frac{rD_i - rU_i}{YD_i - YU_i} \right) = 0 \quad (95)$$

From Equation 95 we find:

$$\frac{\partial f_i}{\partial X_i} = \frac{X_i}{\sqrt{X_i^2 + Z_i^2}} = \frac{X_i}{r l_i} \quad (96)$$

$$\frac{\partial f_i}{\partial Y_i} = - \frac{YD_i - YU_i}{YD_i - YU_i} \quad (97)$$

$$\frac{\partial f_i}{\partial Z_i} = \frac{Z_i}{\sqrt{X_i^2 + Z_i^2}} = \frac{Z_i}{r l_i} \quad (98)$$

$$\sqrt{\left(\frac{\partial f_i}{\partial X_i}\right)^2 + \left(\frac{\partial f_i}{\partial Y_i}\right)^2 + \left(\frac{\partial f_i}{\partial Z_i}\right)^2} = \frac{\sqrt{YD_i - YU_i^2 + rD_i - rU_i^2}}{YD_i - YU_i} \quad (99)$$

Thus, for frustum nodes,

$$\cos \alpha_1 = \frac{X_1}{r_{11}} \frac{YD_1 - YU_1}{\sqrt{(YD_1 - YU_1)^2 + (rD_1 - rU_1)^2}} \quad (100)$$

$$\cos \alpha_2 = \frac{X_2}{r_{12}} \frac{YD_2 - YU_2}{\sqrt{(YD_2 - YU_2)^2 + (rD_2 - rU_2)^2}}$$

$$\cos \beta_1 = \frac{-rD_1 - rU_1}{\sqrt{(YD_1 - YU_1)^2 + (rD_1 - rU_1)^2}} \quad (101)$$

$$\cos \beta_2 = \frac{-rD_2 - rU_2}{\sqrt{(YD_2 - YU_2)^2 + (rD_2 - rU_2)^2}} \quad (102)$$

$$\cos \gamma_1 = \frac{Z_1}{r_{11}} \frac{X \ YD_1 - YU_1}{\sqrt{(YD_1 - YU_1)^2 + (rD_1 - rU_1)^2}} \quad (103)$$

$$\cos \gamma_2 = \frac{Z_2}{r_{12}} \frac{X \ YD_2 - YU_2}{\sqrt{(YD_2 - YU_2)^2 + (rD_2 - rU_2)^2}} \quad (104)$$

To facilitate computations, we define:

\tilde{A}_1 (computer name is A1) as:

$$\tilde{A}_1 \equiv \frac{-rD_1 - rU_1}{\sqrt{(YD_1 - YU_1)^2 + (rD_1 - rU_1)^2}} \quad (105)$$

\tilde{A}_2 (computer name is A2) as:

$$\tilde{A}_2 \equiv \frac{-(rD_2 - rU_2)}{\sqrt{(YD_2 - YU_2)^2 + (rD_2 - rU_2)^2}} \quad (106)$$

\tilde{B}_1 (computer name is B1) as:

$$\tilde{B}_2 \equiv \frac{(YD_1 - YU_1)}{\sqrt{(YD_1 - YU_1)^2 + (rD_1 - rU_1)^2}} \quad (107)$$

\tilde{B}_2 (computer name is B2) as:

$$\tilde{B}_2 \equiv \frac{(YD_2 - YU_2)}{\sqrt{(YD_2 - YU_2)^2 + (rD_2 - rU_2)^2}} \quad (108)$$

So,

$$\begin{aligned} \cos \alpha_1 &= \frac{X_1}{r1_1} \tilde{B}_1 & \cos \alpha_2 &= \frac{X_2}{r1_2} \tilde{B}_2 \\ \cos \beta_1 &= \tilde{A}_1 & \cos \beta_2 &= \tilde{A}_2 \\ \cos \gamma_1 &= \frac{Z_1}{r1_1} \tilde{B}_1 & \cos \gamma_2 &= \frac{Z_2}{r1_2} \tilde{B}_2 \end{aligned} \quad (109)$$

Because the geometry of the frustum is axisymmetric, it is convenient to utilize cylindrical coordinates to facilitate the integration of Equation 89.

For cylindrical coordinates:

$$\begin{aligned} X_1 &= r1_1 \cos \phi_1 & X_2 &= r1_2 \cos \phi_2 \\ Z_1 &= r1_1 \sin \phi_1 & Z_2 &= r1_2 \sin \phi_2 \end{aligned} \quad (110)$$

where, $\cos \phi_1$ has the computer name CPL, and
 $\sin \phi_1$ has the computer name SPL.

Equation 196 then becomes:

$$\cos \alpha_1 = \tilde{B}_1 \cos \phi_1 \qquad \cos \alpha_2 = \tilde{B}_2 \cos \phi_2 \qquad (111)$$

$$\cos \beta_1 = \tilde{A}_1 \qquad \cos \beta_2 = \tilde{B}_2 = \tilde{A}_2 \qquad (112)$$

$$\cos \gamma_1 = \tilde{B}_1 \sin \phi_1 \qquad \cos \gamma_2 = \tilde{B}_2 \sin \phi_2$$

If the normal to the inside of the frustum is required for either surface, the signs of A and B are changed for that surface. This situation is detected within the program by an input variable VECT (I), I=1 for the source node, I=2 for the receiver node. If the outside of a frustum surface is of concern, VECT (I) = +1 for that surface. If the inside of a frustum surface is of concern, VECT (I) = -1 for that surface.

We can write:

$$\bar{N}_1 = \tilde{B}_1 \cos \phi_1 \bar{i} + \tilde{A}_1 \bar{j} + \tilde{B}_1 \sin \phi_1 \bar{k}$$

and, (113)

$$\bar{N}_2 = \tilde{B}_2 \cos \phi_2 \bar{i} + \tilde{A}_2 \bar{j} + \tilde{B}_2 \sin \phi_2 \bar{k}$$

Using Equation 110 with Equation 95, we can express $\bar{\rho}$ in cylindrical coordinates as:

$$\begin{aligned} \bar{\rho} = & \left(r_{l2} \cos \phi_2 - r_{l1} \cos \phi_1 \right) \bar{i} + \left(Y_2 - Y_1 \right) \bar{j} \\ & + \left(r_{l2} \sin \phi_2 - r_{l1} \sin \phi_1 \right) \bar{k} \end{aligned} \qquad (114)$$

We can now determine $\cos \theta_1$ and $\cos \theta_2$ from the following vector dot product definitions and Equations 113 and 114:

$$\bar{\rho} \cdot \bar{N}_1 \equiv |\bar{\rho}| |\bar{N}| \cos \theta_1 \qquad (115)$$

$$-\bar{\rho} \cdot \bar{N}_2 \equiv |\bar{\rho}| |\bar{N}_2| \cos r_1 \quad (116)$$

$$|\bar{N}_1| \equiv 1, |\bar{N}_2| = 1 \quad (117)$$

$$|\rho| = \sqrt{\bar{\rho} \cdot \bar{\rho}} \quad (118)$$

$$|\bar{\rho}| = \sqrt{(rl_2 \cos \phi_2 - rl_1 \cos \phi_1)^2 + (Y_2 - Y_1)^2 + (rl_2 \sin \phi_2 - rl_1 \sin \phi_1)^2}$$

After some algebraic manipulation and use of trigonometric identities, such as $\cos^2 \phi + \sin^2 \phi = 1$ and $\cos(\phi_2 - \phi_1) = \cos \phi_2 \cos \phi_1 + \sin \phi_2 \sin \phi_1$, Equation 118 can be written as:

$$|\bar{\rho}| = \sqrt{rl_1^2 + rl_2^2 - 2rl_1rl_2 \cos(\phi_2 - \phi_1) + (Y_2 - Y_1)^2} \quad (119)$$

Also,

$$\rho^2 = rl_1^2 + rl_2^2 - 2rl_1rl_2 \cos(\phi_2 - \phi_1) + (Y_2 - Y_1)^2 \quad (120)$$

The quantity ρ^2 is given the computer name RH02.

From Equations 200 through 206, we obtain:

$$\cos \phi_1 = \frac{(rl_2 \cos \phi_2 - rl_1 \cos \phi_1) \tilde{B}_1 \cos \phi_1 + (Y_2 - Y_1) \tilde{A}_1 + (rl_2 \sin \phi_2 - rl_1 \sin \phi_1) \tilde{B}_1 \sin \phi_1}{\sqrt{rl_1^2 + rl_2^2 - 2rl_1rl_2 \cos(\phi_2 - \phi_1) + (Y_2 - Y_1)^2}}$$

or, with some algebraic manipulations and with the aforementioned trigonometric identities, we obtain:

$$\cos \theta_1 = \frac{\tilde{B}_1 rl_2 \cos(\phi_2 - \phi_1) - \tilde{B}_1 rl_1 + (Y_2 - Y_1) \tilde{A}_1}{\sqrt{rl_1^2 + rl_2^2 - 2rl_2rl_1 \cos(\phi_2 - \phi_1) + (Y_2 - Y_1)^2}} \quad (121)$$

and,

$$\cos \theta_2 = \frac{-(r_{l2} \cos \phi_2 - r_{l1} \cos \phi_1) \tilde{B}_2 \cos \phi_2 - (Y_2 - Y_1) \tilde{A}_2 - (r_{l2} \sin \phi_2 - r_{l1} \sin \phi_1) \tilde{B}_2 \sin \phi_2}{\sqrt{r_{l1}^2 + r_{l2}^2 - 2r_{l1}r_{l2} \cos(\phi_2 - \phi_1) + (Y_2 - Y_1)^2}}$$

or

$$\cos \theta_2 = \frac{\tilde{B}_2 r_{l1} \cos(\phi_2 - \phi_1) - \tilde{B}_2 r_{l2} - (Y_2 - Y_1) \tilde{A}_2}{\sqrt{r_{l2}^2 + r_{l1}^2 - 2r_{l1}r_{l2} \cos(\phi_2 - \phi_1) + (Y_2 - Y_1)^2}} \quad (122)$$

The remaining quantities that must be expressed in terms of cylindrical coordinates or evaluated are dA_1 , dA_2 , and A_1 . We also evaluate A_2 at this time.

An infinitesimal area dA_i on a dY_i slice of a frustum is displayed in Figure 10, along with the nomenclature that will be used to evaluate dA_i .

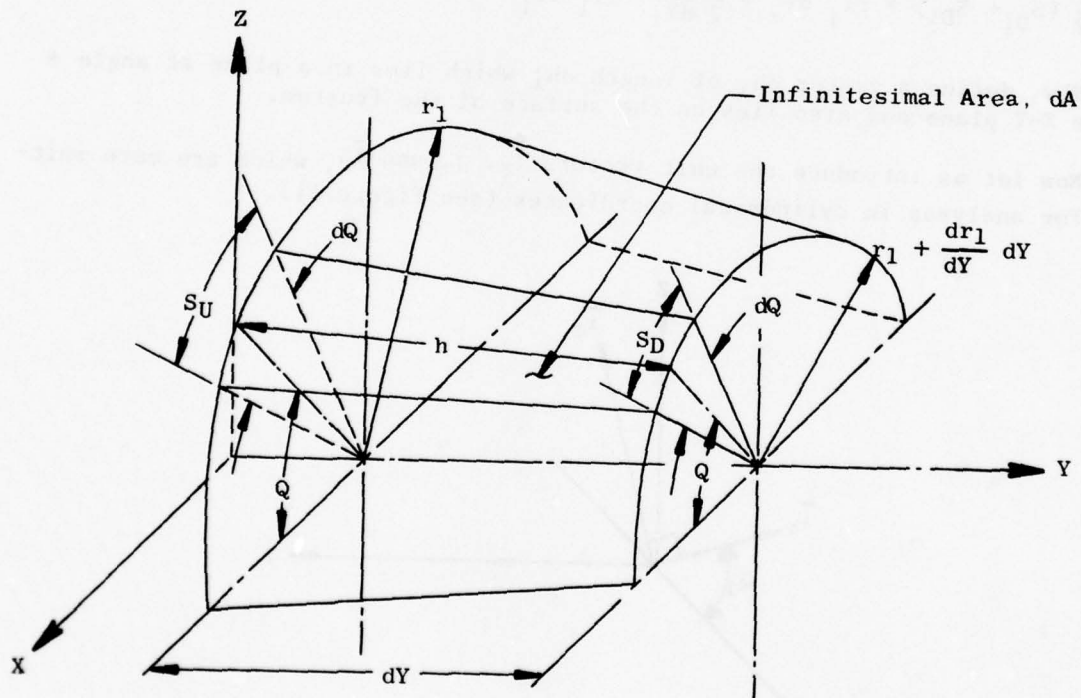


Figure 10. Geometry Used to Determine the Infinitesimal Area Expression for a Frustum.

The elemental area is formed by two planes that are normal to the Y axis and two planes which contain Y axis and have dihedral angles $\phi - d\phi/2$ and $\phi + d\phi/2$ with respect to the X-Y plane.

The elemental area is essentially a trapezoid. Therefore ($i=1$) for the source node, $i=2$ for the receiver):

$$dA_i = \frac{1}{2} (S_{Ui} + S_{Di}) dh_i \quad (123)$$

where,

dh_i = the slant altitude of the element for angle ϕ_i ,

$$S_{Ui} = r l_i d\phi_i \quad S_{Di} = \left(r l_i + \frac{dr l_i}{dY_i} \right) d\phi_i$$

and,

$$\frac{1}{2} (S_{Ui} + S_{Di}) = r l_i d\phi_i + \frac{1}{2} \frac{dr l_i}{dY_i} dY_i d\phi_i \quad (124)$$

Now, define a vector dh_i of length dh_i which lies in a plane at angle ϕ to the X-Y plane and also lies on the surface of the frustum.

Now let us introduce the unit vectors \bar{i}_ϕ , \bar{j} , and \bar{i}_r , which are more suitable for analyses in cylindrical coordinates (see Figure 11).

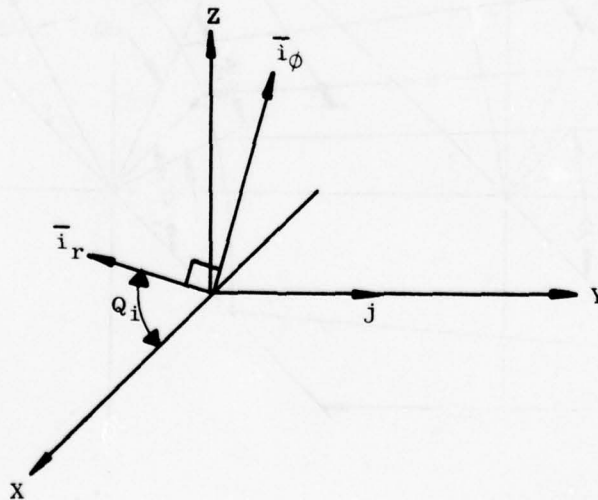


Figure 11. Unit Vectors for Cylindrical Coordinates.

We can write in term of \bar{i}_r , \bar{i}_ϕ , and \bar{j} :

$$\overline{dh}_i = drl_i \bar{i}_r + 0 \bar{i}_\phi + dY_i \bar{j}$$

From Equation 90 we will find $drl_i = \frac{(rD_i - rU_i)}{(YD_i - YU_i)} dY_i$

$$\therefore (dh_i)^2 = (\overline{dh}_i) \cdot (\overline{dh}_i) = \left[\frac{(rD_i - rU_i)^2}{(YD_i - YU_i)^2} + 1 \right] dY_i^2$$

or,

$$dh_i = \frac{dY_i \sqrt{(rD_i - rU_i)^2 + (YD_i - YU_i)^2}}{YD_i - YU_i} = \frac{dY_i}{\tilde{B}_i} \quad (125)$$

Now substitute Equations 212 and 211 into Equation 210 to obtain:

$$dA_i = \frac{rl_i}{\tilde{B}_i} dY_i d\phi_i + \frac{1}{2} \frac{drl_i}{dY_i} dY_i d\phi_i \frac{dY_i}{\tilde{B}_i} \approx \frac{rl_i}{\tilde{B}_i} dY_i d\phi_i \quad (126)$$

$$\therefore A_i = \int_{YU_1}^{YD_1} \frac{rl_i}{\tilde{B}_i} dY_i \int_{\phi_1=0}^{\phi_1=2\pi} d\phi_i = 2\pi \int_{YU_1}^{YD_i} \frac{rl_i}{\tilde{B}_i} dY_i$$

Substitute Equation 90 into the above equation to obtain:

$$A_i = \frac{2\pi}{\tilde{B}_i} \int_{YU_1}^{YD_1} \left[rU_1 + \frac{(rD_1 - rU_1)}{(YD_1 - YU_1)} Y_1 - \frac{(rD_1 - rU_1)}{(YD_1 - YU_1)} YU_1 \right] dY_1$$

or,

$$A_1 = \frac{\pi}{\tilde{B}_1} \left(rU_1 + rD_1 \right) \left(YD_1 - YU_1 \right) \quad (127)$$

Substitute Equation 107 into Equation 127 to obtain:

$$A_1 = \pi \left(rU_1 + rD_1 \right) \left(YD_1 - YU_1 \right)^2 + \left(rD_1 - rU_1 \right)^2 \quad (128)$$

In a similar manner, it can be found that:

$$A_2 = \pi \left(rU_2 + rD_2 \right) \left(YD_2 - YU_2 \right)^2 + \left(rD_2 - rU_2 \right)^2 \quad (129)$$

Equations 128 and 129 are used in the program to find A_1 and A_2 .

We are now in a position to rewrite the integrand of Equation 89 in terms of variables which are suitable for integration in cylindrical coordinates. This expression is obtained by substituting Equations 121, 122, 120, and 126 into Equation 89:

$$\begin{aligned} F_{1-2} = & \frac{1}{A_1} \int_{\phi_{1,lo}}^{\phi_{1,up}} \int_{YU_1}^{YD_1} \int_{YU_2}^{YD_2} \int_{\phi_{2,lo}}^{\phi_{2,up}} \frac{\tilde{B}_1 r l_2 \cos(\phi_2 - \phi_1) - \tilde{B}_1 r l_1 + (Y_2 - Y_1) \tilde{A}_1}{r l_1^2 + r l_2^2 - 2 r l_2 r l_1 \cos(\phi_2 - \phi_1) + (Y_2 - Y_1)^2} \\ & \times \frac{\tilde{B}_2 r l_1 \cos(\phi_2 - \phi_1) - \tilde{B}_2 r l_2 - (Y_2 - Y_1) \tilde{A}_2}{r l_1^2 + r l_2^2 - 2 r l_2 r l_1 \cos(\phi_2 - \phi_1) + (Y_2 - Y_1)^2} \\ & \times \frac{1}{\pi} \times \left[\frac{1}{r l_1^2 + r l_2^2 - 2 r l_2 r l_1 \cos(\phi_2 - \phi_1) + (Y_2 - Y_1)^2} \right] \\ & \times \frac{r l_1 d\phi_1 dY_1}{\tilde{B}_1} \times \frac{r l_2 dY_2 d\phi_2}{\tilde{B}_2} \quad (130) \end{aligned}$$

where $\phi_{1,up}$, $\phi_{2,up}$, $\phi_{1,lo}$, and $\phi_{2,lo}$ are appropriate limits for ϕ_1 and ϕ_2 to be determined in subsequent analyses.

We now seek to simplify the integrand of Equation 130. Consider first the product of the two numerators:

$$\begin{aligned}
 & \left[\tilde{B}_1 r l_2 \cos(\phi_2 - \phi_1) - \tilde{B}_1 r l_1 + (Y_2 - Y_1) \tilde{A}_1 \right] \times \left[\tilde{B}_2 r l_1 \cos(\phi_2 - \phi_1) - \tilde{B}_2 r l_2 (Y_2 - Y_1) \tilde{A}_2 \right] \\
 &= \tilde{B}_1 \tilde{B}_2 r l_1 r l_2 \cos^2(\phi_2 - \phi_1) - \tilde{B}_1 \tilde{B}_2 r l_1^2 \cos(\phi_2 - \phi_1) \\
 &+ \tilde{B}_1 \tilde{A}_1 r l_1 (Y_2 - Y_1) \cos(\phi_2 - \phi_1) - \tilde{B}_1 \tilde{B}_2 r l_2^2 \cos(\phi_2 - \phi_1) \\
 &+ \tilde{B}_1 \tilde{B}_2 r l_1 r l_2 - \tilde{B}_2 \tilde{A}_1 r l_2 (Y_2 - Y_1) - \tilde{B}_1 \tilde{A}_2 r l_2 (Y_2 - Y_1) \cos(\phi_2 - \phi_1) \\
 &+ \tilde{B}_1 \tilde{A}_2 r l_1 (Y_2 - Y_1) - \tilde{A}_1 \tilde{A}_2 (Y_2 - Y_1)^2 \\
 &= \tilde{B}_1 \tilde{B}_2 r l_1 r l_2 \cos^2(\phi_2 - \phi_1) + -\tilde{B}_1 \tilde{B}_2 r l_1^2 + \tilde{B}_2 \tilde{A}_1 r l_1 (Y_2 - Y_1) \\
 &- \tilde{B}_1 \tilde{B}_2 r l_2^2 - \tilde{B}_1 \tilde{A}_2 r l_2 (Y_2 - Y_1) \cos(\phi_2 - \phi_1) \\
 &+ \tilde{B}_1 \tilde{B}_2 r l_1 r l_2 - \tilde{B}_2 \tilde{A}_1 r l_2 (Y_2 - Y_1) + \tilde{B}_1 \tilde{A}_2 r l_1 (Y_2 - Y_1) \\
 &- \tilde{A}_1 \tilde{A}_2 (Y_2 - Y_1)^2
 \end{aligned}$$

We now define:

$$CI_1 \equiv \tilde{B}_1 \tilde{B}_2 r l_1 r l_2 \quad \text{where the computer name for } CI_1 \text{ is } CII. \quad (131)$$

$$CI_2 \equiv \tilde{B}_2 \tilde{A}_1 r l_1 (Y_2 - Y_1) - \tilde{B}_1 \tilde{B}_2 r l_1^2 - \tilde{B}_1 \tilde{B}_2 r l_2^2 - \tilde{B}_1 \tilde{A}_2 r l_2 (Y_2 - Y_1) \quad (132)$$

where the computer name for CI₂ is CI2.

$$CI_2 \equiv \tilde{B}_1 \tilde{B}_2 r_{11} r_{12} - \tilde{B}_2 \tilde{A}_1 r_{12} (Y_2 - Y_1) + \tilde{B}_1 \tilde{A}_2 r_{11} (Y_2 - Y_1) - \tilde{A}_1 \tilde{A}_2 (Y_2 - Y_1) \quad (133)$$

where the computer name for CI₃ is CI3.

Now, consider the terms of the denominator:

We define:

$$C \equiv r_{11}^2 + r_{12}^2 + (Y_2 - Y_1)^2 \quad (134)$$

where the program name for this group is also C.

$$\text{Let } D \equiv 2r_{12}r_{11} \quad (\text{program name} = D) \quad (135)$$

Equation 217 can now be written:

$$F_{1-2} = \frac{1}{\pi A_1} \int_{\phi_{1,10}}^{\phi_{1,up}} \int_{Y_{U1}}^{Y_{D1}} \int_{Y_{U2}}^{Y_{D2}} \int_{\phi_{2,10}}^{\phi_{2,up}} \frac{C_{11} \cos^2(\phi_2 - \phi_1)}{[C - D \cos(\phi_2 - \phi_1)]^2} \quad (136)$$

$$+ \frac{C_{12} \cos(\phi_2 - \phi_1)}{C - D \cos(\phi_2 - \phi_1)^2} + \frac{C_{13}}{[C - D \cos(\phi_2 - \phi_1)]^2} \frac{r_{11} r_{12} d\phi_2 dY_2 dY_1 d\phi_1}{\tilde{B}_1 \tilde{B}_2}$$

Consider the evaluation of the first integration; that is, the integration with respect to ϕ_2 where Y_1 , ϕ_1 , and Y_2 are assumed to be held constant.

$$\text{We now define } \phi = \phi_2 - \phi_1 \text{ (no computer name for } \tilde{\phi}) \quad (137)$$

For integration with respect to ϕ_2 alone:

$$d\tilde{\phi} = d\phi_2 \quad (138)$$

Also, when:

$$\phi_2 = \phi_{2,lo}, \quad \tilde{\phi}_{lo} = \phi_{2,lo} - \phi_1 \quad (139)$$

$$\phi_2 = \phi_{2,up}, \quad \tilde{\phi}_{up} = \phi_{2,up} - \phi_1$$

The first integral then becomes:

$$EI_{20} = \int_{\tilde{\phi}_{lo}}^{\tilde{\phi}_{up}} \left[\frac{C_{I1} \cos^2 \tilde{\phi}}{(C - D \cos \tilde{\phi})^2} + \frac{C_{I2} \cos \tilde{\phi}}{(C - D \cos \tilde{\phi})^2} + \frac{C_{I3}}{(C - D \cos \tilde{\phi})^2} \right] d\tilde{\phi} \quad (140)$$

The computer name for EI_{20} is EI_{20} .

We now define:

$$EI_4 \equiv \int_{\tilde{\phi}_{lo}}^{\tilde{\phi}_{up}} \frac{\cos \tilde{\phi} d\tilde{\phi}}{(C - D \cos \tilde{\phi})^2} \quad (141)$$

$$EI_2 \equiv \int_{\tilde{\phi}_{lo}}^{\tilde{\phi}_{up}} \frac{\cos \tilde{\phi} d\tilde{\phi}}{(C - D \cos \tilde{\phi})^2} \quad (142)$$

and,

$$EI_1 \equiv \int_{\tilde{\phi}_{lo}}^{\tilde{\phi}_{up}} \frac{d\tilde{\phi}}{(C - D \cos \tilde{\phi})^2} \quad (143)$$

Computer names for EI_1 , EI_2 , and EI_4 are $EI1$, $EI2$, and $EI4$, respectively.

We now integrate Equations (141), (142), and (143). Let us define:

$$X \equiv \tan (\tilde{\phi}/2) \quad (144)$$

Then, since $\tan^2 (\tilde{\phi}/2) + 1 = \sec^2(\tilde{\phi}/2)$ from trigonometry, we see that (145)

$$1+X^2 = \sec^2(\tilde{\phi}/2) = \frac{1}{\cos^2(\tilde{\phi}/2)} \quad (146)$$

We also know from trigonometry that:

$$\cos \frac{\tilde{\phi}}{2} = \frac{1+\cos \tilde{\phi}}{2}$$

or

$$2 \cos^2(\tilde{\phi}/2) - 1 = \cos \tilde{\phi} \quad (147)$$

Combining Equations 233 and 234, we find:

$$\cos \tilde{\phi} = \frac{2}{1+X^2} - 1 = \frac{1-X^2}{1+X^2} \quad (148)$$

From Equation 145, we have:

$$\tilde{\phi} = 2 * \arctan X$$

and, then:

$$d\tilde{\phi} = \frac{2}{1+X^2} \quad (149)$$

We now substitute Equation 148 and 149 into Equation 141 to evaluate EI_4 :

$$EI_4 = \int_{X_{lo}}^{X_{up}} \frac{\left[\frac{1-X^2}{1+X^2} \right]^2 \times \frac{2}{1+X^2} dX}{\left[C-D \left(\frac{1-X^2}{1+X^2} \right)^2 \right]}$$

or

$$EI_4 = \int_{X_{10}}^{X_{up}} \frac{2(1-X^2)^2 dX}{(1+X^2) [(C-D) + (C+D)X^2]^2} \quad (151)$$

We must expand the integrand expression of Equation 150 into partial fractions in order to integrate Equation 150:

$$\frac{2(1-X^2)^2}{(1+X^2) [(C-D) + (C+D)X^2]^2} = \quad (152)$$

$$\frac{\bar{A} + \bar{B}X}{(1+X^2)} + \frac{\bar{E} + \bar{F}X}{[(C-D) + (C+D)X^2]} + \frac{\bar{G} + \bar{H}X}{[(C-D) + (C+D)X^2]^2}$$

where \bar{A} , \bar{B} , \bar{E} , \bar{F} , \bar{G} , and \bar{H} are constants to be determined

Clearing the fractions from Equation 151 yields:

$$\begin{aligned} 2-4X^2+2X^4 &= (A+BX) [(C-D)+(C+D)X^2]^2 \\ &= (\bar{E}+\bar{F}X)(1+X^2) [(C-D)+(C+D)X^2] \\ &\quad + (\bar{G}+\bar{H}X)(1+X^2) \end{aligned}$$

After some algebraic manipulation, we obtain:

$$\begin{aligned} 2-4X^2+2X^4 &= [\bar{A}(C-D) \bar{E}(C-D) + \bar{G}] \\ &\quad + [\bar{B}(C-D)^2 + \bar{F}(C-D) + \bar{H}]X \\ &\quad + [2(C-D)(C+D) + \bar{A} + 2\bar{E}\bar{C} + \bar{G}]X^2 \\ &\quad + [2\bar{B}(C-D)(C+D) + 2\bar{F}\bar{C} + \bar{H}]X^3 \\ &\quad + [\bar{A}(C-D)^2 + \bar{E}(C+D)]X^4 \\ &\quad + [\bar{B}(C+D)^2 - (C+D)\bar{F}]X^5 \end{aligned}$$

If we now set the coefficients of equal powers of X on the left and right of Equation (152) equal, we obtain the following set of simultaneous equations in \bar{A} , \bar{B} , \bar{E} , \bar{F} , \bar{G} , and \bar{H} .

$$x^0: 2 = (C-D)^2 \bar{A} + (C-D)\bar{E} + \bar{G} \quad (153)$$

$$x^1: 0 = (C-D)^2 \bar{B} + (C-D)\bar{F} + \bar{H} \quad (154)$$

$$x^2: -4 = 2(C-D)(C+D)\bar{A} + 2C\bar{E} + \bar{G} \quad (155)$$

$$x^3: 0 = 2(C-D)(C+D)\bar{B} + 2C\bar{F} + \bar{H} \quad (156)$$

$$x^4: 2 = (C+D)^2 \bar{A} + (C+D)\bar{E} \quad (157)$$

$$x^5: 0 = (C+D)^2 \bar{B} + (C+D)\bar{F} \quad (158)$$

We now solve the above set of equations for \bar{A} , \bar{B} , \bar{E} , \bar{F} , \bar{G} , and \bar{H} .

$$\text{From Equation 244, } F = -(C+D) B \quad (159)$$

Substitute Equation 245 into Equation 241 to get:

$$\bar{H} = 2D(C-D) \bar{B}$$

Substitute Equations 158 and 159 into Equation 156 to get $-4D^2 \bar{B} = 0$. Assuming r_{l2} and r_{l1} do not equal zero (see Equation 142), then $d \neq 0$ and,

$$\bar{B} = 0, \quad \bar{H} = 0, \quad \text{and } \bar{F} = 0 \quad (160)$$

From Equation 157 we can obtain:

$$\bar{E} = \frac{2}{(C+D)} - (C+D)\bar{A} \quad (161)$$

Substitute Equation 248 into Equation 240 to get:

$$G = 2D(C+D)\bar{A} = \frac{4D}{(C+D)} \quad (162)$$

Substitute Equation 248 into Equation 243 to get:

$$\bar{G} - 2D(C+D)\bar{A} = \frac{-8C-4D}{(C+D)} \quad (163)$$

Now solve Equations 162 and 163 simultaneously to get $A = (2/D^2)$

and,

$$G = \frac{4C^2}{D(C+D)} \quad (164)$$

and with Equation 161, find that:

$$\bar{E} = \frac{-2C^2-4CD}{D^2(C+D)} \quad (165)$$

We can write Equation 151 as follows:

$$\frac{2(1-X^2)^2}{(1+X^2)[(C-D)+(C+D)X^2]} = \frac{(2/D^2)}{1+X^2} + \frac{\frac{-2C^2-4CD}{D^2(C+D)}}{[(C-D)+(C+D)X^2]} + \frac{\frac{4C^2}{D(C+D)}}{[(C-D)+(C+D)X^2]^2} \quad (167)$$

The integral EI_4 (see Equation 150), now amounts to integrating each one of the terms in Equation 167.

From a table of integrals, we can find that:

$$\frac{(2/D^2)dX}{(1+X^2)} = \frac{2}{D^2} \arctan X \quad (168)$$

In a similar way,

$$\begin{aligned} & \frac{-2C^2-4CD}{D^2(C+D)} \times \frac{dX}{[(C-D)(C+D)X^2]} \\ &= \frac{-2C-4CD}{D^2(C+D)(C-D)} \times \sqrt{\frac{C+D}{C-D}} \times \int \frac{\frac{C-D}{C+D} dX}{1 + \frac{C+D}{C-D} X^2} \end{aligned} \quad (169)$$

Now, consider:

$$\begin{aligned} & \frac{4C^2}{D(C+D)} \times \frac{dX}{[(C-D)+(C+D)X^2]^2} = \\ & \frac{4C^2}{D(C+D)(C-D)^2} \times \int \frac{dX}{\left[1 + \frac{(C+D)}{(C-D)} X^2\right]^2} \end{aligned} \quad (170)$$

To integrate Equation 170, we make a change of variable, let:

$$\tan^2 W = \frac{(C+D)}{(C-D)} X^2 \quad (171)$$

so that:

$$\sec^2 W = 1 + \tan^2 W = 1 + \frac{C+D}{C-D} X^2 \quad (172)$$

From Equation 258:

$$\tan W = \sqrt{\frac{C+D}{C-D}} X \quad (173)$$

and

$$\sec^2 W dW = \sqrt{\frac{C+D}{C-D}} dX \quad (174)$$

so:

$$dX = \sqrt{\frac{C-D}{C+D}} \sec^2 W dW \quad (175)$$

Upon substituting Equations 175 and 172 into Equation 170, we obtain the following form of integral:

$$\frac{4C^3}{D(C+D)(C-D)^2} \int \frac{dX}{\left[1 + \frac{(C+D)}{(C-D)} X^2\right]} = \frac{4C^2}{D(C+D)(C-D)^2} \sqrt{\frac{C-D}{C+D}} \int \cos^2 W dW \quad (176)$$

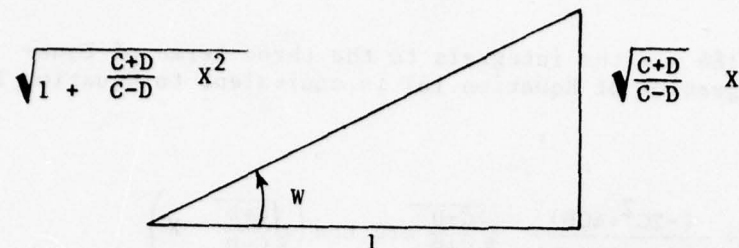
$$\text{Now,} \quad \int \cos^2 W dW = \left(\frac{1 + \cos 2W}{2} \right) dW = \frac{W}{2} + \frac{1}{4} \sin 2W \quad (177)$$

$$\begin{aligned} \therefore \frac{4C^2}{D(C+D)(C-D)^2} \sqrt{\frac{C-D}{C+D}} \int \cos^2 W dW \\ = \frac{4C^2}{D(C+D)(C-D)^2} \sqrt{\frac{C-D}{C+D}} \left(\frac{W}{2} + \frac{\sin 2W}{4} \right) \end{aligned} \quad (178)$$

From Equation 260, we have:

$$W = \arctan \frac{C+D}{C-D} X$$

and, from the sketch below, we see:



$$\sin W = \frac{\frac{C+D}{C-D}}{\sqrt{1 + \frac{C+D}{C-D} x^2}} \quad (180)$$

and,

$$\cos W = \frac{1}{\sqrt{1 + \frac{C+D}{C-D} x^2}} \quad (181)$$

We now note from trigonometry that

$$\sin 2W = 2 \sin W \cos W \quad (182)$$

Therefore:

$$\sin 2W = \frac{2x \sqrt{\frac{C+D}{C-D}}}{\left[1 + \left(\frac{C-D}{C+D}\right) x^2\right]} \quad (183)$$

We can now substitute Equations 179 and 183 into Equation 178, which is equivalent to Equation 170 to get the result:

$$\begin{aligned} & \frac{4C^2}{D(C+D)(C-D)^2} \int \frac{dx}{\left[1 + \frac{C+D}{C-D} x^2\right]} = \\ & + \frac{2C^2}{D(C+D)(C-D)^2} \sqrt{\frac{C-D}{C+D}} \arctan\left(\sqrt{\frac{C+D}{C-D}} x\right) \\ & + \frac{2C^2}{D(C+D)(C-D)} \times \frac{x}{(C-D) + (C+D)x^2} \end{aligned} \quad (184)$$

Equation 168, 169, and 184 are the integrals to the three terms of Equation 167. Because integration of Equation 167 is equivalent to Equation 150, we can write:

$$EI_4 = \left[\frac{2}{D^2} \arctan X + \frac{(-2C^2 + 4CD)}{D^2(C+D)(C-D)} \sqrt{\frac{C-D}{C+D}} \arctan \left(\sqrt{\frac{C+D}{C-D}} X \right) \right. \\ \left. + \frac{2C^2}{D(C+D)(C-D)^2} \sqrt{\frac{C-D}{C+D}} \arctan \left(\sqrt{\frac{C+D}{C-D}} X \right) \right. \\ \left. + \frac{2C^2}{D(C+D)(C-D)} \times \frac{X}{(C-D)(C+D)X^2} \right]_{X_{10}}^{X_{up}} \quad (185)$$

We desire to express Equation 185 in terms of ϕ . We can accomplish this by using Equation 145 and the fact that:

$$\tilde{\phi} = 2 \arctan X \quad (186)$$

When this is done, we obtain:

$$EI_4 = \left[\frac{\tilde{\phi}}{D^2} + \frac{2C^2}{D^2(C+D)(C-D)^2} \sqrt{\frac{C-D}{C+D}} \arctan \left(\sqrt{\frac{C+D}{C-D}} \tan \frac{\tilde{\phi}}{2} \right) \right. \\ \left. + \frac{2C^2}{D(C+D)(C-D)^2} \times \frac{\tan \frac{\tilde{\phi}}{2}}{\left[1 + \frac{(C+D)}{(C-D)} \tan^2 \left(\frac{\tilde{\phi}}{2} \right) \right]} \right]_{\phi_{10}}^{\phi_{up}} \quad (187)$$

Which is the result desired for Equation 228.

For purposes of computation of Equation 274 in the computer, the following variables are defined:

$\tilde{\phi}_{up}$ (computer name PHIU)

$\tilde{\phi}_{10}$ (computer name PHIL)

SU2 (computer name SU2) = $\sin(\tilde{\phi}_{up}/2)$

$$CU_2 \text{ (computer name CU2)} = \cos (\tilde{\phi}_{up}/2)$$

$$TU_2 \text{ (computer name TU2)} = SU_2/CU_2 = \tan \left(\frac{\phi_{up}}{2} \right)$$

The reader should recall that the computer does not have a tangent function in its library.

Likewise:

$$SL_2 \text{ (computer name SL2)} = \sin (\tilde{\phi}_{lo}/2)$$

$$CL_2 \text{ (computer name CL2)} = \cos (\tilde{\phi}_{lo}/2)$$

$$TL_2 \text{ (computer name TL2)} = SL_2/CL_2$$

We also define:

$$CMD \text{ (computer name CMD)} = (C-D)$$

$$CPD \text{ (computer name CPD)} = (C+D)$$

$$Q_1 \text{ (computer name Q1)} = CPD/CMD$$

$$Q_2 \text{ (computer name Q2)} = CMD/CPD$$

$$SQ_1 \text{ (computer name SQ1)} = \sqrt{Q_1} = \sqrt{\frac{C+D}{C-D}}$$

$$SQ_2 \text{ (computer name SQ2)} = \sqrt{Q_2} = \sqrt{\frac{C-D}{C+D}}$$

$$Q_3 \text{ (computer name Q3)} = 2xC/(CPD \times CMD)^2 = \frac{2C}{(C+D)(C-D)^2}$$

$$Q_4 \text{ (computer name Q4)} = 2xD/(CPD \times CMD)^2 = \frac{2D}{(C+D)(C-D)^2}$$

$$ATU_2 \text{ (computer name ATU2)} = SQ_1 \times TU_2$$

$$= \frac{C+D}{C-D} \tan \frac{\tilde{\phi}_{up}}{2}$$

$$ATL_2 \text{ (computer name ATL2)} = SQ_1 \times TL_2$$

$$\sqrt{\frac{C+D}{C-D}} \tan \left(\frac{\phi_{up}}{2} \right)$$

$$AU \quad (\text{computer name AU}) = \arctan (ATU_2)$$

$$= \arctan \left[\sqrt{\frac{C+D}{C-D}} \tan \left(\frac{\tilde{\phi}_{up}}{2} \right) \right]$$

$$AL \quad (\text{computer name AL}) = \arctan (ATL_2)$$

$$= \arctan \left[\sqrt{\frac{C+D}{C-D}} \tan \left(\frac{\phi_{10}}{2} \right) \right]$$

$$Q_{5U} \quad (\text{computer name } Q_{5U}) = \frac{TU_2}{(1+Q_1 \times TU_2)^2}$$

$$\frac{\tan \left(\frac{\phi_{up}}{2} \right)}{1 + \frac{C+D}{C-D} \tan^2 \left(\frac{\phi_{up}}{2} \right)}$$

$$Q_{5L} \quad (\text{computer name } Q_{5L}) = \frac{TL_2}{(1+Q_1 \times TL_2)^2}$$

In terms of the foregoing definitions, we can write EI_4 as follows:

$$\begin{aligned} EI_4 = & \frac{1}{D^2} (\phi_{up} - \tilde{\phi}_{Lo}) \times Q_3 \times \frac{(2D^2 - C^2)}{D^2} \times SQ_2 \times (AU - AL) \\ & + Q_3 \times \frac{C}{D} \times (Q_{5U} - Q_{5L}) \end{aligned} \quad (188)$$

We now proceed to integrate Equations 142 and 143. If we use Equations 148 and 149, Equation 229 can be written

$$EI_2 = \int_{X_{Lo}}^{X_{up}} \frac{2(1-X^2)dX}{[(C-D)+(C+D)X^2]^2} \quad (189)$$

and Equation 230 can be written

$$EI_1 = \int_{X_{Lo}}^{X_{up}} \frac{2(1+X^2)dX}{[(C-D)+(C+D)X^2]^2} \quad (190)$$

$$\int_{X_{lo}}^{X_{up}} \frac{dX}{[(C-D)+(C+D)X^2]^2} = \frac{2}{(C-D)^2} \int_{X_{lo}}^{X_{up}} \frac{dX}{\left[1 + \frac{C+D}{C-D} X^2\right]^2} \quad (191)$$

and

$$\int_{X_{lo}}^{X_{up}} \frac{X^2 dX}{[(C-D)+(C+D)X^2]^2} = \frac{2}{(C-D)^2} \int_{X_{lo}}^{X_{up}} \frac{X^2 dX}{\left[1 + \frac{C+D}{C-D} X^2\right]^2} \quad (192)$$

But:

$$\begin{aligned} \int_{W_{lo}}^{W_{up}} \sin^2 W dW &= \left[\frac{W}{2} - \frac{\sin 2W}{4} \right]_{W_{lo}}^{W_{up}} \\ &= \left[\frac{W}{2} = \frac{\sin W \cos W}{2} \right]_{W_{lo}}^{W_{up}} \end{aligned} \quad (198)$$

We now wish to replace W with X. From Equation 281, we have:

$$W = \arctan \left(\sqrt{\frac{C+D}{C-D}} X \right) \quad (199)$$

The sketch shows:

$$\sin W = \frac{\sqrt{\frac{C+D}{C-D}} X}{\sqrt{1 + \frac{C+D}{C-D} X^2}} \quad (200)$$

$$\cos W = \frac{1}{\sqrt{1 + \frac{C+D}{C-D} X^2}} \quad (201)$$

Using Equations 199, 200, and 201, we can rewrite Equation 198 as:

$$\int_{W_{lo}}^{W_{up}} \sin^2 W dW = \left[\frac{1}{2} \arctan \left(\sqrt{\frac{C+D}{C-D}} X \right) - \frac{1}{2} \frac{\sqrt{\frac{C+D}{C-D}} X}{\left[1 + \left(\frac{C+D}{C-D} \right) X^2 \right]} \right]_{X_{lo}}^{X_{up}}$$

Equation 197 becomes:

$$2 \int_{X_{10}}^{X_{up}} \frac{X^2 dX}{\left[(C-D)^2 + \frac{(C+D)}{(C-D)} X^2 \right]^2} = \frac{1}{(C-D)(C+D)} \sqrt{\frac{C-D}{C+D}} \times$$

$$\left[\arctan \left(\sqrt{\frac{C+D}{C-D}} X - \frac{X}{(C-D)(C+D) \left[1 + \frac{(C+D)}{(C-D)} X^2 \right]} \right) \right]_{X_{10}}^{X_{up}} \quad (203)$$

Upon substituting Equations 193 and 203 into Equation 189 one obtains:

$$EI_2 = \int_{X_{10}}^{X_{up}} \frac{2(1-X)^2 dX}{\left[(C-D) + (C+D)X^2 \right]^2} = \left[\sqrt{\frac{C-D}{C+D}} \times \frac{2D}{(C-D)^2(C+D)} \arctan \left(\sqrt{\frac{C+D}{C-D}} X \right) + \right.$$

$$\left. \frac{2C}{(C-D)^2(C+D)} \frac{X}{1 + \frac{(C+D)}{(C-D)} X^2} \right]_{X_{10}}^{X_{up}} \quad (204)$$

In like manner, substitute Equations 193 and 203 into Equation 190 to obtain the following equation:

$$EI_1 = \left[\sqrt{\frac{C-D}{C+D}} \times \frac{2C}{(C-D)^2(C+D)} \times \arctan \left(\sqrt{\frac{C+D}{C-D}} X^2 \right) + \frac{2D}{(C-D)^2(C+D)} \times \right.$$

$$\left. \frac{X}{1 + \frac{C+D}{C-D} X^2} \right]_{X_{10}}^{X_{up}}$$

Now, substitute Equations 145 and 186 to express Equations 204 and 205 in terms of $\tilde{\phi}$:

$$EI_2 = \left[\sqrt{\frac{C-D}{C+D}} \times \frac{2D}{(C-D)^2(C+D)^2} \times \arctan \left(\sqrt{\frac{C+D}{C-D}} \tan \frac{\tilde{\phi}}{2} \right) \right. \\ \left. + \frac{2C}{(C-D)^2(C+D)} \times \frac{\tan \left(\frac{\tilde{\phi}}{2} \right)}{1 + \frac{C+D}{C-D} \tan^2 \left(\frac{\tilde{\phi}}{2} \right)} \right]_{\tilde{\phi}_{10}}^{\tilde{\phi}_{up}} \quad (206)$$

AD-A078 436

GENERAL ELECTRIC CO CINCINNATI OH AIRCRAFT ENGINE GROUP F/G 17/5
ADVANCED INFRARED SIGNATURE PREDICTION PROGRAM, SPECTRAL CALCUL--ETC(U)
NOV 79 M E WILTON N00140-76-C-1072
R78AE6314 NL

UNCLASSIFIED

2 OF 3

AD
A078 436



and,

$$EI_1 = \left[\sqrt{\frac{C-D}{C+D}} \times \frac{2C}{(C-D)^2(C+D)} \times \arctan \left(\sqrt{\frac{C+D}{C-D}} \tan \frac{\tilde{\phi}}{2} \right) + \frac{2D}{(C-D)^2(C+D)} \times \frac{\tan \frac{\tilde{\phi}}{2}}{1 + \frac{(C+D)}{(C-D)} \tan^2 \frac{\tilde{\phi}}{2}} \right]_{\tilde{\phi}_{10}}^{\tilde{\phi}_{up}} \quad (207)$$

If we now use the computer variable definitions of pages 84, 85, and 86, we can write Equation 293 as:

$$EI_2 = SQ_2 \times Q_4 \times (A_U - A_L) + Q_3 \times (Q_{5U} - Q_{5L}) \quad (208)$$

and Equation 215:

$$EI_1 = SQ_2 \times Q_3 \times (A_U - A_L) + Q_4 \times (Q_{5U} - Q_{5L}) \quad (209)$$

We now return to Equation 227, and rewrite it on the basis of Equations 228, 229, and 230 as:

$$EI_{20} = CI_1 \times EI_4 + CI_2 \times EI_2 + CI_3 \times EI_1 \quad (210)$$

where CI_1 , CI_2 , and CI_3 are defined in Equations 131, 132, and 133, and EI_1 , EI_2 , and EI_4 are given by Equations 208, 209, and 188. The CI 's and EI 's are functions of Y_1 , Y_2 , and ϕ_1 .

The equation for the view factor, Equation 136, can now be written:

$$F_{1-2} = \frac{1}{\pi A_1} \int_{\phi_{10}}^{\phi_{1up}} \int_{YU_1}^{YD_1} \int_{YU_2}^{YD_2} \frac{EI_{20} r_{11} r_{12} d\phi_1 dY_1 dY_2}{\tilde{B}_1 \tilde{B}_2} \quad (211)$$

for given values of Y_1 , Y_2 , and ϕ_1 . If we take advantage of the symmetry of the problem, we can find EI_{20} using half the range of the $\tilde{\phi}$ limits. Equation 211 then becomes:

$$F_{1-2} = \frac{2}{\pi A_1} \int_{\phi_{10}}^{\phi_{1up}} \int_{YU_1}^{YD_1} \int_{YU_2}^{YD_2} EI_{20} \frac{r_{11} r_{12} d\phi_1 dY_1 dY_2}{\tilde{B}_1 \tilde{B}_2} \quad (212)$$

where the "2" is introduced because of symmetry arguments which will be discussed in the section dealing with the determination of the integration limits.

We now define:

G_I (computer name GI) as:

$$G_I \equiv \frac{2 \times r_{12} \times EI_{20}}{\pi |\tilde{B}_2|} \quad (213)$$

Equation 212 is now written:

$$F_{1-2} = \frac{1}{A_1} \int_{\phi_{1,10}}^{\phi_{1,up}} \int_{Y_{U1}}^{Y_{D1}} \int_{Y_{U2}}^{Y_{D2}} r_{11} G_I \frac{d\phi_1 dY_1 dY_2}{|\tilde{B}|} \quad (214)$$

Now, consider the integration with respect to Y_2 (see Figure 12). This integration is evaluated by a numerical integration technique called the Legendre-Gauss Quadrature formula. For integration over an interval of ΔY_2 , this formula is:

$$\int_{\tilde{Y}_2}^{\tilde{Y}_2 + \Delta Y_2} G_I dY_2 = \frac{\Delta Y_2}{18} \left[5G_I(Y_2') + 8G_I(Y_2'') + 5G_I(Y_2''') \right] \quad (215)$$

where Y_2' is the midpoint of an interval of length ΔY_2 , and Y_2'' is from Y_2' , and Y_2''' , and Y_2''' is $\frac{-\sqrt{15}}{5} \times \frac{\Delta Y_2}{2}$ from Y_2'' . It is to be understood that $G_I(Y_2')$ means the value of G_I evaluated for $Y_2 = Y_2'$.

Computer variable names associated with the variables of Equation 215 are:

$$G_I(Y_2') = G_L \text{ (computer name GL)}$$

$$G_I(Y_2'') = G_M \text{ (computer name GM)}$$

$$G_I(Y_2''') = G_R \text{ (computer name GR)}$$

$$\Delta Y_2 = D_{Y2} \text{ (computer name DY2)}$$

$$D_{Y2} = (Y_{D2} - Y_{U2}) / D_{IV2}$$

D_{IV2} [computer name DIV(2)] is an input, and it is the number of integration ΔY_2 's to be used for the integration over the receiver node surface. (Also computer named NYD2.) The left end of the integration interval of length $\Delta Y_2 = D_{Y2}$ is denoted Y_K (computer name = YK).

Interval index = m (computer name M, PM).

In general,

$$\tilde{Y}_2 = Y_K = Y_{U2} + (m-1) \times D_{Y2} \quad (216)$$

$$Y'_2 = Y_K + \frac{D_{Y2}}{2} (1 - C_{K1}) \quad (217)$$

$$C_{K1} = \sqrt{15/5} \text{ (computer name = CK1)}$$

(The computer name for Y'_2 is Y2)

$$Y''_2 = Y_K + D_{Y2}/2 \quad (218)$$

(The computer name for Y''_2 is Y2)

$$Y'''_2 = Y_K + \frac{D_{Y2}}{2} (1 + C_{K1}) \quad (219)$$

(The computer name for Y'''_2 is Y2)

Equation 215 is applied repeatedly to obtain:

$$R = \int_{Y_{U2}}^{Y_{D2}} G_I dY_2 = \sum_{m=1}^{m=D_{IV2}} \frac{\Delta Y_2}{18} (5G_{L,m} + 8G_{M,m} + 5G_{R,m}) \quad (220)$$

(The computer name for R is R)

Equation 214 now becomes:

$$F_{1-2} = \frac{1}{A_1} \int_{\phi_{1,1o}}^{\phi_{1,up}} \int_{Y_{U1}}^{Y_{D1}} r_{11} R \frac{D\phi_1}{|B_1|} dY_1 \quad (221)$$

Consider the integration with respect to Y_1 (see Figure 13). (The following applies for no radial support shadowing!!) We use the Legendre-Gauss numerical integration formula to evaluate this integral:

$$\int_{\tilde{Y}_1}^{\tilde{Y}_1 + Y_1} r_{11} \left| \frac{R dY_1}{\tilde{B}_1} \right| = \frac{1}{|\tilde{B}_1|} \frac{\Delta Y_1}{18} \left[5r_{11}(Y'_1)R(Y'_1) + 8r_{11}(Y''_1)R(Y''_1) + 5r_{11}(Y'''_1)R(Y'''_1) \right] \quad (222)$$

where Y_1'' is the midpoint of an interval of length ΔY_1 , and Y_1' is $-\sqrt{15/5} \times \Delta Y_1/2$ from Y_1'' . It is to be understood that $R(Y_1')$ means the value of R evaluated at $Y_1 = Y_1'$. Computer variable names associated with the variables of Equation 222 are:

$$RL \text{ (computer name RL)} = Rl_1(Y_1')R(Y_1')/|\tilde{B}_1|$$

$$RM \text{ (computer name RM)} = rl_1(Y_1'')R(Y_1'')/|\tilde{B}_1|$$

$$RR \text{ (computer name RR)} = rl_1(Y_1''')R(Y_1''')/|\tilde{B}_1|$$

$$\Delta Y_1 = DY_1 \text{ (computer name DY1)}$$

$$DY_1 = (YD_1 - YU_1)/DIV_1 \quad (223)$$

DIV_1 [computer name $DIV(1)$] is an input, and it is the number of integration ΔY_1 's to be used for the integration over the source node surface. (Also computer named $NYD1$.)

The left end of the integration interval of length $\Delta Y_1 = DY_1$ is denoted Y_j . (Computer name = YJ .)

Interval index = l (computer name L , PL).

In general:

$$Y_1 = Y_j = YU_1 + (l-1) \times DY_1 \quad (224)$$

$$Y_1' = Y_j + \frac{DY_1}{2} \times (1 - CK_1) \quad (225)$$

(The computer name for Y_1' is YL)

$$Y_1'' = Y_j + DY_1/2 \quad (226)$$

(The computer name for Y_1'' is $Y1$)

$$Y_1''' = Y_j + \frac{DY_1}{2} \times (1 + CK_1) \quad (227)$$

(The computer name for Y_1''' is $Y1$)

Equation 222 is applied repeatedly to obtain:

$$F_F = \int_{YU_1}^{YD_1} r_{l_1} \frac{RdY_1}{|B_1|} = \sum_{l=1}^{l=DIV_1} \frac{\Delta Y_1}{18} (5R_{L,l} + 8R_{M,l} + 5R_{R,l}) \quad (228)$$

(The computer name for F_F is FF.)

Equation 221 now becomes:

$$F_{1-2} = \frac{1}{A_1} \int_{\phi_{1,lo}}^{\phi_{1,up}} FF d\phi_1 \quad (229)$$

For no-duct shadowing, FF will not vary as ϕ_1 varies. This is due to the cylindrical symmetry of the problem. For given values of Y_1 and Y_2 , one point on the circumference of the source frustum sees just as much of the receiver frustum as any other point on the circumference. The smallest value of $\phi_1 = \phi_{1,up} = 0$, and the largest value of $\phi_1 = \phi_{1,up} = 2\pi$.

$$F_{1-2} = \frac{2\pi}{A_1} FF \quad (230)$$

By the reciprocity relationship of radiation, we can write the following equation:

$$F_{2-1} = A_1 F_{1-2}/A_2 \quad (231)$$

(1) Disc Nodes and Frustum Nodes

The discussion so far has dealt strictly with the determination of the integration formulas for finding view factors between frustum nodes. We now consider the modifications of the integration for the case that one of the nodes is a disc. The geometry of a disc is shown in Figure 14.

The disk variables and their corresponding computer names are as follows:

YU_i , $YU(I)$ = axial distance from the reference plane to the plane of the disc ($I=1$ for the source node; $I=2$ for the receiver node). YD_i , $YD(I)$ = axial distance from the reference plane to the plane of the disc. ($I=1$ for the source, $I=2$ for the receiver node.)

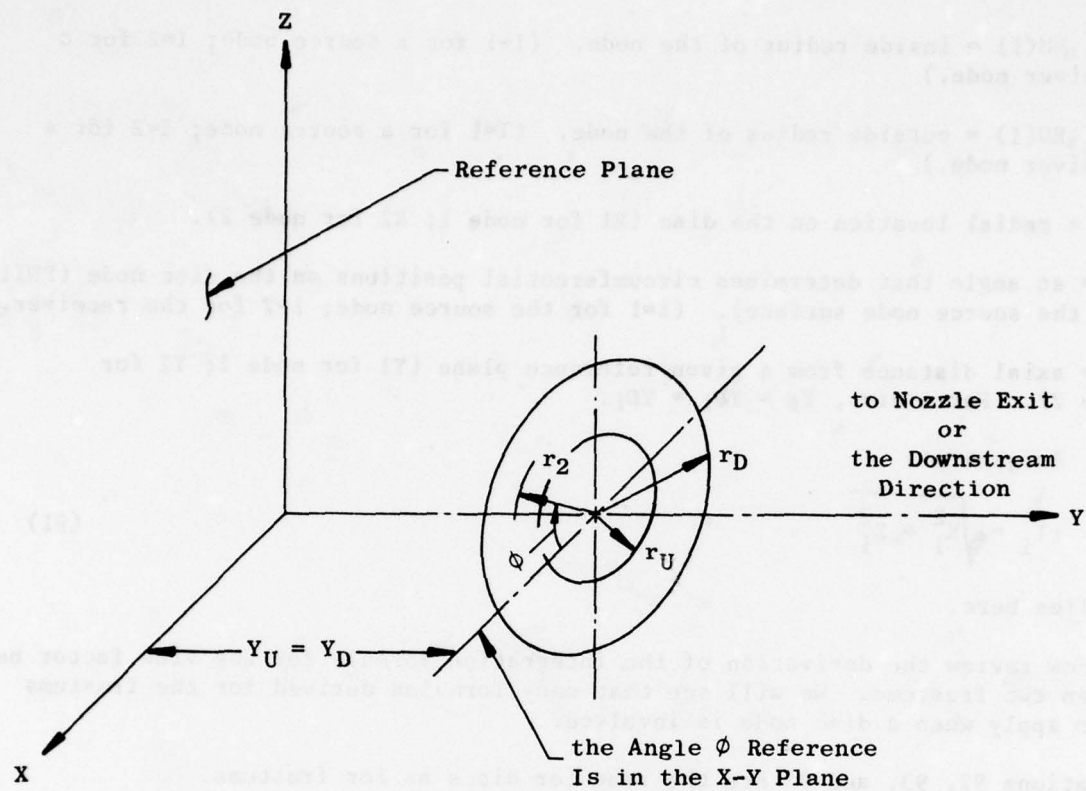


Figure 14. Definition of the Variables Required for a Disc Node.

Note YU_i for a disc. The computer uses this fact to discern that the node is a disc and not a frustum node.

$rU_i, RU(I)$ = inside radius of the node. ($I=1$ for a source node; $I=2$ for a receiver node.)

$rD_i, RD(I)$ = outside radius of the node. ($I=1$ for a source node; $I=2$ for a receiver node.)

rl_i = radial location on the disc ($R1$ for node 1; $R2$ for node 2).

ϕ_i = an angle that determines circumferential positions on the disc node ($PHI1$ for the source node surface). ($i=1$ for the source node; $i=2$ for the receiver.)

Y_i = axial distance from a given reference plane ($Y1$ for node 1; $Y2$ for node 2). For a disc, $Y_i = YU_i = YD_i$.

In general:

$$rl_i = \sqrt{X_i^2 + Z_i^2} \quad (91)$$

applies here.

We now review the derivation of the integration formula for the view factor between two frustums. We will see that many formulas derived for the frustums also apply when a disc node is involved.

Equations 92, 93, and 94 are the same for discs as for frustums.

Equation 95 now becomes:

$$f_i = Y - YU_1 = 0 \text{ for } rU_1 \leq \sqrt{X^2 + Z^2} \leq rD_1 \quad (95')$$

Equation 96 becomes:

$$\frac{\partial f_i}{\partial X_i} = 0 \quad (96')$$

Equation 97 becomes:

$$\frac{\partial f_i}{\partial Y_i} = 1 \quad (97')$$

Equation 98 becomes:

$$\frac{\partial f_i}{\partial Z_i} = 0 \quad (98')$$

Equation 99 becomes:

$$\sqrt{\left(\frac{\partial f_i}{\partial X_i}\right)^2 + \left(\frac{\partial f_i}{\partial Y_i}\right)^2 + \left(\frac{\partial f_i}{\partial Z_i}\right)^2} = 1 \quad (99')$$

Equation 100 becomes:

$$\cos \theta_i = 0 \quad (100')$$

Equation 101 and/or Equation 102 becomes:

$$\cos \beta_i = 1 \quad (101') \text{ or } (102')$$

Equation 103 and/or Equation 104 becomes:

$$\cos \gamma_i = 0 \quad (103') \text{ or } (104')$$

We will still use Equations 105 and 106 for discs as well as frustums.

We see that because

$$YD_i = YU_i, A_i = -1, \text{ and } B_i = 0$$

we can still accept Equations 107 through 112 for discs, provided we adopt the following convention with respect to the normal to the surface. We agree to make the input parameter VECT(I) negative for a disc node if the outward normal to the side of the disc of interest points downstream. If the outward normal to the side of the disc of interest points upstream, input VECT(I) = +1. If VECT(I) is positive, the signs of Equations 107 through 112 are used. If VECT(I) = -1, the signs of Equations 105 or 106 and 104 or 108 are changed.

Equation 113 can be applied to a disc node, if \tilde{A}_1 and \tilde{B} are evaluated as stated in the foregoing.

Equations 114 through 122 apply both to discs and frustums.

The elemental area for a disc node is different from that for a frustum (see Figure 15). The derivation of a differential area on a disc node is given here. The elemental area is formed by two arcs of radii rl_i and $rl_i + drl_i$ and two radial lines set at angles ϕ_i and $\phi_i + d\phi_i$ to the X-Y plane.

The elemental area is approximately a trapezoid.

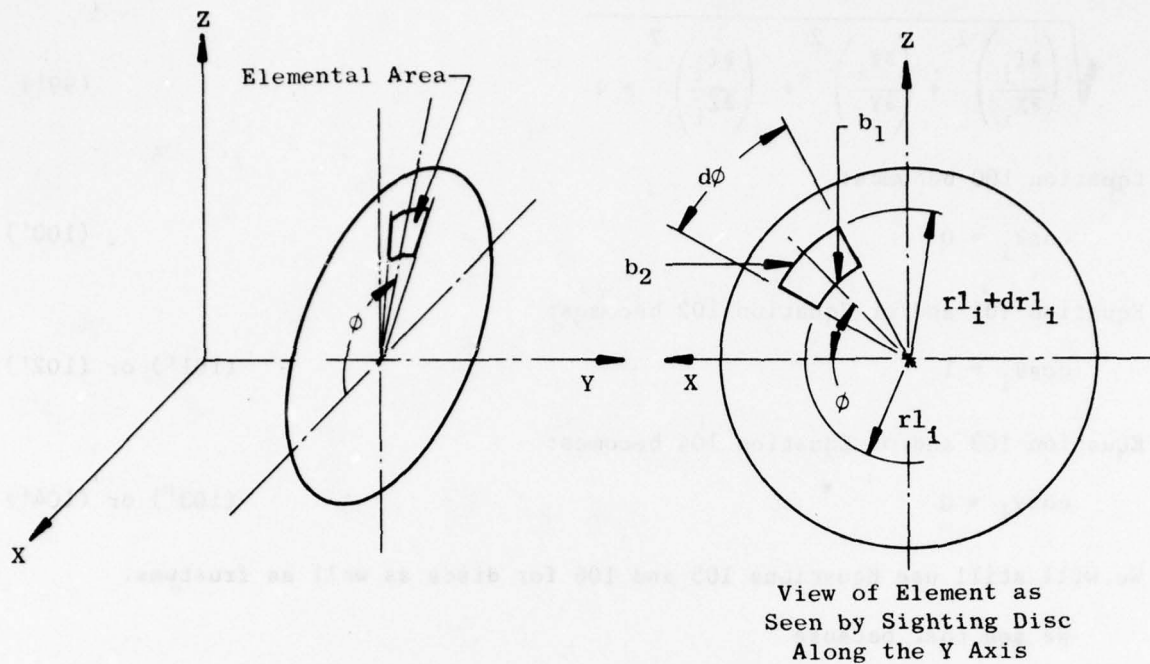


Figure 15. Geometry Used to Determine the Expression for the Elemental Area on a Disc.

Hence:

$$dA_i = 1/2(b_{2i} + b_{1i}) dr_{1i}$$

where,

$$b_{2i} = (r_{1i} + dr_{1i}) d\phi_i; \quad b_{1i} = r_{1i} d\phi_i$$

and,

$$dA_i = 1/2 (r_{1i} + dr_{1i} + r_{1i}) \phi_i dr_{1i}$$

or,

$$dA_i = r_{1i} d\phi_i dr_{1i} \quad (126')$$

if the term involving higher-order differentials is ignored.

The surface area of a disc still can be determined by either Equation 128 or 129 because, for YD_1 and YU_1 , the equations reduce to $A_i = \pi (rD_i^2 - rU_i^2)$ which is the surface area of a disc with inner and outer radii rU_i and rD_i .

We see that the expression for the integrand constituents for Equation 89 is now known for disc nodes as well as for frustums. If we evaluate the parameters \tilde{B}_1 and \tilde{A}_1 (see Equations 105 through 108) correctly for discs or frustums, then the equations for ρ^2 (Equation 120), $\cos \theta_1$ (Equation 121) and $\cos \theta_2$ (Equation 122), and expression for dA_1 and dA_2 differ between frustum and disc nodes (compare Equation 126 with Equation 213').

Let us now define:

$$I = \frac{\cos \theta_1 \cos \theta_2}{2}$$

From the foregoing arguments, the expression for I in cylindrical coordinates will be the same for the following combinations of node types:

Case (1): the source node is a frustum and the receiver node is a frustum.

Case (2): the source node is a frustum and the receiver node is a disc.

Case (3): the source node is a disc and the receiver node is a frustum.

Case (4): the source node is a disc and the receiver node is a disc.

The forms of the integral are written here for each of the foregoing cases:

Case 1:

$$F_{1-2} = \frac{1}{A_1} \int_{d_{1,10}}^{\phi_{1,up}} \int_{Y_{U1}}^{Y_{D1}} \int_{Y_{U2}}^{Y_{D2}} \int_{d_{2,10}}^{\phi_{2,up}} I \frac{r_{12} d\phi_2 dY_2 r_{11} dY_1 d\phi_1}{\pi \tilde{B}_2 \tilde{B}_1} \quad (130')$$

Case 2:

$$F_{1-2} = \frac{1}{A_1} \int_{\phi_{1,10}}^{\phi_{1,up}} \int_{Y_{U1}}^{Y_{D1}} \int_{r_{U2}}^{r_{D2}} \int_{\phi_{2,10}}^{\phi_{2,up}} I \frac{r_{12} d\phi_2 dr_{12} r_{11} dY_1 d\phi_1}{\pi \tilde{B}_1} \quad (232)$$

Case 3:

$$F_{1-2} = \frac{1}{A_1} \int_{\phi_{1,lo}}^{\phi_{1,up}} \int_{r_{U1}}^{r_{DI}} \int_{Y_{U2}}^{Y_{D2}} \int_{\phi_{2,lo}}^{\phi_{2,up}} I \frac{r_{12} d\phi_2 dY_{12} r_{11} dr_{11} d\phi_1}{\pi \tilde{B}_2} \quad (233)$$

Case 4:

$$F_{1-2} = \frac{1}{A_1} \int_{d_{1,lo}}^{\phi_{1,up}} \int_{r_{U1}}^{r_{D1}} \int_{r_{U2}}^{r_{D2}} \int_{d_{2,lo}}^{\phi_{2,up}} I \frac{r_{12} d\phi_2 dr_{12} r_{11} dr_{11} d\phi_1}{\pi} \quad (234)$$

we note that $\int_{\phi_{2,lo}}^{\phi_{2,up}} I d\phi_2$ is the same for all four cases. The evaluation of

this integral has been discussed for Case 1. We note in particular that (for given values of Y_1 , r_{11} , ϕ_1 , Y_2 , and r_{12}) the value of the integral can be given a number, and we represented this number in Equation 140 as E_{120} . That is:

$$E_{120} = \int_{\phi_{2,lo}}^{\phi_{2,up}} I d\phi_2 = \int_{\phi_{lo}}^{\tilde{\phi}_{up}} I d\tilde{\phi} \quad (235)$$

As for Case 1, Equation 212, we can write Equations 232, 233, and 234 as follows:

Case 2:

$$F_{1-2} = \frac{2}{A_1} \int_{\phi_{1,lo}}^{\phi_{1,up}} \int_{Y_{U1}}^{Y_{D1}} \int_{r_{U2}}^{r_{D2}} E_{120} \frac{r_{11} r_{12} dr_{12} dY_{11} d\phi_1}{\pi \tilde{B}_1} \quad (236)$$

Case 3:

$$F_{1-2} = \frac{2}{A_1} \int_{\phi_{1,lo}}^{\phi_{1,up}} \int_{r_{U1}}^{r_{D1}} \int_{Y_{U2}}^{Y_{D2}} E_{120} \frac{r_{11} r_{12} dY_{12} dr_{11} d\phi_1}{\pi \tilde{B}_2} \quad (237)$$

Case 4:

$$F_{1-2} = \frac{1}{A_1} \int_{\phi_{1,10}}^{\phi_{1,up}} \int_{r_{U1}}^{r_{D1}} \int_{r_{U2}}^{\phi_{2,up}} E_{I20} \frac{r_{11} r_{12} dr_{12} dr_{11} d\phi_1}{\pi} \quad (238)$$

The remainder of the integrations for the four cases are numerical integrations.

We define G_I (see Equation 213 for Case 1) as follows for each of the cases:

Case 2:

$$G_I = \frac{2r_{12} E_{I20}}{\pi} \quad (239)$$

Case 3:

$$G_I = \frac{2r_{12} E_{I20}}{\pi |\tilde{B}_2|} \quad (240)$$

Case 4:

$$G_I = \frac{2r_{12} E_{I20}}{\pi} \quad (241)$$

As for Equation 301 it is now written:

Case 2:

$$F_{1-2} = \frac{1}{A_1} \int_{\phi_{1,10}}^{\phi_{1,up}} \int_{Y_{U1}}^{Y_{D1}} \int_{r_{U2}}^{r_{D2}} \frac{r_{11} G_I dr_{12} dY_1 d\phi_1}{|\tilde{B}_1|} \quad (242)$$

Case 3:

$$F_{1-2} = \frac{1}{A_1} \int_{\phi_{1,10}}^{\phi_{1,up}} \int_{r_{U1}}^{r_{D1}} \int_{Y_{U2}}^{Y_{D2}} r_{11} G_I dY_2 dr_{11} d\phi_1 \quad (243)$$

Case 4:

$$F_{1-2} = \frac{1}{A_1} \int_{\phi_{1,lo}}^{\phi_{1,up}} \int_{r_{U1}}^{r_{D1}} \int_{r_{U2}}^{r_{D2}} G_I r_{l1} dr_{l2} dr_{l1} d\phi_1 \quad (244)$$

The numerical integration of $\int_{r_{U2}}^{r_{D2}} G_I dr_2$ for Cases 2 and 4 (Equations 242 and 244) is discussed below. The numerical integration of $\int_{Y_{U2}}^{Y_{D2}} G_I dY_2$ for

Case 3, Equation 243 proceeds just as illustrated for Case 1, ending with Equation 307.

The evaluation of $\int_{r_{U2}}^{r_{D2}} G_I dr_{12}$ is based on the Legendre-Gauss numerical integration, just as the $\int_{Y_{U2}}^{Y_{D2}} G_I dY_2$ was.

The key difference between the formulas for the two integrals is that the parameter r_{l2} is substituted for Y in Equation 213 through 221.

In place of Equation 218, we will write:

$$\int_{\tilde{r}_{12}}^{\tilde{r}_{12} + \Delta r_{12}} G_I dr_{12} = \frac{\Delta r_{12}}{18} \left[5 G_I(r'_{12}) + 8 G_I(r''_{12}) + 5 G_I(r'''_{12}) \right]$$

where r'_{12} is the midpoint of an interval of length Δr_{12} , r'_{12} is

$$- \frac{\sqrt{15}}{5} \frac{\Delta r_{12}}{2} \text{ from } r'_{12} \text{ and } r'''_{12} \text{ is } \frac{\sqrt{15}}{5} \left(\frac{\Delta r_{12}}{2} \right)$$

from r'_{12} . Computer variable names associated with the variables of Equation 215 are:

$$G_I(r'_{12}) = G_L \text{ (computer name GL)}$$

$$G_I(r'''_{12}) = G_M \text{ (computer name GM)}$$

$$G_I(r_{12}''') = G_R \text{ (computer name GR)}$$

$$\Delta r_{12} = DR_2 \text{ (computer name DR2)}$$

$$DR_2 = (r_{D2} - r_{U2}) / DIV_2$$

DIV_2 [computer name $DIV(2)$] is an input, and it is the number of integration Δr_{12} 's to be used for the integration over the receiver disc surface (also, computer named NYD_2).

The left end of the integration interval of length ($\Delta r_{12} = DR_2$) is denoted r_{12K} (computer name RK). See Figure 16.

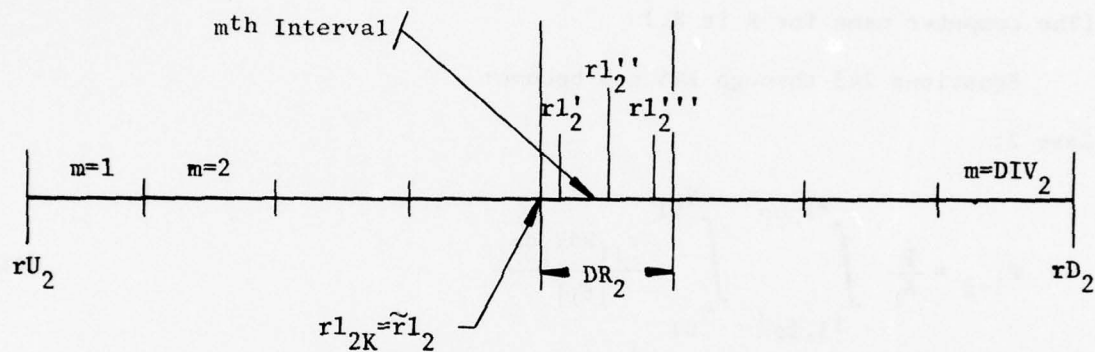


Figure 16. Subdivisions of Receiver Node Radial Length for Numerical Integration.

Interval index = m (computer name M or PM)

In general:

$$\tilde{r}_{12} = r_{12K} = r_{U2} + (m-1) D_{R2} \quad (245)$$

$$r_{12} = r_{12K} + \frac{D_{R2}}{2} (1 - C_{K1}) \quad (246)$$

(The computer name for r_{12} is R_2)

$$r_{12}'' = r_{12K} + \frac{D_{R2}}{2} \quad (247)$$

(The computer name for r_{12}'' is R_2)

$$r_{12}''' = r_{12K} + \frac{D_{R2}}{2} (1 + C_{K1}) \quad (248)$$

(The computer name for r_{12}''' is R2.)

Equation 215 is applied repeatedly to obtain:

$$R = \int_{rU_2}^{rD2} G_I dr_{12} = \sum_{m=1}^{m=D_{IV2}} \frac{D_{R2}}{18} \left[5G_{L,m} + 8G_{M,m} + 5G_{R,m} \right]$$

(The computer name for R is R.)

Equations 243 through 245 now become:

Case 2:

$$F_{1-2} = \frac{1}{A_1} \int_{\phi_{1,1o}}^{\phi_{1,up}} \int_{Y_{UI}}^{Y_{D1}} \frac{r_{11} R dY_1 d\phi_1}{|B_1|} \quad (249)$$

Case 3:

$$F_{1-2} = \frac{1}{A_1} \int_{\phi_{1,1o}}^{\phi_{1,up}} \int_{r_{U1}}^{r_{D1}} r_{11} R dr_{11} d\phi_1 \quad (250)$$

Case 4:

$$F_{1-2} = \frac{1}{A_1} \int_{\phi_{1,1o}}^{\phi_{1,up}} \int_{r_{U1}}^{r_{D1}} r_{11} R de_{11} d\phi_1 \quad (251)$$

We note that Equation 249 is identical in form to Equation 221 and that Equations 250 and 251 are identical in form.

We now consider the further numerical integration of Equations 249 through 251. First, we will consider the integration for the case that no shadowing due to radial support members occurs. The numerical integration

of Equation 249 proceeds exactly as that for Equation 221. The numerical integration of Equations 250 and 251 is discussed here (see Figure 17).

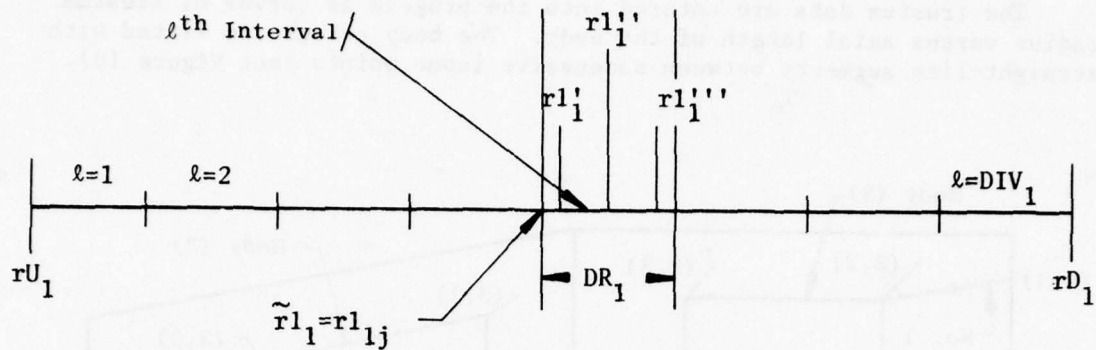


Figure 17. Subdivision of Source Node Radial Length for Numerical Integration.

Interval index = 1 (computer name is L, PL).

The integration again is accomplished with the use of the Legendre-Gauss integration formula.

$$\int_{\tilde{r}_{11}}^{\tilde{r}_{11} + D_{R1}} r_{11} R dr_{11} = \frac{D_{R1}}{18} \left[5r'_{11} R(r'_{11}) + 8r'_{11}' R(r'_{11}') + 5r'_{11}'' R(r'_{11}'') \right] \quad (252)$$

where r'_{11} is the midpoint of an interval of length $\Delta r_{11} = D_{R1}$, r'_{11} is

$$\frac{\sqrt{15}}{5} \frac{\Delta r_{11}}{2} \text{ from } r'_{11}', \text{ and } r'_{11}'' \text{ is } \frac{\sqrt{15}}{5} \frac{\Delta r_{11}}{2} \text{ from } r'_{11}.$$

Computer variable names associated with the variables of Equation 252:

$$R_L \text{ (computer name RL)} = r'_{11} R(r'_{11})$$

$$R_M \text{ (computer name RM)} = r'_{11}' R(r'_{11}')$$

$$R_R \text{ (computer name RR)} = r'_{11}'' R(r'_{11}'')$$

$$\Delta r_{11} = D_{R1} \text{ (computer name DR1)}$$

$$D_{R1} = (R_{D1} - R_{U1}) / D_{IV1} \quad (253)$$

D_{IV1} [computer name DIV(1)] is an input, and it is the number of integration Δr_{11} 's to be used for the integration over the source node surface (also computer named NYD1).

(2) Frustum Shadowing

The frustum data are entered into the program as curves of frustum radius versus axial length of the body. The body curves are fitted with straight-line segments between successive input points (see Figure 18).

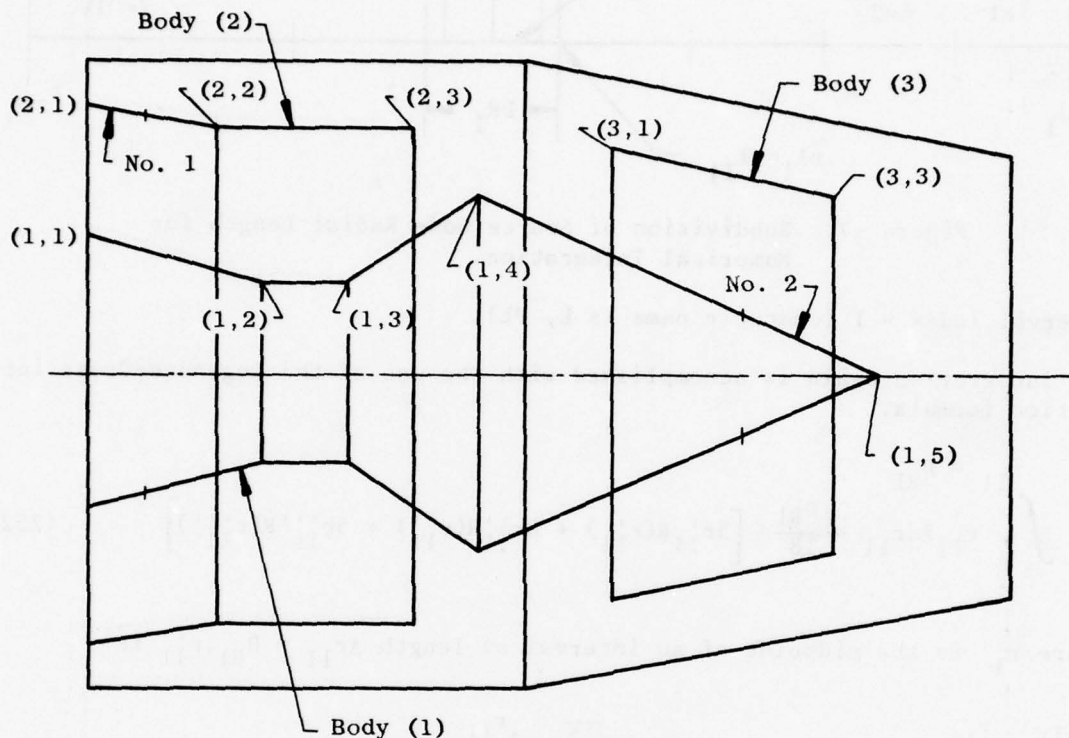


Figure 18. Schematic of Engine Surface Frustums.

A typical exhaust system with a source node, No. 1, and a receiver node, No. 2, and shadowing bodies is shown in the above figure. Note the double indices used to identify the points of the shadowing bodies.

The first task performed by the computer for frustum shadowing is to locate the coordinates Y_1 and Y_2 relative to a given shadowing body. This is done with subroutine FINDIT. If we number the line segments of the body curve in increasing order as we progress from the most upstream location of the body to the most downstream point, then the following locations have the following position numbers for Body 1.

The left end of the integration interval of length D_{R1} is denoted r_{11j} (computer name is RJ).

$$\tilde{r}_{11} = r_{11j} = r_{U1} + (\ell-1) D_{R1} \quad (254)$$

$$\tilde{r}_{11} = r_{11j} + \frac{D_{R1}}{2} (1 - C_{K1}) \quad (255)$$

(The computer name for r'_{11} is R1.)

$$r'_{11} = r_{11j} + \frac{D_{R1}}{2} \quad (256)$$

(The computer name for r''_{11} is R1.)

$$r''_{11} = r_{11j} + \frac{D_{R1}}{2} (1 + C_{K1}) \quad (257)$$

(The computer name for r'''_{11} is R1.)

Equation 252 is applied repeatedly to obtain:

$$F_F = \int_{r_{U1}}^{r_{D1}} r_{11} R dr_{11} = \sum_{\ell=1}^{\ell=D_{IV1}} \frac{D_{R1}}{18} \left[5R_{L,\ell} + 8R_{M,\ell} + 5R_{R,\ell} \right] \quad (258)$$

(The computer name for F_F is FF.)

Equations 258 or 228 are the techniques for integrating Equations 249 and 250 with respect to Y_1 or r_{11} as appropriate. Equations 248 through 250 can now be written:

$$F_{1-2} = \frac{1}{A_1} \int_{\phi_{1,10}}^{\phi_{1,up}} F_F d\phi_1 \quad (\text{Reference Equation 229})$$

As was the situation for the integration of Equation 229, F_F will not vary as ϕ_1 varies because of the cylindrical symmetry of the problem. Thus, we can find F_{1-2} by using Equation 230; and Equation 231 gives F_{2-1} .

<u>Point Location</u>	<u>Segment Number on Body 1</u>
(a) Point upstream of Body 1	0
(b) $Y_{F1} \leq Y \leq Y_{F2}$	1
(c) $Y_{F2} \leq Y \leq Y_{F3}$	2
(d) $Y_{F3} \leq Y < Y_{F4}$	3
(e) $Y_{F4} \leq Y < Y_{F5}$	4
(f) $Y_{F5} \leq Y$	5

The body segment number is given the names NY1 for Y₁ and NY2 for Y₂.

Once the segment numbers NY1 and NY2 have been determined for a given body, the program goes to subroutine CODE. This program provides further detail about the shadowing to be studied. The results obtained by CODE are tabulated below. ICODE or IC is the parameter which the computer uses to record the findings of subroutine CODE.

<u>Value of IC or ICODE</u>	<u>Meaning of the Value of IC or ICODE Assigned</u>
1	Y ₁ is upstream of the shadowing body, and Y ₂ is downstream of the shadowing body.
2	Y ₁ is upstream of the shadowing body, and Y ₂ lies between the minimum and maximum Y values of the shadowing body.
3	Y ₁ is between the minimum and maximum Y values of the shadowing body, and Y ₂ is upstream of it.
4	Y ₁ is between the minimum and maximum Y values of the shadowing body, and Y ₂ is downstream of it.
5	Both Y ₁ and Y ₂ lie between the minimum and the maximum Y values of the shadowing body.

<u>Value of IC or ICODE</u>	<u>IC or ICODE Assigned</u>
6	Y_1 is downstream of the body, and Y_2 lies between the minimum and the maximum Y values for the shadowing body.
7	Y_1 is downstream of the shadowing body, and Y_2 is upstream of it.
8	Both Y_1 and Y_2 lie downstream of the shadowing body or both lie upstream of it.

The shadowing study now branches depending on whether $Y_1 = Y_2$ or $Y_1 \neq Y_2$. The following discussion deals with $Y_1 \neq Y_2$, and the case Y_1 or Y_2 will be treated later. If $Y_1 \neq Y_2$ and IC (or ICODE) = 8, no shadowing occurs for the specified Y_1 and Y_2 and the shadowing body under consideration. The program then examines shadowing for a next shadowing body if it exists. If no further shadowing bodies exist, shadowing by the radial support members (if any) will be considered.

If $Y_1 \neq Y_2$ and IC \neq 8, the computer next goes to subroutine CANSEE. Subroutine CANSEE determines whether the source node point (Y_1, r_{11}, ϕ) can see any of the receiver nodes for the given Y_2 . It also decides whether the outside surface of the shadowing body causes the shadowing or whether it is the inside surface of the body that causes the shadowing. In some cases it may determine that the shadowing body causes no shadowing at all.

The results obtained by program CANSEE are summarized below for the computer variable name ISEE.

<u>Code</u>	<u>Meaning</u>
ISEE = 1	No shadowing is caused by the shadowing body of interest.
ISEE = 2	The shadowing body causes shadowing with its outside surface. The receiver node at Y_2 cannot be seen for $\phi = 180^\circ$.
ISEE = 3	The shadowing body causes shadowing with its outside surface. The receiver node at Y_2 cannot be seen for $\phi = 0^\circ$.
ISEE = 4	The shadowing body causes complete shadowing.
ISEE = 5	The shadowing body causes shadowing with its outside surface. However, the receiver node can be seen at $\phi = 0$ and $\phi = 180^\circ$.

The parameter ISEE directs the flow of the computations used to determine the visibility limits for $\tilde{\phi}$ when shadowing bodies are present. For ISEE = 1, no shadowing exists and the program is instructed to test the next shadowing body for shadowing. For ISEE = 4, the parameter GI is set equal to zero to correspond to a completely shadowed situation. For ISEE = 3, intersections of the field vision of the source point, as it looks at the receiver at Y_2 with the shadowing body, are sought. From these intersections, angles can be computed from which one can determine the visibility limits for $\tilde{\phi}$. For ISEE = 3 and = 5, intersections of the source point of vision with the shadowing body also are sought. In addition, the existence of lines of sight from the source point to the receiver (that are tangent to the shadowing body) also are determined. The location of the intersections and the tangency conditions then are used to find angles from which appropriate visibility limits are selected for $\tilde{\phi}$. The visibility limits and the integration limits then are examined, and appropriate limits are determined when shadowing bodies are present.

Shadowing RING is used for ISEE = 2, 3, and 5 and details of the program are presented in Section IVD.1.b. This subprogram is used to study the intersections of the field of vision of the source node point and the shadowing body.

The geometry involved in determining the intersection is shown in Figure 19. In this case, the shadowing body consists of two frustums. The cone of vision of the source node point as it looks at the receiver node at Y_2 is a cone with its apex at the source node point and its base at the position Y_2 . The cone of vision shown in Figure 19 lies mostly inside the shadowing body, and the intersection of the cone of vision with the shadowing body shows where the cone of vision lies outside the shadowing body. Since the lines of sight from the source point to the receiver node lie on the surface of the cone of vision, the portion of the cone that passes through the shadowing body corresponds to the blocked vision of the source node. It follows, therefore, that the source node can see the receiver for the limiting $\tilde{\phi}$ shown in Figure 19 to $360 - \tilde{\phi}$. Section IV.D.1.b lists the equations used to determine the limiting $\tilde{\phi}$.

For ISEE = 3, the computations of Section IV.D.1.b are performed at each slope breakpoint of the shadowing body that lies between Y_1 and Y_2 . The largest $\tilde{\phi}$ value obtained for the shadowing body then is chosen. The limits of visibility of the source node point for the receiver at Y_2 then lies between $\tilde{\phi}$ maximum and $360 - \tilde{\phi}$. The limits using symmetry of the integrand are $\tilde{\phi}$ maximum to 180° .

For ISEE = 2 or = 5, subprogram RING again is used. In addition, subprogram BODY is used. Subprogram BODY looks for possible lines of sight (source node point to the receiver at $Y = Y_2$) which are tangent to the shadowing body. When a tangency is determined, the angle $\tilde{\phi}$ for which it occurs is determined. The $\tilde{\phi}$ angles found with program BODY and program RING then are examined to select the visibility limits when ISEE = 2 or = 5. The details of program BODY are presented in Section IV.D.1.c.

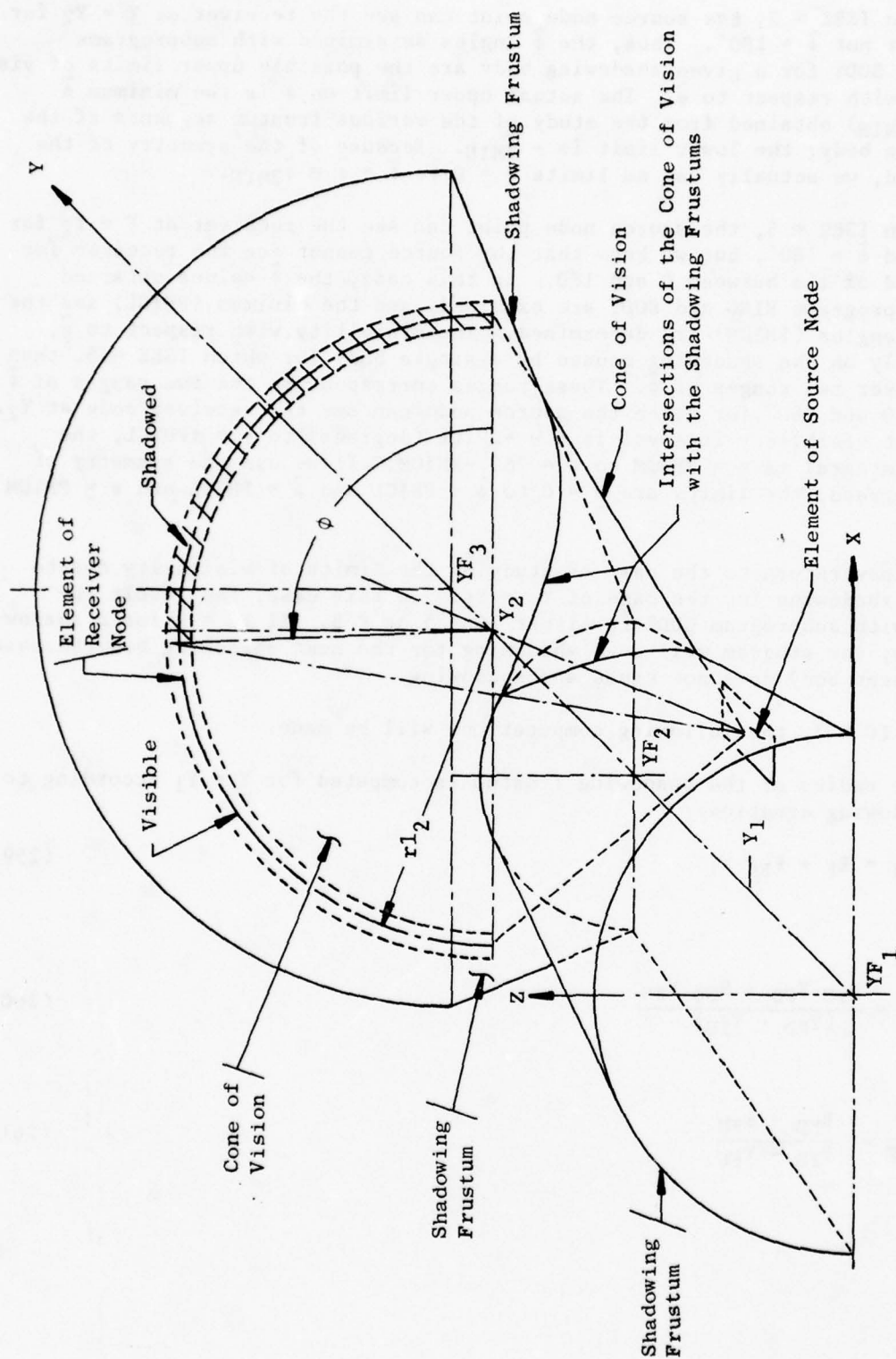


Figure 19. Geometry Involved in a Typical Visibility Determination Performed by Subroutine RING.

When $ISEE = 2$, the source node point can see the receiver at $Y = Y_2$ for $\tilde{\phi} = 0$ but not $\tilde{\phi} = 180^\circ$. Thus, the $\tilde{\phi}$ angles determined with subprograms RING and BODY for a given shadowing body are the possible upper limits of visibility with respect to $\tilde{\phi}$. The actual upper limit on ϕ is the minimum $\tilde{\phi}$ value ($\tilde{\phi}_{MIN}$) obtained from the study of the various frustum segments of the shadowing body; the lower limit is $-\tilde{\phi}_{MIN}$. Because of the symmetry of the integrand, we actually use as limits $\tilde{\phi} = 0$ to $\tilde{\phi} = \tilde{\phi} = \tilde{\phi}_{2MIN}$.

When $ISEE = 5$, the source node point can see the receiver at $Y = Y_2$ for $\tilde{\phi} = 0$ and $\tilde{\phi} = 180^\circ$, but we know that the source cannot see the receiver for some band of $\tilde{\phi}$'s between 0 and 180. In this case, the $\tilde{\phi}$ values obtained from subprograms RING and BODY are examined, and the minimum (PHICL) and the maximum angles (PHICM) are determined. The visibility with respect to $\tilde{\phi}$, based only on the shadowing caused by a single body for which $ISEE = 5$, then exists over two ranges of $\tilde{\phi}$. These ranges correspond to the two ranges of $\tilde{\phi}$ between 0 and 360° for which the source node can see the receiver node at Y_2 . The first visibility interval is $\tilde{\phi} = -PHICL$ (degrees) to $\tilde{\phi} = +PHICL$, the second interval is $\tilde{\phi} = PHICM$ to $\tilde{\phi} = 360 - PHICM$. If we use the symmetry of the integrand, the limits are $\tilde{\phi} = 0$ to $\tilde{\phi} = PHICL$ and $\tilde{\phi} = PHICL$ and $\tilde{\phi} = PHICM$ to 180° .

We now return to the case of studying the limits of visibility due to frustum shadowing for the case of $Y_2 = Y_1$. In this case, the result obtained with subprogram CODE is either $IC = 5$ or $IC = 8$. If $IC = 8$ for a shadowing body, the program will seek shadowing for the next shadowing body because the present body does not cause any shadowing.

If $IC = 5$, the following computations will be made.

The radius of the shadowing frustum is computed for $Y = Y_1$ according to the following equation:

$$r_{c1} = E_F + F_{FF} Y_1 \quad (259)$$

where,

$$E_F = \frac{R_{FU} Y_{FD} - R_{FD} Y_{FU}}{(Y_{FD} - Y_{FU})} \quad (260)$$

$$F_{FF} = \frac{R_{FD} - R_{FU}}{Y_{FD} - Y_{FU}} \quad (261)$$

R_{FU} is the upstream radius of a shadowing frustum (this is an input value for the program).

R_{FD} is the downstream radius of the shadowing frustum (this is an input value).

Y_{FU} is the upstream axial station of the shadowing frustum (this is an input value).

Y_{FD} is the downstream axial station of the shadowing frustum (this is an input value).

The computer now checks to see if either the source node point or the receiver node lies on the shadowing frustum of interest. If one of the two lies on the shadowing frustum, the program seeks shadowing for the next shadowing body if one exists. The shadowing for the present body was effectively determined in the determination of the limits when no intervening bodies lie between the nodes.

If neither the source nor the receiver nodes lie on the shadowing body, the computer next checks to see if the shadowing body causes complete shadowing of the nodes. For $Y_1 = Y_2$, complete shadowing occurs if $r_{l1} < r_{c1} < r_{l2}$ or if $r_{l2} < r_{c1} < r_{l1}$. If either of the inequalities applies, the computer sets $G_I = 0$ in accordance with complete shadowing. If neither inequality applies, the source node point sees a part of the receiver from $-\phi_2$ to some angle $+\phi_2$ which is next determined.

The geometry of the vision situation is shown in Figure 20. In this case, the source node point and the receiver node lie on the same surface. The equation of the shadowing frustum is:

$$X_F^2 + Z_F^2 = r_{c1}^2 \quad (262)$$

and the equation of the limit line of sight is:

$$\frac{X_F - X_1}{X_2 - X_1} = \frac{Z_F - Z_1}{Z_2 - Z_1} \quad (263)$$

We also can write:

$$\begin{aligned} X_1 &= r_{11} \cos \phi_1 & X_2 &= r_{12} \cos \phi_2 \\ Z_1 &= r_{11} \sin \phi_1 & Z_2 &= r_{12} \sin \phi_2 \end{aligned} \quad (264)$$

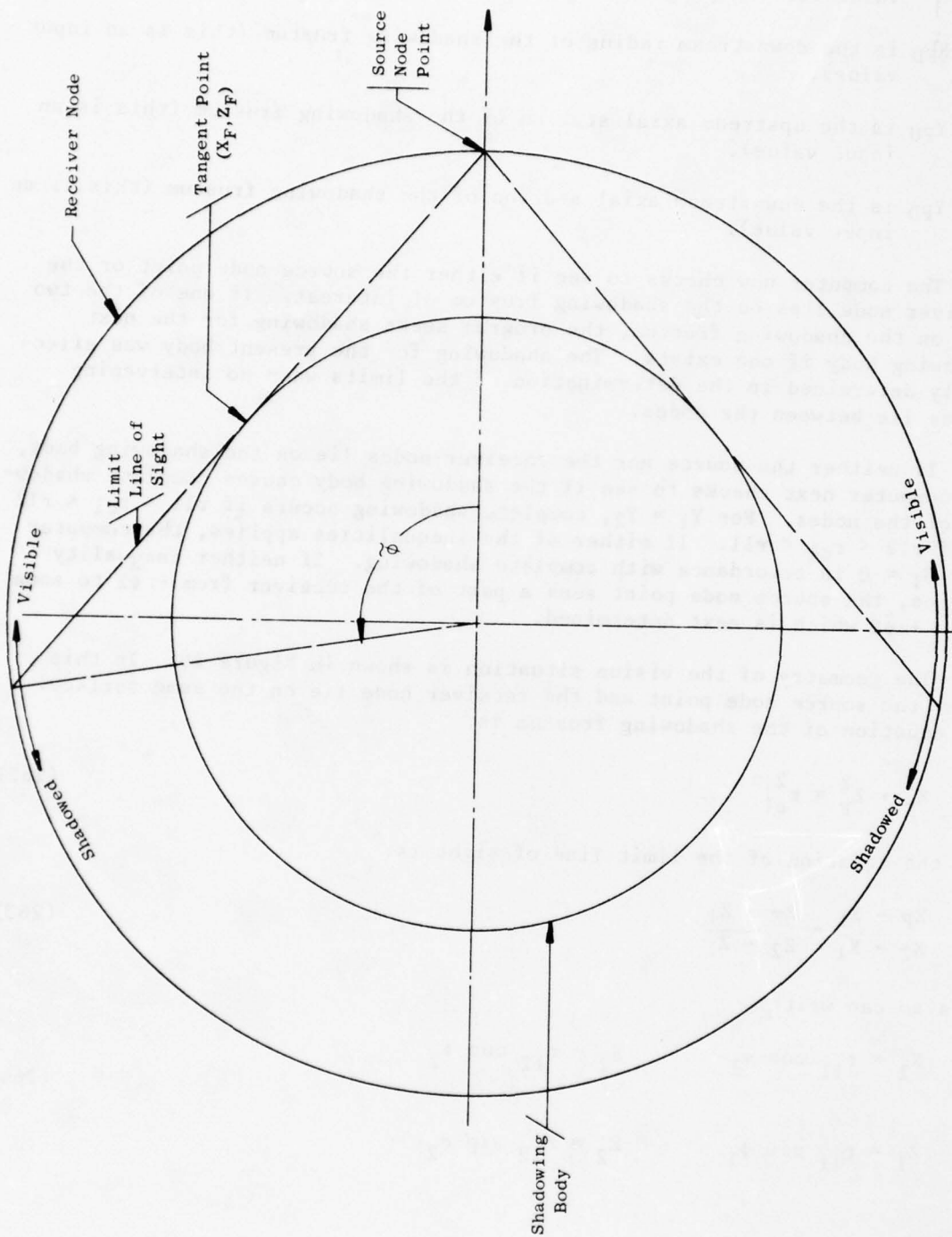


Figure 20. Geometry Associated with the Visibility Studies
Made When $Y_{\text{source}} = Y_{\text{receiver}}$

For tangency, the radius vector $\bar{\rho}$ from the source node point, 1, to a point (X_2, Y_2, Z_2) on the receiver node must be perpendicular to the normal to the frustum \bar{N}_F at the point of tangency:

$$\bar{\rho} \cdot \bar{N}_F = 0 \quad (265)$$

In this case,

$$\bar{\rho} = (X_2 - X_1) \bar{i} + \bar{0} + (Z_2 - Z_1) \bar{k} \quad (266)$$

and,

$$\bar{N}_F = \cos \alpha_F \bar{i} + \cos \beta_F \bar{j} + \cos \gamma_F \bar{k} \quad (267)$$

where,

$$\cos \alpha_F = \frac{X_F (Y_{FD} - Y_{FU})}{r_{c1} \sqrt{(Y_{FD} - Y_{FU})^2 + (R_{FD} - R_{FU})^2}} \quad (268)$$

$$\cos \beta_F = \frac{-(R_{FD} - R_{FU})}{\sqrt{(Y_{FD} - Y_{FU})^2 + (R_{FD} - R_{FU})^2}} \quad (269)$$

$$\cos \gamma_F = \frac{Z_F (Y_{FD} - Y_{FU})}{r_{c1} \sqrt{(Y_{FD} - Y_{FU})^2 + (R_{FD} - R_{FU})^2}} \quad (270)$$

The derivation of the equation for \bar{N}_F is very similar to the presentation given for Equations 93 and 94.

A combination of Equations 265 through 270 yields the following result for the tangency condition:

$$X_2 - X_F \quad X_F + \quad Z_2 - Z_1 \quad Z_F = 0 \quad (271)$$

The governing equations for finding the limit line of sight are Equations 262 through 264 and 271 with the unknowns X_F , X_2 , Z_F , Z_2 , and ϕ_2 . This system of equations was solved as follows: First solve 271 and 263 for X_F and Z_F :

$$X_F = \frac{(X_1 Z_2 - Z_1 X_2)(Z_2 - Z_1)}{(X_2 - X_1)^2 + (Z_2 - Z_1)^2} \quad (272)$$

$$Z_F = \frac{(Z_1 X_2 - X_1 Z_2)(X_2 - X_1)}{(X_2 - X_1)^2 + (Z_2 - Z_1)^2} \quad (273)$$

Substitution of Equation 264 into Equations 272 through 282 yields the following equations in the single unknown variable ϕ_2 .

$$X_F = \frac{r_{11} r_{12} \sin(\phi_2 - \phi_1) [r_{12} \sin \phi_2 - r_{11} \sin \phi_1]}{r_{12}^2 + r_{11}^2 - 2 r_{12} r_{11} \cos(\phi_2 - \phi_1)} \quad (274)$$

$$Z_F = \frac{r_{11} r_{12} \sin(\phi_2 - \phi_1) [r_{12} \cos \phi_2 - r_{11} \cos \phi_1]}{r_{12}^2 + r_{11}^2 - 2 r_{12} r_{11} \cos(\phi_2 - \phi_1)} \quad (275)$$

Substitution of Equations 274 and 275 into Equation 262 yields the following quadratic equation for $\cos(\phi_2 - \phi_1)$:

$$A_{AF} \cos^2(\phi_2 - \phi_1) + B_{BF} \cos(\phi_2 - \phi_1) + C_{CF} = 0. \quad (276)$$

where

$$A_{AF} = 1 \quad (277)$$

$$B_{BF} = -2 r_{c1}^2 / (r_{11} r_{12}) \quad (278)$$

$$C_{CF} = \frac{r_{c1}^2 r_{12}^2 + r_{11}^2}{r_{11} r_{12}} - 1 \quad (279)$$

The quadratic Equation 226 is solved for $\cos(\phi_2 - \phi_1)$ by means of subprogram QUAD. To qualify as a proper solution to the problem, the computer requires that the point (X_F, Y_F, Z_F) lies between (X_1, Y_1, Z_1) and (X_2, Y_2, Z_2) .

After the visibility limits have been determined for each shadowing body in the exhaust system, a set of integration limits is selected from the results of the analysis and the visibility limits. Let us suppose for the sake of demonstration of the computer program, that the following axisymmetric shadowing visibility results were obtained from the shadowing body study:

- (a) 3 shadowing bodies cause outside-surface shadowing (ISEE = 2).
The visibility limits for each body are as follows:

Body A: $\tilde{\phi} = 0^\circ$ to $\tilde{\phi} = 80^\circ$

Body B: $\tilde{\phi} = 0^\circ$ to $\tilde{\phi} = 95^\circ$

Body C: $\phi = 0^\circ$ to $\tilde{\phi} = 90^\circ$

- (b) 3 shadowing bodies cause inside-surface shadowing (ISEE = 3).
The visibility limits for these bodies are the following:

Body D: $\tilde{\phi} = 10^\circ$ to $\tilde{\phi} = 180^\circ$

Body E: $\tilde{\phi} = 15^\circ$ to $\tilde{\phi} = 180^\circ$

Body F: $\phi = 12^\circ$ to $\tilde{\phi} = 180^\circ$

- (c) 3 shadowing bodies cause shadowing for which ISEE = 5.
The ranges of $\tilde{\phi}$ for which the view of the source node point is blocked are as follows:

Body G: $\tilde{\phi} = 20^\circ$ to $\tilde{\phi} = 25^\circ$

Body H: $\tilde{\phi} = 22^\circ$ to $\tilde{\phi} = 45^\circ$

Body I: $\tilde{\phi} = 40^\circ$ to $\tilde{\phi} = 45^\circ$

The computer program now examines the results of (a) and decides that the appropriate limits of visibility for the shadowing caused by bodies A, B, and C are $\tilde{\phi} = 0^\circ$ to 80° . That is the combined outside surface shadowing caused by bodies A, B, and C is such that the source node point can only see the receiver node at Y_2 for $\tilde{\phi} = 0$ to 80° . (Note that 80° is the minimum upper limit of the three upper limits given for A, B, and C). The limits for the results of (b) are next examined. In this case, the computer decides that appropriate visibility limits are $\phi = 15^\circ$ to $\tilde{\phi} = 180^\circ$. The combined visibility caused by inside-surface shadowing ranges from the maximum of the lower limits for bodies D, E, and F (i.e., 16° to 180°).

The computer next selects visibility limits which are compatible with both the inside and the outside surface shadowing caused by bodies A, B, C, D, E, and F. The limits for bodies A, B, and C were as follows:

$$\tilde{\phi} = 0^\circ \text{ to } \tilde{\phi} = 80^\circ.$$

The limits for bodies D, E, and F were:

$$\tilde{\phi} = 15^\circ \text{ to } \tilde{\phi} = 18^\circ.$$

The compatible limits are therefore:

$$\tilde{\phi} = 15^\circ \text{ to } \tilde{\phi} = 80^\circ.$$

If the minimum visibility limit for bodies D, E, and F (inside shadowing) had been greater than the maximum visibility limit for bodies A, B, and C (outside shadowing) the computer would have set $G_I = 0$ to correspond to complete shadowing.

The visibility limits obtained thus far, $\tilde{\phi} = 15^\circ$ to $\tilde{\phi} = 80^\circ$, are next compared to the integration limits arrived at by means of the studies of radial supports (not operable in the present version of SCORPIO-N) where the upper limit is $\tilde{\phi}_{up}$ and the lower is $\tilde{\phi}_{lo}$. One of the following situations illustrated in Figure 21 will apply.

For the situations represented by Figures 21a and 21b, the integral value G_I is set equal to zero. This is done because the range of $\tilde{\phi}$, for which the analyses for radial supports shows $\cos \theta_1$ and $\cos \theta_2$ would be positive, is not within the range of $\tilde{\phi}$ for which the source node point can see the receiver node at Y_2 . For those cases in which the two ranges of $\tilde{\phi}$ overlap, the integration limits (based on symmetry of the integrand) are as follows):

Figure	Minimum Limit	Maximum Limit
21(c)	$\tilde{\phi}_{lo}$	80 degrees
21(d)	15 degrees	80 degrees
21(e)	15 degrees	$\tilde{\phi}_{up}$
21(f)	$\tilde{\phi}_{lo}$	$\tilde{\phi}_{up}$

If there were no bodies for which $ISEE = 5$, (and no shadowing ducts or radial support members), the limits tabulated above would be used for the evaluation of the integral G_I . In the example we proposed previously, however, three bodies caused $ISEE = 5$ -type shadowing, and we now accordingly modify the integration limits tabulated above.

When $ISEE = 5$ shadowing occurs, the computer selects integration limits which are compatible with the results of the limits, $\tilde{\phi}_{MIN}$ and $\tilde{\phi}_{MAX}$, arrived at in the foregoing paragraph and the shadowed ranges of $\tilde{\phi}$ caused by the $ISEE = 5$ shadowing. In the figure below, the range of integration for $\tilde{\phi}$ is laid-out as a bar graph. The ranges of $\tilde{\phi}$ which are shadowed by the $ISEE = 5$ shadowing (example of page) are depicted by cross-hatching. Possible positions for $\tilde{\phi}_{MIN}$ and $\tilde{\phi}_{MAX}$ are shown above the graph.

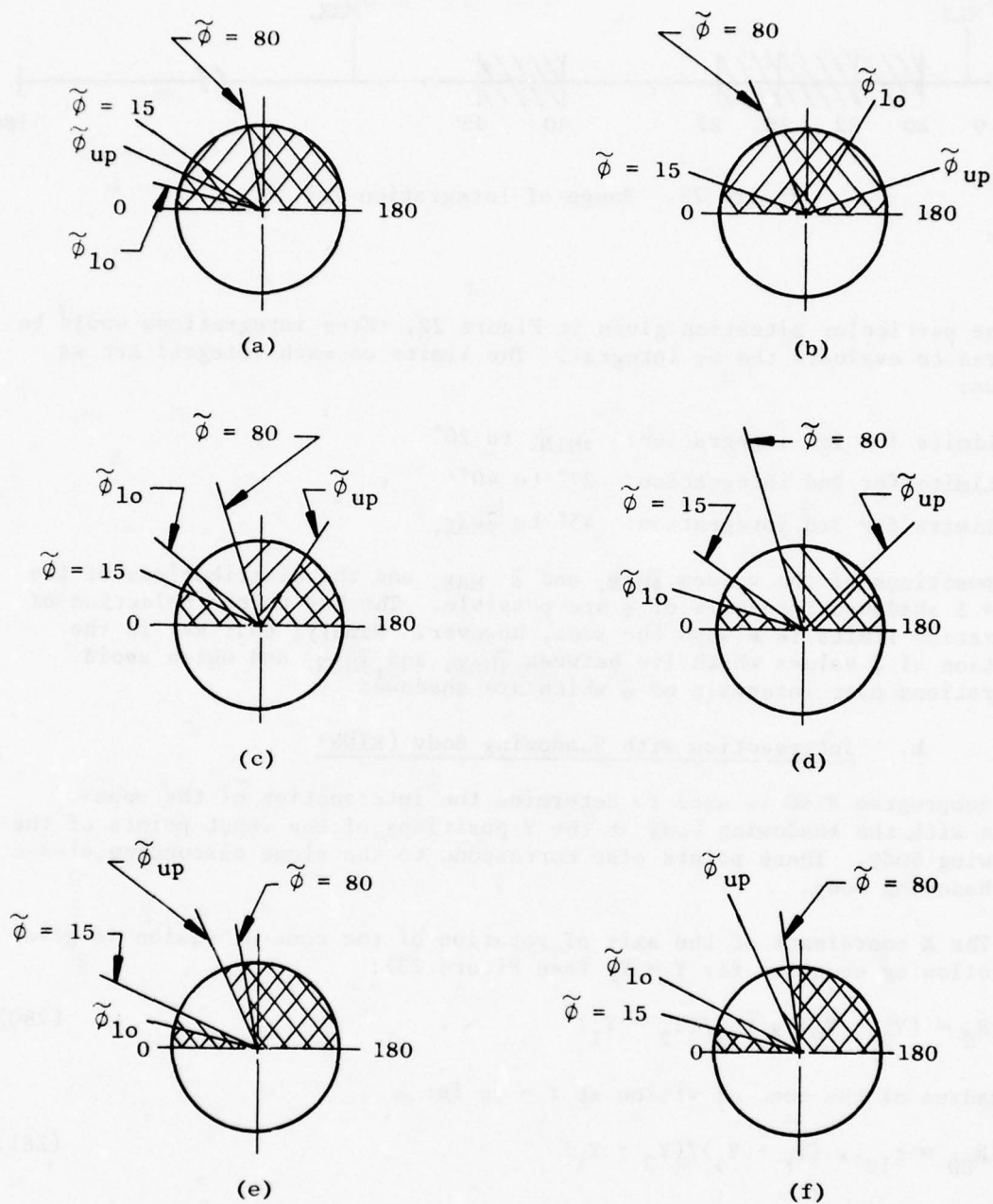


Figure 21. Schematic of Visibility Limits.

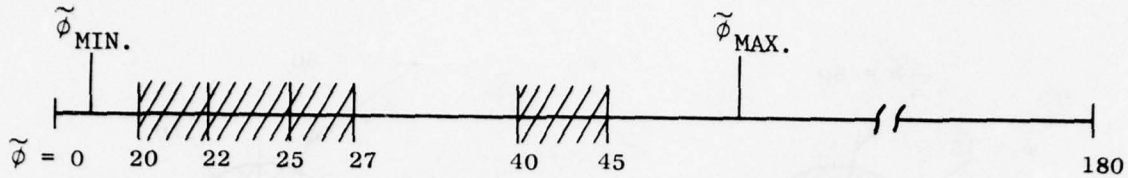


Figure 22. Range of Integration for $\tilde{\phi}$.

For the particular situation given in Figure 22, three integrations would be required to evaluate the G_I integral. The limits on each integral are as follows:

Limits for 1st integration: $\tilde{\phi}_{MIN.}$ to 20°

Limits for 2nd integration: 27° to 40°

Limits for 3rd integration: 45° to $\tilde{\phi}_{MAX.}$

Many positions of the values $\tilde{\phi}_{MIN.}$ and $\tilde{\phi}_{MAX.}$ and the distributions of the $I_{SEE} = 5$ shadowed intervals of $\tilde{\phi}$ are possible. The key to the selection of integration limits is always the same, however. Namely, that key is the selection of $\tilde{\phi}$ values which lie between $\tilde{\phi}_{MAX.}$ and $\tilde{\phi}_{MIN.}$ and which avoid integrations over intervals of $\tilde{\phi}$ which are shadowed.

b. Intersection with Shadowing Body (RING)

Subprogram RING is used to determine the intersection of the cone of vision with the shadowing body at the Y positions of the input points of the shadowing body. These points also correspond to the slope discontinuities of the shadowing body.

The X coordinate of the axis of rotation of the cone of vision is given by the following equation for $Y = Y_F$ (see Figure 23):

$$R_C = (Y_2 - Y_F) \times r_{11} / (Y_2 - Y_1) \quad (280)$$

The radius of the cone of vision at $Y = Y_F$ is:

$$R_{HO} = r_{12} \times (Y_F - Y_1) / (Y_2 - Y_1) \quad (281)$$

The equation of the shadowing body at $Y = Y_F$ is:

$$X_F^2 + Z_F^2 = r_F^2 \quad (282)$$

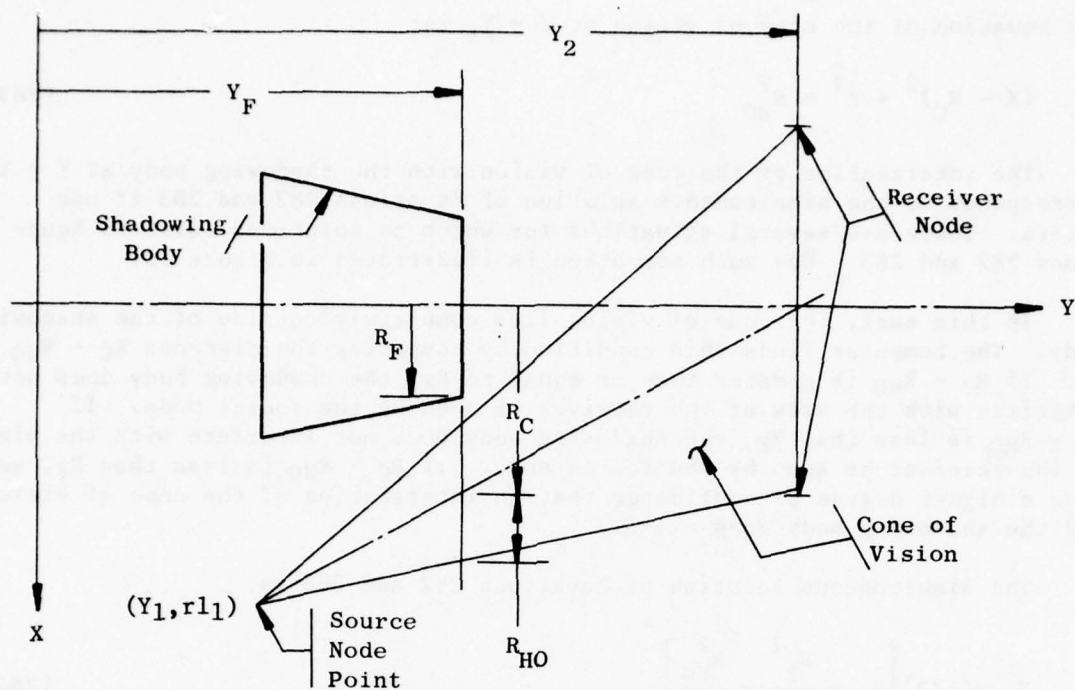


Figure 23. Sample Situation with No Solution.

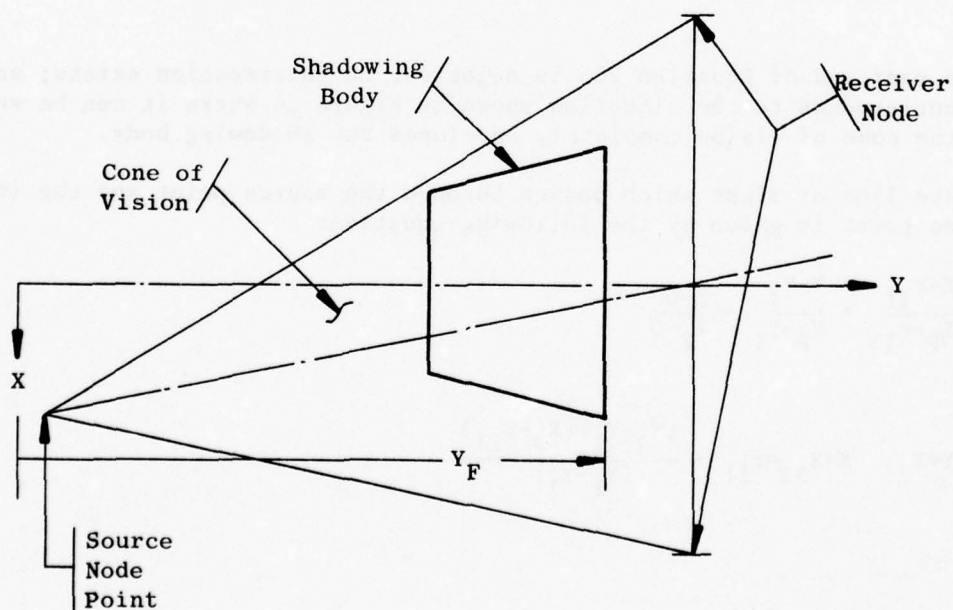


Figure 24. Cone of Vision Envelopes Shadowing Body.

The equation of the cone of vision at $Y = Y_F$ is:

$$(X - R_C)^2 + Z^2 = R_{HO}^2 \quad (283)$$

The intersection of the cone of vision with the shadowing body at $Y = Y_F$ corresponds to the simultaneous solution of Equations 282 and 283 if one exists. There are several situations for which no solutions exist to Equations 282 and 283. One such situation is illustrated in Figure 23.

In this case, the cone of vision lies completely outside of the shadowing body. The computer finds this condition by comparing the distance $R_C - R_{HO}$ to R_F . If $R_C - R_{HO}$ is greater than or equal to R_F , the shadowing body does not interfere with the view of the receiver as seen by the source node. If $R_C - R_{HO}$ is less than R_F , the shadowing body does not interfere with the view of the receiver as seen by the source node. If $R_C - R_{HO}$ is less than R_F , we have a higher degree of confidence that an intersection of the cone of vision and the shadowing body does exist.

The simultaneous solution of Equations 282 and 283 is:

$$X_F = (1/2) \left[R_C + \frac{R_F^2}{R_C} - \frac{R_{HO}^2}{R_C} \right] \quad (284)$$

$$Z_F^2 = R_F^2 - X_F^2 \quad (285)$$

If the radicand of Equation 285 is negative, no intersection exists; and this corresponds to the situation shown in Figure 24 where it can be seen that the cone of vision completely envelopes the shadowing body.

The line of sight which passes through the source point and the intersection point is given by the following equation:

$$\frac{X - r_{11}}{X_F - r_{11}} = \frac{Y - Y_1}{Y_F - Y_1} = \frac{Z - 0}{Z_F - 0} \quad (286)$$

For:

$$Y = Y_2: \quad X = X_{2R} = r_{11} + \frac{(Y_2 - Y_1)(X_F - r_{11})}{(Y_F - Y_1)} \quad (287)$$

It follows that:

$$\cos \phi_2 = \frac{X_{2R}}{r_{12}} \quad (288)$$

from which we can find ϕ_2 as shown in Figure 24. Equation 288 completes the computations of program RING.

Because of the cylindrical symmetry of the bodies involved in the problem, the foregoing equations apply to the case $\phi_1 \neq 0$.

All we must realize is that we need only rotate the X - Z axes so that the xy plane lies in the plane of ϕ_1 . However, we do need to rewrite Equation 288 as follows:

$$\cos \tilde{\phi} = \frac{X_{2R}}{r_{12}} \quad (289)$$

$$\tilde{\phi} = \phi_2 - \phi_1 \quad (290)$$

c. Tangent to Shadowing Body (BODY)

Subprogram BODY is used to determine if a line of sight from the source node point (Y_1, r_{11}, ϕ_1) to the receiver node at (Y_2, r_{12}, ϕ_2) is possibly tangent to a shadowing body ininterposed between the source and receiver positions.

The geometry associated with finding the tangent line is shown in Figure 25. We desire the X, Y, Z position of the tangent point and then the angle $\tilde{\phi}$ for which the line is tangent to the shadowing body or frustum.

We first concern ourselves with the geometry of the shadowing frustum. The equation of the frustum surface is:

$$R_F = R_{FU} + \frac{R_{FD} - R_{FU}}{Y_{FD} - Y_{FU}} (Y - Y_{FU}) \quad (291)$$

where,

R_F is the radius of the frustum at any axial station Y.

Y_{FU} is the upstream axial coordinate of the frustum. This is a program input.

Y_{FD} is the downstream axial coordinate of the frustum. This is a program input.

R_{FU} is the radius of the frustum at $Y = Y_{FU}$. This is a program input.

R_{FD} is the radius of the frustum at $Y = Y_{FD}$. This is a program input.

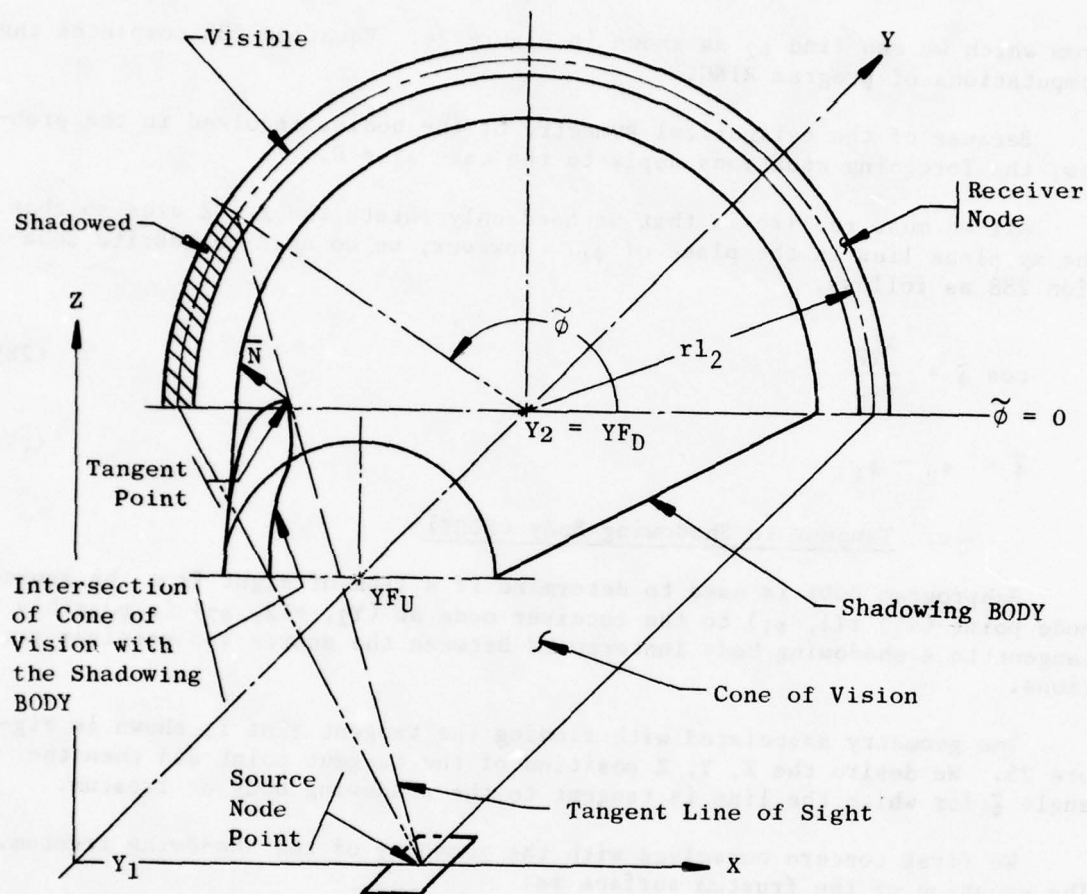


Figure 25. Geometry Involved in a Typical Visibility Determination Performed by Subroutine BODY.

A rearrangement of Equation 291 yields:

$$R_F = E_F + F_F \times Y \quad (292)$$

where,

$$E_F = \frac{R_{FU} Y_{FD} - R_{FD} Y_{FU}}{Y_{FD} - Y_{FU}} \quad (293)$$

$$F_F = \frac{R_{FD} - R_{FU}}{(Y_{FD} - Y_{FU})} \quad (294)$$

The subprogram at this time checks to see if both the source node point and the receiver node lie on the shadowing frustum (Equation 292). If they do, no tangent line can be found, and the subprogram signifies no tangent line exists by setting $I\theta N = 1$. The main program uses $I\theta N = 1$ to let it know that it should check other frustum portions of the shadowing BODY (if they exist) to determine if lines of sight can be tangent to them.

If one (or both) of the source node point or the receiver node does not lie on the shadowing frustum, the following check is made. Does either the source point or the receiver node lie inside of the cone of which the shadowing frustum is a portion? If one or the other does, no tangent line of sight is possible, and the computer program is told to test other frustums of the shadowing BODY. No tangent line of sight is possible in such a case because no line can pass from the inside of the cone of the frustum without piercing its surface. A piercing line can never be perpendicular to the local normal to the cone of the frustum, which is a requirement for a line to be tangent to a surface.

If both the source node point and the receiver node lie outside the cone of the frustum, the possibility of a tangent line to the frustum is increased. We now look at the equations which are used to seek the tangency condition. The fundamental requirement for a tangency condition is that the line of sight be perpendicular to the normal to the frustum at some point of the frustum surface. That is:

$$\bar{N}_F \cdot \bar{\rho} = 0 \quad (295)$$

where \bar{N}_F is the local normal to the frustum and $\bar{\rho}$ is the vector from the source node point to some point on the receiver node at $1/2$.

The equation for $\bar{\rho}$ is given by Equation 92 and is rewritten here for convenience:

$$\bar{\rho} = (X_2 - X_1) \bar{i} + (Y_2 - Y_1) \bar{j} + (Z_2 - Z_1) \bar{k} \quad (92)$$

The determination of normals to frustums is discussed earlier. We use those results to write the following equations for the normal, \bar{N}_F :

$$\bar{N}_F \cos \alpha_F \bar{i} + \cos \beta_F \bar{j} + \cos \gamma_F \bar{k} \quad (93)$$

$$\cos \alpha_F = \frac{X_F}{R_F} \tilde{B}_F \quad (100)$$

$$\cos \beta_F = \tilde{A}_F \quad (109)$$

$$\cos \gamma_F = \frac{Z_F}{R_F} \tilde{B}_F$$

where X_F , Z_F , and R_F are the X , Z , and r coordinates of the shadowing frustum at the point of tangency. \tilde{A}_F and \tilde{B}_F are given by the following equations:

$$\tilde{A}_F = \frac{-(R_{FD} - R_{FU})}{(Y_{FD} - Y_{FU})^2 + (R_{FD} - R_{FU})^2} \quad (105)$$

$$\tilde{B}_F = \frac{\frac{Y_{FD} - Y_{FU}}{2}}{(Y_{FD} - Y_{FU})^2 + (R_{FD} - R_{FU})^2} \quad (106)$$

When the above equations are substituted into Equation 295, the following equation is obtained:

$$(X_2 - X_1) \tilde{B}_F \frac{X_F}{R_F} + \tilde{A}_F (Y_2 - Y_1) + (Z_2 - Z_1) \tilde{B}_F \frac{Z_F}{R_F} = 0 \quad (296)$$

We now make use of the fact that the receiver node at $Y = Y_2$ is a circle; that is:

$$X_2^2 + Z_2^2 = r_{12}^2 \quad \text{and,}$$

$$X_2 = r_{12} \cos \phi_2 \quad (297)$$

$$Z_2 = r_{12} \sin \phi_2 \quad (298)$$

Substitute Equations 297 and 298 into Equation 296 to obtain:

$$\begin{aligned} (r_{12} \cos \phi_2 - X_1) \frac{\tilde{B}_F X_F}{R_F} + \tilde{A}_F (Y_2 - Y_1) \\ + (r_{12} \sin \phi_2 - Z_1) \frac{\tilde{B}_F Z_F}{R_F} = 0 \end{aligned} \quad (299)$$

Another set of equations which can be used here are those for the line of sight; they are:

$$\frac{X_F - X_1}{X_2 - X_1} = \frac{Y_F - Y_1}{Y_2 - Y_1} \quad (300)$$

$$\frac{Y_F - Y_1}{Y_2 - Y_1} = \frac{Z_F - Z_1}{Z_2 - Z_1} \quad (301)$$

We also need to relate X_F , Z_F , and R_F by the following equation:

$$R_F^2 = X_F^2 + Z_F^2 \quad (302)$$

The key equations which need to be solved simultaneously to find the tangency point (X_F , Y_F , Z_F , and R_F) and the angle ϕ_2 for which the tangency occurs are Equations 292, 299, 300, 301, and 302. We outline only the main points of this simultaneous solution in what follows.

Solve Equation 300 for X_F and solve Equation 301 for Z_F . Substitute the resulting Equations into Equation 299 to get the following result:

$$\begin{aligned} \tilde{B}_F X_1 r_{12} \cos \phi_2 - X_1^2 + \tilde{B}_F \frac{(Y_F - Y_1)}{(Y_2 - Y_1)} r_{12} \cos \phi_2 - X_1^2 \\ + \tilde{A}_F R_F (Y_2 - Y_1) + \tilde{B}_F Z_1 r_{12} \sin \phi_2 - Z_1^2 \\ + \tilde{B}_F \frac{(Y_F - Y_1)}{(Y_2 - Y_1)} r_{12} \sin \phi_2 - Z_1^2 = 0. \end{aligned} \quad (303)$$

Substitute Equation 292 into Equation 303 to get the following after some rearrangement and use of the equations:

$$X_1 = r_{11} \cos \phi_1 \quad (304)$$

$$Z_1 = r_{11} \sin \phi_1 \quad (305)$$

The result obtained is:

$$Y_F = \frac{C_1 - C_2 \cos (\phi_2 - \phi_1)}{C_3 - C_4 \cos (\phi_2 - \phi_1)} \quad (306)$$

where,

$$C_1 = \tilde{B}_F Y_2 r_{11}^2 + Y_1 r_{11}^2 - \tilde{A}_F E_F Y_2 - Y_1^2 \quad (307)$$

$$C_2 = \tilde{B}_F (Y_1 + Y_2) r_{12} r_{11} \quad (308)$$

$$C_3 = \tilde{B}_F r_{12}^2 + r_{11}^2 + \tilde{A}_F E_F Y_2 - Y_1^2 \quad (309)$$

$$C_4 = 2r_{12} r_{11} \tilde{B}_F \quad (310)$$

Equation 306 relates ϕ_2 to Y_F . We need another equation relating ϕ_2 to Y_F to solve the problem. To obtain this second equation, we begin with Equation 302. Substitute solutions for X_F and Z_F as obtained from Equations 300 and 301 into Equation 302 and square both sides of the resulting equation.

$$\begin{aligned} R_F^2 = X_1 + \frac{(Y_2 - Y_1)}{(Y_2 - Y_1)} r_{12} \cos \phi_2 - X_1^2 \\ + Z_1 + \frac{(Y_F - Y_1)}{(Y_2 - Y_1)} r_{12} \sin \phi_2 - Z_1^2 \end{aligned} \quad (311)$$

Upon usage of Equations 304 and 305, we obtain the following result after some work:

$$R_F^2 = r_{11}^2 + \frac{2(Y_F - Y_1)}{(Y_2 - Y_1)} r_{12} r_{11} \cos(\phi_2 - \phi_1)^2 - r_{11} + \frac{(Y_F - Y_1)^2}{(Y_2 - Y_1)^2} \left[r_{12}^2 + r_{11}^2 - 2r_{12} r_{11} \cos(\phi_2 - \phi_1) \right] \quad (312)$$

We now substitute Equation 379 into Equation 399 for R_F and obtain the following result:

$$Y_F^2 \left[C_5 + C_6 \cos(\phi_2 - \phi_1) \right] + Y_F \left[C_7 - C_8 \cos(\phi_2 - \phi_1) \right] + \left[C_9 + C_{10} \cos(\phi_2 - \phi_1) \right] = 0 \quad (313)$$

where,

$$C_5 = E_F^2 (Y_2 - Y_1)^2 - (r_{12}^2 + r_{11}^2) \quad (314)$$

$$C_6 = 2r_{12} r_{11} \quad (315)$$

$$C_7 = 2Y_1 (r_{12}^2 + r_{11}^2) + 2(Y_2 - Y_1) r_{11}^2 \quad (316)$$

$$C_8 = 2(Y_2 + Y_1) r_{12} r_{11} \quad (317)$$

$$C_9 = (E_F^2 - r_{11}^2) (Y_2 - Y_1)^2 - Y_1^2 r_{12}^2 + Y_1^2 r_{11}^2 - 2Y_1 Y_2 r_{11}^2 \quad (318)$$

$$C_{10} = 2r_{12} r_{11} Y_2 Y_1 \quad (319)$$

The solution to the problem can now be found by the simultaneous solution of Equation 313 and 306. We do this by substituting Equation 305 for Y_F into Equation 313 and solve for $\cos(\phi_1 - \phi_2)$.

The result of the substitution and subsequent reduction to an equation in $\cos(\phi_2 - \phi_1)$ is Equation 319.

$$\begin{aligned} A_{AF} \cos^3(\phi_2 - \phi_1) + B_{BF} \cos^2(\phi_2 - \phi_1) \\ + C_{CF} \cos(\phi_2 - \phi_1) + D_{DF} = 0 \end{aligned} \quad (319)$$

where,

$$A_{AF} = C_2^2 C_6 - C_4 C_2 C_8 + C_4^2 C_{10} \quad (320)$$

$$\begin{aligned} B_{BF} = & -2C_1 C_2 C_6 + C_2^2 C_5 + C_4 (C_1 C_8 + C_2 C_7) \\ & + C_3 C_1 C_8 + C_9 C_4^2 - 2C_3 C_4 C_{10} \end{aligned} \quad (321)$$

$$\begin{aligned} C_{CF} = & C_1^2 C_2 C_5 - C_1 C_7 C_4 \\ & - C_3 (C_1 C_8 + C_2 C_7) - 2C_9 C_3 C_4 + C_3^2 C_{10} \end{aligned} \quad (322)$$

$$D_{DF} = C_1^2 C_5 + C_1 C_7 C_3 + C_3^2 C_9 \quad (323)$$

The roots of Equation 407 are found with subprogram CUBIC, from which $(\phi_2 - \phi_1)$ is obtained.

Each of the $(\phi_2 - \phi_1)$ solutions is checked to ensure that it physically agrees with actual geometry of the problem. The first check requires that Y_F be computed according to Equation 306, and we test Y_F to see if it lies between Y_{FU} and Y_{FD} . That is, does the solution $(\phi_2 - \phi_1)$ yield a tangent point that is on the shadowing frustum of interest? Next, does the solution $(\phi_2 - \phi_1)$ yield a tangent point that lies between Y_1 and Y_2 ? Last, does the solution $(\phi_2 - \phi_1)$ and Y_F satisfy Equations 292, 299, 300, 301, and 302? If a solution is found which satisfied all the foregoing tests, it is taken as a valid tangent line solution. The last test is conducted in subprogram CHECK.

E. Exhaust System Heat Balance (TAS1B)

A thermal heat balance is conducted within the exhaust system to provide the temperature distribution along all exhaust system surfaces. Each surface has been subdivided into isothermal segments (nodes); it is the temperature of these segments that is desired. The subprogram TAS1B is employed to compute these temperatures. This subprogram is a modified version of the existing program Thermal Analysis System 1 written by the Jet Propulsion Laboratory, California Institute of Technology for NASA under contract no. NAS7-100.

The nomenclature used within this section is as follows:

- A - surface area, ft²
- C - overall conductance coefficient, Btu/hr ft², ° R
- F - gray body radiation interchange factor, nondimensional
- R - vector
- S - square matrix
- T - temperature, ° R
- σ - Stefan-Boltzmann constant, = 0.1713 × 10⁻⁸ Btu/ft² hr, (° R)⁴

For any given internal exhaust system node, a steady-state energy balance can be stated such that the sum of the energy addition is equal to the sum of the departing energy. The balance for a node i can be written as:

$$\sum_j C_{ij} A_i (T_i - T_l) + \sum_j \sigma A_i F_{ij} (T_i^4 - T_j^4) = 0 \quad (324)$$

and stated such that the net energy exchange from node i is zero.

For a system of nodes, the energy balance can be written in matrix form as:

$$\begin{bmatrix} C_{ij} A_i \end{bmatrix} \begin{pmatrix} T_i \end{pmatrix} + \begin{bmatrix} \sigma A_i F_{ij} \end{bmatrix} \begin{pmatrix} T_i^4 \end{pmatrix} = 0 \quad (325)$$

The solution used follows the Newton-Raphson iteration method for nonlinear algebraic equations utilizing the matrix form:

$$\begin{bmatrix} S_{ij} \end{bmatrix} \begin{pmatrix} T_i \end{pmatrix} = \begin{pmatrix} R_i \end{pmatrix} \quad (326)$$

The off-diagonal elements of the square matrix are:

$$S_{ij} = C_{ij} A_i + 4\sigma A_i F_{ij} T_j^3 \quad (327)$$

while diagonal elements are:

$$S_{ij} = S_{ii} - C_{ij} A_i - 4\sigma A_i F_{ij} T_i^3 \quad (328)$$

The vector R has the form:

$$R_i = -3\sigma A_i F_{ij} (T_i^4 - T_j^4) \quad (329)$$

Subprogram TASIB solves this matrix, Equation 326 for the temperature (T) vector in an iterative manner, revising the failures of temperature in matrix S and R with each iterative step until the process converges on a final solution.

F. Special Computation Considerations

Module SIGNIR is basically self-contained, dependent only upon the system model produced from the physical exhaust system configuration. With the latitude provided in exhaust system configurations, certain specific items concerning a system may be required of the user in order to complete the model and derive the desired information. The following sections are included to assist the user. They cover a method to establish the required form for pressure loss and heat transfer parameters necessary for program input.

1. Pressure Loss Parameters

When surface cooling is employed by the exhaust system, the pressure loss characteristics must be supplied by the program user to define the particular cooling system configuration employed. Program input data require values of the loss coefficient (K) and the flow exponent (n) for specific segments of the cooling system. If these values are not available from measured data, they must be acquired through empirical data presented in available reference material such as Reference 4.

The nomenclature used within this section is as follows:

A	- flow area, ft ²
B	- loss coefficient, psf/(lb/sec) ⁿ
K _t	- nondimensional loss coefficient
\dot{m}	- mass flow rate, lb/sec
n	- flow exponent
q	- dynamic pressure, lb/ft ²
u	- flow velocity, ft/sec
Δp_t	- change in total pressure, lb/ft ²
ρ	- fluid density, lb/ft ³
ρ_{std}	- density at standard atmospheric temperature and pressure, lb/ft ³
s	- fluid density ratio (ρ/ρ_{std})

The form of the pressure loss equation used by SIGNIR is:

$$\sigma \Delta P_t = K (\dot{m})^n \quad (330)$$

in which K is a dimensional loss parameter and $n \approx 2$. These values can be obtained directly from the system test data. When flow loss estimations are required, other empirical loss data must be utilized. These frequently are presented as a dimensionless loss parameter (K_t) versus the flow Reynolds number. The pressure loss associated with this loss parameter is defined by the equation:

$$\Delta P_t = K_t q, \quad (331)$$

where,

$$q = \frac{1}{2} \rho u^2 \quad (332)$$

Using a value of two for exponent n, these two loss parameters are related by:

$$K = K_t / (2 \rho_{std} A^2) \quad (333)$$

where the area (A) is that associated with the dynamic pressure (q) used in Equation 331. For pressure losses which occur in series, the loss coefficient is computed by the equation

$$K = \frac{1}{2 \rho_{std}} \left[\sum_i \left(\frac{A^2}{K_t} \right)_i^{1/2} \right]^{-2} \quad (334)$$

When a parallel flow system is employed, the required loss coefficient is computed by the equation:

$$K = \frac{1}{2 \rho_{std}} \left[\sum_i \left(\frac{A^2}{K_t} \right)_i^{1/2} \right]^2 \quad (335)$$

Equations 422 and 423, based on $n = 2$, provide the user a means of computing the loss coefficient for systems in which estimated values are required.

2. Heat Transfer Parameters

Special paths of heat flow for the exhaust system mathematical model can be established by the user to supplement the basic program process. These improve the program's general heat balance by incorporating the characteristics of a specific system through defining additional heat transfer paths to heat sources or sinks. Heat transfer parameters are used to define the barrier to heat transfer for any surface coolant supply system and to special

fluid nodes. In both cases, an overall heat transfer coefficient is required by the program to describe this barrier to heat flow if it is to be included in the heat balance.

The following is a list of nomenclature used within this section.

- A - area normal to heat flow path, ft²
- a - Reynolds number - exponent
- b - Prandtl number - exponent
- c - convection coefficient constant
- h - convection film coefficient, Btu/hr-ft²-°R
- k - conductivity, Btu/hr-ft-°R
- L - characteristic length, ft
- Pr - Prandtl number
- Re - Reynolds number
- t - material thickness, ft
- U - overall heat transfer coefficient, Btu/hr-ft²-°R

Subscripts:

- d - duct
- i - inner
- o - outer

For a surface cooling system, an overall heat transfer coefficient (UA) can be employed to establish the barrier for a heat path from a known heat source to the coolant passing through the coolant supply ducting system. If the coolant flow rate is provided as a fixed program input, a coefficient is not required. If the heat source is such that no heat transfer will occur (source and coolant temperatures identical), a UA value of one will permit proper program operation without requiring that the user compute the actual value. When the temperature difference exists between the coolant and the heat source, a supply system overall heat transfer coefficient should be computed by the user for program input. The path from the heat source to the coolant normally will pass through a series of barriers which are both the inside and outside gas films and duct conduction. For this series configuration, the overall heat transfer coefficient can be computed by the equation:

$$UA = 1 / \left[\left(\frac{1}{hA} \right)_i + \left(\frac{t}{kA} \right)_d + \left(\frac{1}{hA} \right)_o \right] \quad (336)$$

The value of conduction (k) for the duct is a material property and can be found in reference material such as Reference 22. Convection film coefficients are functions of gas flow properties and the duct configuration. These normally are evaluated through an equation of the form:

$$h = c \frac{k}{L} (R_e)^a (P_r)^b \quad (337)$$

Values for the constants of a, b, and c are usually presented as a function of Reynolds number for a specific configuration that can be found in numerous references; two common references are 24 and 25.

When special fluid nodes have been incorporated in the exhaust system model, an overall heat transfer coefficient is required to define the barrier to heat transfer between the fluid node and its adjacent node in the system. These normally will follow a path from a surface to a fluid node passing through a conducting wall and a convection film. The overall heat transfer coefficient is computed in a manner similar to that presented; in this particular case, the equation is found to be:

$$UA = A / \left(\frac{t}{k} + \frac{1}{h} \right) \quad (338)$$

Again, the values of k and h must be obtained based on empirical data.

With these equations, the user can provide the overall heat transfer required as program input in most of the cases that will confront him.

G. Radiation Coefficients and Source Emissions (SIRER)

The radiosity leaving any surface is a combination of the direct emissions and the reflections of emissions from other surfaces. The subroutine SIRER determines the radiation coefficients of R'_{ij} , which relates the radiation ultimately leaving surface i to the emissive power originating at surface j.

The nomenclature used within this section is as follows:

- A - area
- B - radiosity
- D - matrix defined by Equation 345
- F - angle factors or view factors
- H - irradiance
- N - number of surfaces
- R - radiation coefficients
- T - temperature
- W - radiant emittance
- δ - Kroneker delta
- ϵ - emissivity
- ψ - matrix defined by Equation 343

Subscripts

- b - black body
- i, j, k - relate to surfaces
- λ - spectral

Consider a system of surfaces or nodes with view factors, F_{ij} relating node i to node j.

For each node, i , the portion of monochromatic radiosity relating to surface k is:

$$B_{\lambda ik} A_i = \delta_{ik} \epsilon_{\lambda i} W_{b\lambda i} A_i + (1 - \epsilon_{\lambda i}) H_{\lambda ik} \quad (339)$$

where,

$W_{b\lambda i}$ is the spectral black body emissive power at temperature, T_i , per unit area.

$H_{\lambda ik}$ is the incident spectral radiation on surface, i , due to source temperature, T_k , and is dependent on the radiosity from all surfaces.

$$H_{\lambda ik} = \sum_{j=1}^N F_{ji} B_{\lambda jk} A_j \quad (340)$$

where: $F_{ij} A_i = F_{ji} A_j$ is the angle factor relating node i to node j .

N = total number of nodes or surfaces.

Substitution of Equation 340 into Equation 339 yields:

$$B_{\lambda ik} A_i = \delta_{ik} \epsilon_{\lambda i} W_{b\lambda i} A_i + (1 - \epsilon_{\lambda i}) \sum_{j=1}^N F_{ij} B_{\lambda jk} A_j \quad (341)$$

or,

$$\sum_{j=1}^N \left(\frac{\delta_{ji}}{1 - \epsilon_{\lambda i}} - F_{ji} \right) A_j B_{\lambda jk} = \frac{\delta_{ik} \epsilon_{\lambda k} W_{b\lambda k} A_k}{(1 - \epsilon_{\lambda i})} \quad (342)$$

Equation 342 represents N sets of N equations to be solved for the B_{λ} 's.

Let:

$$\psi_{ij} = \left[\frac{\delta_{ij}}{1 - \epsilon_{\lambda i}} - F_{ji} \right] A_j \quad (343)$$

and:

$$B_{\lambda jk} = R_{\lambda jk} W_{b\lambda k} \quad (344)$$

Then,

$$\sum_{j=1}^N \psi_{ij} R_{\lambda jk} W_{b\lambda k} = \delta_{ik} \left[\frac{\epsilon_{\lambda k} A_k}{1 - \epsilon_{\lambda k}} \right] W_{b\lambda k} \quad (345)$$

or,

$$\bar{\psi} \cdot \bar{R} = \bar{D} \quad (346)$$

where,

$\bar{\psi}$ is the matrix $[\psi_{ij}]$

\bar{D} is the matrix $\left[\frac{\delta_{ik} \epsilon_{\lambda k} A_k}{(1 - \epsilon_{\lambda k})} \right]$

\bar{R} is the matrix of radiation coefficients $[R_{ij}]$

SIRER solves Equation 346 iteratively for the radiation coefficients.

SIRER also calculates DE, the direct source emissions; RE, the reflected source emissions; and, CE, the cumulated source emissions for each node, each wavelength band, and each aspect angle.

$$DE_k = \int_{\lambda_1}^{\lambda_2} \epsilon_{\lambda k} A_k W_{b\lambda k} d\lambda \quad (347)$$

$$RE_k = \sum_j \int_{\lambda_1}^{\lambda_2} R_{\lambda jk} W_{b\lambda j} A_k d\lambda - DE_k \quad (348)$$

$$CE_k = \sum_k \int_{\lambda_1}^{\lambda_2} R_{\lambda jk} W_{b\lambda k} A_j d\lambda \quad (349)$$

where each band integral is evaluated by subdividing the interval into 10 equally spaced regions and using Simpson's rule.

$$W_{b\lambda k} = \frac{C_1}{\lambda^5} \left(\frac{C_2}{\lambda T_k} - 1 \right) \quad (350)$$

and,

$$C_1 = 76805.4$$

$$C_2 = 25884$$

λ in microns

T in $^{\circ} R$

W in watts/steradian/micron/in.²

SECTION V

PLUME EMISSION/ABSORPTION (PLUMIR)

A. Introduction

The plume IR module calculates the emission/transmission characteristics of the IR-active gaseous constituents in the external flow field (outer plume), in the internal hot gases (inner plume), and in the atmosphere, as seen by an observer. The analysis uses molecular band models to describe the spectral distribution of the average intensity and width of the spectral lines within the bands. These models are derived from quantum theory and then modified to match homogeneous empirical data for a wide range of pressures, temperatures, and wavelengths.

The PLUMIR problem divides into three distinct parts:

- Selection of rays and step sizes to thoroughly span the plume and to account for discontinuities and steep gradient regions in the flow field while optimizing for greatest efficiency.
- Development of a gaseous transmission model that calculates as accurately as feasible and as efficiently as possible. Without careful attention, this model could be used as many as 500 times for each wavelength or 50,000 times for each observer location and normal wavelength band selection of rays, ray step sizes, wavelength step sizes, and calculation points.
- The information from this module is stored on the problem tape for interaction with the airframe, engine, and totalling and lock-on modules. The third section of PLUMIR, therefore, is one of book-keeping.

B. Geometrical Considerations

1. Flow Field Centerline (TRAJCT)

An approximate method is used to determine the curvature of a jet's axis by a lateral flow. It consists of finding the curvature from the condition of the balancing of the force caused by the pressure difference at the forward and back surfaces of the jet by a centrifugal force. The results are used to predict the flow field curvature under the influence of a crosswind.

Let an element with a cross-sectional area, A_n (perpendicular to the jet's axis), and the length in the direction of the jet axis, dl , meet an external flow of fluid with a velocity, U_a , parallel to the x-axis. The density of the fluid in the jet is ρ_j ; the density of the external flow is ρ_a , and the vector of the jet mean velocity is directed tangentially to the jet axis at a local angle, α , to the x-axis. (See Figure 26 and 27).

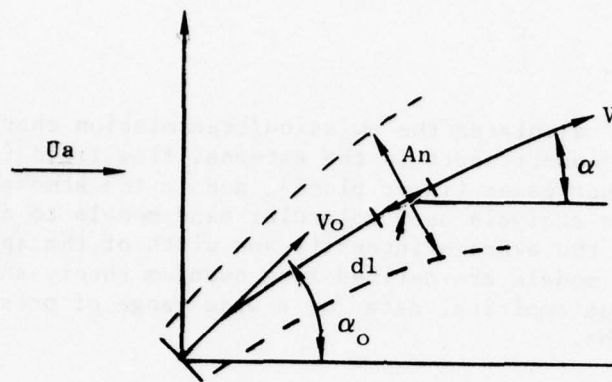


Figure 26. Schematic of Flow in a Crosswind.

$$\frac{dy}{dx} = \tan \alpha$$

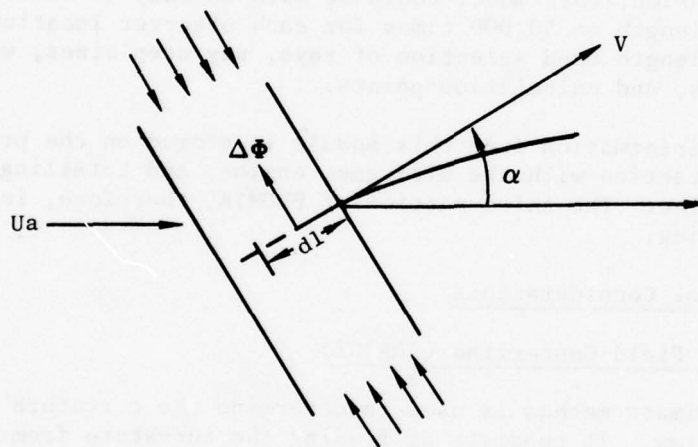


Figure 27. Schematic Indicating Balance of Forces.

$$\frac{dy}{dx} = \tan \alpha \quad (1)$$

Investigation of arrow wings shows that if the axis of the wing forms some angle, α , with the direction of the velocity of the undisturbed flow, U_a , then the aerodynamic force acting on the wing is proportional to the dynamic pressure due to the component of the stream velocity which is normal to the axis of the wing:

$$F = C_n F_n \rho_a \frac{U_a \sin^2 \alpha}{2} \quad (2)$$

where C_n is the force coefficient which depends on the shape of the wing and F_n is a characteristic surface area of the wing.

It is possible to approximate a curved jet by an arrow wing with a curved axis. The jet is divided into elementary parts of length, dl , over which the density and velocity are assumed constant. The characteristic area is taken to be the projection of an element of the jet into the plane parallel to the jet axis and perpendicular to the plane of the jets axis:

$$dF_n = h dl$$

where h is the width of the jet in the z -direction.

Thus, a solid surface is substituted for the jet. The edge of the surface should be curved in the direction of the velocity of external flow as deflected by the jet. From experimental aerodynamics, the coefficient for such a surface element is of the order of one.

$$C_n = 1$$

Thus, the force of the flow pressure on the element of a curved jet is:

$$dF = \frac{C_n \rho_a U_a^2}{2} h \sin^2 \alpha dl \quad (3)$$

The centrifugal force acting on the mass ΔM of the same element on the jet equals:

$$d\phi = \frac{v_j^2}{R} \Delta M = \frac{v_j^2}{R} \rho_j A_n dl \quad (4)$$

where R is the local radius of curvature of the jet axis. According to the assumed condition of equilibrium:

$$dF = -d\phi$$

or,

$$C_n \rho_a U_a^2 h R \sin^2 \alpha = -2 \rho_j V_j^2 A_n \quad (5)$$

$$\text{where } R = \frac{(1 + y'^2)^{1.5}}{y''}$$

and, since $y' = \tan \alpha$:

$$\sin \alpha = \frac{\tan \alpha}{1 + \tan^2 \alpha} = \frac{y'}{(1 + y'^2)^{.5}} \quad (6)$$

If it is now assumed that the component of the total momentum of the jet perpendicular to the direction of the undistributed flow remains constant in the first approximation, then:

$$\rho_j V_j^2 A_n \sin \alpha = \rho_{j_0} V_{j_0}^2 A_{n_0} \sin \alpha_0 = \text{constant, where a subscript } o \text{ applies at the nozzle exit.}$$

Then,

$$R \sin^3 \alpha = \frac{y'^3}{y''} = \frac{-2}{C_n} \frac{A_{n_0}}{h} \frac{\rho_{j_0} V_{j_0}^2}{\rho_a U_a^2} \sin \alpha_0 \quad (7)$$

As indicated by analysis of the experimental data presented in Figure 28, the cross section of a jet under the action of a lateral external flow is deformed, acquiring a horseshoe-shaped contour even at a slight distance ($L/d_0 \approx 1.5$) from the exit. If we assume that the width of the horseshoe-shaped cross section is proportional to x (instead of L) and that the rate of expansion is the same as that of a rectangular jet ($C = 0.22$), we obtain:

$$h = 2.25 d_0 + 0.22x \quad (8)$$

where d_0 defines a circle of area equal to the initial cross-sectional area of the jet.

Then Equation 7 can be written:

$$\frac{y'^3}{y''} = \frac{2}{C_n} \frac{\pi d_0^2}{9d_0 + .88x} \frac{\rho_{j_0} V_{j_0}^2}{\rho_a U_a^2} \sin \alpha \quad (9)$$

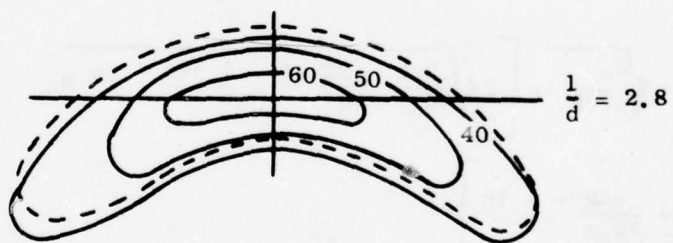
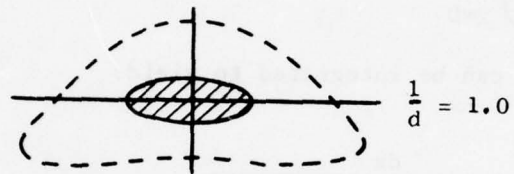
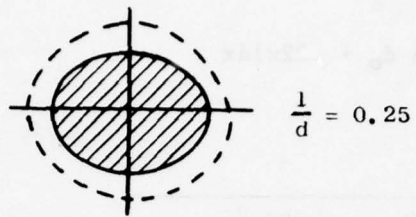


Figure 28. Cross-Sectional Configurations of a Jet in a Lateral Flow at Various Distances from the First Section.

Letting $z = y'$ and $k = \frac{C_n \rho_a U_a^2}{d_o \rho_{j_o} V_j^2} \sin \alpha_o$,

$$\frac{dz}{z} = \frac{-2k}{\pi d_o} (2.25 d_o + .22x) dx$$

or

$$\frac{1}{z} = \frac{dx}{dy} = -\sqrt{\frac{4.5k}{\pi}} x + \frac{.22x^2}{4.5 d_o} + C_1 \quad (10)$$

The integration constant $C_1 = \cot^2 \alpha_o$ is found from the boundary condition

$$\cot \alpha_o = \left(\frac{dx}{dy} \right)_{x=0}$$

Equation (9) then can be integrated to yield:

$$y + C_2 = \int \frac{dx}{\sqrt{\frac{.22kx^2}{\pi d_o} + \frac{4.5kx}{\pi} \cot^2 \alpha_o}}$$

where,

$$y + C_2 = \sqrt{\frac{d_o}{.22k}} \ln \left[2 \sqrt{\frac{.22k}{\pi d_o} \frac{.22kx^2}{\pi d_o} + \frac{4.5kx}{\pi} \cot^2 \alpha_o} + \frac{.44k}{\pi d_o x} + \frac{4.5k}{\pi} \right] \quad (11)$$

@ $y = 0, x = 0$

or,

$$C_2 = \sqrt{\frac{\pi d_o}{.22k}} \ln \left[2 \sqrt{\frac{.22k}{d_o} \cot^2 \alpha_o + \frac{4.5k}{\pi}} \right]$$

Thus,

$$y = \sqrt{\frac{\pi d_o}{.22k}} \ln \left[\frac{\sqrt{\frac{.22k}{\pi d_o} \frac{.22kx^2}{\pi d_o} + \frac{4.5kx}{\pi} \cot^2 \alpha_o + \frac{.44kx}{\pi d_o} + \frac{4.5k}{\pi}}}{\sqrt{\frac{.22k}{\pi d_o} \cot \alpha_o + \frac{4.5k}{\pi}}}\right]$$

or,

$$\frac{y}{d_o} = \sqrt{39a} \ln \left[\frac{10 + \frac{x}{d_o} + \sqrt{\left(\frac{x}{d_o}\right)^2 + 20 \frac{x}{d} + 7a \cot^2 \alpha_o}}{10 + \sqrt{7a} \cot \alpha_o} \right] \quad (12)$$

where,

$$a = \frac{\rho_{j_o} v_{j_o}^2}{C_n \rho_a U_a^2} \sin^2 \alpha_o$$

A comparison of theory and data from Reference 26 is shown in Figure 29.

2. Ray Selection (TRAJCT, ALA)

The plume IR emissions are calculated by selecting a number of rays that emanate from the observer and span the plume. Best accuracy will be obtained either by using a larger number of rays or by a judicious selection of a lesser number of truly representative rays. Because of the large number of calculations involved, it is worthwhile to evaluate the IR for as few rays as feasible while still maintaining the accuracy.

The criteria used for the selection of the rays are:

1. The rays should be more closely spaced in the higher temperature regions near the exhaust exit.
2. Regions internal to the exhaust system should not be lumped with external regions because the characteristics are different.

To solve this problem, the following geometrical assumptions have been made:

1. The coordinate system is selected such that the centerline of the flow field lies in the XY plane.

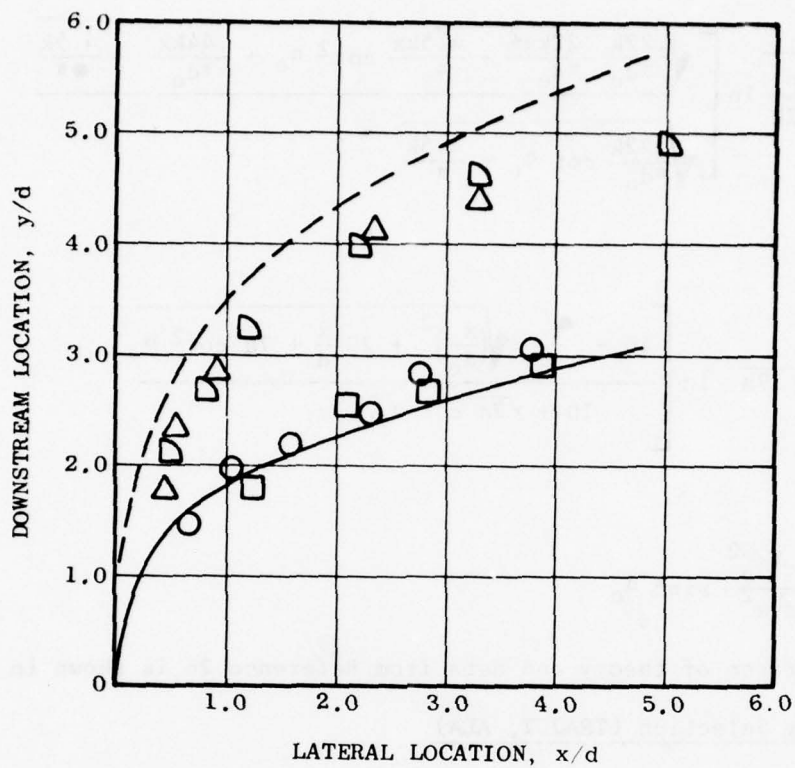


Figure 29. The Axis of a Jet in a Lateral Deflecting Flow.

2. The axis of the exhaust system coincides with the X-axis.
3. The crosswind always turns the flow toward the positive Y axis.
4. The exhaust plane is angled γ degrees to the X-axis.

Five flow field axes are selected as follows:

The first axis is a line in the X-Y plane that passes through the origin and (usually) the final point (PD) of the flow field centerline. If the axis so chosen is within 20 degrees of the observer line of sight through the origin it is rotated to a position 20 degrees from the observer line. This avoids calculation of rays too closely spaced while still ensuring that the rays do pass through the plume.

The remaining 4 axes are chosen to lie parallel to the first but removed from it at distances $+D_1$ and $+D_2$ in a direction normal to the elevation plane to the observer. D_1 is usually $2/3$ the distance from the origin to the exhaust surface and D_2 is twice that distance.

Along each axis, ray intercept points are selected. The calculation rays are lines defined by a ray intercept point and observer location.

The primary intercept points are chosen according to the following algorithm:

$$ZD_i = \frac{R_8}{DXA} \times (R_m)^N \text{ for } N=1, DL \quad (13)$$

where R_m satisfies the relationships:

$$R_m = 1 + \frac{AL}{R_8} (1 - R_m)^{1/DL}$$

AL = length of the Plume

R_8 = Exhaust Exit Radius

DL = approximate number of rays spanning one axis

R_8/DXA = spacing from origin to closest ray intercept point

The portion of the flow field axis associated with each ray is determined by the bisectors of the point being evaluated and its two neighboring points.

3. Additional Ray Intercept Points (Figure 30)

Since the plume internal to the exhaust system has different characteristics than the external plume, the ray point bisectors described above should

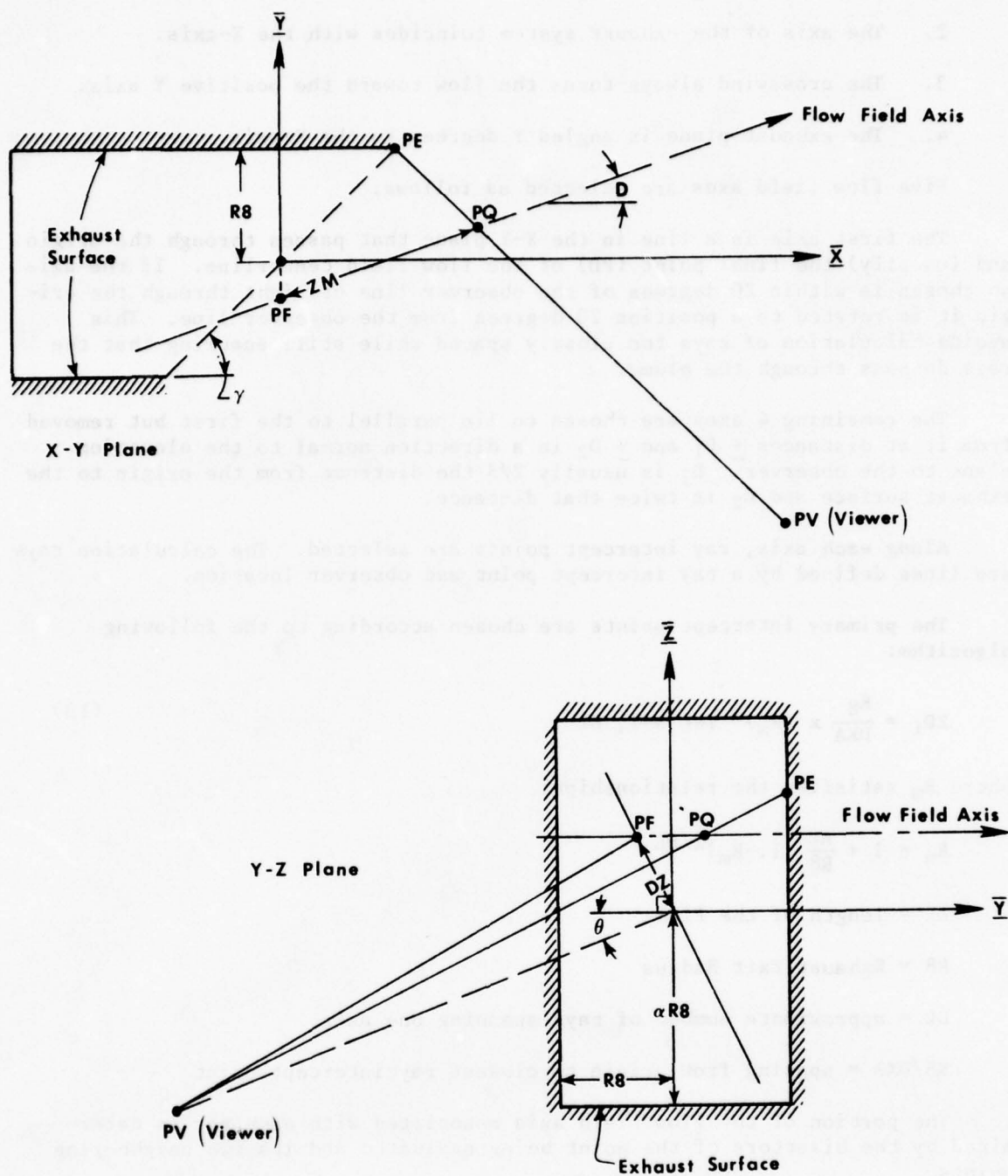


Figure 30. Projections of Exhaust Surfaces to Determine Additional Ray Intercept Points.

coincide with the exhaust exit plane. A similar situation also occurs for when there is an external centerbody surface.

The problem then is to find the rays which intercept both the flow field axis and the exhaust system at the exit plane. For this calculation, the following information is given.

The exhaust exit is rectangular in cross section with a width along the Y axis equal to R8 and along the Z axis, $\alpha R8$.

The flow field axis makes an angle, with the X-axis.

The given information is:

- The observer is located at PV(XV, YV, ZV) where,

$$XV = DS \cos \alpha \cos \theta$$

$$XY = DS \sin \alpha \cos \theta$$

$$ZV = DS \sin \theta$$

(14)

DS = distance to observer

α = aspect angle from tail-on

θ = elevation angle

The exhaust shape is defined by:

$$YE = \pm R8 \text{ for } |ZE| \leq \alpha R$$

$$ZE = \pm \alpha R \text{ for } |YE| \leq R$$

and, $XE = YE / \tan \gamma$

The flowfield axis is given by:

$$Y = X \tan D + DZ \sin \theta \quad (-2YM)$$

(15)

$$Z = DZ \cos \theta$$

YM \neq 0 only for a second plume as described in the subsequent Section V.B.4.

Solution A

Assume:

$$YE = R \quad (R = \pm R8)$$

The equation for the X-Y projection of the viewer ray, PE-OV, is:

$$\frac{Y-YV}{X-XV} = \frac{R-YV}{R/\tan \gamma - XV} = A_0$$

(16)

or,

$$Y = YV + (X-XV) A_0 \quad (17)$$

Combining this with the flow field Equation 15 yields:

$$X \tan D + DZ \sin \theta - 2YM = YX + (X-XV) A_0$$

or,

$$XQ = (YV-XV A_0 + 2YM - DZ \sin \theta) / (\tan D - A_0) \quad (18)$$

The line through PV and XQ extended to the exhaust exit yields:

$$\frac{ZE - ZV}{DZ \cos \theta - ZV} = \frac{R / \tan \gamma - XV}{XQ - XV} \quad (19)$$

or,

$$ZE = ZR + \frac{(DZ \cos D - ZV) \times (R / \tan \gamma - XV) (\tan D - A_0)}{(YV - XV \tan D - DZ \sin \theta + 2YM)} \quad (20)$$

$$\text{If } |ZE| \leq \alpha R8, \text{ then } ZM = XQ / \cos D \quad (21)$$

Solution B

Assume:

$$ZE = \alpha R \quad (R = \pm R8)$$

Then, the equations for the ray, PE-PV, are:

$$\frac{Z-ZV}{X-YV} = \frac{\alpha R - ZV}{XE - XV} \quad (22)$$

$$\frac{Z-ZV}{Y-YV} = \frac{\alpha R - ZV}{XE \tan \gamma - YV}$$

Combining these equations with the flow field Equation 15 yields:

$$XQ - XV = (YE / \tan \gamma - XV) (B_0) \quad (23)$$

$$YQ - YV = (YE / YV) B_0$$

where,

$$B_0 = \frac{ZQ - ZV}{\alpha R - ZV} = \frac{DZ \cos \theta - ZV}{\alpha R - ZV} \quad (24)$$

and,

$$\begin{aligned}
 Y &= X \tan D + DZ \sin \theta - 2YM \\
 &= XV + B_0 (YE/\tan \alpha - XV) \tan D + DZ \sin \theta \\
 &= YV + (YE - YV) B_0
 \end{aligned}
 \tag{25}$$

from which,

$$YE = \frac{1 - B_0 (XV \tan D - YV) + DZ \sin \theta - 2YM}{B_0 (1 - \tan D / \tan \gamma)}
 \tag{26}$$

If $|YE| \leq R$, $ZM = XQ/CD$

where,

$$XQ = XV (1 - B_0) + B_0 YE / \tan \gamma
 \tag{27}$$

4. Plume Through Plume Calculations

Often two identical engines are installed on a given aircraft. These engines usually are located symmetrically about the airframe centerline which coincides, for in-flight conditions, with the crosswind direction. The further plume will never be completely obscured by the near plume, but may contribute as little as 15% of the total radiation.

The analysis of two plumes is performed by creation of an "image" half plane and treating the extension of the viewer ray into the image plane as a reflection back through the forward plume in the "real" plane.

a. Critical Angle

The obscurance is most effective when the viewer is in the horizontal plane. If the viewer lies at an elevation angle too far removed from the horizontal, the obscurance effects can be neglected. The critical angle of elevation for the plume-through-plume calculation to be deactivated is defined by:

$$\theta_{CR} = \tan^{-1} (\alpha R8 / YM \cos \delta)
 \tag{28}$$

where, $\alpha R8$ is the half width of the exhaust system normal to the plane of the flow field and $YM \cos \delta$ is half the distance between the centers of the exhaust exits (see Figure 31).

If the evaluation angle exceeds the critical value, the program will comment on that fact and calculate for one plume only. The final result then must be the sum of the results for the two plumes evaluated separately, one at the specified aspect angle and one at the image angle.

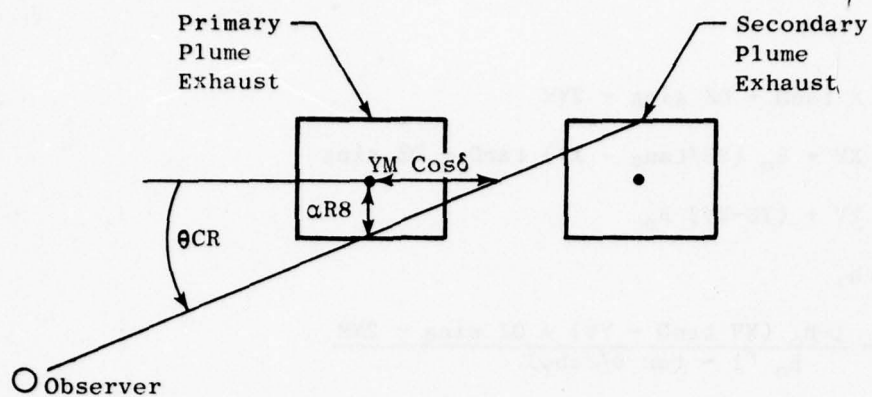


Figure 31. Critical Elevation Angle for Plume-Through-Plume Calculation.

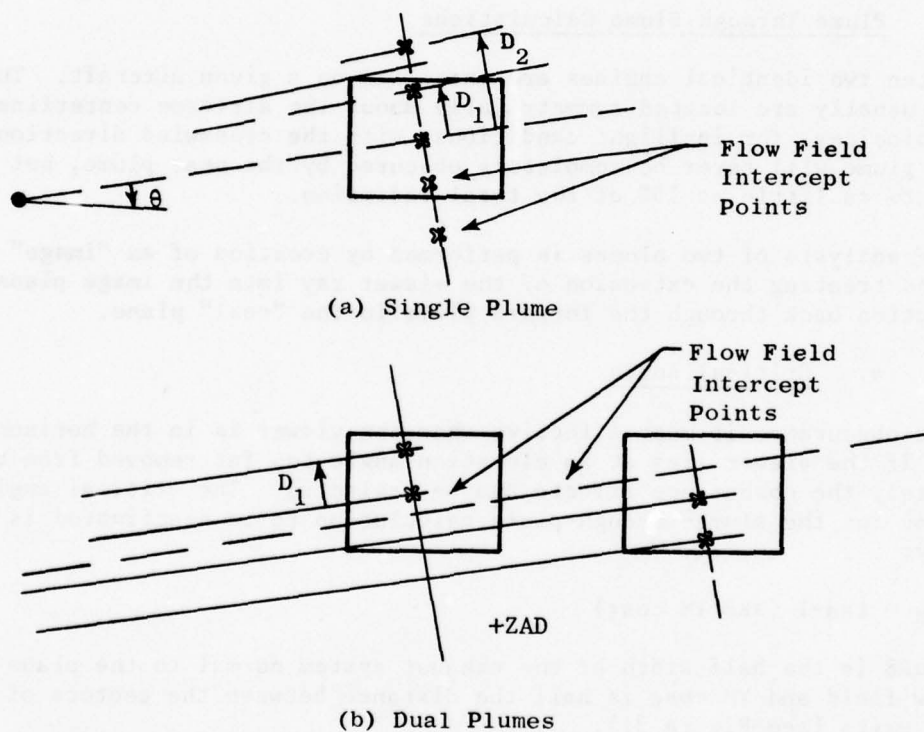


Figure 32. Flow Field Intercept Points for Single and Dual Plumes.

b. Flow Field Axes

For a single plume, the flow field axes were selected to lie in the X-Y plane and in planes removed at distances normal to the evaluation plane to best represent the region associated with each ray as shown in Figure 32a.

For two plumes, the best representations are selected as the planes passing through points

1. bisecting the two systems
2. the origin of both systems
3. points D1 removed from the origin

This selection is determined by the limitation to only five axes which are symmetrically located about the initial axis. This distribution is assumed in the TOTALR module and cannot be modified easily.

The projection of the two exhaust systems in the X-Y plane is shown in Figure 32b. The following information is considered known:

1. The primary exhaust is centered at $X = 0, Y = 0, Z = 0$ with its centerline along the X axis.
2. The secondary exhaust is centered at $X = -2YM \cos\delta \sin\delta;$
 $Y = 2YM \cos\delta \cos\delta$ (29)
 $Z = 2ZAD.$
3. The plane of symmetry is defined in the X-Y plane by:

$$Y = X \tan\delta + YM \quad (30)$$

where δ is the crosswind angle.

4. The flow field axis is defined by:

$$Y = X \tan D + D1 \sin\theta \quad (31)$$

5. The exhaust exit plane is inclined at an angle, γ , to the X-axis.

c. Method of Calculation

The plume/atmosphere of the ray is calculated in the same manner as for a single plume in the real half-plane (see Figure 33). The extension into the image plane at D' is handled as if the observer were located at the image viewer point (Pv') and the intercept was at D". The problem reduces to finding the value of D' (or D") and the point Pv'.

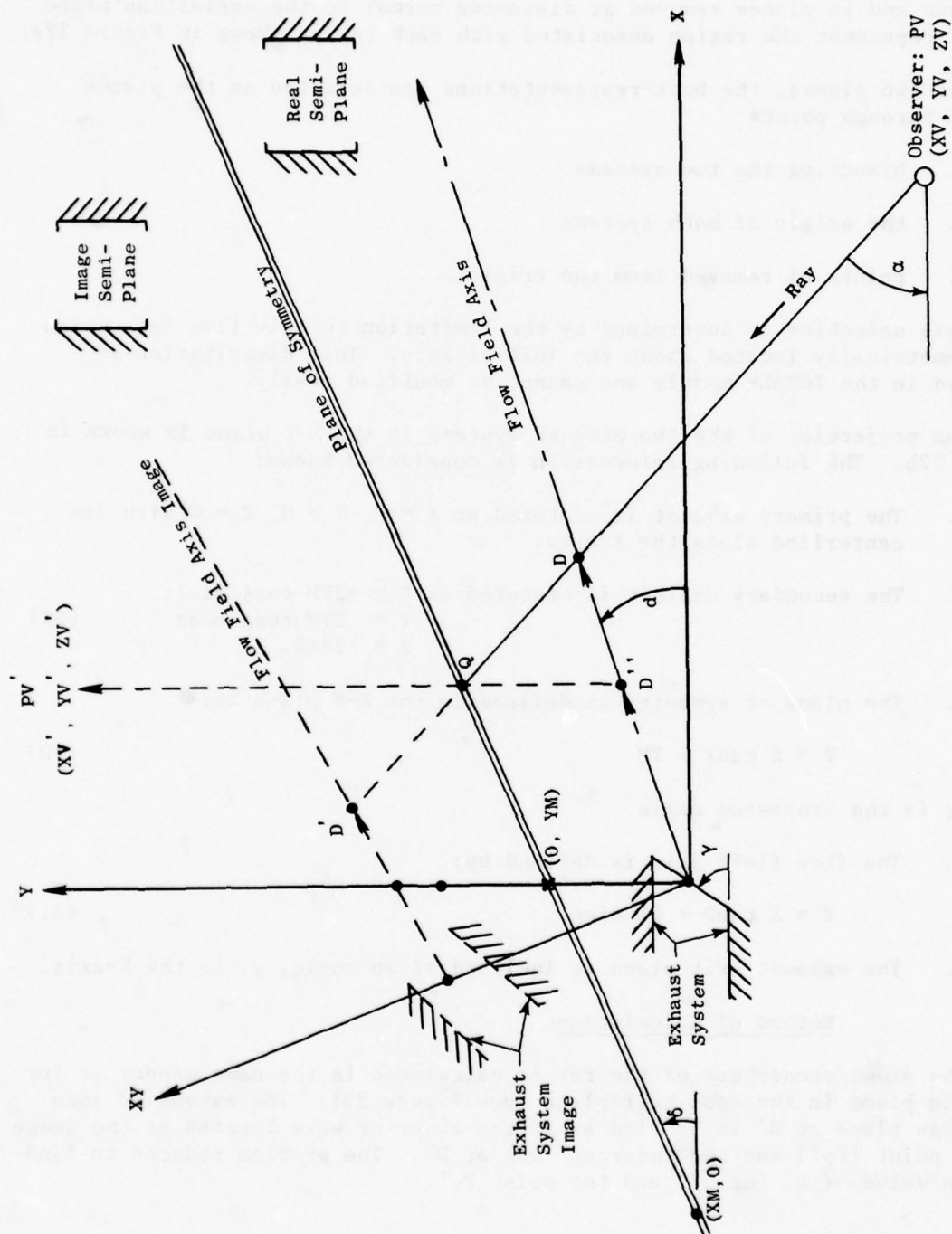


Figure 33. X-Y Projection of Primary Exhaust System and Image Exhaust System About Plane of Symmetry.

To Find an Image Point

The image of any point (X, Y, Z) is found as described in Figure 34.

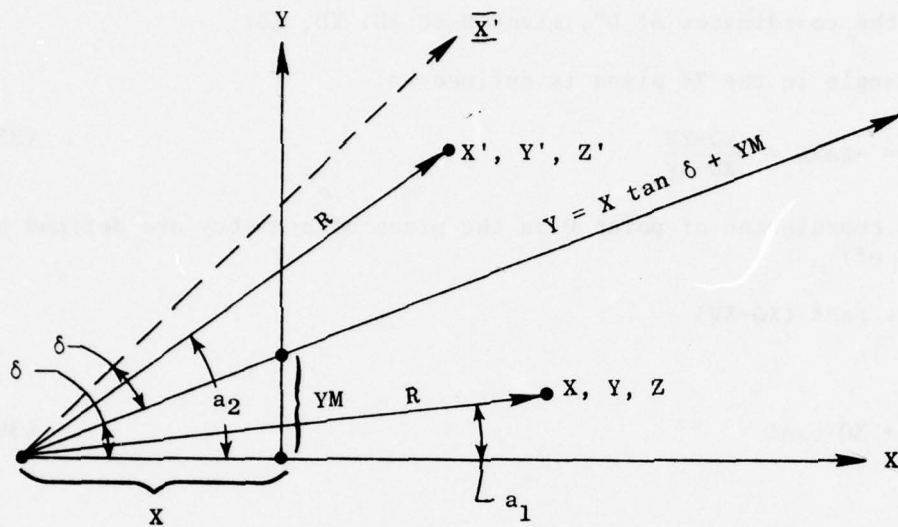


Figure 34. Image of a Single Point.

Let:

$$XM = YM / \tan \delta$$

$$a_1 = \tan^{-1} Y / (X - XM)$$

$$a_2 = 2\delta - a_1$$

$$R = (X - XM) / \sqrt{1 + \tan^2 a_1}$$

(32)

Then:

$$Y' = R \sin a_2$$

$$X' = R \cos a_2$$

$$Z' = Z$$

(33)

and,

$$\text{Image } (X, Y, Z) = (X' Y', Z') \quad (34)$$

To Find Coordinates of D''

To find the coordinates of D'', given D at XD, YD, ZD:

The ray angle in the XY plane is defined as:

$$+ \tan \delta = -\text{TANA} = \frac{YD-YV}{XD-XV} \quad (35)$$

The X, Y coordinates of point Q on the plane of symmetry are defined by the intercept of:

$$YQ = YV + \tan \delta (XQ-XV)$$

and,

$$YQ = YM + XQ \tan \delta \quad (36)$$

Therefore:

$$XQ = \frac{(YV - XV \tan \alpha - YM)}{(\tan \delta - \tan \alpha)} \quad (37)$$

The ray to point Q from the observer image is then defined by:

$$\frac{Y-YV'}{X-XV'} = \frac{YQ-YV'}{XQ-XV'} = A' \quad (38)$$

The intercept of this ray with the flow field axis ($Y=X \tan D + D_i \sin \theta$) is:

$$Y = YV' + A' (X''-XV') = X'' \tan D - D_i \sin \theta \quad (39)$$

or,

$$X'' = \frac{YV'-A'XV'-D_i \sin \theta}{\tan D-A'} \quad (40)$$

$$D'' = X''/CD$$

The value of Z (ZD'') at the point D'' is derivable then from the relationships:

$$\frac{ZQ-ZV}{XQ-XV} = \frac{ZD-ZV}{XD-XV}$$

and,

(41)

$$\frac{ZQ-ZV'}{XQ-XV'} = \frac{ZD''-ZV'}{XD''-XV'}$$

5. Plume-Ray Segments (STARTA)

A schematic projection of the plume in the XY plane is shown in Figure 35. The procedure used in STARTA is to 1) find the intersection of the ray with each of the lines bounding the plume, 2) test each intercept to determine whether they lie on the segment of interest, 3) select the points corresponding to the maximum and minimum values of X, 4) test whether the points exceed the limits in the Z direction and, if so, shorten the ray segment, and 5) test that both points are not internal to the exhaust system.

The ray is defined originally by a distance D along the flow field axis. This value of D is used to calculate a point, D' which defines the intercept of the ray with the Y axis. The ray then is defined by:

$$Y = D' + X \tan A \quad (42)$$

The flow field boundaries themselves are defined by the lines:

$$\begin{aligned} \ell 1: Y &= -X/\tan D + RA \\ \text{where } RA &= -XD/\tan D + YD. \end{aligned} \quad (43)$$

$$\begin{aligned} \ell 2: Y &= -GMA \times RZ \times TN2 - RZ - X \times TN2 \\ \text{where } RZ &\text{ is the width of the exhaust} \\ &\text{in the Y-plane; } TN2 \text{ is the slope of the} \\ &\text{line from PZ2 to PQ, the line from} \\ &\text{PZ2 to PL, or zero, whichever is less.} \end{aligned} \quad (44)$$

$$\ell 3: Y = \pm RZ, \text{ the sides of the exhaust system.} \quad (45)$$

$$\ell 4: X = XE, \text{ the inner boundary of the exhaust system.} \quad (46)$$

$$\begin{aligned} \ell 5: Y &= B + X \tan D \\ \text{where } B &= XD/\tan D + RD - RQ/\sin D \end{aligned} \quad (47)$$

$$\begin{aligned} \ell 6: Y &= X \tan 1 + B \\ \text{where } B &= 1.2 \times RZ \\ TN1 &= \text{Slope of the line from } (0, B) \text{ to PV.} \end{aligned} \quad (48)$$

C. Gaseous Emissions

When examined spectrally, radiation from a jet engine varies from the characteristically smooth distribution of graybody radiation because of the gaseous effects of the plume and atmosphere. Gaseous molecules absorb and emit in specific wavelength bands. From tail-on, the graybody emissions from internal exhaust hot parts predominate over most wavelengths and the gaseous effects are evident only as absorption "dips". From broadside, the broader emission from the hot plume is absorbed partially by the cooler atmosphere leaving two emissions "spikes".

The gaseous emission/absorption effects through the nonhomogeneous paths of plume and atmosphere to an observer depends on the molecular behavior of the gaseous constituents.

The analytical base for the SCORPIO calculation model is derived in the following paragraphs.

The nomenclature used in this section is as follows:

a	$(\gamma_N + \gamma_C)/\gamma_D$
B_e, B_1, B_2	Rotational constants for each gas
c	Speed of light
C	Concentration of IR-active constituent
C	Correction parameter for partially overlapped lines
d	Spectral line spacing
E	Energy level
g	Statistical weight or degeneracy of a state
h	Planck's constant
I	Moment of inertia of molecule
J	Irradiant energy
k	Boltzmann's constant
k	Absorption coefficient
L	Total ray length
n	Vibrational quantum number
n	An integer
N	Number of energy states
N	Blackbody Emissive Power per unit area
NDZ	Measure of size of subareas for calculation
P	Probability of local absorption coefficient
P_E	Effective broadening pressure
r	Radial distance from engine centerline
\bar{S}	Spectral line intensity
\bar{S}	Average spectral line intensity
T	Temperature, ° R
u	$h\nu/kT$
x	Axial distance from nozzle
x	Distance along a ray
X	Optical path length (concentration * density * distance)

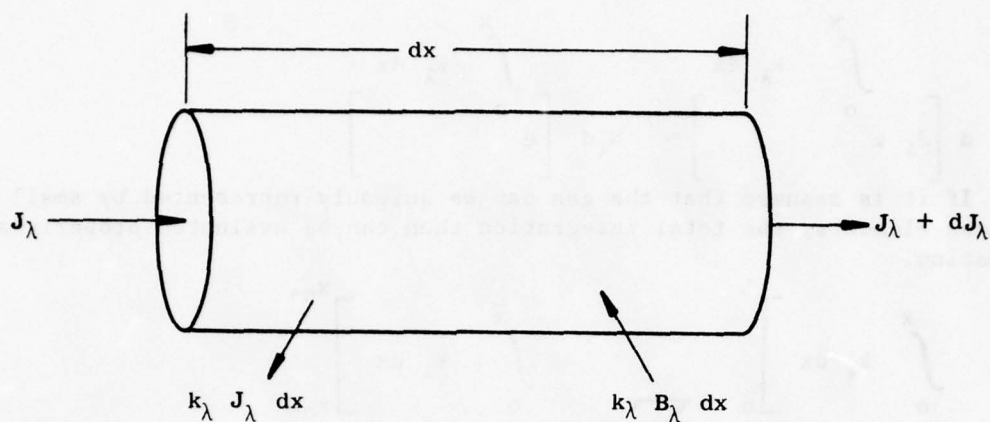
α	Integrated band intensity
β	$hc/4B_e kT$
γ	Spectral line half width
Δ_h	Difference in wave number of band lead and band center
δ	Integral change in vibrational quantum number
δ	Derac Delta function
ϵ	Emissivity
λ	Wavelength, μm
ν	Frequency
ψ	Functions associated with correction parameter, C
ξ	$(\omega - \omega_u)/\nu D$
ρ	Radiation density
ρ	Density
τ	Transmissivity
ω, ω'	Wave number, cm^{-1}
ΔW_{v0}	Value of energy level above the ground state
$\Delta \omega_e$	Difference in wave number of band center resulting from electronic emissions

Subscripts

o	At origin of ray
$1,2,3$	Locations on engine surface
C	Collision broadening
D	Doppler broadening
e	equivalent
i	Principle quantum number
j	Transition
$n, n+, n-$	Ray element
N	Natural line broadening
P, R, Q	Associated with P, R, Q branches respectively
r	Typical value
u	At upper level of transition
ν	Specific frequency
λ	Specific wavelength

1. Transfer Equation

The equation for the radiation along a single ray is formulated as follows. Consider the intensity of radiation for a small element of a ray.



A Small Volume Element of a Ray

J_λ is the intensity of radiation at wavelength, λ , entering the element.

$J_\lambda + dJ_\lambda$ is the intensity of radiation leaving the element.

k_λ is the absorbed in the element per unit distance. The emission and absorption coefficients are equivalent at the same temperature and wavelength.

N_λ is the blackbody emissive power associated with the temperature of the element at wavelength, λ . A radiation balance on the element leads to the transfer equation:

$$dJ_\lambda + k_\lambda J_\lambda dx = k_\lambda N_\lambda dx \quad (49)$$

or,

$$d \left[J_\lambda e^{\int_0^x k_\lambda dx} \right] = N_\lambda d \left[e^{\int_0^x k_\lambda dx} \right]$$

If it is assumed that the gas can be suitably represented by small homogeneous elements, the total integration then can be evaluated properly as a summation.

$$J_\lambda e^{\int_0^L k_\lambda dx} = \sum_n N_{\lambda n} e^{\int_0^{x_{n+}} k_\lambda dx} \left[e^{\int_{x_{n-}}^{x_{n+}} k_\lambda dx} \right]$$

where $N_{\lambda k}$ has been assumed constant from x_{n+} to x_{n-} .

$$J_{\lambda L} e^{\int_0^L k_\lambda dx} - J_{\lambda 0} = \sum_n N_{\lambda n} \left[e^{\int_0^{x_{n+}} k_\lambda dx} - e^{\int_0^{x_{n-}} k_\lambda dx} \right]$$

or,

$$J_{\lambda L} = J_{\lambda 0} e^{-\int_0^L k_\lambda dx} + \sum_n N_{\lambda n} \left[e^{-\int_{x_{n+}}^L k_\lambda dx} - e^{-\int_{x_{n-}}^L k_\lambda dx} \right] \quad (50)$$

$J_{\lambda 0}$ represents the surface emissions as has been discussed already.

The expression:

$$e^{-\int_{x_n}^L k_\lambda dx}$$

represents $\tau(L-x_n)$, the transmissivity over the path from x_n to L . Equation (50) therefore, can, be rewritten as:

$$J_{\lambda L} = J_{\lambda 0} \tau(L) + \sum_n N_{\lambda n} \left[\tau(L - x_{n+}) - \tau(L - x_{n-}) \right] \quad (51)$$

The subsequent analysis and discussion are concerned with the evaluation of these transmissivities.

On a per steradian of source basis, the spectral radiant intensity at the observer becomes:

$$J_{\lambda 0} = \sum_n N_{\lambda n} \Delta \tau_n r_n^2 \quad (52)$$

where $1/r_n^2$ is equal to one steradian.

2. Molecular Behavior of Gases

The spectral distribution of radiation from gaseous molecules is not continuous but is found only at selected wavelengths as discrete spectral lines. The location and intensity of the possible lines for each molecular type can be determined approximately by detailed quantum analysis. Any given molecule can vibrate only in specific states and only in one state at a time. The probability that a photon of energy will be absorbed depends on the probability of its meeting a molecule that is in a proper state to receive the energy of that photon.

The analysis that follows defines the possible line distributions of a single molecule and relates the result to the transmission along a finite nonhomogeneous path.

Absorption or emission by a gas is the result of combined vibrational, rotational, and electronic transitions from one energy level to another.

$$h\nu = hc\omega = \Delta E_{\text{vib}} + \Delta E_{\text{rot}} + \Delta E_{\text{elec}} \quad (53)$$

Quantum mechanics can predict theoretical emission and absorption spectra for gas molecules in terms of fundamental parameters. The predictions are based on solutions to the Schrödinger wave equation of Quantum Theory. For gases other than the simplest diatomic molecules at low temperature levels, the solution can become complicated and impractical. However, complex molecules can be approximated by simple molecules to determine their gross behavior. This is the approach taken in SCORPIO-N. The triatomic molecules CO_2 and H_2O are analyzed as simple harmonic-oscillator, rigid-rotator systems.

An exact derivation of the equations used is beyond the scope of this report. An attempt is made, however, to provide a quantitative physical meaning to the parameters involved. The justification of the approximations and the theory lines in the validity of the results obtained.

To understand the behavior of a molecule, it is instructive to consider the behavior of a simple diatomic harmonic oscillator, rigid rotator as shown in Figure 36. The atoms of the molecule rotate rigidly about its center of mass. If its rotation energy is increased slightly, the size of the orbit is increased a small amount. Since energy is gained or lost by discrete amounts, photons, the changes are not continuous.

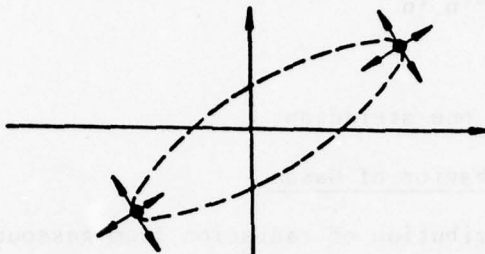


Figure 36. Schematic of a Diatomic Molecule.

The atoms also are free to vibrate along the axis or normal to the axis joining the two atoms. The frequencies at which an atom can vibrate are distinct and specified by molecular constants (mass, radius). There is a fundamental frequency for each diatomic molecule.

A triatomic molecule is more complex because vibration patterns can be composed of various combinations of vibrations of the individual atoms. There are three fundamental frequencies, ν_i , associated with each triatomic molecule. Each molecule can vibrate at any multiple of the fundamental frequencies. These multipliers, the vibration quantum numbers, define the specific state of the vibration of the molecule. Absorption or emission occurs when a molecule changes from one energy state to another.

A change in vibration state is a large change from one energy level to another. The frequency at the center of a spectral emission or absorption band corresponds to the change in vibrational energy. If a vibrational change were never accompanied by a rotational change, the observable emission band would be a single spectral line. In fact, rotational energy changes occur simultaneously with vibrational changes, and the corresponding frequencies are observable as bands of spectra lines. These bands are broader at high temperature where sufficient energy is available to excite higher rotational states.

Individual spectral lines have a finite width dependent on the transport and molecular properties of the gas. The lines may be distorted or may partially or completely overlap as the width-to-spacing ratio varies.

3. Vibrational Energy

Emission (or absorption) by a gas is principally the result of a transition from one vibration state to another and consequent release (or acquisition) or quanta of energy. The permissible energy states of a gas can be specified by the principle quantum numbers (n_1, n_2, n_3). Associated with each quantum number, n_i , there is a fundamental or natural vibration frequency, ν_i , as given in Table 5 for CO_2 and H_2O .

Table 5. Fundamental Frequencies of CO_2 and H_2O .

Quantum Number	CO_2	H_2O
n_i	$\nu_i \text{ (cm}^{-1}\text{)}$	$\nu_i \text{ (cm}^{-1}\text{)}$
1	1388	3651.7
2	667	1595
3	2349	3755.8

The energy W , stored in an active vibrational mode is obtained approximately from:

$$W = hc \sum_{i=1}^3 n_i \nu_i \quad (54)$$

where $u_i = h\nu_i/kT$

The transitions can be noted by:

$$n_i \rightarrow n_i + \delta_{ij} \quad (55)$$

where i refers to the i th quantum number, j to a particular emission band, and the δ 's to the corresponding changes in the quantum numbers.

Since each quantum numbers, n_i , can assume all values from 0 to ∞ , a particular set of δ 's gives rise to an emission band containing a number of transitions. The strongest or most probable transition is that for which the lower level is the lowest possible state. This generally is the ground state for which $n_1 = n_2 = n_3 = 0$. The emission bands and corresponding basic level transitions being considered in SCORPIO-N are listed in Table 6.

The integrated intensity of a specific emission band contains contributions from the basic level transitions and from the "hot" transitions for which the lower level is above the ground state. The integrated intensity of a "hot" transition $\alpha_j(n_i)$ is related to the ground level transition, $\alpha_j(0)$, by:

$$\frac{\alpha_j(n_i)}{\alpha_j(0)} = \sum_{i=1}^3 \left[\frac{(n_i + \delta_{ij})!}{n_i! \delta_{ij}!} e^{-u_i n_i} \right] \quad (56)$$

The total contribution for all transitions is found by summing equation (56) over all n_i .

or:

$$\frac{\alpha_j}{\alpha_j(0)} = \sum_{i=1}^3 \sum_{n_i=0}^{\infty} \left[\frac{(n_i + \delta_{ij})!}{n_i! \delta_{ij}!} \lambda_i e^{-u_i n_i} \right] \quad (57)$$

where $\lambda_i = 1$ for nongenerated transitions and equals the redundancy for degenerate vibrations.

Given the mathematical relationship:

$$(1-X)^{-R} = \sum_{N=0}^{\infty} \frac{(R+N-1)!}{(R-1)! N!} X^N \quad (58)$$

equations (57) for $\lambda_i = 1$ becomes:

$$\frac{\alpha_j}{\alpha_j(0)} = \prod_{i=1}^3 (1 - e^{-u_i})^{-(\delta_{ij}+1)} \quad (59)$$

The integrated intensity of the transition for which the lower level is the ground state can be found from a number of texts as:

Table 6. Transition Band Centers and Integrated Intensity.

Gas	Wave Number at Band Center ω_j (cm^{-1})	Wavelength λ_j (μ)	Transition $n_1 n_2 l n_3$ $n'_1 n'_2 l' n'_3$	Integrated Band Intensity α_j (300K) (cm^{-2}) atm^{-1}
H ₂ O	10273	0.94	121 000	0.17
	8757	1.14	111 000	0.872
	7221	1.38	101 000	22.77
	5335	1.87	011 000	28.1
	3755	2.66	001 000	263.4
	3650	2.74	100 000	27.05
	3151	3.17	020 000	2.23
	1595	6.3	010 000	485.4
	0	20+	000 000	159.9
CO ₂	5109	1.96	20 ⁰ ₁ 00 ⁰ ₀	0.426
	4984	2.01	12 ⁰ ₁ 00 ⁰ ₀	1.01
	4861	2.06	04 ⁰ ₁ 00 ⁰ ₀	0.272
	*3716	2.69	10 ⁰ ₁ 00 ⁰ ₀	42.3
	*3609	2.77	02 ⁰ ₁ 00 ⁰ ₀	28.5
	*2349	4.26	00 ⁰ ₁ 00 ⁰ ₀	2706.
	2094	4.78	12 ² ₁ 01 ¹ ₀	0.02
	2077	4.81	11 ¹ ₀ 00 ⁰ ₀	0.127
	1933	5.17	03 ¹ ₀ 00 ⁰ ₀	0.083
	1064	9.40	00 ⁰ ₁ 02 ⁰ ₀	0.0532
	961	10.41	00 ⁰ ₁ 10 ⁰ ₀	0.0291
	742	13.50	11 ¹ ₀ 02 ² ₀	0.22
	721	13.87	10 ⁰ ₀ 01 ¹ ₀	7.5
	*667	15.0	01 ¹ ₀ 00 ⁰ ₀	240.0

*Isotope Not Included

$$\frac{\alpha_j(0)}{\alpha_{oj}(0)} = \frac{(1 - e^{-u_{ij}})^{\delta_{ij}}}{\prod_i (1 - e^{-u_i})^{g_i}} \frac{T_0}{T} \quad (60)$$

where $\alpha_{oj}(0)$ is the integrated band intensity evaluated at a reference temperature, T_0 ;

g_i if the degeneracy of the i th vibrational mode ($g_i = 1$ implies no degeneracy).

For H_2O : $g_i = 1, 1, 1$

For CO_2 : $g_i = 1, 2, 1$

(61)

Combining equations (59) and (60) for $g_i = 1$ yields:

$$\frac{\alpha_j}{\alpha_{oj}(L)} = \frac{(1 - e^{-hc\omega/kT})}{\prod_{i=1}^3 (1 - e^{-u_i})^{\delta_{ij}}} \frac{T_0}{T} \frac{e^{-\Delta W_{vo}/kT}}{e^{-\Delta W_{vo}/kT_0}} \quad (62)$$

where now:

$\alpha_{oj}(0)$ has been replaced by $\alpha_{oj}(L)e^{\Delta W_{vo}}$ to account for the cases for which the basic transition $\alpha_{oj}(L)$ is itself a "hot" state with an energy $E = hc(\Delta W_{vo})$ above the ground state (see Table 7).

For the liner molecule, CO_2 , allowance must be made for the degeneracy of the second vibration. The degeneracy is introduced through the additional quantum number ℓ , which measures the angular momentum in units of $h/2$. Since ℓ can assume all the values from $-n_2$ to $+n_2$, there is a redundancy $\lambda_2 = 2n_2 + 1$ associated with ν_2 frequency if the slight difference in energy level associated with different ℓ 's is ignored. Therefore, the second summation of equation (57) becomes:

Table 7. Equation and Constants for Energy Levels.

$$\frac{W}{hc} = \sum_{i=1}^3 \left(c_i n_i + \frac{1}{2} \right) + \sum_{i=1}^3 \sum_{j=1}^3 b_{ij} \left(n_i + \frac{1}{2} \right) \left(n_j + \frac{1}{2} \right) + \ell^2 \left[d_0 + \sum_{i=1}^3 d_i \left(n_i + \frac{1}{2} \right) \right] - c_0$$

	H ₂ O	C ¹² O ₂ 16	*C ¹³ O ₂ 16
c ₀	0	1.7	1.7
c ₁	3825.3	1351.2	1351.2
c ₂	1653.9	672.2	652.3
c ₃	3935.6	2396.4	2328.3
b ₁₁	-43.8	-0.3	$\left\{ \begin{array}{l} \text{Approximately} \\ \text{the same} \\ \text{as CO}_2 \end{array} \right\}$
b ₁₂	-20.0	5.7	
b ₁₃	-155.0	-21.9	
b ₂₂	-19.5	1.3	
b ₂₃	-19.8	-11.0	
b ₃₃	-46.8	-12.5	
d ₀		1.3075	
d ₁		0.00058	
d ₂	ℓ = 0	-0.00045	
d ₃		0.00307	

*Note this "isotope" of carbon dioxide contributes sufficiently to be considered near the principle vibrational band centers.

$$\begin{aligned}
& \sum_{n_2=0}^{\infty} \frac{(2n_2 + 1)(n_2 + \delta_{2j})!}{n_2! \delta_{2j}!} e^{-u_2 n_2} \\
&= \sum_{n_2=0}^{\infty} \frac{(n_2 + \delta_{2j})!}{n_2! \delta_{2j}!} e^{-u_2 n_2} + \sum_{n_2=1}^{\infty} \frac{2(n_2 - 1 + \delta_{2j} + 1)}{(n_2 - 1)! (\delta_{2j} + 1)!} (\delta_{2j} + 1) e^{-u_2 n_2} \\
&= (1 - e^{-u_2})^{-\delta_{2j} + 1} + 2(\delta_{2j} + 1) e^{-u_2} (1 - e^{-u_2})^{-\delta_{2j} + 2} \quad (63)
\end{aligned}$$

$$\begin{aligned}
& \text{or,} \quad \sum_2 = \frac{(1 - e^{-u_2}) + 2(\delta_{2j} + 1)e^{-u_2}}{(1 - e^{-u_2})^{\delta_{2j} + g_2}} \\
&= D_2 / (1 - e^{-u_2})^{\delta_{2j} + g_2} \quad (64)
\end{aligned}$$

where $D_2 = 1 + (1 + 2\delta_{2j})e^{-u_2}$ can be thought of as a factor to account for the degeneracy of the second vibrational mode.

4. Partially Overlapped Lines

The parameters controlling the spectral emissivity are the average line intensity, S/d , and the average line half width, γ/d . To account for the line structure, an equivalent emission band can be defined which gives the correct spectral transmissivity in the two limiting cases. For completely overlapped lines, the transmissivity through a homogeneous gas of optical path length, X , is given by:

$$\tau = \exp - \prod_{i=1}^3 \sum_{n_i=0}^{\infty} (S_{ij}/d)^{n_i} \quad (65)$$

Therefore, the equivalent line-to-spacing ratio is:

$$(S/d)_e = \prod_{i=1}^3 \sum_{n_i=0}^{\infty} (S_{ij}/d)^{n_i} \quad (66)$$

For completely nonoverlapped strong lines, the transmissivity is given by:

$$\tau = \exp - \prod_{i=1}^3 \sum_{n_i=0}^{\infty} \left(\pi \frac{S_{ij}}{d} \frac{\gamma_{ij}}{d} x \right)^{1/2} \quad (67)$$

$$\text{or: } \tau = \exp - \left[\pi (S/d)_e (\gamma/d)_e x \right]^{1/2} \quad (68)$$

where γ_{ij} is the half-width of the line.

For simplicity, γ/d is taken to be proportional to γ_0/d , the basic level width-to-spacing parameter or $\gamma/d = \epsilon \gamma_0/d$ where ϵ is independent of temperature.

The equivalent value of γ/d , then is defined as the product of $\epsilon \gamma_0/d$ and $C^2(u_i, \delta)$, a function of temperature to be determined.

Using equations (66) and (68) we have:

$$\left(\frac{\gamma}{d_e} \right) \left(\frac{S}{d_e} \right) = \left(\frac{S}{d_e} \right) \left(\frac{\gamma_0}{d} \right) \prod_{i=1}^3 C^2(u_i, \delta) \quad (69)$$

$$= \prod_{i=1}^3 \left[\sum_{n_i=0}^{\infty} \left(\frac{\gamma_0}{d} \right) \left(\frac{S}{d_e} \right)^{-1/2} \right]^2 \quad (70)$$

Then, since $(S/d)_i$ is proportional to $\alpha(n_i)$:

$$C(u_i, \delta) = \left\{ \sum_{n_i=0}^{\infty} [\alpha(n_i)]^{1/2} \right\}^2 / \sum_{n_i=0}^{\infty} \alpha(n_i)$$

or:

$$C(u_i, \delta) = \left\{ \sum_{n=0}^{\infty} \left[\frac{(n+\delta)! \lambda}{n! \delta!} e^{-un} \right]^{1/2} \right\}^2 / \sum_{n=0}^{\infty} \frac{(n+\delta)! \lambda}{n! \delta!} e^{-nu} \quad (71)$$

The denominator of the above expression has been evaluated previously:

$$\frac{(n + \delta)!}{n! \delta!} \lambda e^{-un} = (1 - e^{-u})^{-(\delta + g)} \left[1 + (1 + 2\delta)e^{-u} \right]^{g-1}$$

The numerator can be evaluated with the aid of the following approximate relationships obtained from Reference 27:

$$\text{Let } \phi(u, \delta) = \sum_{n=0}^{\infty} \left[\frac{(n + \delta)!}{n! \delta!} \exp(-nu) \right]^{1/2} \quad (72)$$

$$\phi(u, 0) = [1 - \exp(-u/2)]^{-1} \quad (73)$$

$$\phi(u, \delta) \approx 1 + \left[\left(\frac{2}{u} \right)^{\delta/2 + 1} \Gamma\left(\frac{\delta}{2} + 1\right) / (\delta!)^{1/2} \right] \quad (74)$$

Then:

$$C^2(u, \delta) = \psi^2(u, \delta) (1 - e^{-u})^{\delta + g} \quad (75)$$

where,

$$\psi^2(u, \delta) = \phi^2(u, \delta) \text{ for } g = 1$$

For the 2nd vibrational mode of $\text{CO}_2(g = 1)$:

$$\text{Let } S = \sum_{n=0}^{\infty} \left[\frac{(2n + 1)(n + \delta)!}{n! \delta!} \exp(-un) \right]^{1/2} \quad (76)$$

Let:

$$F(n) = \left[\frac{(n + \delta)!}{(n - 1)! \delta!} \exp(-un) \right]^{1/2} \quad (77)$$

Then:

$$S = 1 + \sum_{n=1}^{\infty} \left(\frac{2n + 1}{n} \right)^{1/2} F(n) = 1 + \sqrt{3} \sum_{n=1}^{\infty} \left(\frac{2n + 1}{3n} \right)^{1/2} F(n) \quad (78)$$

Since $F(n)$ is falling off exponentially with n , not too much error is introduced by the approximation:

$$S \approx 1 + \sqrt{3} \sum_{n=1}^{\infty} F(n) \quad (79)$$

or,

$$S = 1 + \sqrt{3} \sum_{m=0}^{\infty} \left[\frac{(m + \delta + 1)!}{m! (\delta + 1)!} (\delta + 1) e^{-(m+1)u} \right]^{1/2}$$

$$= 1 + \sqrt{3(\delta + 1)/e^u} \phi(u, \delta + 1) \quad (80)$$

Then:

$$\psi(u, \delta) = 1 + \sqrt{3(\delta + 1)} \phi^2(u, \delta + 1) e^{-u} [1 + (1 \pm 2\delta) e^{-u}] \quad (81)$$

for $u = u_2$ of CO_2

5. Rotational Energy

Use of fundamental quantum mechanical solutions to the Schrödinger equation results in expressions for the energy levels of a rigid rotator as:

$$E(K) = \frac{h^2}{8\pi^2 I} K(K+1) \quad (82)$$

where I is the moment of inertia of the molecule.

The quantum number, K , measures total angular momentum and is $(2K + 1)$ - fold degenerate in the absence of a magnetic field.

Selection rules dictate that changes in rotation can only be of the following kinds:

$K \rightarrow K + 1$	(P - branch)
$K \rightarrow K$	(Q - branch)
$K \rightarrow K - 1$	(R - branch)

The Q - branch will be missing if the molecule has no permanent dipole moment (i.e., for CO_2).

Consider the transitions between two different molecular states

$$E_{R1} hc = B_1 K_1 (K_1 + 1) \quad (83)$$

$$E_{R2} hc = B_2 K_2 (K_2 + 1)$$

$$R - \text{branch: } \omega_R = \frac{E_{R1} - E_{R2}}{hc} = (B_1 + B_2)K + (B_1 - B_2)K^2$$

$$Q - \text{branch: } \omega_R = \frac{E_{R1} - E_{R2}}{hc} = (B_1 + B_2) (K) (K + 1) \quad (84)$$

$$P - \text{branch: } \omega_R = \frac{E_{R1} - E_{R2}}{hc} = - (B_1 + B_2)K + (B_1 - B_2)K^2$$

where K is the larger of the two values K_1, K_2 in each case.

Since the quantities B_1 and B_2 refer to different states, they may differ considerably. If so, the quadratic terms will soon make themselves felt. As K increases, the trend of ω_R in one branch will be to reverse or fold back on itself. At that point in the spectrum, the lines are crowded together forming a "band head." A band of this type can be represented graphically by means of a FORTRAT diagram on which each line is represented by a dot. (See Figure 37). From available data, we can determine the location of the band head, Δ_h as a function of pressure and temperature for each band. Consider P-R branches with an observable band head at $\omega_R = \Delta_h$.

$$\Delta = |\omega_R| = (B_1 + B_2) K - (B_2 - B_1) K^2 \quad (85)$$

$$\Delta = 2 \bar{B} K - \frac{(B_2 - B_1)}{4\bar{B}^2} (2 \bar{B} K)^2$$

where $\bar{B} = (B_1 + B_2)/2$

If $\theta = 2\bar{B}K$, then:

$$\Delta = \theta - c \theta^2 \quad (86)$$

$$@ \Delta = 0 \quad \theta = 0, 1/c$$

$$@ \Delta = \Delta_h \quad \theta = 1/2c \quad \left(\text{since } \frac{d\Delta}{d\theta} = 0 \right)$$

Then,

$$\Delta_h = \frac{1}{2c} - \frac{1}{4c} = \frac{1}{4c} \quad c = 1/(4\Delta_h) \quad (87)$$

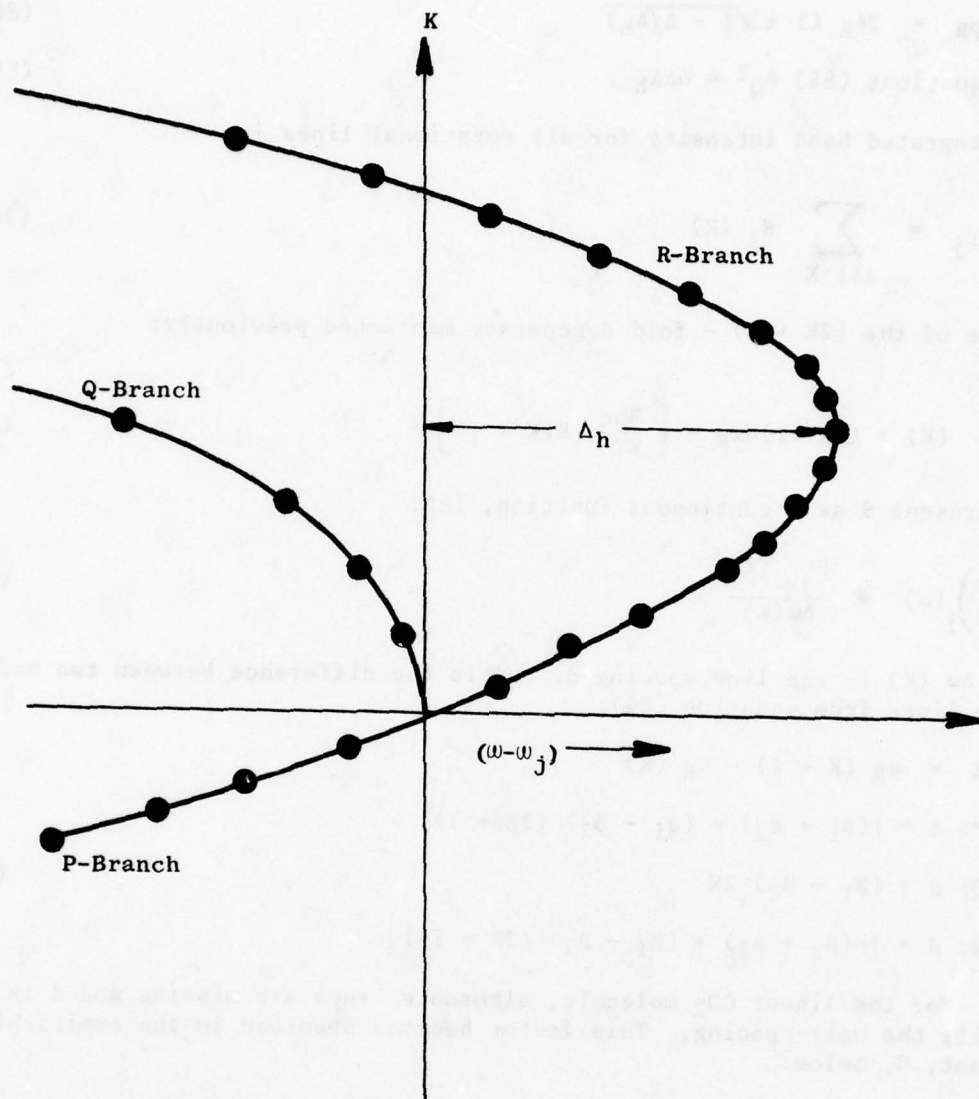


Figure 37. Schematic FORTRAT Diagram.

$$\theta^2 - 4\Delta_h \theta + 4\Delta_h = 0$$

$$\theta_{PR} = 2\Delta_h (1 \pm \sqrt{1 - \Delta/\Delta_h}) \quad (88)$$

$$\text{From Equations (84)} \quad \theta_Q^2 = 4\Delta_h \quad (89)$$

The integrated band intensity for all rotational lines is:

$$a_{Tj} = \sum_{\text{all } K} S_j(K) \quad (90)$$

Because of the $(2K + 1)$ - fold degeneracy mentioned previously:

$$\frac{S}{d}(K) \approx (2K + 1) \exp - \left[\frac{Bhc}{KT} K(K + 1) \right] \quad (91)$$

To represent S as a continuous function, let:

$$\left(\frac{S}{d} \right)_j(\omega) = \frac{S_j(K)}{\Delta\omega(K)} \quad (92)$$

where $\Delta\omega(K)$ is the line spacing d , and is the difference between two neighboring lines from equation (84):

$$d = \omega_R(K + 1) - \omega_R(K)$$

$$P: d = |(B_1 + B_2) + (B_1 - B_2)(2K + 1)|$$

$$Q: d = (B_1 - B_2) 2K \quad (94)$$

$$R: d = |-(B_1 + B_2) + (B_1 - B_2)(2K + 1)|$$

NOTE: For the linear CO_2 molecule, alternate lines are missing and d is actually the half-spacing. This factor becomes absorbed in the empirical constant, C , below.

Expressing $\frac{S}{d} d\omega$ in terms of θ for P, R branches:

$$\omega = \theta - \theta^2/4\Delta_h \quad (95)$$

$$d\omega = (1 - \theta/2\Delta_h)$$

$$d = 2\bar{B} (1 - \theta/2\Delta_h)$$

$$\frac{S}{d} d\omega = \frac{C \theta e^{-\beta\theta^2}}{2\bar{B}} d\theta \quad \text{where} \quad \beta = \frac{hc}{4BkT} \quad (96)$$

and C is a function of temperature and pressure to be determined empirically from the integrated band intensity, α_{PR} .

$$\alpha_{PR} = \int_{\text{all } \omega} \frac{S}{d} d\omega = 2 \left(\frac{C}{2\bar{B}} \int_0^{\infty} \theta e^{-\beta\theta^2} d\theta \right) = 2 \frac{C}{4\bar{B}\beta}$$

or

$$C = 2\bar{B}\beta \alpha_{PR} \quad (97)$$

and

$$\frac{S}{d}(\omega) d\omega = \beta \alpha_{PR} \theta e^{-\beta\theta^2} d\theta \quad \text{or} \quad \frac{S}{d}(\omega) \Delta\omega = \frac{\beta \alpha_{PR} \theta e^{-\beta\theta^2}}{1 - \frac{\theta}{2} \Delta_h} [\Delta\omega] \quad (98)$$

For the Q-branch:

$$\omega = \theta^2/4\Delta_h$$

$$d\omega = (\theta/2\Delta_h) d\theta$$

$$d = \bar{B} \theta/4\Delta_h \quad (99)$$

$$\frac{S}{d} d\omega = \frac{C \theta e^{-\beta\theta^2}}{\bar{B}\theta} (4\Delta_h) \frac{\theta}{2\Delta_h} d\theta \quad (100)$$

$$\int_{\text{all } \omega} \frac{S}{d} d\omega = \int_0^{\infty} \frac{2C\theta e^{-\beta\theta^2}}{\bar{B}} d\theta = \frac{C}{\bar{B}\beta} = \alpha_Q \quad (101)$$

$$C = \bar{B}\beta \alpha_Q \quad (102)$$

and,

$$\frac{S}{d} = 4\beta\Delta_h \alpha_Q e^{-\beta\theta^2} \quad (103)$$

6. Spectral Lines

The assumption of a continuous spectrum, where actually many discrete fine lines exist, gives a result for the average line intensity at a point, which is valid only if the lines do not overlap. In practical application, not only do the lines overlap as functions of wavelength but any particular line may or may not exist at a given point as a finite path is traversed. It is necessary, therefore, to examine the shape of individual lines, the probability of their existence along a path, and the effect of partial overlapping of the lines to determine the actual transmissivity along a finite gas path.

Natural Broadening

A single shift in energy level results in a single emission line. This line is not without breadth, however. The natural width of a spectral line is associated with the Heisenberg Uncertainty Principle, according to which:

$$\Delta E_u \Delta t_u \sim \frac{h}{2\pi} \quad (104)$$

where ΔE_u and Δt_u denote, respectively, the uncertainty in the upper level from which the transition occurs and the uncertainty in the time during which the upper state was occupied.

A similar lack of precision exists in the definition of the lower level. The spectral absorption coefficient for lines broadened only by natural uncertainty is given by:

$$P(|\omega - \omega_j|) d\omega = \frac{S}{\pi} \frac{\gamma_N d\omega}{(\omega - \omega_j)^2 + \gamma_N^2} \quad (105)$$

where γ_N = natural half width

S is a measure of the local absorption

P can be considered the probability shape of the line or spectral absorption coefficient

Collision Broadening

Collision broadening introduces a shift in frequency caused by the collision of molecules during a transition. At very low pressures, the effect is small. At high pressures the natural broadening itself can be neglected.

The two effects can be combined to yield an expression for the spectral absorption coefficient as:

$$k(|\omega - \omega_j|) d\omega = \frac{S}{\pi} \frac{(\gamma_N + \gamma_c) d\omega}{(\omega - \omega_j)^2 + (\gamma_N + \gamma_c)^2}$$

where γ_c , the half-width due to collision broadening, normally varies linearly with pressure and inversely with the square root of temperature:

$$\gamma_c = \gamma_{c_0} \left(\frac{P}{P_0} \right) \sqrt{\frac{T_0}{T}} \left(\frac{P_E}{P} \right) \quad (107)$$

Doppler Broadening

Doppler broadening results from the effect of the motion of the center of mass of a molecule on the emitted frequency during transition. The inclusion of this effect into the relationship for the spectral absorption coefficient yields the following result (Reference 28):

$$k(|\omega - \omega_j|) d\omega = \frac{S}{\pi \omega} \left(\frac{mc^2}{2\pi kT} \right)^{1/2} (\gamma_N + \gamma_c) \times \left\{ \int_{-\infty}^{\infty} \exp \frac{\left[\frac{mc^2(\omega' - \omega_j)^2}{2kT\omega_j^2} \right] d\omega'}{[(\omega - \omega_j) - (\omega' - \omega_j)]^2 + (\gamma_N + \gamma_c)^2} \right\} d\omega \quad (108)$$

$$\text{Letting } \gamma_D = \omega_j \frac{2kT}{mc^2}^{1/2} \quad (109)$$

$$a = (\gamma_N + \gamma_c) / \gamma_D$$

$$z = \frac{\omega - \omega_j}{\gamma_D}$$

$$y = (\omega' - \omega_j) / \gamma_D$$

$$k(|\omega - \omega_u|) d\omega = \frac{S}{\sqrt{\pi} \gamma_D} \frac{a}{\pi} \int_{-\infty}^{\infty} \frac{e^{-y^2}}{[(y - \xi)^2 + a^2]} d\omega \quad (110)$$

Equation (110) (see Section V.C.10) integrates to:

$$k(|\omega - \omega_u|) = \frac{S}{\sqrt{\pi} \gamma} e^{a^2 - \xi^2} \left[\cos 2a\xi - \frac{2}{\sqrt{\pi}} \sum_{n=0}^{\infty} \frac{(\xi^2 + a^2)^{\frac{2n+1}{2}}}{n! (2n+1)} \sin a \right] \quad (111)$$

$$\text{where } \alpha = (2n+1) \tan^{-1} \frac{a}{\xi} - 2a\xi$$

or can be integrated numerically.

7. Effect of Line Structure Along a Path

Because of the uncertainties in the exact states of the emitting and absorbing molecules, the rate of absorption of energy can only be predicted statistically. Mayer and Goody have independently developed a statistical treatment to account for the fine line structure along a finite path. (Reference 28) Assume:

(1) $\Delta\omega = nd =$ a spectral interval with n lines of mean spacing d . (112)

(2) $P(S, \bar{S}_i) = \delta(S - \bar{S}_i)$ = probability that the i th line will have an intensity S_i ; δ is the Dirac delta function. (113)

(3) The absorption coefficient for the i th line is proportional to the line intensity. $k_r = S_r$

The fractional transmission associated with the r th line through an optical path X at the wave number ω is:

$$\tau_r(\omega) = \exp\left(-\int S_r \, dX\right) \quad (114)$$

The probability of having n sets of lines, the r th of which has an intensity S_r in the wave interval $d\omega_1 \dots d\omega_n$ is

$$P = \prod_{r=1}^n P(\bar{S}, S_r) \, dS_r \, d\omega_r \quad (115)$$

The mean fractional transmission at wave number, ω , for all possible lines and all possible arrangements over the interval $\Delta\omega$, therefore is:

$$\bar{\tau}(\omega) = \frac{1}{(\Delta\omega_n)} \int_{\Delta\omega} d\omega_1 \dots d\omega_n \int_0^\infty \prod_{r=1}^n P(S, S_r) e\left[-\int_0^X S_r \, dX\right] dS, \dots dS_r \quad (116)$$

For a homogeneous path, each of the integrals in equation (116) is identical, and the equation can be simplified immediately.

For a nonhomogeneous path, the order of the integrals in equation (116) is immaterial. Therefore, the lines theoretically can be redistributed to form a quasi-homogeneous media for which an equivalent value of $k \bar{S} \, dX$ can be obtained. Assume this has been done and that $k_e \bar{S}_e \, dX$ is the equivalent value.

The probability also can be redefined in terms of the equivalent parameters as:

$$P(S_r, \bar{S}_e) = \delta(S_r - \bar{S}_e) \quad (117)$$

All the integrals of equation (116) are not identical, and the resulting expression for the mean fractional transmissivity is:

$$\bar{\tau}(\omega) = \left[1 - \frac{1}{nd} \int_{\Delta\omega} d\omega \int_0^\infty P(S, \bar{S}_e) \left(1 - e^{-S \bar{S}_e X} \right) dS \right]^n \quad (118)$$

and * as $n \rightarrow \infty$

$$\tau \rightarrow \exp \left\{ -\frac{1}{d} \int_{-\infty}^{\infty} \left[\int_0^{\infty} \left(P(S, \bar{S}_2) (1 - e^{-s_e S e^X}) dS \right) d\omega \right] \right\} \quad (119)$$

Equations 118 and 119 yield:

$$\tau = \exp \left[-\frac{\gamma_D}{d} \int_{-\infty}^{\infty} (1 - e^{-s_e S e^X}) d\xi \right]$$

where: $\xi = (|\omega - \omega_u|)/\gamma_D$

and, $s_e = k(|\omega - \omega_u|)/S$

as defined by equation (110). (120)

Expressing the exponential as a summation, equation (120) can be written:

$$\tau = \exp \left[-\frac{2}{\sqrt{\pi}} \frac{SX}{d} \sum_{n=1}^{\infty} \left(\frac{SX}{\gamma_D \sqrt{\pi}} \right)^{n-1} I(n, a) \right] \quad (121)$$

where:

$$I(n, a) = \frac{1}{n!} \int_0^{\infty} \left[\frac{a}{\pi} \int_{-\infty}^{\infty} \frac{e^{-y^2}}{[(y-\xi)^2 + a^2]} dy \right]^n d\xi \quad (122)$$

* If $\tau = \left(1 - \frac{A}{n} \right)^n$
 $= 1 - A + \dots \frac{(-1)^r A^r n!}{(n-r)! n^r r!}$

For large n :

$$\frac{n!}{(n-r)! n^r} = \frac{n(n-1)(n-2)\dots}{n \cdot n \cdot n \dots} = 1$$

and,

$$\tau \approx 1 - A + \dots \frac{(-1)^r A^r}{r!} = e^{-A}$$

For the special case when $a = 0$, equation (111) becomes:

$$k(|\omega - \omega_u|) = \frac{S}{\sqrt{\pi} \gamma_D} e^{-\xi^2} \quad (123)$$

and equation (121) becomes:

$$\tau = \exp \left[\frac{2}{\sqrt{\pi}} \frac{SX}{d} \sum_{n=1}^{\infty} \left(\frac{-SX}{\gamma_D \sqrt{\pi}} \right)^{n-1} \frac{1}{n!} \int_{-\infty}^{\infty} e^{-n\xi^2} d\xi \right] \quad (124)$$

and,

$$I(n, 0) = \frac{\sqrt{\pi}/2}{n! (n)} \quad (125)$$

The values of $I(n, a)$ have been evaluated for $a \geq 20$. For larger values of a , Doppler broadening can be neglected, and an expression for the transmissivity is given by:

$$\tau = \left[\exp - \frac{SX}{d} \sqrt{1 + \frac{SX}{\pi \gamma_N}} \right] \quad (126)$$

derived as follows:

The probability that the i th line will have an equivalent intensity, \bar{S}_e , is assumed to be a Poisson distribution function:

$$P(S, \bar{S}_e) = \frac{1}{\bar{S}_e} e^{-S/\bar{S}_e} \quad (127)$$

Substitution of this expression into Equation (93) yields

$$\tau = \exp \left[-\frac{1}{d} \int_{-\infty}^{\infty} d\omega \int_0^{\infty} e^{-S/\bar{S}_e} \left(1 - e^{-\bar{S}_e s_e X} \right) d \frac{S}{\bar{S}_e} \right]$$

or

$$\tau = \exp \left(-\frac{1}{d} \int_{-\infty}^{\infty} \frac{\bar{S}_e s_e X}{1 + \bar{S}_e s_e X} d\omega \right) \quad (128)$$

When Doppler broadening is negligible for absorption coefficient, equation (106) can be used and equation (128) becomes:

$$\tau = \exp \left[-\frac{1}{d} \int_{-\infty}^{\infty} \frac{S_e X / \pi}{(1 + v^2)} \frac{dv}{\left(1 + \frac{\bar{S}_e X}{\pi b (1 + v^2)} \right)} \right] \quad (129)$$

where:

$$v = (\omega - \omega_j) / (\gamma_N + \gamma_c)$$

$$b = \gamma_N + \gamma_c$$

Letting, $u = v \sqrt{1 + \bar{S}_e X / \pi b}$

Equation (129) reduces to equation (126)

$$\begin{aligned} \tau &= \exp \left[-\frac{\bar{S}_e X}{d} \left/ \left(1 + \frac{\bar{S}_e X}{\pi b} \right)^{-1/2} \right. \right] \int_{-\infty}^{\infty} \frac{du}{(1 + u^2)} \\ &= \exp \left[-\frac{SX}{d} \left/ \sqrt{1 + \frac{SX}{\pi \gamma_N}} \right. \right] \end{aligned}$$

The Curtis-Godsen approximation, formulated for nonhomogeneous atmospheric paths, states that transmissivity along a nonhomogeneous path can be evaluated for an equivalent homogeneous path with appropriate values for the half width ratio, γ/d , and the line intensity ratio, S/D . Interpreting Curtis-Godsen in a broad sense, the equivalent homogeneous path can be represented by suitable averaged parameters.

In the preceding equations, the equivalent parameters to be evaluated along the nonhomogeneous path must be:

$$\left(\frac{SX}{d} \right)_e = \int_0^{\bar{X}} \left(\frac{S}{d} \right) dX$$

$$\left(\frac{SX}{\gamma_D} \right)_e = \int_0^X \left(\frac{S}{\gamma_D} \right) dX$$

$$\left(\frac{SX}{\gamma_N} \right)_e = \int_0^X \left(\frac{S}{\gamma_N} \right) dX$$

from which,

$$a_e = \left(\frac{S}{\gamma_D} X \right)_e / \left(\frac{S}{\lambda_N} X \right)_e$$

8. Atmospheric Absorption (ATMS)

The high temperature emissions from the gases in the jet engine plume exits over a broader wavelength interval than the lower temperature absorption bands of the atmosphere. The atmospheric path, however, is usually very long and therefore, the absorption of plume emission is almost complete except in the band wings. The radiation detected by a missile falls almost entirely in the wings of the bands.

The amount of radiation transmitted through the atmosphere is highly dependent on the transmissivity of both the emitting and the absorbing media. For this reason, careful attention has been given to the atmospheric absorption as calculated by SCORPIO-N compared with the measured data.

In light of the foregoing analysis, an examination of equation (51) now reveals that the amount of radiation emitted by the jet plume and transmitted through the atmosphere is a function of the transmissivity of the entire non-homogeneous path being considered and cannot be segregated into the transmissivities of the plume and the atmosphere taken separately.

This conclusion is not intuitively obvious but is a direct result of the equations and the fact that the self-attenuation of the plume alters the probability distribution of the lines of radiations being transmitted to the atmosphere and, therefore, alters the rate of absorption by the atmosphere.

9. Derivation of Function γ

For the ν_2 vibration of CO_2 , we consider:

$$\psi(u, \delta) = \sum \frac{(n+1)(n+\delta)!}{n! \delta!} e^{-un/2} = \sum F_n \quad (134)$$

and,

$$F_0 + 2 F_1 + 3 F_2 + \dots \approx F_0 + 2[F_1 + 2 F_2 + 3 F_3 + \dots] \quad (135)$$

(for which the first two terms are accurate and the remainder are only approximate).

Then:

$$\psi(u, \delta) \approx F_0 + 2 \sum_{n=1}^{\infty} \frac{n(n+\delta)}{n! \delta!} e^{-un/2}$$

AD-A078 436

GENERAL ELECTRIC CO CINCINNATI OH AIRCRAFT ENGINE GROUP F/G 17/5
ADVANCED INFRARED SIGNATURE PREDICTION PROGRAM. SPECTRAL CALCUL--ETC(U)
NOV 79 M E WILTON N00140-76-C-1072
R78AEG314 NL

UNCLASSIFIED

3 OF 3

AD
A078 436



END
DATE
FILMED
1-80
DOC

$$\begin{aligned}\psi(u, \delta) &= 1 + 2 \sum_{m=0}^{\infty} \left[\frac{(m+\delta+1)!}{m! (\delta+1)!} \right]^{1/2} \sqrt{\delta+1} e^{-um/2} e^{-u/2} \\ &= 1 + [2(\delta+1)e^{-u/2}] \phi(u, \delta+1) \quad (\text{for } g_i = 2)\end{aligned} \quad (136)$$

$$\frac{\gamma}{d} e_j = \frac{\gamma_j}{d} \prod_{i=1,3} \psi^2(u_i, \delta_{ij}) (1 - e^{-u_i})^{\delta_{ij} + g_i} \quad (137)$$

where

$$\psi(u_i, \delta) = \phi(u_i, \delta) \quad \text{for } g_i = 1 \quad (138)$$

10. Evaluation of Lines with Combined Doppler, Natural, and Collision Broadening

The expression for the line shape, P , is given from equation 110 by:

$$\frac{P}{P'} = \frac{a}{\pi} \int_{-\infty}^{\infty} \frac{e^{-y^2} dy}{(y-\xi)^2 + a^2} \quad (139)$$

where

$$a = (\gamma_N + \gamma_c) / \gamma_D$$

$$\xi = (\omega - \omega_j) / \gamma_D$$

$$y = (\omega' - \omega_j) / \gamma_D$$

$$P' = S / (\sqrt{\pi} \gamma_D)$$

In terms of partial fractions, equation (139) becomes:

$$\frac{P}{P'} = \frac{i}{2\pi} \int_{-\infty}^{\infty} \left[\frac{e^{-y^2}}{(y - \xi + ia)} - \frac{e^{-y^2}}{(y - \xi - ia)} \right] dy = \frac{1}{2\pi} [I(1,0) - I(-1,0)] \quad (140)$$

where,

$$I(m, b) = \frac{e^{-y^2 + b(y - \xi + ima)} dy}{(y - \xi + ima)} \quad (141)$$

Now:

$$\begin{aligned} \frac{\partial I(m, b)}{\partial b} &= \int_{-\infty}^{\infty} e^{-\left(y - \frac{b}{2}\right)^2} dy \left[e^{\frac{b^2}{4} - b(\xi - ima)} \right] \\ &= \sqrt{\pi} e^{\frac{b}{2} - \xi + ima} e^{-\xi - ima} \end{aligned} \quad (142)$$

Let:

$$u = \frac{b}{2} - \xi + ima$$

$$I(m, 0) = 2\sqrt{\pi} e^{-(\xi - ima)^2} \int_{-\xi + ima}^{u_0} e^{u^2} du \quad (143)$$

$$\int e^{u^2} du = \sum_n \frac{(u^2)^n}{n!} du = \sum_n \frac{u^{2n+1}}{n! (2n+1)}$$

and

$$I(m, 0) = 2\sqrt{\pi} e^{-(\xi - ima)^2} \left[c_{m0} - \sum \frac{(-\xi + ima)^{2n+1}}{(2n+1)n!} \right] \quad (144)$$

but:

$$-\xi + ima = (\xi^2 + a^2)^{1/2} e^{(\pi - m\theta)i}$$

$$\text{where } \theta = \tan^{-1} a/\xi$$

Therefore:

$$\frac{p}{p'} = \frac{i}{\sqrt{\pi}} e^{a^2 - \xi^2} e^{2a\xi i} \left\{ c_+ - \sum \left[\frac{(\xi^2 + a^2)^{\frac{2n+1}{2}}}{n! (2n+1)} e^{i(2n+1)(\pi - \theta)} \right] \right\}$$

$$-e^{-2a\xi i} c_- - \sum \frac{(\xi^2 + a^2)^{\frac{2n+1}{2}}}{n! (2n+1)} e^{i(2n+1)(\pi+\theta)} \quad (145)$$

when $a = 0$:

$$\frac{P}{P'} = e^{-\xi^2} \quad (146)$$

or

$$\frac{i}{\sqrt{\pi}} e^{-\xi^2} (c_+ - c_-) = e^{-\xi^2} \quad (147)$$

and,

$$\frac{P}{P'} = e^{a^2 - \xi^2} \left[\cos 2a\xi - \frac{2}{\sqrt{\pi}} \sum_{n=0}^{\infty} \frac{(\xi^2 + a^2)^{\frac{2n+1}{2}}}{n! (2n+1)} \sin \alpha \right] \quad (148)$$

where,

$$a = (2n+1) \tan^{-1} \frac{a}{\xi} - 2a\xi$$

Equation (148) is valuable for evaluating P/P' for small values of a . Equation (139) can be integrated numerically for large values of a .

Using Simpson's Rule:

$$\frac{P}{P'} = \frac{a}{\pi} \sum_{n=1}^{\infty} \frac{C_n e^{y_n^2}}{(y_n - \xi)^2 + a^2} \frac{\Delta y}{3} \quad (149)$$

where,

$$y_n = n\Delta y$$

$$C_0 = 1$$

$$C_n = 4 \text{ (n, odd)}$$

$$C_n = 2 \text{ (n, even)}$$

Let $s = P/P'$.

Along a path, X,

$$\ln \tau = -\frac{1}{d} \int_{-\infty}^{\infty} \left(1 - e^{\frac{SsX}{\gamma_D \sqrt{\pi}}} \right) d\omega' \quad (150)$$

$$\begin{aligned} \text{or } \ln \tau &= \frac{2\gamma_D}{d} \int_{-\infty}^{\infty} \sum_{n=1}^{\infty} \left(\frac{-SsX}{\gamma_D \sqrt{\pi}} \right)^n \frac{1}{n!} d\xi \\ &= -\frac{2}{\sqrt{\pi}} \frac{SX}{d} \sum_{n=1}^{\infty} (-A)^{n-1} I(n, a) \end{aligned} \quad (151)$$

where

$$A = SX/(\sqrt{\pi} \gamma_D)$$

$$I(n, a) = \frac{1}{n!} \int_0^{\infty} s^n d\xi \quad (152)$$

For large values of SX:

$$\ln \tau = \frac{\gamma_D}{d} \int_{-\infty}^{\infty} \left(1 - e^{-SsX} \right) d\xi \quad (153)$$

Since s decreases rapidly with ξ , the value of $e^{-SsX} \approx 1$ for $SsX < < 1$.

For large values of A , the summation of equation (148) will not converge. In this case, consider the function:

$$F(\xi) = e^{-SsX}$$

where s decreases as ξ increases.

For small values SsX , $F(\xi) \approx 1$

For large values of SsX , $F(\xi) \approx 0$

For large values of SX , $F(\xi)$ approaches at step function ξ of the form.

$$F(\xi) = 1 \text{ for } SsX < 1$$

$$F(\xi) = 0 \text{ for } SsX > 1$$

From equation (150):

$$\ln \tau = \frac{\gamma_D}{d} \int_{-\infty}^{\infty} \left(1 - e^{\frac{-SsX}{\gamma_D \sqrt{\pi}}} \right) du \approx -2 \frac{\gamma_D}{d} \xi_0 \quad (154)$$

where

$$\frac{SX}{\gamma_D \sqrt{\pi}} S(\xi_0) = 1$$

ξ_0 can be evaluated for the extreme values of a .

11. Summary of Gaseous Emission Theory

An expression for transmissivity in the infrared has been derived from fundamental relationships which includes the effects of:

- (1) nonhomogeneity
- (2) line structure along a path
- (3) partial overlapping of lines
- (4) line-broadening effects
- (5) natural, collision, and Doppler broadening.

The relationships derived from the theory and used in the subroutine are listed below:

- (1) The transfer equation along a ray,

$$J_\lambda = J_{\lambda_0} \tau(L) + \sum_n N_{\lambda_n} [\tau(L - x_{n+}) - \tau(L - x_{n-})]$$

- (2) Planck's Black Body Law,

$$N_{\lambda_n} = 2\pi hc^2 / \lambda^5 (e^{hc/\lambda T_n} - 1)$$

- (3) Mean Transmissivity

$$\tau = \tau \left[\left(\frac{SX}{d} \right)_e, \left(\frac{SX}{\gamma_N} \right)_e, \left(\frac{SX}{\gamma_D} \right)_e \right]$$

- (4) Optical Path Length,

$$\bar{X} = \int c \rho dX = \text{integral of the density-concentration product along a path.}$$

- (5) Equivalent Line Parameters for a nonhomogeneous path:

$$\left(\frac{SX}{d} \right)_e, \left(\frac{SX}{\gamma_N} \right)_e, \left(\frac{SX}{\gamma_D} \right)_e, a_e$$

are evaluated by equations (130) through (133)

- (6) Half width to spacing adjustment for partially overlapped lines:

$$(\gamma/d)_e = \epsilon \frac{\gamma_o}{d} \prod_{i=1}^3 C^2(u_i, \delta)$$

where,

$C(u, \delta)$ is defined by equation (71)

- (7) The local line-intensity-to-spacing ratio

$$\frac{S}{d} = \frac{\beta \alpha_{PR} \theta e^{-\beta \theta^2}}{(1 - \theta/2\Delta_h)} \quad (P, R \text{ branches})$$

$$\frac{S}{d} = 4\beta \Delta_h \alpha_Q e^{-\beta \theta^2} \quad (Q \text{ Branch})$$

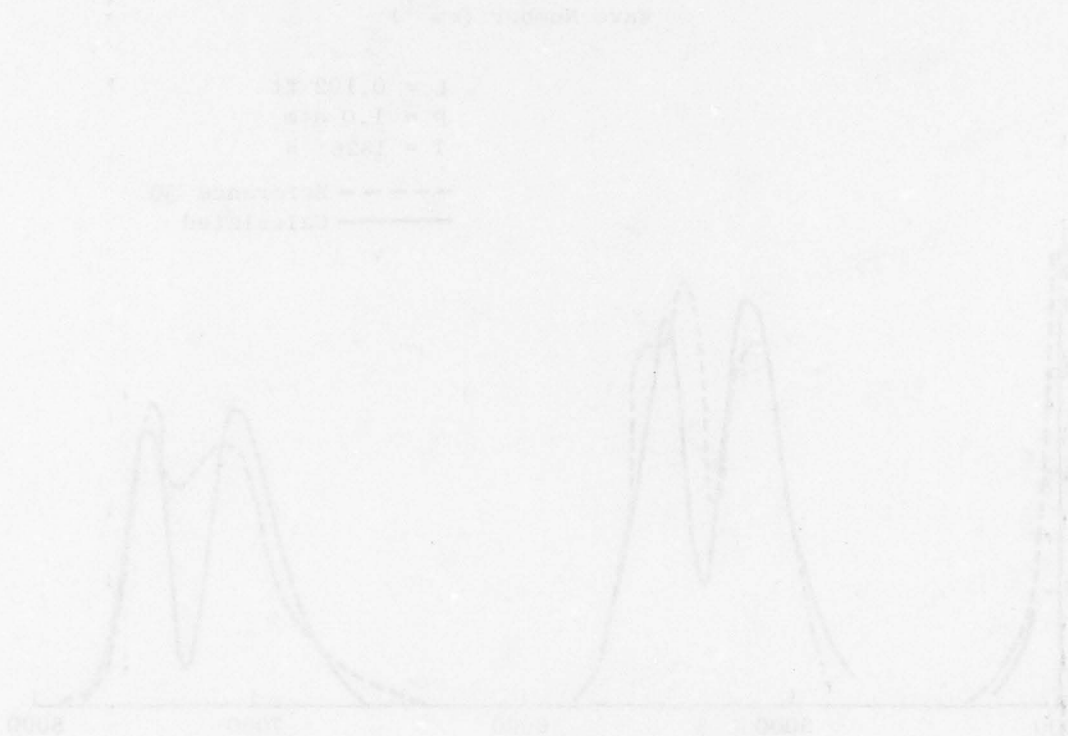
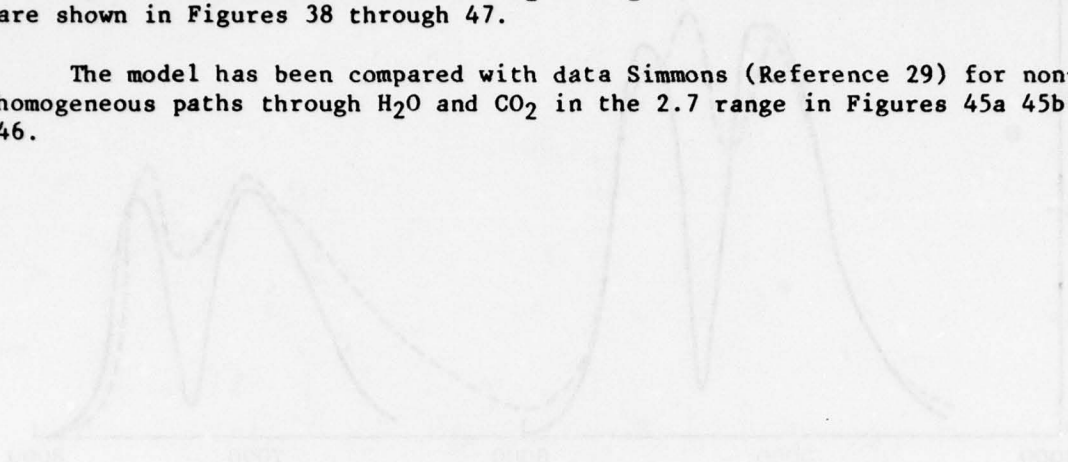
where $\theta_{PR} = 2 \Delta_h (1 \pm \sqrt{1 - \Delta/\Delta_h})$

$$\theta_Q = 2\sqrt{\Delta\Delta_h}$$

Certain of the parameters in the preceding relationships are not currently known. Δ_h , β_1 , β_2 , and γ/d involved in equations (98) and (103) may

be functions of temperature, pressure, or band center and are determined by fitting the theoretical values of CO_2 and H_2O with selected measured values are shown in Figures 38 through 47.

The model has been compared with data Simmons (Reference 29) for non-homogeneous paths through H_2O and CO_2 in the 2.7 range in Figures 45a 45b and 46.



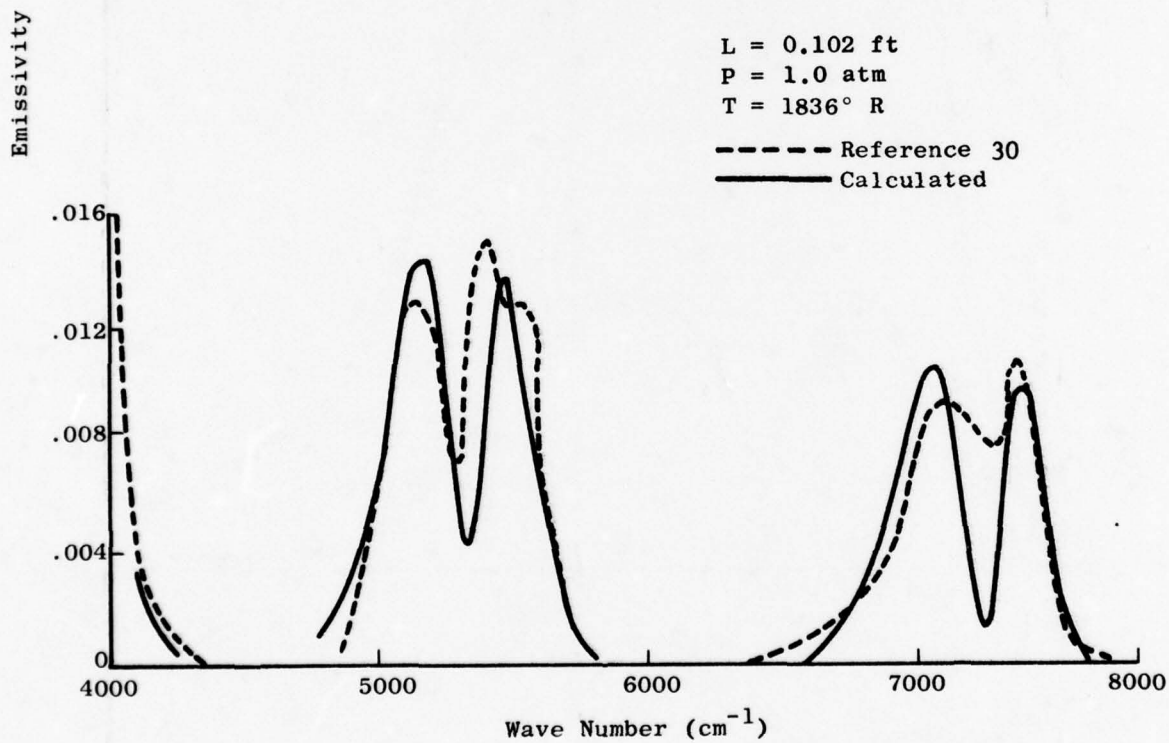
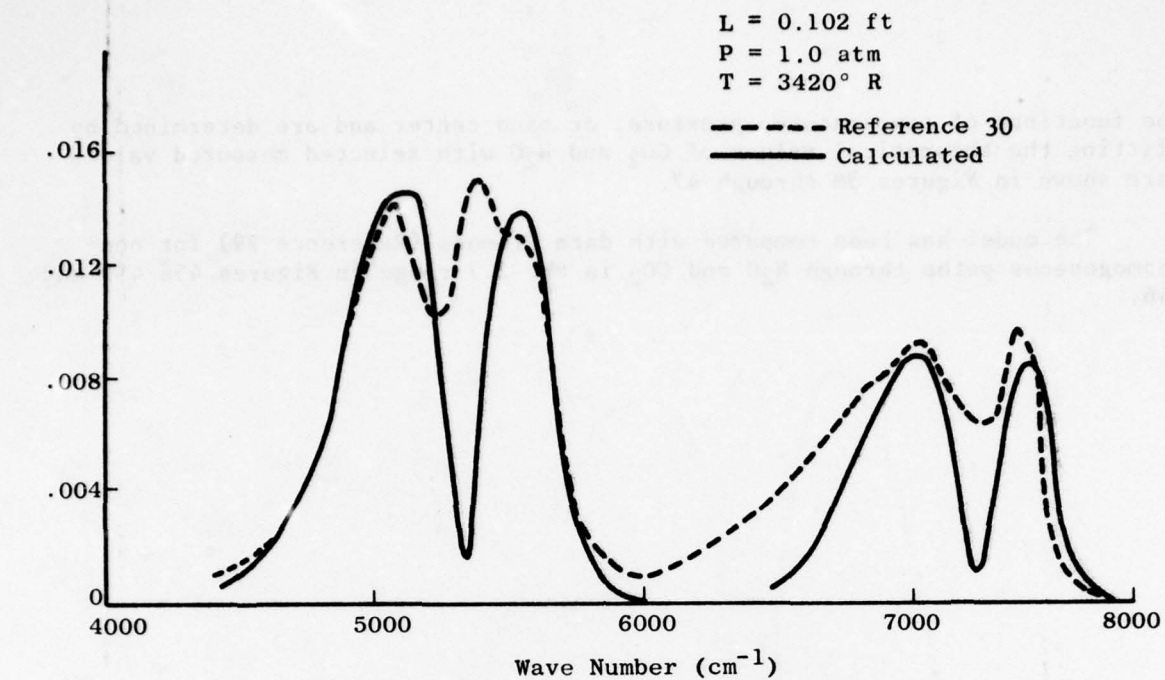


Figure 38. Emissivity of H_2O , 1.38 and 1.8 μ Bands.

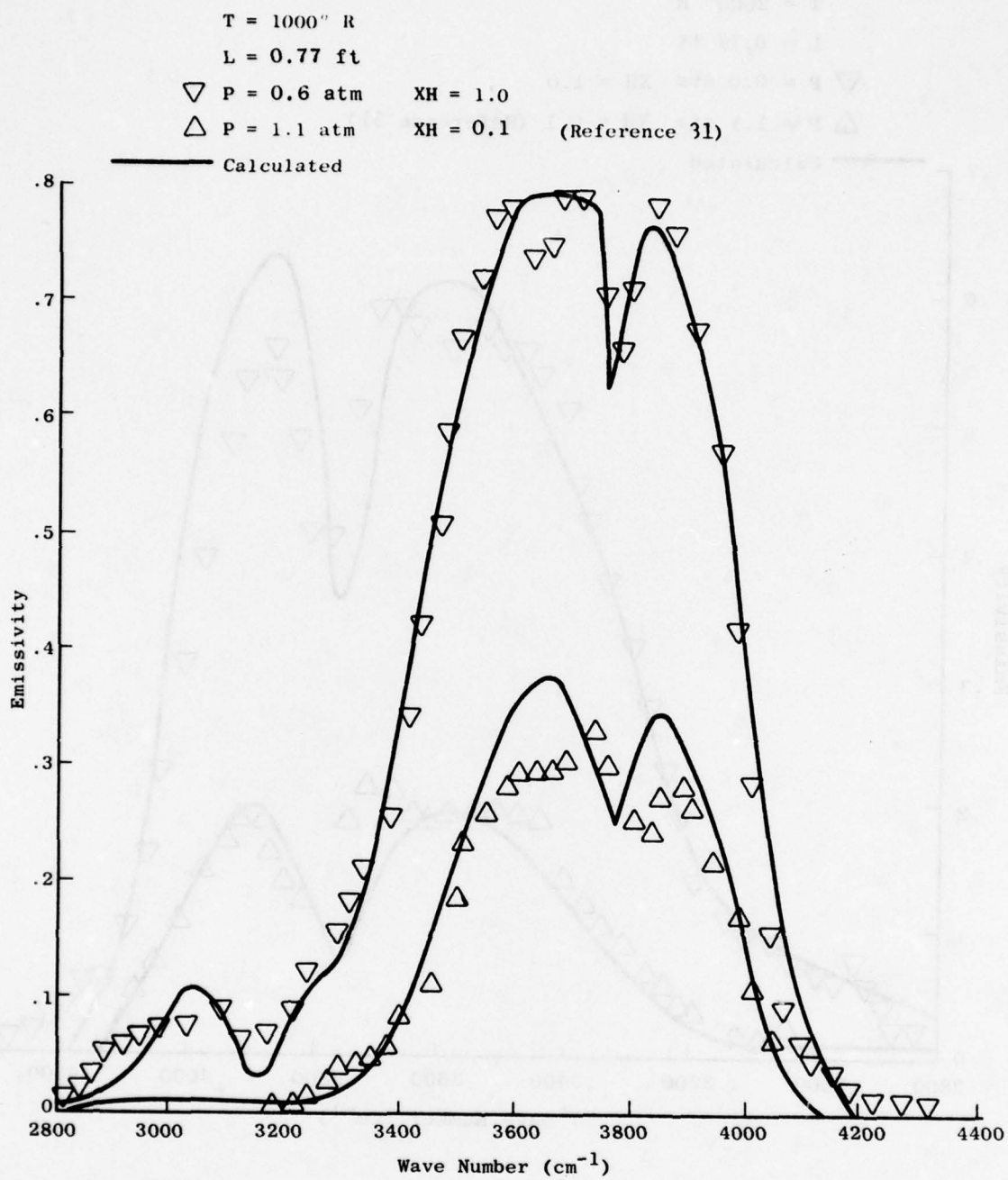


Figure 39. Emissivity of H_2O , 2.7μ Band for $T = 1000^\circ \text{ R}$.

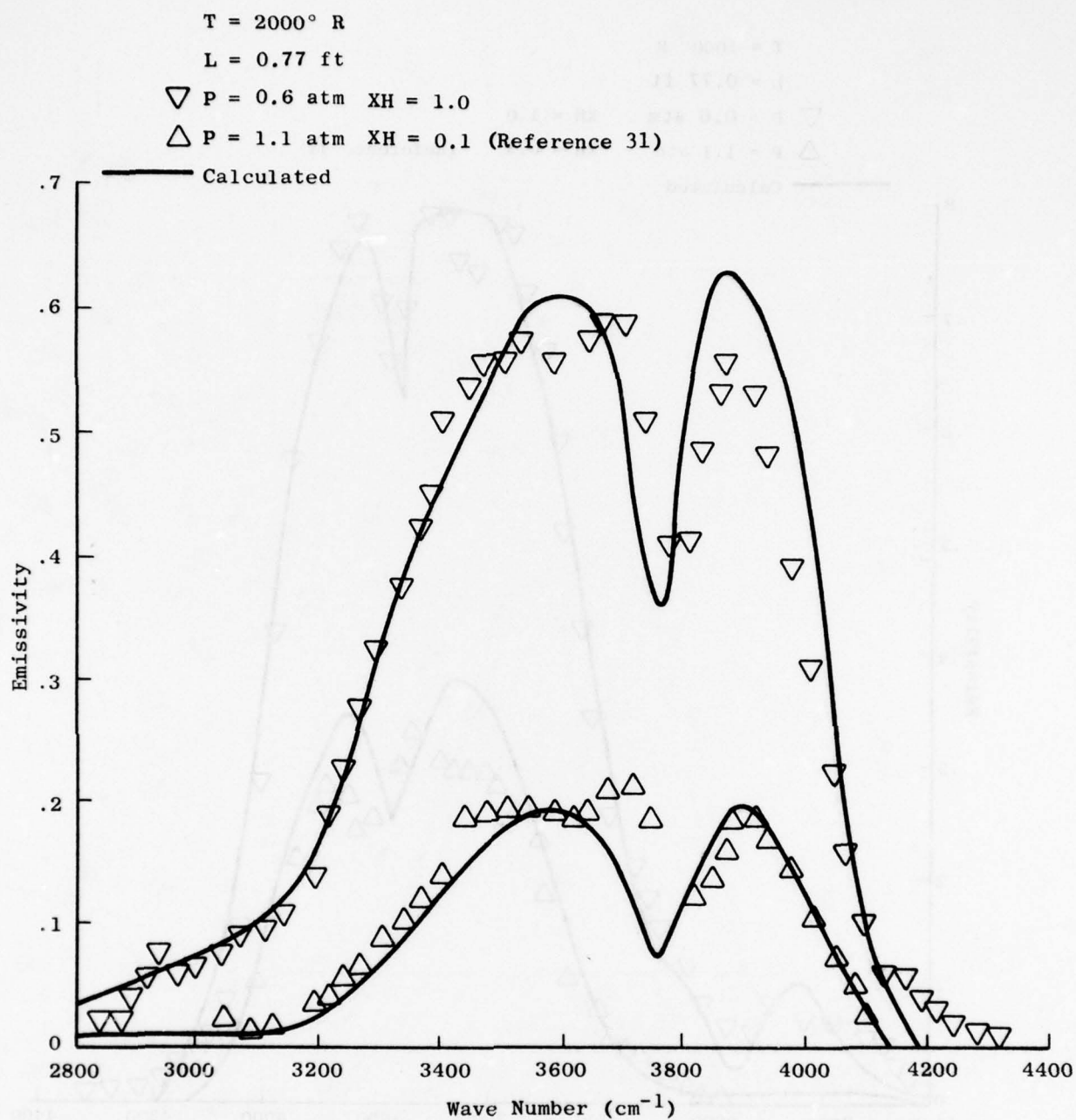


Figure 40. Emissivity of H_2O , 2.7μ Band for $T = 2000^{\circ} \text{ R}$.

$T = 2160^{\circ} \text{ R}$

$L = 7.75 \text{ cm}$

$P = 1.0 \text{ atm}$ 100% CO_2

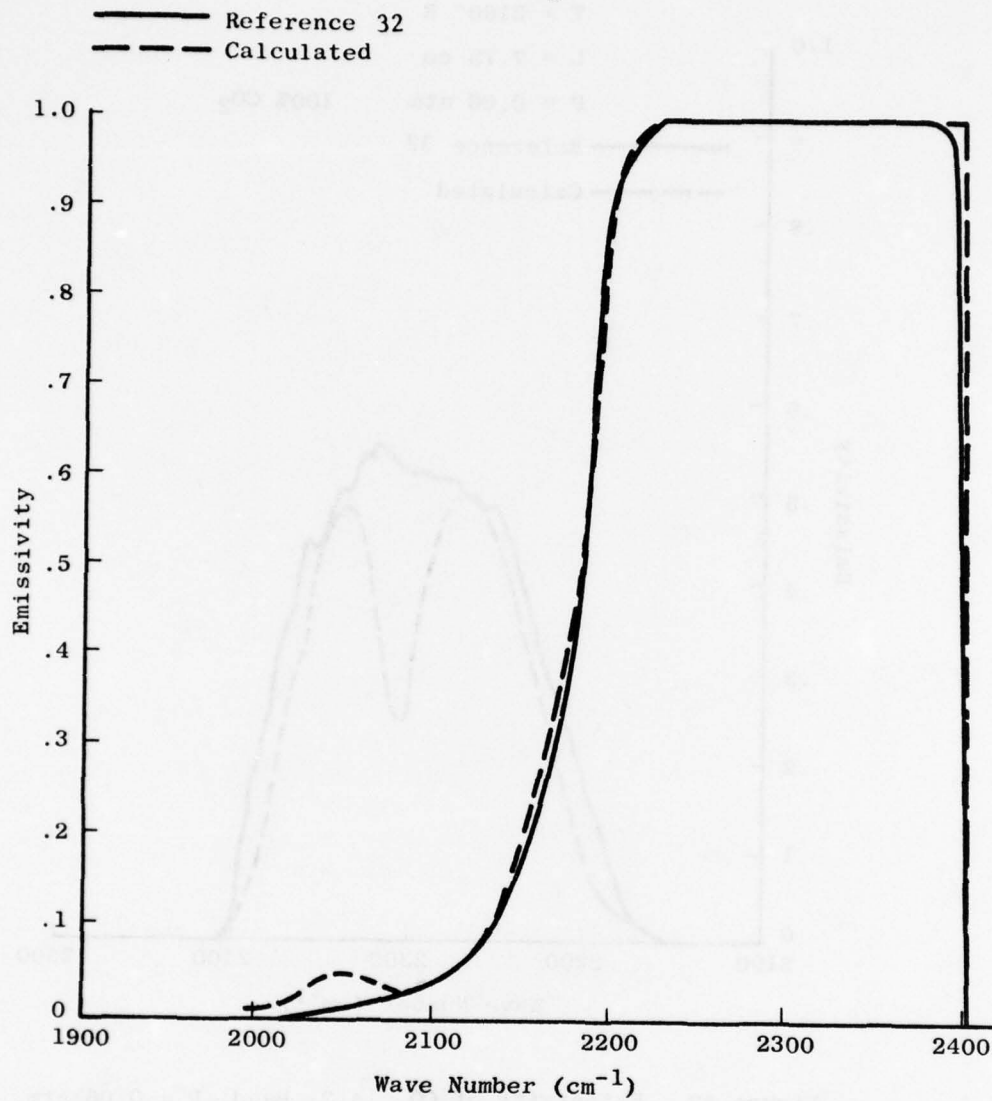


Figure 41. Emissivity of CO_2 , 4.3μ Band, $P = 1.0 \text{ Atms.}$

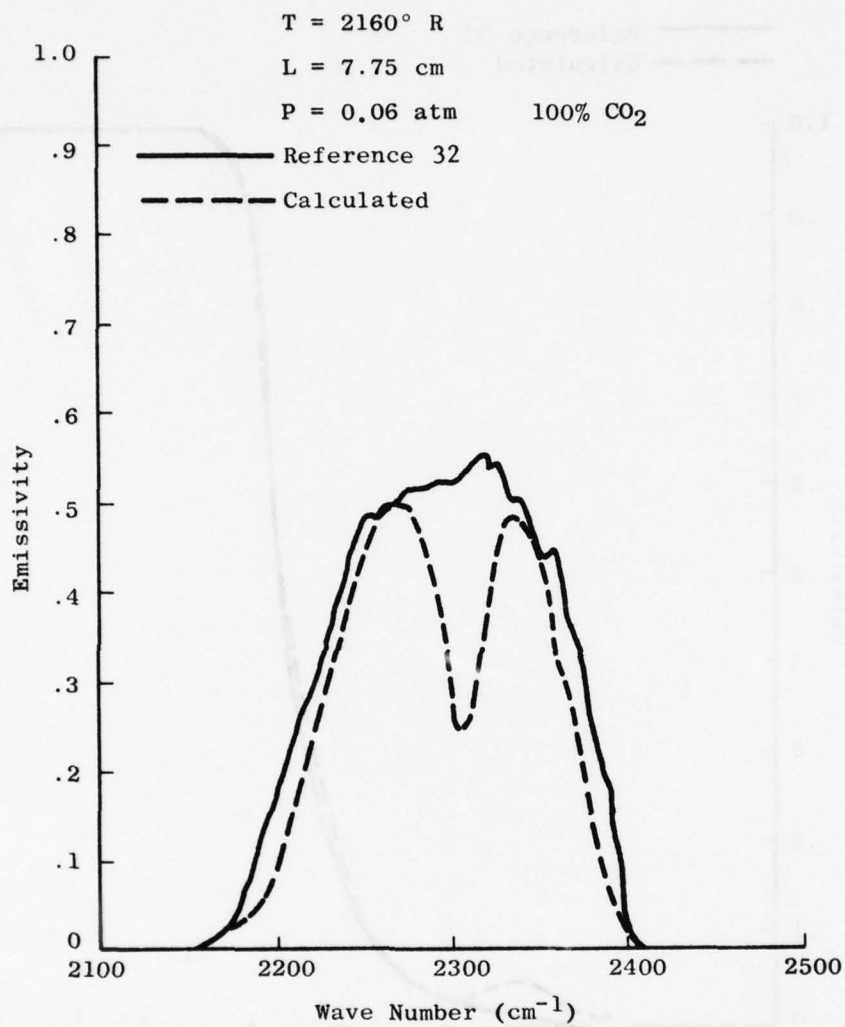


Figure 42. Emissivity of CO_2 , 4.3μ Band, $P = 0.06 \text{ Atm.}$

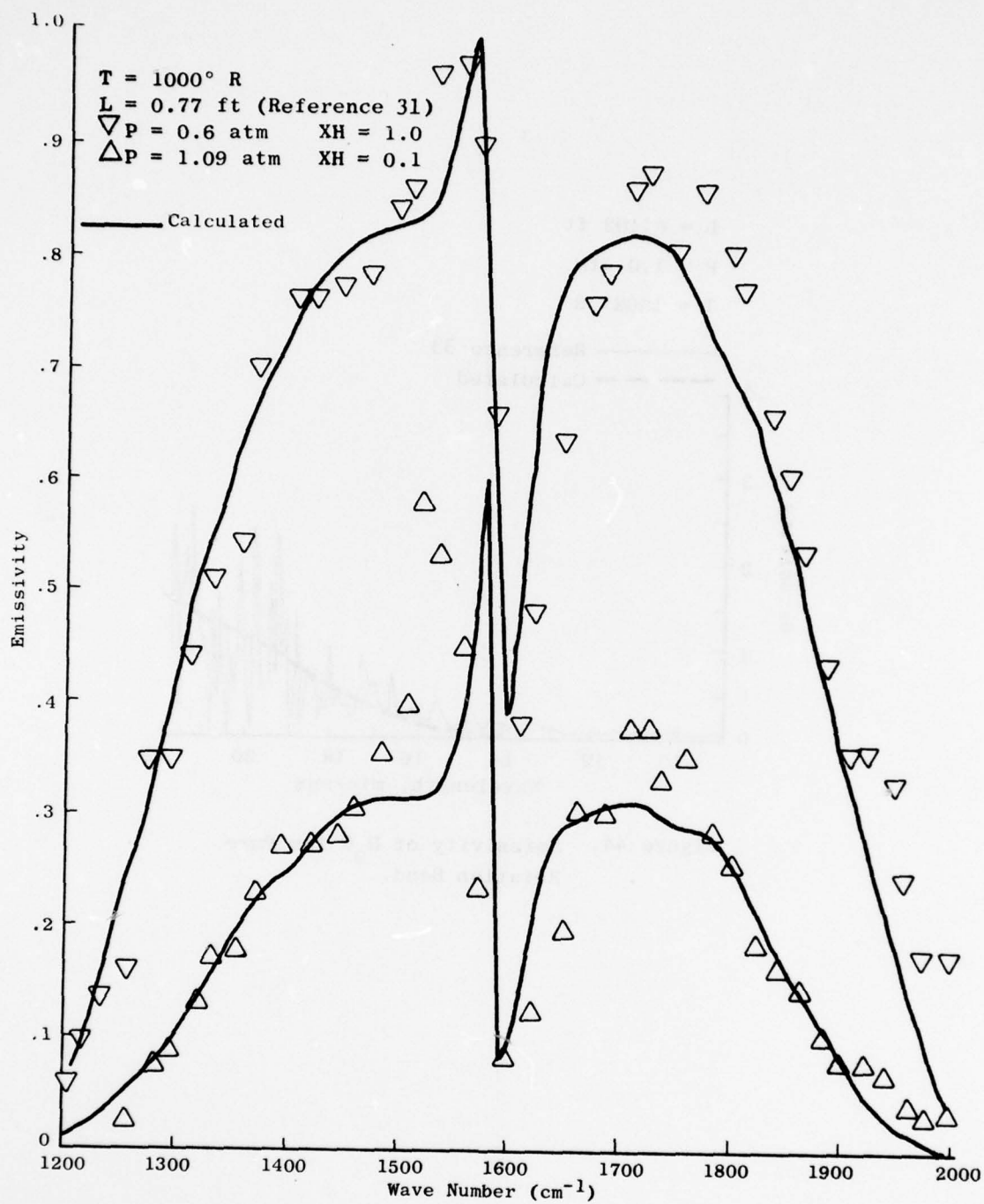


Figure 43. Emissivity of H_2O , 6.3μ Band.

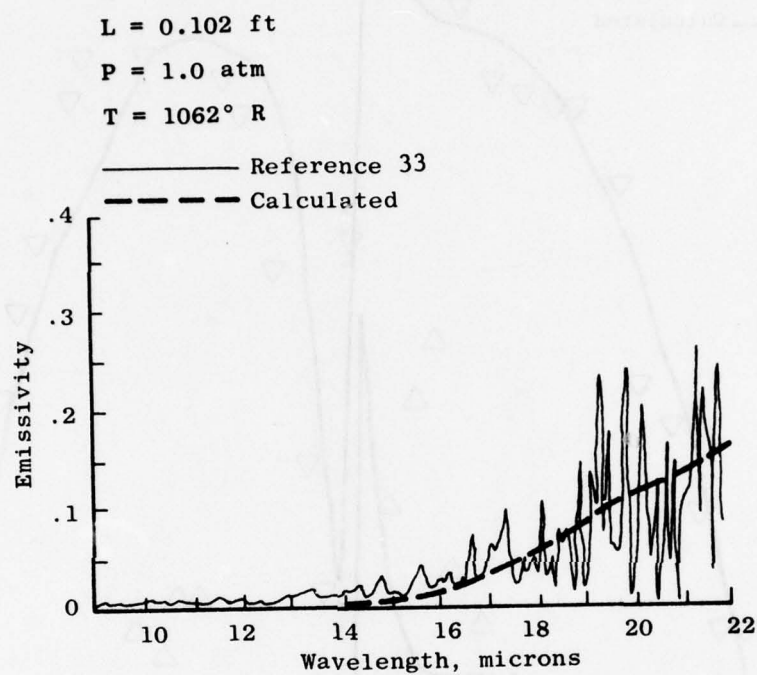


Figure 44. Emissivity of H_2O for Pure Rotation Band.

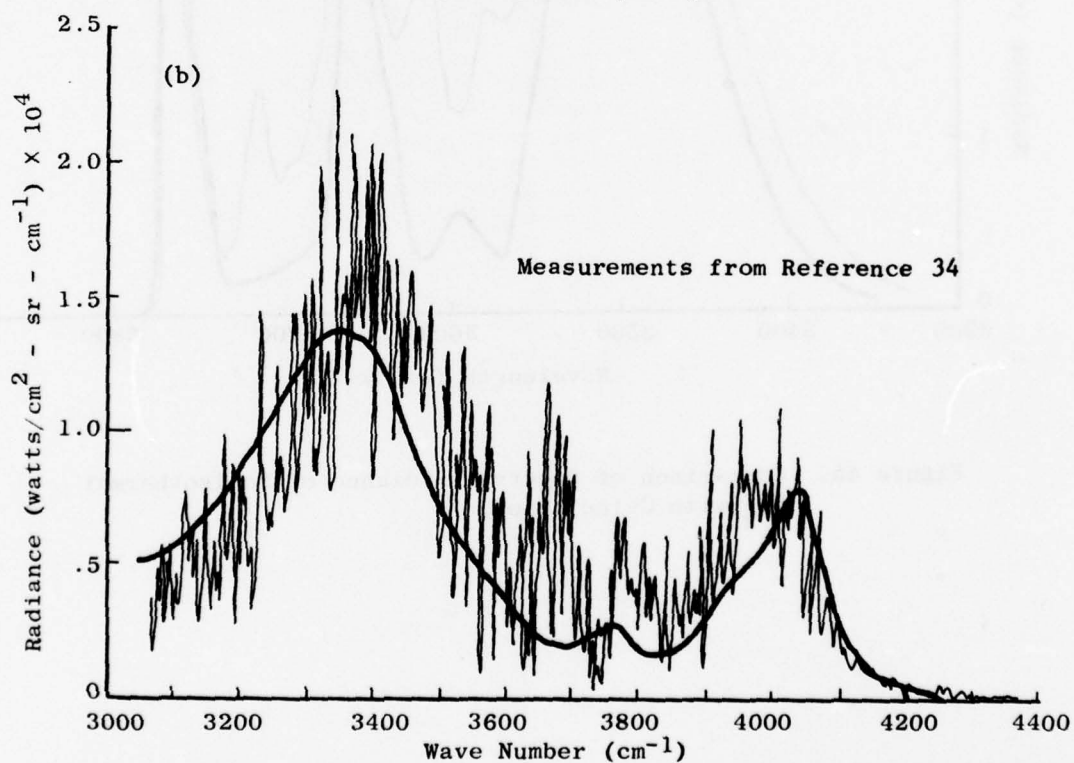
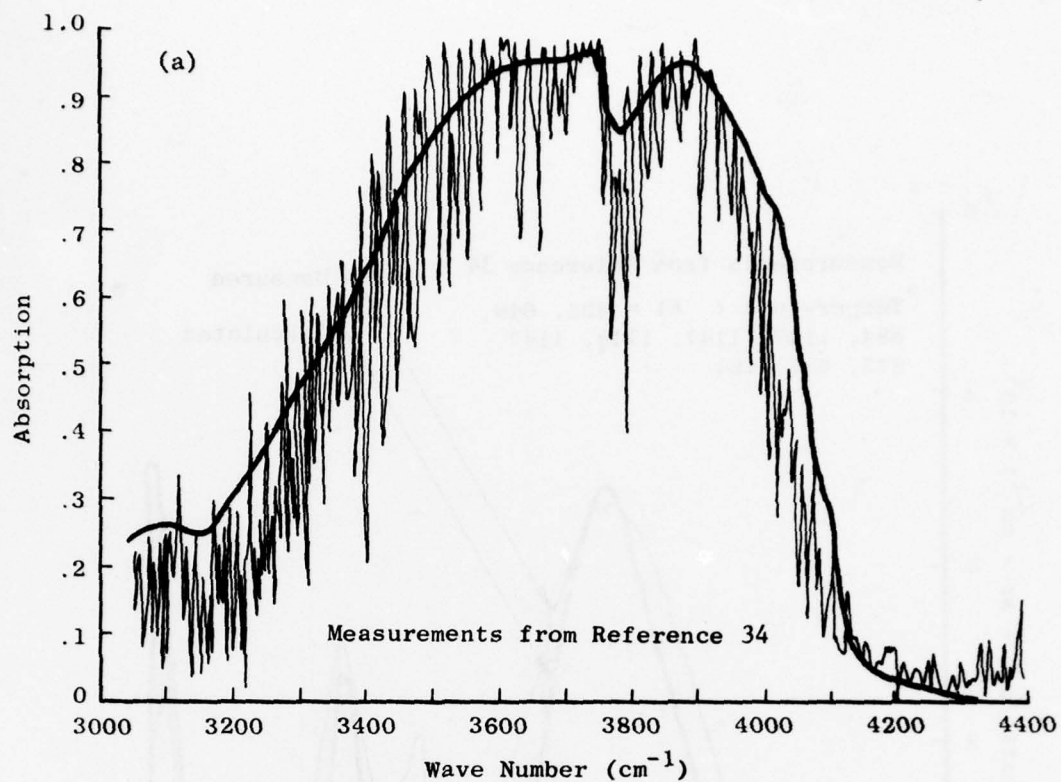


Figure 45. Comparison of Spectral Radiance of Nonisothermal H_2O with Calculation.

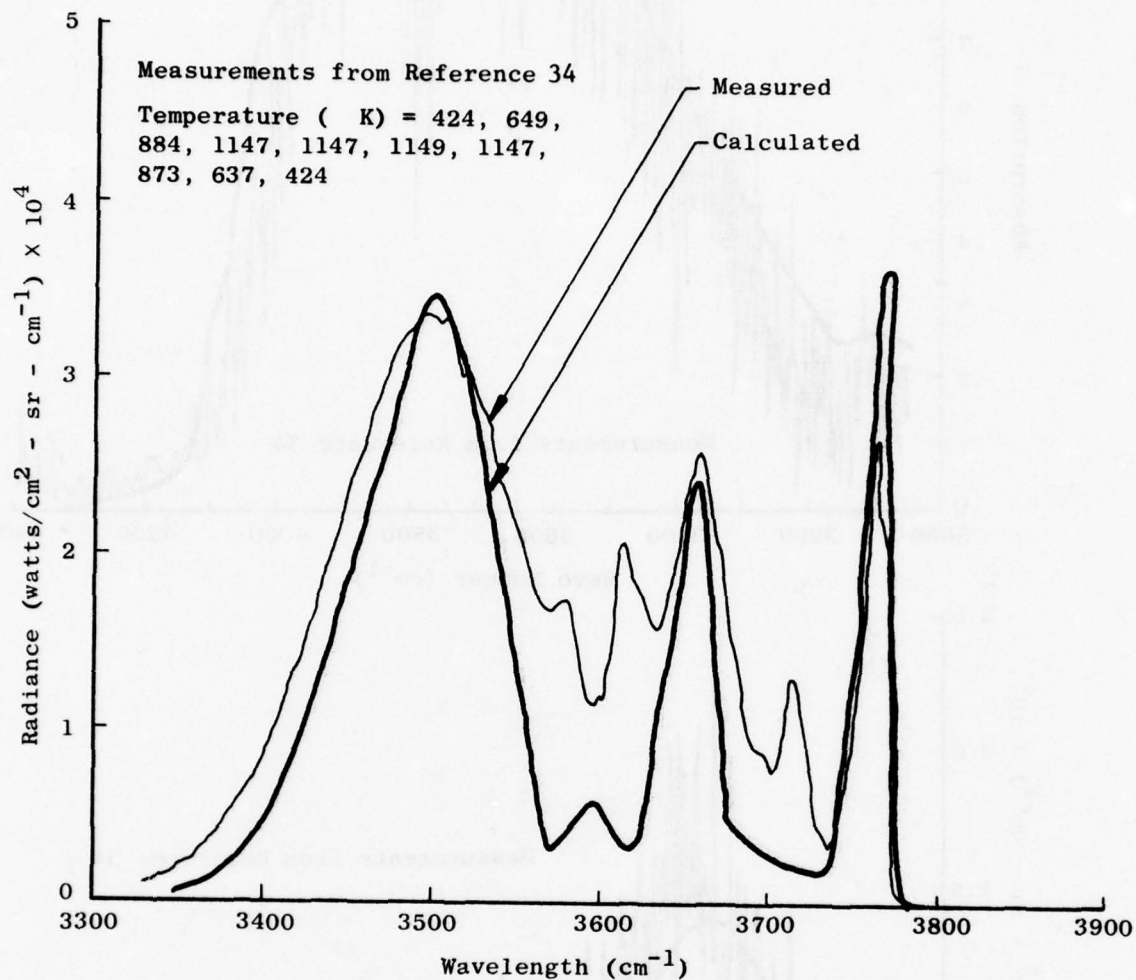
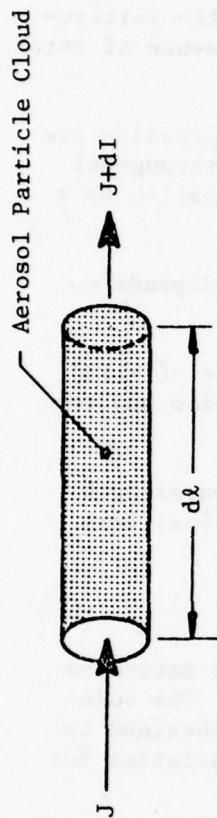
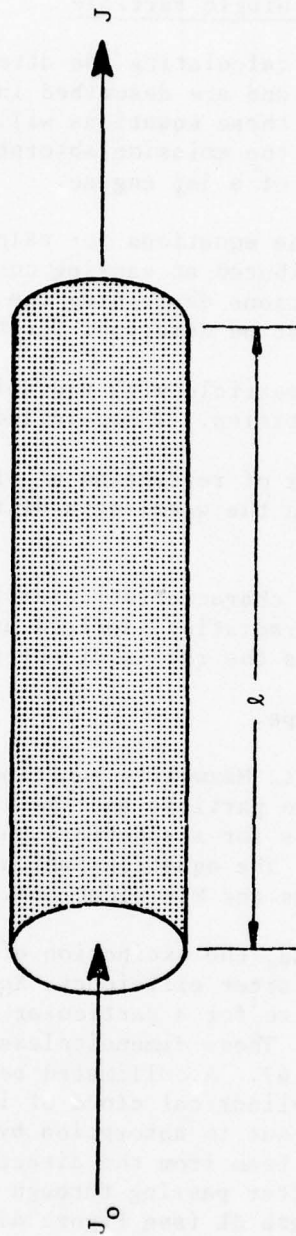


Figure 46. Comparison of Spectral Radiance of Nonisothermal CO₂ with Calculation.



(a) Differential element of a cylindrical cloud of aerosol particles which absorbs and scatters the incident beam.



(b) Cylindrical cloud of aerosol particles which absorbs and scatters the incident radiation beam.

Figure 47. Cylindrical Cloud of Aerosol Particles Which Absorbs and Scatters the Incident Beam.

D. PARTICULATE ATTENUATION

1. Attenuation by a Single Particle

General equations for calculating the attenuation of radiation by a cloud of particles are available and are described in detail in References 34 and 35. In the following sections, these equations will be developed for the particular problem of calculating the emission/absorption due to the presence of aerosol particles in the plume of a jet engine.

In order to develop the equations for calculating the IR suppression due to aerosol particles distributed at varying concentration levels throughout the engine plume, the equations describing the attenuation of radiation by a single aerosol particle must be described first.

The interaction of a particle with radiation incident on it depends on several dimensionless quantities. These include:

1. The complex index of refraction n' of the particle [$n' = n(1-ik)$] which varies with the wavelength of the incoming radiation and the type of particle.
2. The ratio of the characteristic particle dimension to wavelength of the incoming radiation (defined as $2\pi R/\lambda$ for a spherical particle, where R is the radius of the particle).
3. The particle shape.

Given these properties, Maxwell's equations can be solved to determine the interaction between the particle and the incoming radiation. The solution of Maxwell's equations for a spherical particle, which was obtained by Mie in 1908, may be used. The equations which result from this solution for a sphere are referred to as the Mie equations.

From the Mie equations, the extinction efficiency, X_T , the absorption efficiency, X_A , and the scatter efficiency, X_S , can be calculated for a given particle type and size for a particular wavelength of the radiation incident on the particle. These dimensionless quantities can be defined as follows, utilizing Figure 47. A collimated beam having a wavelength and intensity I traverses a cylindrical cloud of identical particles, and the beam is attenuated partly due to absorption by the particles and partly due to any deflections of the beam from the direction of propagation of the beam (particle scattering). After passing through a differential element of the cloud of particles of length dL (see Figure 47a), the intensity of the beam is reduced by dI . Now the fractional decrease in intensity of the beam over small distances is proportional to the distance, or:

$$-\frac{dJ}{J} = KdL \quad (156)$$

where K is the proportionality constant.

Referring to Figure 47b, equation (156) can be integrated over the total length of the particle cloud. The results is:

$$J = J_0 e^{-KL} \quad (157)$$

The proportionality constant in the absence of scatter is the absorption coefficient, K_A ; in the presence of absorption, it is the scatter coefficient, K_S ; and, in the presence of both particle absorption and scattering, it is the total attenuation or extinction coefficient, K_T , which is equal to the sum of K_A and K_S .

$$K_T = K_A + K_S \quad (158)$$

If the coefficients K_T , K_A and K_S are divided by the number of particles per unit volume (concentration) in the particle cloud, the resulting areas are defined as the particle cross section C_T , C_A , and C_S . The ratios of C_T , C_A , and C_S to the geometrical cross section of the particle (πR^2 for a spherical particle) are defined as the extinction efficiency X_T , the absorption efficiency X_A , and the scattering efficiency X_S , respectively. Therefore,

$$X_T = K_T / (\text{conc}) / (\pi R^2) \quad (159)$$

$$X_A = K_A / (\text{conc}) / (\pi R^2) \quad (160)$$

$$X_S = K_S / (\text{conc}) / (\pi R^2) \quad (161)$$

The Mie equations, which can be used to calculate the values of X_T , X_A , and X_S for a spherical particle, can be summarized as follows:

Applicable terms used in the Mie equations are defined below:

n' \equiv complex index refraction

X \equiv size parameter ($X = 2\pi R/\lambda$)

Y $\equiv n'X$

The equations for the extinction efficiency, absorption efficiency, and the scattering efficiency then can be written as follows:

$$X_T = \frac{2}{X^2} \sum_{m=1}^{\infty} (2m+1) \text{Real} (a_m + b_m) \quad (162)$$

$$X_S = \frac{2}{X^2} \sum_{m=i}^{\infty} (2m+1) (|a_m|^2 + |b_m|^2) \quad (163)$$

$$X_A = X_T - X_S$$

where a_m and b_m (the amplitude functions) are given by:

$$a_m = \frac{S'_m(Y)S_m(X) - n'S'_m(X)S_m(Y)}{S'_m(Y)\phi'_m(X) - n'\phi'_m(X)S_m(Y)} \quad (164)$$

$$b_m = \frac{n'S'_m(Y)S_m(X) - S'_m(X)S_m(Y)}{n'S'_m(Y)\phi'_m(X) - \phi'_m(X)S_m(Y)} \quad (165)$$

where $S_m(Z)$ and $\phi_m(Z)$ are defined as:

$$S_m(Z) = \frac{\pi Z}{2}^{1/2} J_{m+1/2}(Z) \quad (166)$$

$$\phi_m(Z) = S_m(Z) + i C_m(Z) \quad (167)$$

and,

$$C_m(Z) = (-1)^m \frac{\pi Z}{2}^{1/2} J_{-m-1/2}(Z) \quad (168)$$

Here $J_{m+1/2}$ and $J_{-m-1/2}$ are Bessel functions of the positive and negative half-orders. The partial differentials $s'_m(Z)$ and $\phi'_m(Z)$ are defined as:

$$s'_m(Z) = \frac{\partial S_m}{\partial Z} \quad (169)$$

$$\phi'_m(Z) = \frac{\partial \phi_m}{\partial Z} \quad (170)$$

When the particle is small enough that the maximum particle dimension is less than 0.2 wavelength, measured in the particle ($2R \leq 0.2 \lambda/n$), the Mie equations reduce to the following simplified equations:

$$X_A = \frac{24n^2 K X}{[n^2(1-K^2)+2]^2 + 4n^4 K^2} \quad (171)$$

and

$$X_S = \frac{8}{3} X^4 \frac{[n^2(1-k^2)-1][n^2(1-k^2)+2]+4n^4k^2)^2+36n^4k^2}{[n^2(1-k^2)+2]^2+4n^4k^2)^2} \quad (172)$$

In order to determine how the quantities X_T , X_S , and X_A vary with particle size, the Mie scattering equations were solved for graphite which has an index of refraction of $n' = 2(1-0.6i)$. The variation of the extinction coefficient as a function of the size parameter X is plotted in Figure 48. The extinction coefficient varies approximately linearly up to the small particle limit, X_L (defined previously) which for $n = 2$ is just:

$$X_L = \frac{2\pi R}{\lambda} = \frac{0.2\pi}{n} = \frac{0.2\pi}{2} = 0.314 \quad (173)$$

After the small particle limit, the extinction efficiency, X_T , rises to a maximum at approximately $X = 1.0$, and then X_T asymptotically approaches a value of $X_T = 2$ at large values of the size parameter.

In Figure 48, the ratio of X_S/X_A is plotted as a function of the size parameter X . It can be concluded, that, when the size parameter X is less than the small particle limit $X_L = 0.314$, scattering is negligible and the extinction coefficient is due only to particle absorption. However, as X increases past this value, X_S becomes increasingly important in the value of the total extinction. It is important to note that the values of X_T , X_A and X_S vary significantly with the particle size and the wavelength of the radiation incident on the particle.

Also, from equation (171) and (172), it can be seen that the extinction coefficient will vary markedly with the complex index of refraction $n' = n \cdot (1-iK)$. The complex index of refraction varies widely for different materials and, for a given material, it also can vary significantly with the wavelength of the incoming radiation. In Reference 36, the complex index of refraction for various carbonaceous materials was shown to vary significantly with the wavelength of the incoming radiation. Figure 49 shows that the index of refraction for carbonaceous materials also can vary significantly with wavelength.

2. Attenuation by a Cloud of Particles

In the previous section, the equations required to calculate the values of X_T , X_S , and X_A , given the properties of the particle (radius, index of refraction) and the wavelength of the incident radiation, were determined. In this section, these equations will be extended to determine the attenuation of a beam of radiation through a cloud of aerosol particles with a given size distribution.

Referring to Figure 50, consider a beam of radiation (ray) of intensity, J , passing normal to the surface element, dA , and traversing a distance, dL .

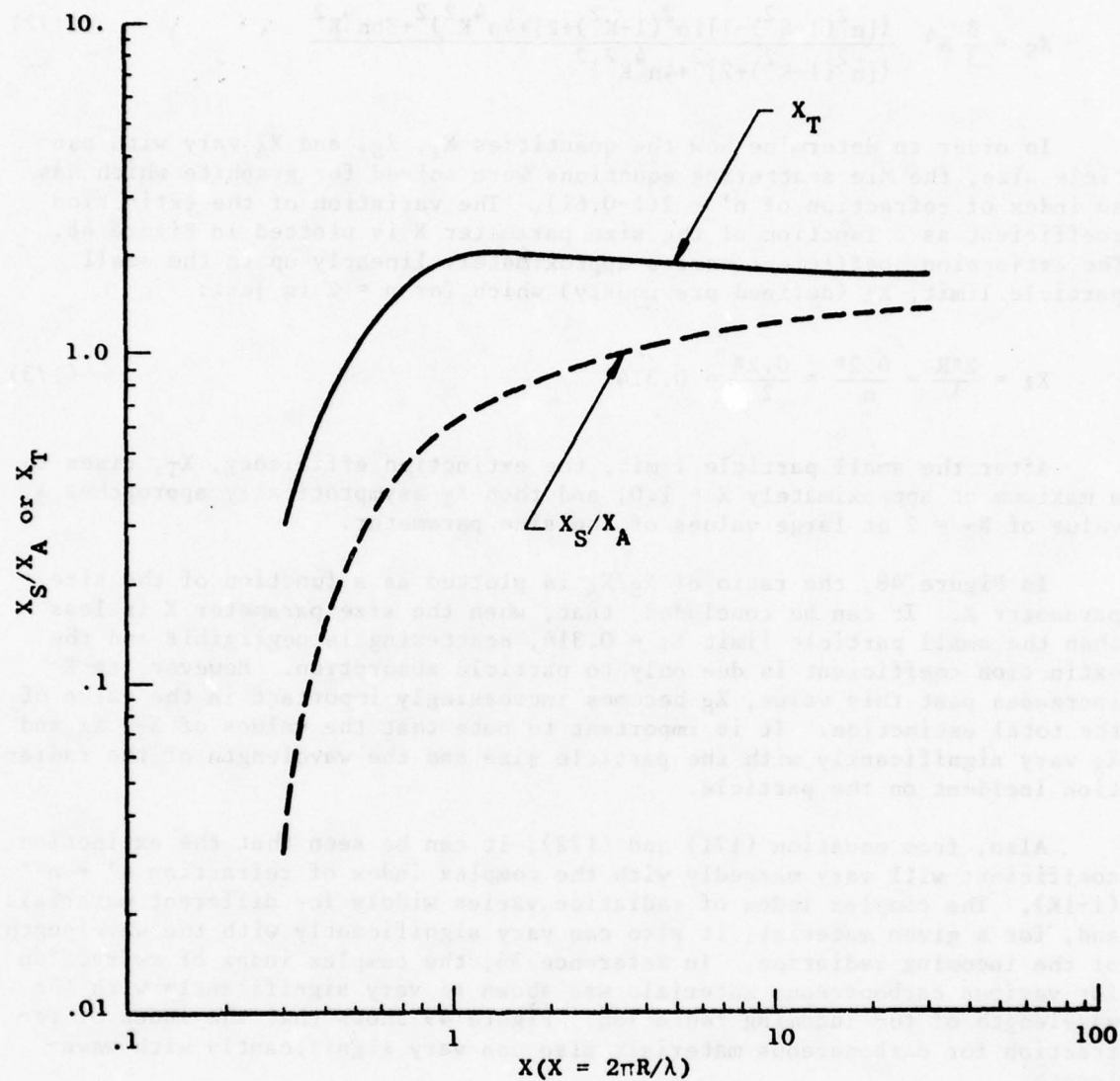


Figure 48. Extinction Efficiency X_T and Ratio of Scatter to Absorption Efficiency for a Graphite Sphere as a Function of the Size Parameter X .

Curves 1-4 are graphites; 5-9, coals; 10 and 11, coal burning soots; 12, oil furnace soot; 13, natural gas soot; 14, carbon black; 15, chimney soot; 16, activated charcoal.

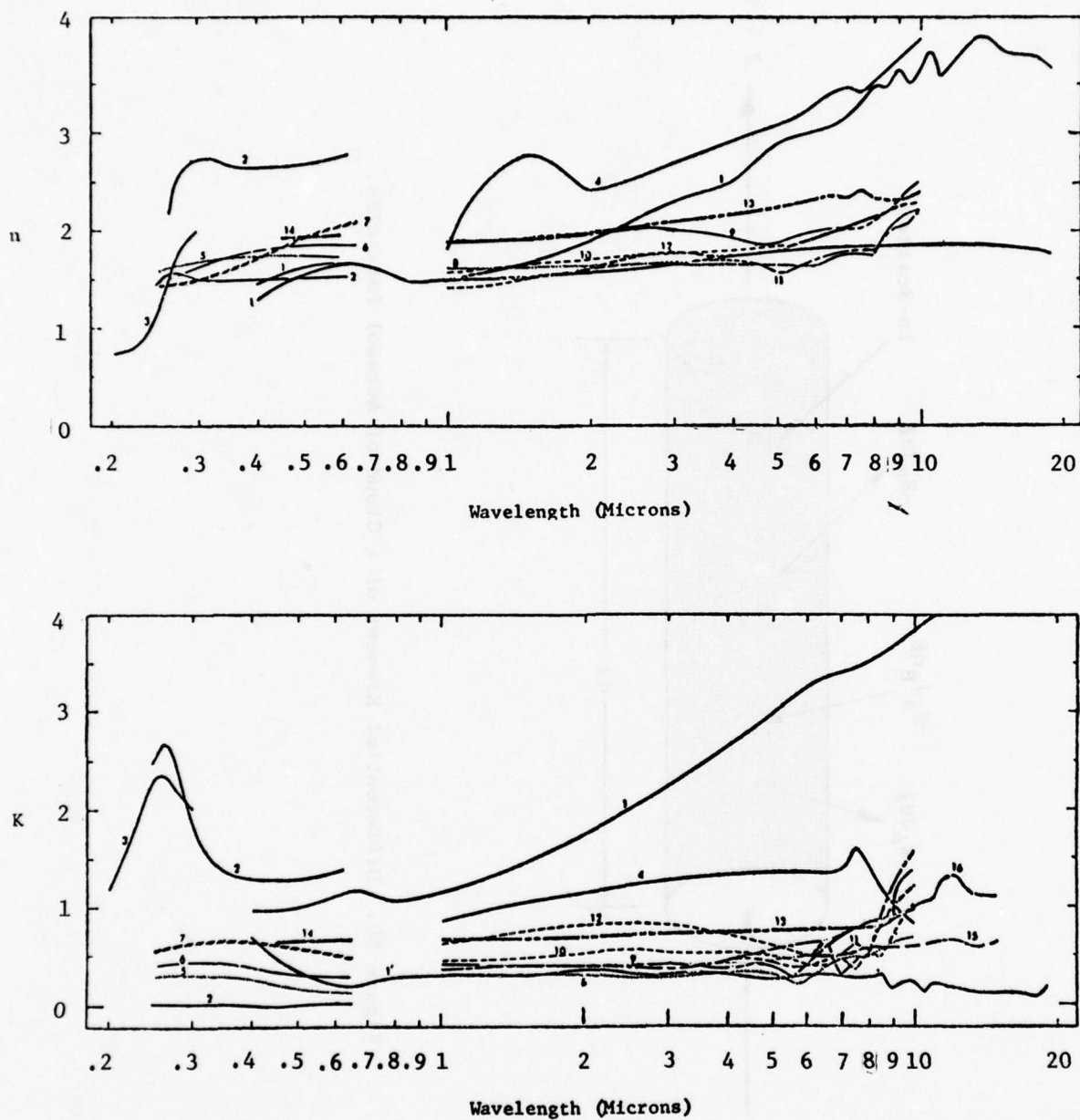


Figure 49. Complex Index of Refraction of Carbonaceous Materials as a Function of Wavelength.

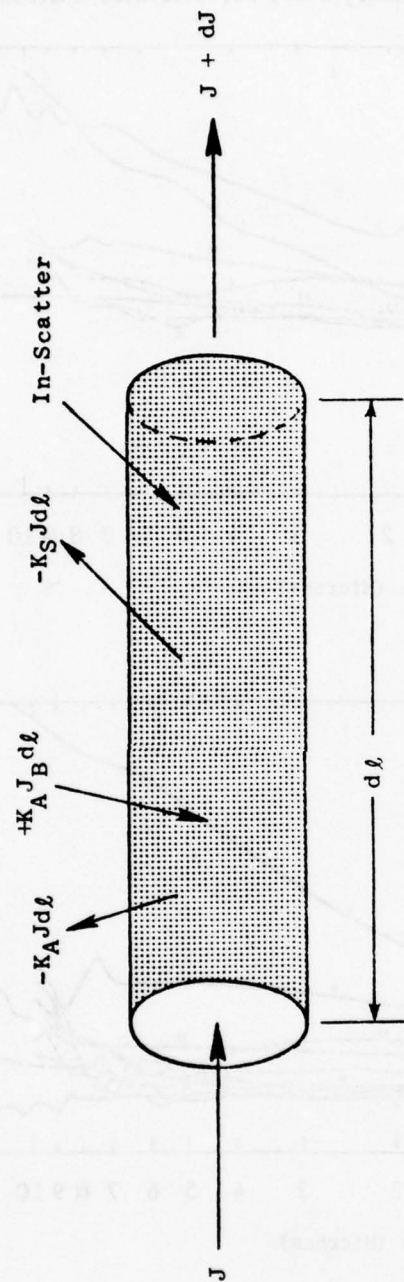


Figure 50. Differential Element of a Cloud of Aerosol Particles.

This volume contains particles at a temperature, T , which are emitting black-body radiation with an intensity, I_B . The contributions of various factors to the change in intensity of the beam are:

- $K_A J d\ell$ due to absorption

+ $K_A J_B d\ell$ due to the blackbody emission of the particles at T

- $K_S J d\ell$ due to out-scatter

plus a term due to in-scatter.

The in-scatter term takes into account the case where a ray which is traveling in a different direction than the incident ray strikes a particle and is scattered in the direction of the incident ray. This term can only be included in the analytical model for a Monte-Carlo-type analysis. Therefore, this term is not included in the equations for this analytical model. There are situations in which this neglected term may induce significant errors in the analysis. Now, summation of the above terms (neglecting in-scatter) yields:

$$\frac{dJ}{d\ell} = -(K_A + K_S)J + K_A J_B \quad (174)$$

or

$$\frac{dJ}{d\ell} = -K_T J + K_A J_B \quad (175)$$

Expressions for K_T and K_A now must be developed from the definition of these quantities given previously. Since these quantities vary with the wavelength of the ray, the subscript λ must be added to the terms:

$$K_{T\lambda} = \left(\frac{\text{particles}}{\text{volume}} \right) (\pi R^2) (X_{T\lambda}) \quad (176)$$

and

$$K_{A\lambda} = \left(\frac{\text{particles}}{\text{volume}} \right) (\pi R^2) (X_{A\lambda}) \quad (177)$$

Of course, $X_{T\lambda}$ and $X_{A\lambda}$ can be determined from the Mie equations for any given particle size, wavelength, and particle index refraction at that wavelength. The concentration of particles per unit volume is a quantity which must be determined for any given problem. For a given particle size distribution in the cloud of particles, the quantities $K_{T\lambda}$ and $K_{A\lambda}$ can be determined by summing overall particle sizes. Where " F_i " is defined as the fraction of the total weight of aerosol having a given particle size:

$$K_{T\lambda} = \sum_{\substack{i = \\ \text{all particle sizes}}} \left(\frac{\text{particles}}{\text{volume}} \right) (\pi R_i^2) (X_{T\lambda})_i F_i \quad (178)$$

and

$$K_{A\lambda} = \sum_{\substack{i = \\ \text{all particle sizes}}} \left(\frac{\text{particles}}{\text{volume}} \right) (\pi R_i^2) (X_{A\lambda})_i F_i \quad (179)$$

Therefore, equation (175) now becomes:

$$\frac{dJ_\lambda}{d\ell} = \left[\sum_i \left(\frac{\text{particles}}{\text{volume}} \right) (\pi R_i^2) X_{T\lambda}_i F_i \right] J + \left(\sum_i \pi R_i^2 X_{A\lambda}_i F_i \right) J_B \quad (180)$$

This equation then represents the change in intensity dJ_λ , of a ray having a wavelength λ over a differential length $d\ell$ due to aerosol particles of various sizes dispersed over the volume shown in Figure 50.

Since the particles are dispersed in the engine exhaust plume, where significant concentrations of CO_2 and H_2O are present, terms for absorption of the incident ray by these gases and the contributions of the blackbody emission of these particles to the incident ray from equation (55) must be included in equation (180) prior to integration.

When both particles and gases are present in a ray segment, the radiation balance becomes:

$$dJ_\lambda + k_\lambda J_\lambda dx + K_{T\lambda} J_\lambda dx = k_\lambda B_\lambda dx + K_{A\lambda} B_\lambda dx \quad (181)$$

It should be noted that B_λ for the gas and the aerosol have been set equal to each other in this equation. This was done because it is assumed that the temperature of the gas and the aerosol will be equal in a ray segment. Equation (181) also can be written as:

$$d \left[J_\lambda e^{\int_0^x (k_\lambda + K_{T\lambda}) dx} \right] = \frac{k_\lambda + K_{A\lambda}}{k_\lambda + K_{T\lambda}} B_\lambda d \left[e^{\int_0^x (k_\lambda + K_{T\lambda}) dx} \right] \quad (182)$$

Now, since it is assumed that the ray shown in Figure 51 can be represented by small homogeneous segments, the total integration over the ray then can be evaluated properly as a summation:

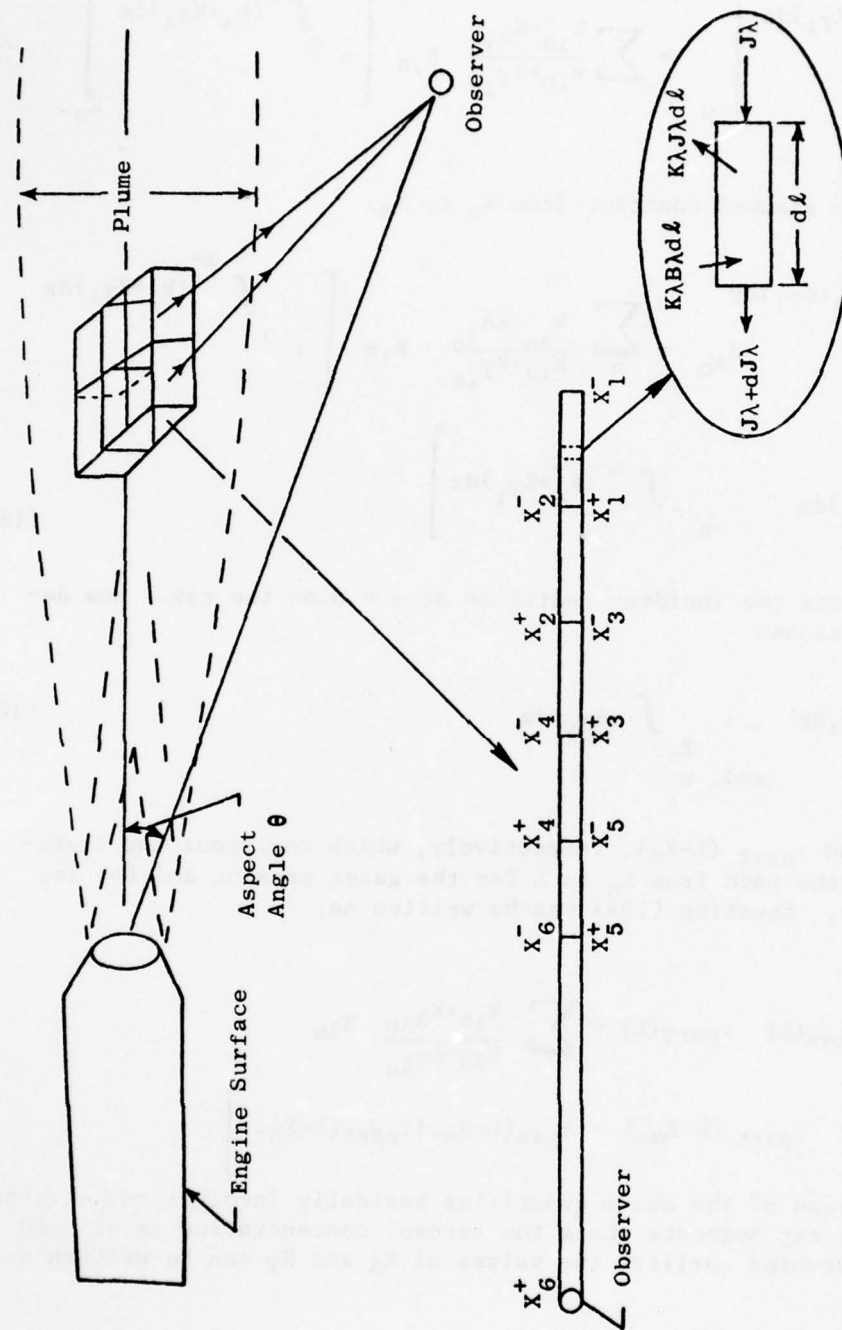


Figure 51. Schematic Demonstrating the Computational Technique Used in PLUMIR.

$$\left[J_{\lambda} e^{\int_0^x (k_{\lambda} + K_{T\lambda}) dx} \right]_0^L = \sum_n \frac{k_{\lambda n} + K_{A\lambda n}}{k_{\lambda n} + K_{T\lambda n}} B_{\lambda n} \left[e^{\int_0^x (k_{\lambda} + K_{T\lambda}) dx} \right]_{X_{n-}}^{X_{n+}} \quad (183)$$

where $B_{\lambda n}$ has been assumed constant from X_n to X_{n-}

$$J_{\lambda L} e^{\int_0^L (k_{\lambda} + K_{T\lambda}) dx} - J_{\lambda 0} = \sum_n \frac{k_{\lambda n} + K_{A\lambda n}}{k_{\lambda n} + K_{T\lambda n}} B_{\lambda n} \left[e^{\int_0^{X_{n+}} (k_{\lambda} + K_{T\lambda}) dx} - e^{\int_0^{X_{n-}} (k_{\lambda} + K_{T\lambda}) dx} \right] \quad (184)$$

where $J_{\lambda 0}$ represents the incident radiation at $x = 0$ on the ray. Now defining the expressions:

$$e^{-\int_{X_n}^L k_{\lambda} dx} \quad \text{and} \quad e^{-\int_{X_n}^L K_{T\lambda} dx} \quad (185)$$

as $\tau_{\text{gas}}(L-X_n)$ and $\tau_{\text{part}}(L-X_n)$, respectively, which represent the transmissivities over the path from X_n to L for the gases present and for the particles present. Equation (184) can be written as:

$$J_{\lambda L} = J_{\lambda 0} \tau_{\text{gas}}(L) \tau_{\text{part}}(L) + \sum_n \frac{k_{\lambda n} + K_{A\lambda n}}{k_{\lambda n} + K_{T\lambda n}} B_{\lambda n} \left[\tau_{\text{gas}}(L-X_{n-}) \tau_{\text{part}}(L-X_{n+}) - \tau_{\text{gas}}(L-X_{n-}) \tau_{\text{part}}(L-X_{n-}) \right]$$

The calculation of the above quantities basically involves calculating K_A and K_T for all ray segments where the aerosol concentration is assumed constant. As presented earlier, the values of K_A and K_T can be written as follows:

$$K_{T\lambda} = \sum_i \left(\frac{\text{particles}}{\text{volume}} \right) \pi R_i^2 X_{T\lambda i} F_i \quad i = \text{all particle sizes} \quad (178)$$

$$K_{A\lambda} = \sum_i \frac{\text{particles}}{\text{volume}} \pi R_i^2 X_{T\lambda i} F_i \quad i = \text{all particle sizes} \quad (179)$$

Given the particle size distribution of the aerosol, the complex index of refraction of the aerosol, and the concentration of the aerosol in the plume, the quantities of K_T and K_A can be calculated. The aerosol size distribution and the complex index of refraction of the aerosol are quantities peculiar to the particles selected and must be directly input into the SCORPIO-N computer program. As to the determination of the aerosol concentration in particles/volume for any ray segment, the program calculates the aerosol concentration at all locations in the engine plume using an option in the JETMIX module which allows for the calculation of the concentration of all constituents of the plume, given the conditions at the jet engine nozzle exit. The use of this option to calculate the concentrations is described in Section III.E.

$$\text{particles/volume} = \frac{M_a \left(\frac{P_o}{RT} \right) (WT)}{\left(\frac{4}{3} \pi R^3 \right) \rho_a} \quad (187)$$

where M_a = mole fraction of the particles in a ray segment

P_o = static pressure of the external flow

R = gas constant

$\frac{4}{3} \pi R^3$ = volume of a single particle with a radius R

ρ_a = density of the particle material (lb/ft³)

Putting this expression for the particle concentration into equation (178) yields:

$$K_{T\lambda} = \sum_{\substack{i \\ \text{particle} \\ \text{sizes}}} \frac{M_a \frac{P_o}{RT} WT}{\frac{4}{3} \pi R_i^3 \rho_a} F_i \pi R_i^2 X_{T\lambda i} \quad (188)$$

$$K_{A\lambda} = \sum_{\substack{i \\ \text{particle} \\ \text{sizes}}} \frac{M_a \left(\frac{P_o}{RT} \right)_{WT}}{\left(\frac{4}{3} \pi R_i^3 \right) \rho_a} F_i R_i^2 X_{A\lambda i} \quad (189)$$

These equations can be simplified to yield:

$$K_{T\lambda} = \frac{M_a \left(\frac{P_o}{RT} \right)_{WT}}{\rho_a \left(\frac{4}{3} \pi \right)} \sum_{\substack{i \\ \text{particle} \\ \text{sizes}}} \frac{F_i X_{T\lambda i}}{R_i} \quad (190)$$

and

$$K_{A\lambda} = \frac{M_a \left(\frac{P_o}{RT} \right)_{WT}}{\rho_a \left(\frac{4}{3} \pi \right)} \sum_{\substack{i \\ \text{particle} \\ \text{sizes}}} \frac{F_i X_{A\lambda i}}{R_i} \quad (191)$$

SECTION VI

TOTAL SPECTRAL INTENSITY (TOTALR)

A. General Discussion

The module, TOTALR, uses the output from other modules to determine the combined target spectral radiant intensity at various observer locations.

The output being used from SIGNIR, for internal engine hot parts consists of

$R_{\gamma ij}$ the radiation coefficients for each combination of nodes for specified wavelengths

A_{Ei} the projected area of each node at each viewing angle, α , (in.^2)

T_i the temperature of each node, i , ($^{\circ} \text{R}$)

The output from PLUMIR for the plume and atmosphere is given for each position (viewing angle and distance).

J_{pyr} the spectral radiant intensity per steradian for each ray, r

Ω_r the steradians associated with each ray

τ_{apr} the transmissivity through the plume and the atmosphere for each ray

The output of AMFM consists of

A_F the projected area of each facet for each function of wavelength viewing angle, in.^2

$\epsilon_{\gamma F}$ surface emissivity of each facet as a function of wavelength and viewing angle

T_F temperature of each facet, $^{\circ} \text{R}$

and three tables for each aspect angle containing the following lists

1. F_{AA} facets to be attenuated by atmosphere only
2. F_{Ap} facets to be attenuated by plume and atmosphere
3. F_B facets that block the plume from view

The total spectral intensity at an observer location from the target is then given by

$$J_{TOT\lambda} = \sum_{i_R} J_{p\lambda r} \Omega_r + \left[\sum_i \left(\sum_j R_{\lambda ij} N_{\lambda j} \right) A_{Ei} \right] \tau_{ap\lambda} \\ + \sum_{i_{AP}} \epsilon_{\lambda F} A_F N_{\lambda F} \tau_{ap\lambda} + \sum_{i_{AA}} \epsilon_{\lambda F} A_F N_{\lambda F} \tau_{a\lambda}$$

where

λ = wavelength, microns

T_k = temperature, ° R

i_R = all plume rays not blocked from view by the facets in table FB

i, j = all nodes internal to the engine

i_{AP}, i_{AA} = all facets listed in tables FAP and FAA, respectively.

$N_{\lambda k}$ is the blackbody spectral radiance emitted by a surface at temperature, T_k

$$N_{\lambda k} = \frac{76805.4}{\lambda^5} \left/ \left[e^{\frac{25884.0}{\lambda T}} - 1 \right] \right.$$

watts/sr/ μ /in.²

$\tau_{ap\lambda}$ is the transmissivity through the plume for each ray.

τ_a is the transmissivity through the atmosphere.

The viewing angle and distance are measured from the center of the nozzle exhaust.

In addition, the total target graybody area, AOD, is summed for each aspect angle:

$$AOD = \sum_{i_{AP}} A_F + \sum_{i_{AA}} A_F + \sum_i A_{Ei}$$

B. Blockage for Plume-Airframe Calculations (SUMA, TRANS)

The facets prescribed by the AMFM module which interact with the plume are defined by four coplanar vertices.

The plume is subdivided into five strips defined by the strip centerlines:

$$Z = -Z_2, -Z_1, 0, Z_1, Z_2$$

as used in the PLUMIR module and shown in Figure 52. Z is normal to the viewing direction and X is along the flow axis.

The facet being considered is projected from the observer onto the x-z plane. The interaction of the plume and a facet is pictured schematically in Figure 52.

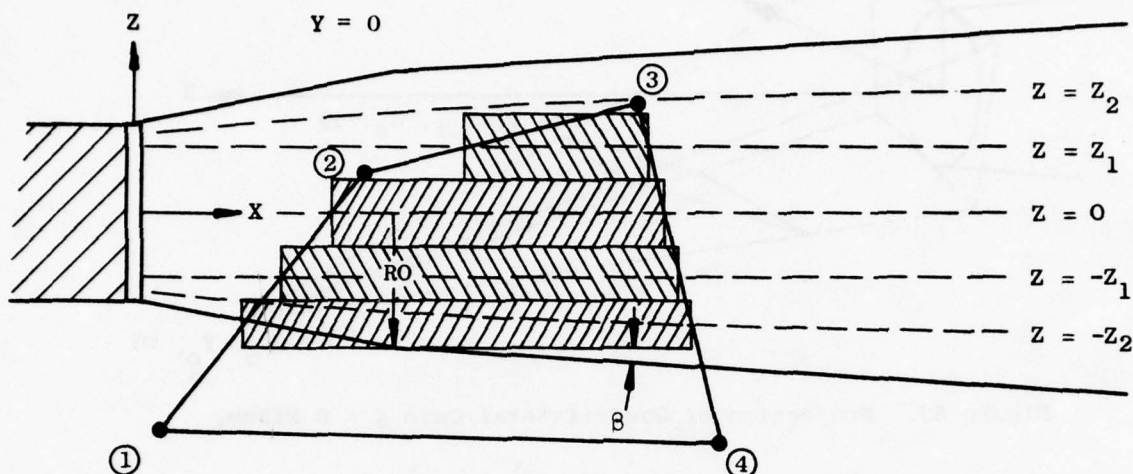


Figure 52. Schematic of Plume Strips With Projection of Quadrilateral Onto Plane Normal to Observer.

For each of the centerlines and for each facet the minimum and maximum values of X ($X_{MIN}(L)$ and $X_{MAX}(L)$) are calculated for which plume emissions are to be excluded or plume transmissivity is to be included. These areas included in the calculations are represented by the shaded areas in Figure 52.

The remaining calculation procedure is straightforward.

C. Blockage of Internal Engine Emissions (ENGOBS)

To compute the effect of engine obstructions:

1. Project the obstructions onto the Y-Z plane of the exhaust system.

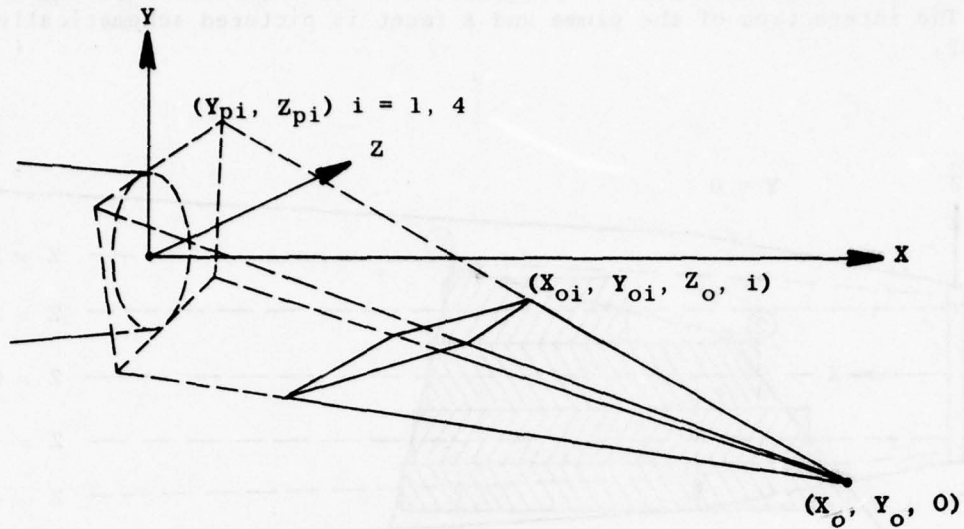


Figure 53. Projection of Quadrilateral Onto $X = 0$ Plane.

$$\frac{Y_{pi} - Y_v}{Y_{oj} - Y_v} = \frac{-X_v}{X_{oj} - X_v} = \frac{Z_{pi}}{Z_{oj}} \quad (i = 1, 4)$$

Assume projected node area of internal engine component, a_i , is the visible part of a thin ring with radius R_i and axial location X_i . Project the ring on the nozzle exit plane (as a circle with center at Y_c and radius, R_c).

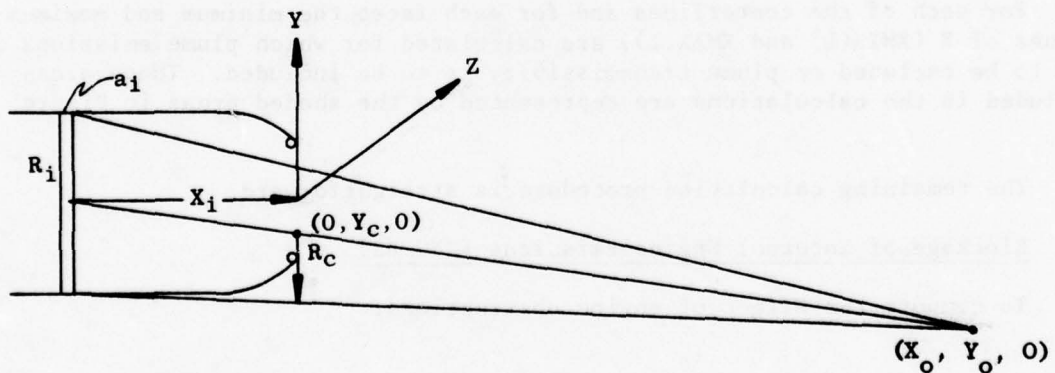


Figure 54. Projection of Node Area Onto $X = 0$ Plane.

$$Y_c = Y_v (X_i)/(X_i - X_v)$$

$$R_c = R_i \cdot X_v/(X_v - X_i)$$

Determine the visible arc angle $\pi - 2\alpha_0$ where α_0 is determined from the intersection of the two circles:

(1) center at $Z = 0, Y = +Y_c$

radius = R_c

(2) center at $Z = 0, Y = 0$

radius = R_8

$$\alpha_0 = \tan^{-1} (Y_1) / \sqrt{R_8^2 - Y_1^2}$$

where

$$Y_1 = (R_c^2 - R_8^2 - Y_c^2) / (-2Y_c)$$

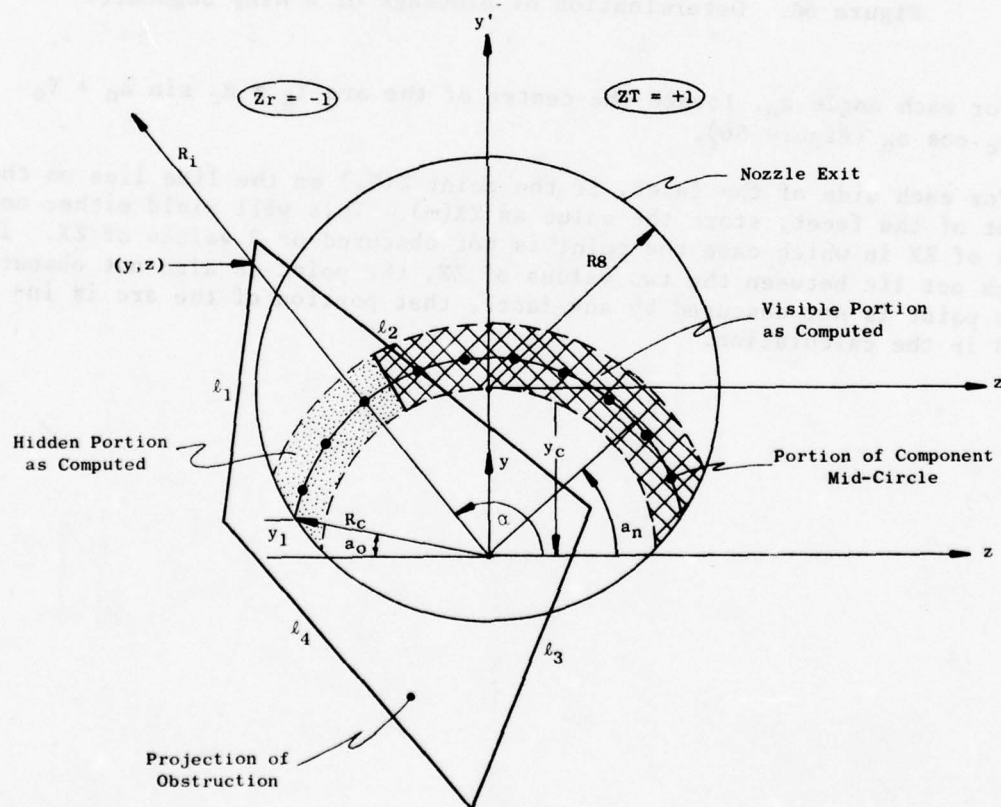


Figure 55. Y-Z Plane with Projections.

Subdivide the arc angle into 40 sectors of size, $da = (\pi - 2a_0)/40$ giving n central angles:

$$a_n = a_0 + \frac{2n-1}{2} da \quad n = 1, 40$$

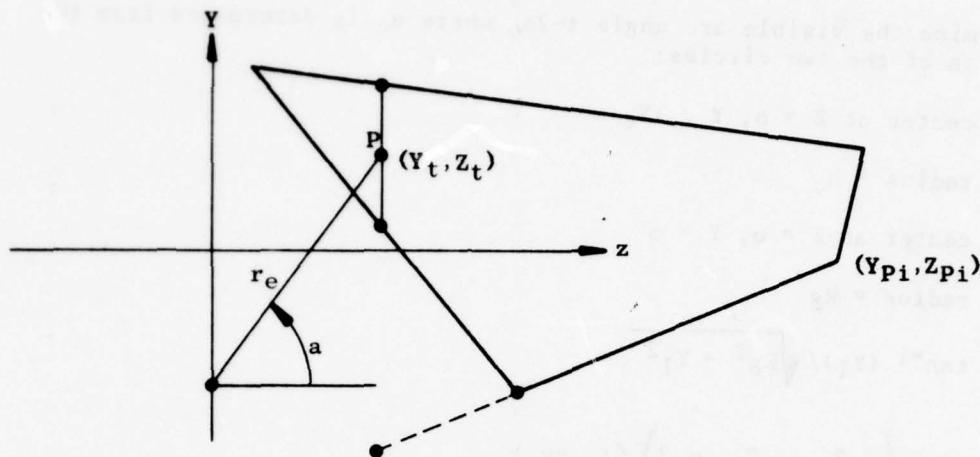


Figure 56. Determination of Blockage of a Ring Segment.

For each angle a_n , locate the center of the arc $Y_t = R_c \sin a_n + Y_c$
 $Z_t = R_c \cos a_n$ (Figure 86).

For each side of the facet, if the point $Z(Y_t)$ on the line lies on the segment of the facet; store the value as $ZX(m)$. This will yield either no values of ZX in which case the point is not obscured or 2 values of ZX . If Z_t does not lie between the two values of ZX , the point is also not obscured. If the point is not obscured by any facet, that portion of the arc is included in the calculation.

SECTION VII

LOCK-ON RANGE

A. Discussion

The lock-on range for a particular missile is determined for each aspect angle as follows:

The total target spectral radiance intensity, $J_{TOT\lambda}$, is available at a number of distances, D_K , from the target. The net target signal-to-noise ratio is given by

$$S_K = \int_{\text{all } \lambda} \frac{(J_{TOT\lambda} - A_{OD} N_{B\lambda}) G_{\lambda} d\lambda}{D_K^2 \cdot NEI} \quad (1)$$

where

A_{OD} is the target graybody area

$N_{B\lambda}$ is background radiance

G_{λ} is the missile spectral sensitivity

NEI is the noise-equivalent input of the missile.

There must be at least two values for lock-on range to be calculated.

The signal-to-noise ratio, S_K , is assumed to vary with distances D_K in a logarithmic quadratic relationship:

$$\ln D_K = a (\ln S_K)^2 + b (\ln S_K) + c \quad (2)$$

The coefficients a , b , and c are evaluated from three values of S_K which span, if possible, the known S/N for lock-on.

If only two values of S_K are available, a linear logarithmic relationship is assumed.

$$\ln D_K = a (\ln S_K) + b \quad (3)$$

There must be at least two values for lock-on range to be calculated.

The background radiances are provided internally in table form. Spectral plots of these backgrounds are provided in Appendix A.

SECTION IX

REFERENCES

1. Wilton, M.E., "Advanced Infrared Signature Prediction Program, (SCORPIO-N) - Volume I - User's Manual," General Electric Company, R77AEG404, January 1978.
2. Wilton, M.E., "Advanced Infrared Signature Prediction Program, (SCORPIO-N) - Volume II - Programmer's Manual," General Electric Company, R77AEG405, May 1977.
3. Harper, M.W., "Atmospheric Transmittance Curves for Several Meteorological Conditions," Electro Magnetics Laboratory, U.S. Army Missile Command, Redstone Arsenal, Alabama, Report No. RE-TR-63-13, March 1963.
4. Glushko, G.S., "Turbulent Boundary Layer on a Flat Plate in an Incompressible Fluid," NASA TTF-10, 080, 1965.
5. Spalding, D.B., et al., "Turbulent Mixing in Combustion Chambers," Northern Research Report No. 1118-1, 1966.
6. Rotta, J., "Statistical Theory of Nonhomogeneous Turbulence," Part II, NASA TT FF-11, June, 1968.
7. Ollerhead, J.B., "On the Prediction of Near Field Noise of Supersonic Jets," NASA CR-857, August, 1967.
8. Eldred, K.M., et al., "Suppression of Jet Noise with Emphasis on the Near Field," ASD-TDR-62-578, February, 1963.
9. Chigier, N.A., Chervensky, A., "Experimental Investigation of Swirling Vortex Motion in Jets," J.Appl. Mech., Trans. ASME, 1967, pp 443-451.
10. Pratt, B.D., and Keffer, J.F., "The Swirling Turbulent Jet," Trans. ASME Journal of Basic Engineering, December 1972, pp 739-748.
11. Kane, R.S., and Pfeffer, R., "Characteristics of Dilute Gas - Solid-Suspensions in Drag Reducing Flow," NASA CR-2267, City University of New York, June 1973.
12. Millikin, R.C., "Size, Optical Properties, and Temperatures of Soot Particles (U)," Journal of Optical Society of America, 1960, Volume 51, p 698.
13. Soo, S.L., "Third Dynamics of Multiphase Systems," Blaisdell Publishing Company, Waltham, Massachusetts, 1967.

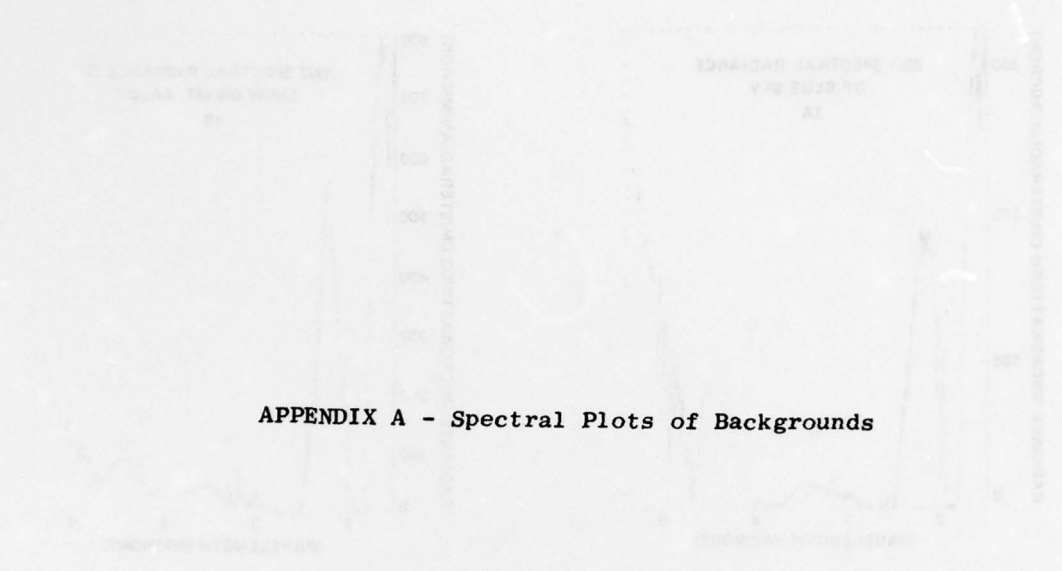
REFERENCES (Cont'd)

14. Bernstein, A., Heiser, W., and Nevenor, C., "Compound Compressible Nozzle Flow," AIAA Paper No. 66-563 presented at the AIAA Second Propulsion Joint Specialist Conference held at Colorado Springs, Colorado, June 13-17, 1966.
15. Sasman, P.K., Cresci, Robert J., "Compressible Turbulent Boundary Layer with Pressure Gradient and Heat Transfer," AIAA Journal, Vol. 4, No. 1, January 1966.
16. Haering, G.W., "A Proposed Correlation Scheme for Gas-Film Cooling Data," Air Force Aero Propulsion Laboratory, TR-66-56, August, 1966.
17. Sellers, J.P., Jr., "Gaseous Film Cooling with Multiple Injection Stations," AIAA Journal, Vol. 1, No. 9, September 1963.
18. London, A.L., and Shah, R.K., "Offset Rectangular Plate-Fin Surfaces, Heat Transfer and Flow Friction Characteristics," Transaction of the ASME, Journal of Engineering for Power, July 1968.
19. Kays, W.M., and London, A.L., "Compact Heat Exchangers," Second Edition, McGraw-Hill Book Company, 1964.
20. Hartnett, J.P., Birkebok, R.C., and Eckert, E.R.G., "Velocity Distribution, Effectiveness and Heat Transfer of Air Injected Through a Tangential Slot into a Turbulent Boundary Layer," Transaction of the ASME, Journal of Heat Transfer, Vol. 83, Series C, No. 3, 1961.
21. Culick, F.E.E., "The Compressible Turbulent Boundary Layer with Surface Mass Transfer," Massachusetts Institute of Technology Naval Supersonic Laboratory, TR-454, August 1960.
22. Foganoli, R.P., and Saydah, A.R., "Turbulent Heat Transfer and Skin-Friction Measurements on a Porous Cone with Air Injection at High Mach Numbers," AIAA Journal, Vol. 4, No. 6, 1966.
23. Wolfe, G.W., "Derivation and Computer Program Development (NVIEW) for the Calculation of Radiation View Factors Between Axisymmetric Sub-Divisions of a Turbine Engine Exhaust System," Vought Aeronautics Division, LTV Aerospace Corporation, Report No. 2-53900/IR-2829, August 1970.
24. Jakob, Max., Heat Transfer, Volume 1, John Wiley and Son, Inc., 1959.
25. McAdams, W.H., "Heat Transmission," McGraw Hill Book Co., Inc., 1954.
26. Abramovich, G.N., "The Theory of Turbulent Jet", The M.I.T. Press, Massachusetts Institute of Technology, Cambridge, Mass.

REFERENCES (Concluded)

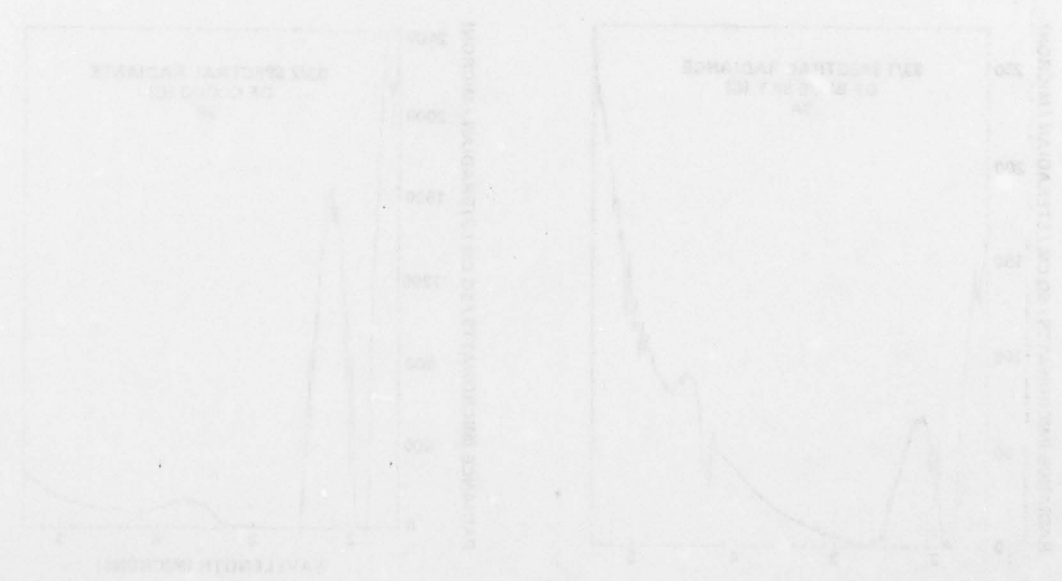
27. Weiner, M.M., and Edwards, D.K., "Theoretical Expression of Water Vapor Spectral Emissivity with Allowance for Line Structure", Int. J. Heat Mass Transfer, Volume II, pp 55-65, Pergamon Press 1968, UNCLASSIFIED.
28. Penner, S.S., Quantitative Molecular Spectroscopy and Gas Emissivities, Addison-Wesley Publishing Co., Inc., Reading, Massachusetts, UNCLASSIFIED.
29. Simmons, F.S., Yamada, H.Y., and Arnold, C.B., "Measurement of Temperature Profiles in Hot Gases by Emission-Absorption Spectroscopy," Infrared and Optics Laboratory, Willow Run Laboratory, NASA CR-72491, WRL 8962-18-F, University of Michigan, April 1969.
30. Ferriso, C.C., and Ludwig, C.G., "Spectral Emissivities and Integrated Intensities of the 1.87, 1.38 and 1.14 H₂O Bands Between 1000° F and 2200° F," J.Chem. Phys. 41, 1668-1624 (1964).
31. Weiner, M.M., and Edwards, D.K., "Theoretical Expression of Water Vapor Spectral Emissivity with Allowance for Line Structure," Int. J. Heat Mass Transfer, Volume II, pp 55-65, Pergamon Press, 1968.
32. Burch, Darrell, E., and Grynak, David, A., "Infrared Radiation Emitted by Hot Gases and its Transmission Through Synthetic Atmospheres," U-1929, Ford Motor Company, Aeronautics Division, February, 1963.
33. Ludwig, C.B., Ferriso, C.C., Malkmus, W., and Boynton, F.P., "High Temperature Spectra of the Pure Rotational Band of H₂O." J. Quantum Spectrosc. Radiat. Transfer, Vol. 5, pp 697-714, Pergamon Press Ltd.
34. Staackman, M., et al., "Final Results of Smoke Screen System Development (U)," June 1966, Prepared for Office of Civil Defense, Office of the Secretary of the Army, Washington, D.C.
35. Van de Hulst, H.C., Light Scattering by Small Particles (U), Wiley and Sons, Inc., New York, 1957.
36. Twitty, J.T., and Weinman, J.A., "Radiative Properties of Carbonaceous Aerosols (U)," Journal of Applied Meteorology, Volume 10, August 1971, pp 725-731.

100% 100% 100% 100% 100%
 100% 100% 100% 100% 100%
 100% 100% 100% 100% 100%
 100% 100% 100% 100% 100%
 100% 100% 100% 100% 100%
 100% 100% 100% 100% 100%

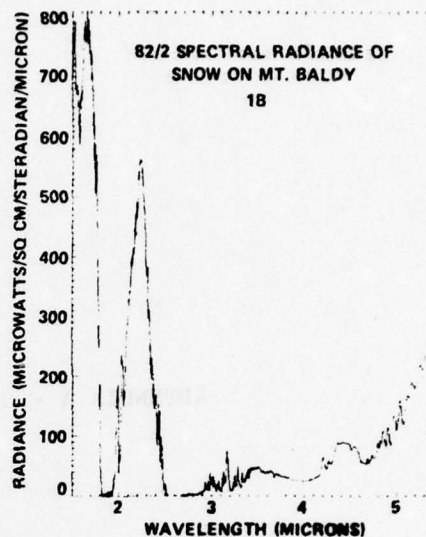
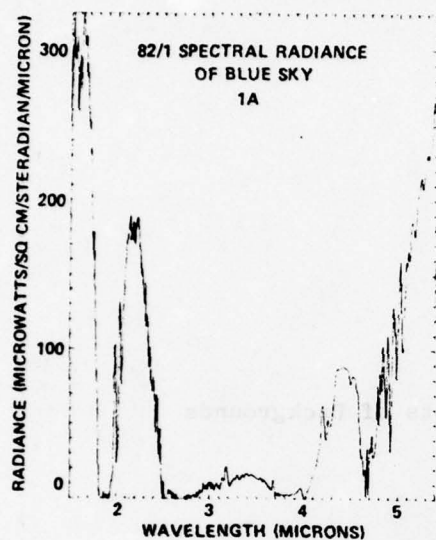


APPENDIX A - Spectral Plots of Backgrounds

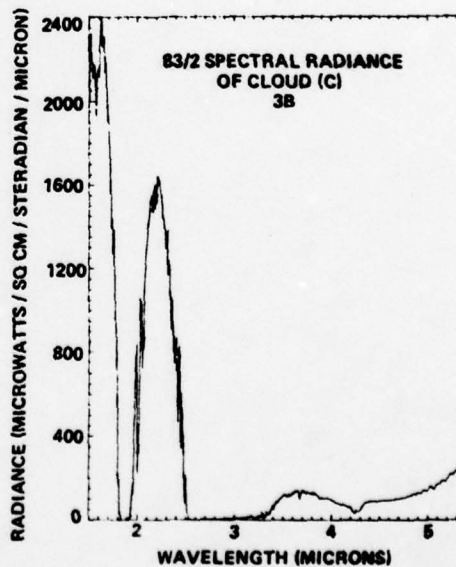
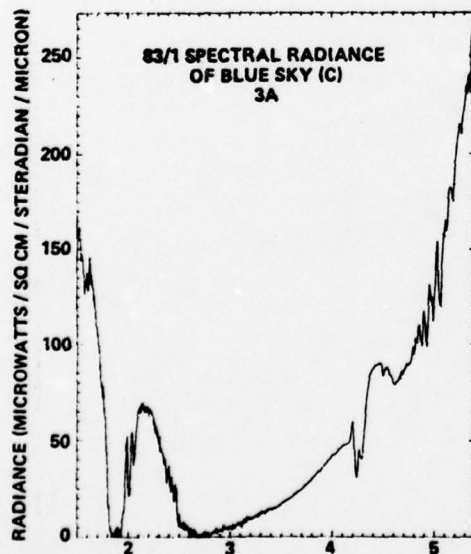
100% 100% 100% 100% 100%
 100% 100% 100% 100% 100%
 100% 100% 100% 100% 100%
 100% 100% 100% 100% 100%
 100% 100% 100% 100% 100%
 100% 100% 100% 100% 100%



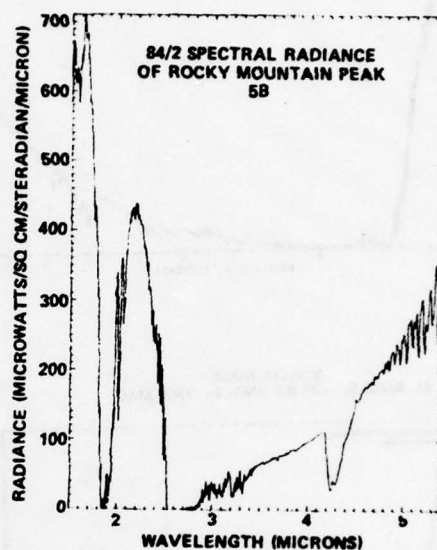
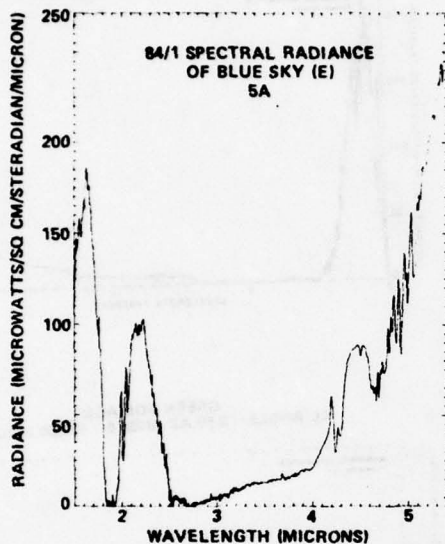
DATE: APRIL 21, 1969, TIME: 1056
 SITE LOCATION: BLUE RIDGE, CALIF
 SITE ELEVATION: 7386 FEET
 SITE TEMP: 64° F, R.H. 34%
 OBJECT EL ANGLE: + 3.5°,
 AZ ANGLE: 135° MAG



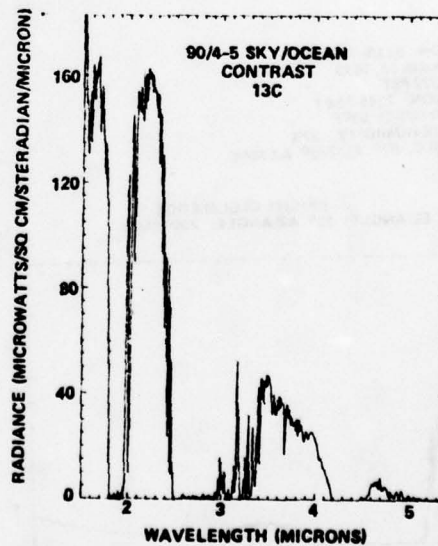
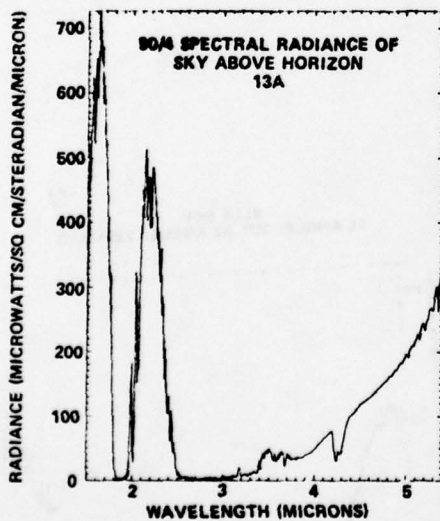
DATE: APRIL 21, 1969, TIME: 1130
 SITE LOCATION: BLUE RIDGE, CALIF.
 SITE ELEVATION: 7386 FEET
 SITE TEMP: 64°F, R.H.: 35%
 OBJECT EL ANGLE: +16°,
 AZ ANGLE: 85° MAG.



DATE: APRIL 21, 1969, TIME: 1155
 SITE LOCATION: BLUE RIDGE, CALIF.
 SITE ELEVATION: 7386 FEET
 SITE TEMP: 64° F, R.H. 37%
 OBJECT EL ANGLE: +9°
 AZ ANGLE: 52° MAG

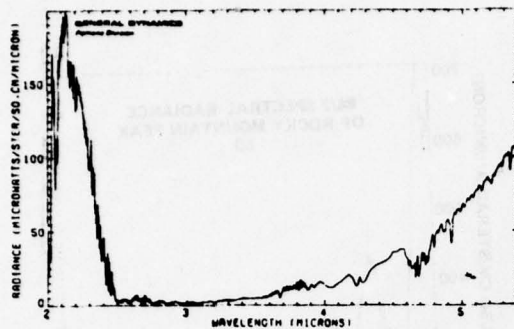


DATE: APRIL 24, 1969, TIME: 1401
 SITE LOCATION: SAN CLEMENTE, CALIF.
 SITE ELEVATION: 250 FEET
 SITE TEMP: 65° F, R.H. 61%
 OBJECT EL ANGLE: 0°
 AZ ANGLE: 285° MAG

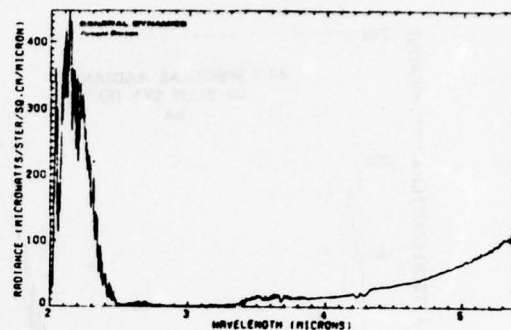


LOCATION: SAN MARCOS PASS
 DATE: MAY 18, 1970
 TIME: 16:22 PST
 ELEVATION: 1850 FEET
 TEMPERATURE: 73°F
 RELATIVE HUMIDITY: 46%
 SUN ANGLE: 19° EL, 242° AZ MAG

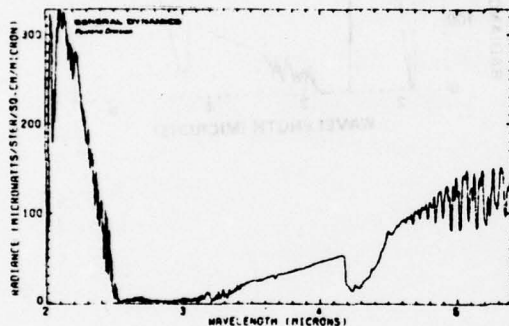
BLUE SKY
 EL ANGLE: -2° AZ ANGLE: 179.2° MAG



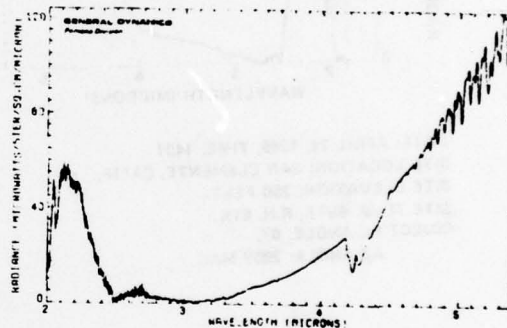
FOG BANK
 EL ANGLE: -2.4° AZ ANGLE: 179.5° MAG



SUNLIT ROCK
 EL ANGLE: -3° AZ ANGLE: 180° MAG



GREEN FOLIAGE
 EL ANGLE: 3.5° AZ ANGLE: 180.5° MAG

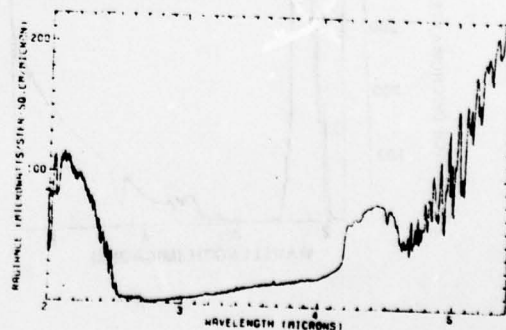


LOCATION: BLUE RIDGE
 DATE: JUNE 15, 1970
 TIME: 1322 PST
 ELEVATION: 7386 FEET
 TEMPERATURE: 63°F
 RELATIVE HUMIDITY: 37%
 SUN ANGLE: 67° EL 228° AZ MAG

BRIGHT CLOUD EDGE
 EL ANGLE: 19° AZ ANGLE: 235° MAG

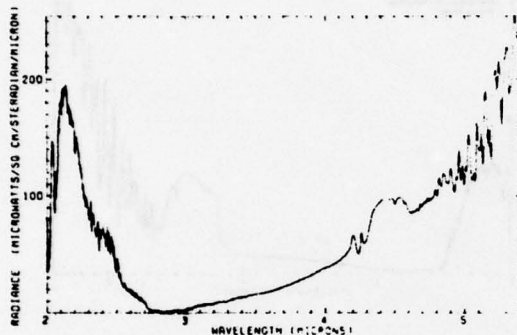


BLUE SKY
 EL ANGLE: 20° AZ ANGLE: 235° MAG

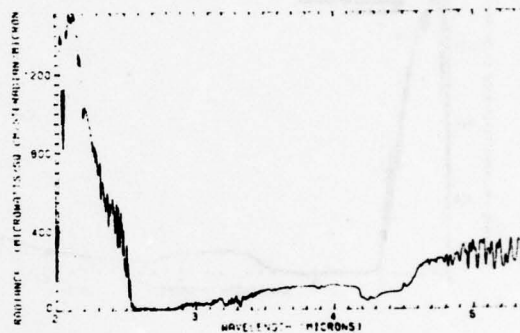


LOCATION: BLUE RIDGE, CALIF
 DATE: JAN 29, 1970
 TIME: 11.32 PST
 ELEVATION: 7386 FEET
 TEMPERATURE: 49°F
 RELATIVE HUMIDITY: 12%
 SUN ANGLE: 37° EL, 155° AZ MAG

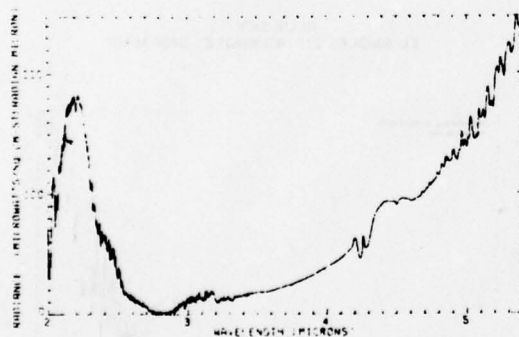
BLUE SKY ABOVE MT. PINION
 EL ANGLE: 9° AZ ANGLE: 230° MAG



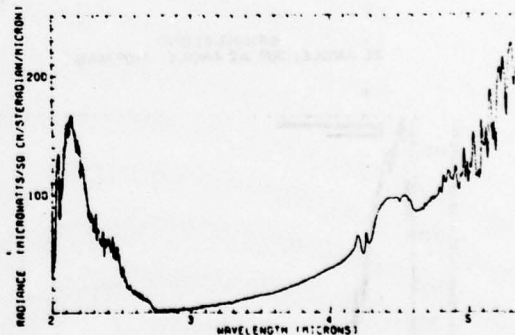
BLUE SKY ABOVE MT. PINION
 EL ANGLE: 8.5° AZ ANGLE: 230° MAG



SNOW COVERED PEAK
 EL ANGLE: 8° AZ ANGLE: 230° MAG

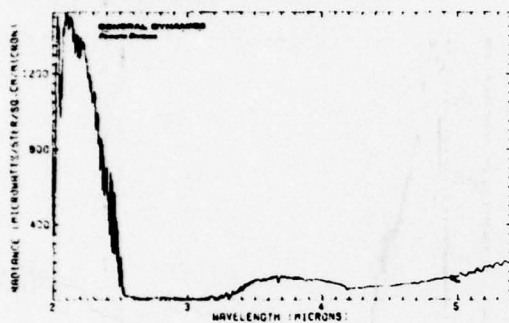


BARE GROUND
 EL ANGLE: 8° AZ ANGLE: 229.5° MAG

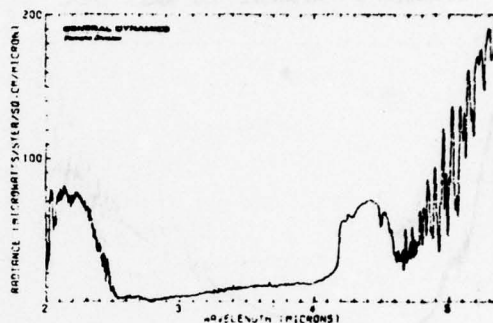


LOCATION: BLUE RIDGE
 DATE: JUNE 15, 1970
 TIME: 1334 PST
 ELEVATION: 7386 FT
 TEMPERATURE: 63°F
 RELATIVE HUMIDITY: 37%
 SUN ANGLE: 64° EL 230° AZ MAG

BLUE SKY
 EL ANGLE: 24.5° AZ ANGLE: 309.5° MAG



BRIGHT CLOUD
 EL ANGLE: 24° AZ ANGLE: 310° MAG

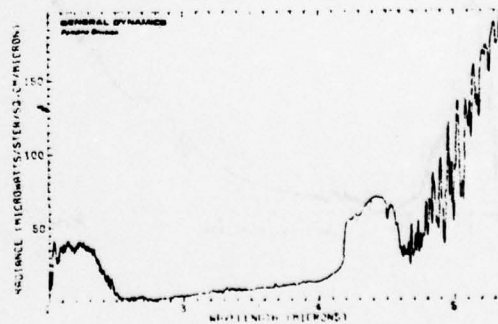


LOCATION: BLUE RIDGE
 DATE: JUNE 15, 1970
 TIME: 1358 PST
 ELEVATION: 7386 FEET
 TEMPERATURE: 63°F
 RELATIVE HUMIDITY: 35%
 SUN ANGLE: 57° EL 235° AZ MAG

BRIGHT CLOUD
 EL ANGLE: 20° AZ ANGLE: 340° MAG

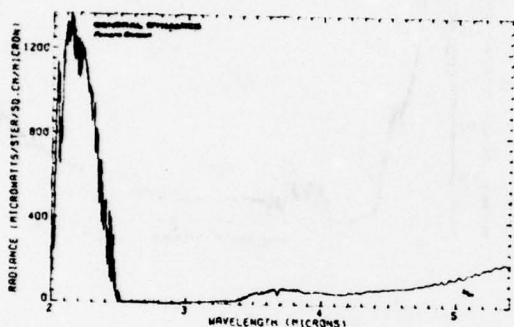


BLUE SKY
 EL ANGLE: 21° AZ ANGLE: 340° MAG

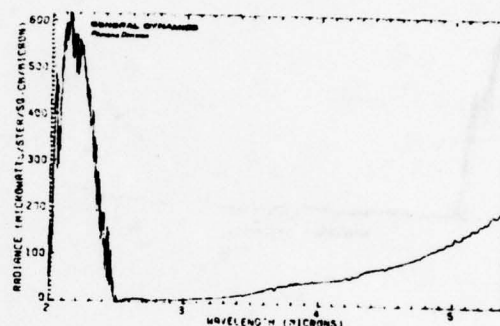


LOCATION: BLUE RIDGE
 DATE: JUNE 15, 1970
 TIME: 1406 PST
 ELEVATION: 7386 FEET
 TEMPERATURE: 62°F
 RELATIVE HUMIDITY: 34%
 SUN ANGLE: 54° EL 236° AZ MAG

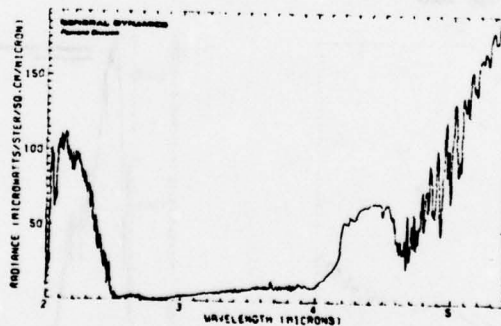
BRIGHT CLOUD
 EL ANGLE: 10° AZ ANGLE: 130° MAG



DARK CLOUD
 EL ANGLE: 9° AZ ANGLE: 130° MAG

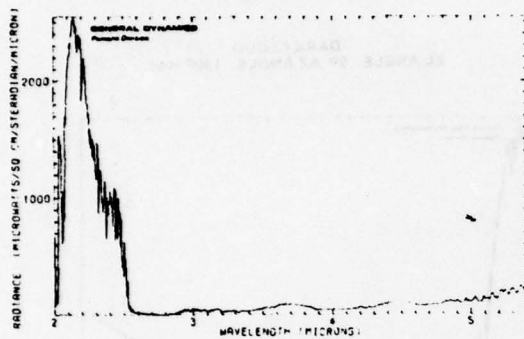


BLUE SKY
 EL ANGLE: 11° AZ ANGLE: 130° MAG

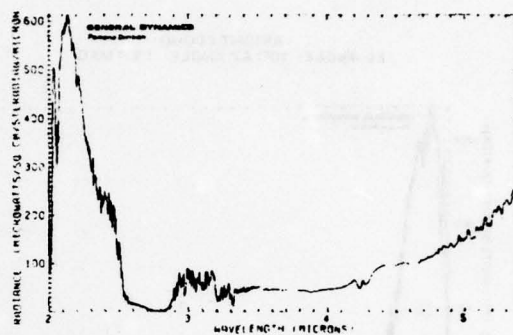


LOCATION: BLUE RIDGE, CALIF.
 DATE: JAN 29, 1970
 TIME: 11:54 PST
 ELEVATION: 7388 FEET
 TEMPERATURE: 49°F
 RELATIVE HUMIDITY: 12%
 SUN ANGLE: 38° EL, 162° AZ MAG

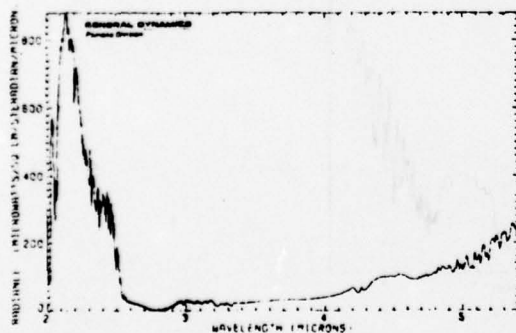
CLOUD COVER OVER MT. BALDY
 EL ANGLE: 7.0° AZ ANGLE: 138° MAG



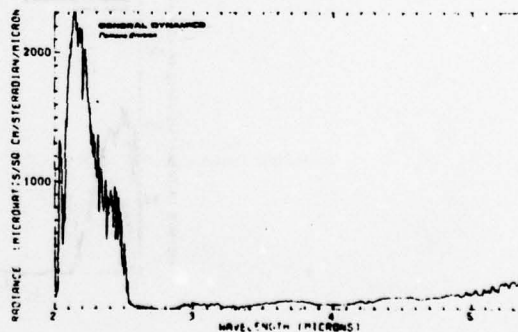
CLOUD COVER
 EL ANGLE: 6.2° AZ ANGLE: 138° MAG



BLUE SKY
 EL ANGLE: 5.5° AZ ANGLE: 138° MAG

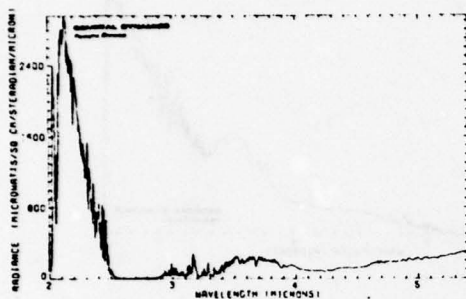


SNOW & ROCK
 EL ANGLE: 5.3° AZ ANGLE: 138° MAG

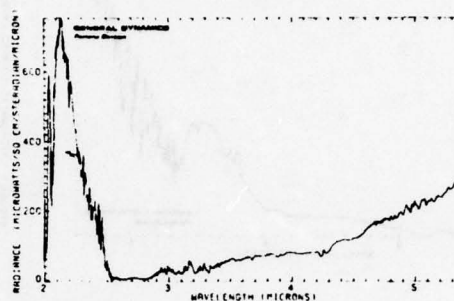


LOCATION: BLUE RIDGE, CALIF.
 DATE: JAN 29, 1970
 TIME: 13 09 PST
 ELEVATION: 7386 FEET
 TEMPERATURE: 50°F
 RELATIVE HUMIDITY: 13.5%
 SUN ANGLE: 35° EL, 180° AZ MAG

SUN LIT LAKE
 EL ANGLE: -2° AZ ANGLE: 175° MAG

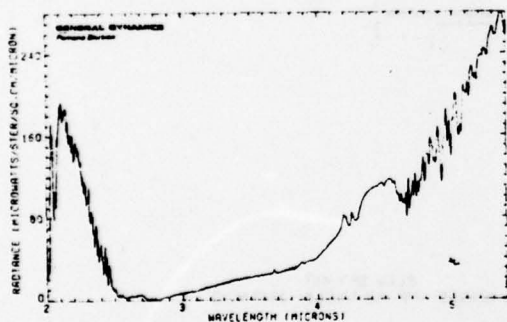


RIGHT OF SUN LIT LAKE
 EL ANGLE: -2° AZ ANGLE: 176° MAG

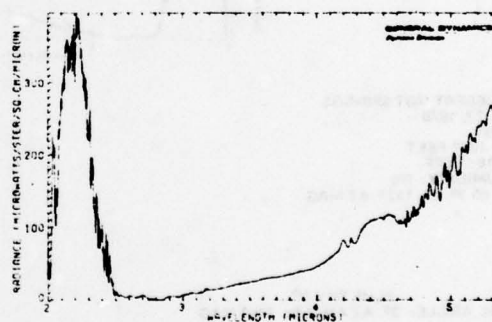


LOCATION: DESERT HOT SPRINGS
 DATE: APRIL 23, 1970
 TIME: 1145 PST
 ELEVATION: 1087 FEET
 TEMPERATURE: 76°F
 RELATIVE HUMIDITY: 9%
 SUN ANGLE: 68° EL 162° AZ MAG

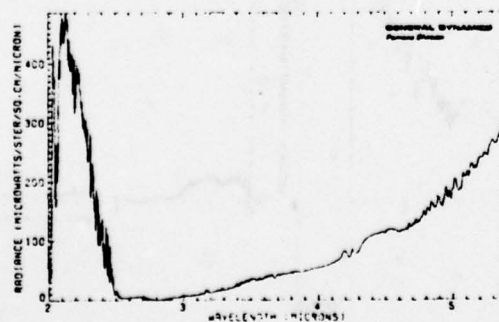
BLUE SKY
 EL ANGLE: 5.2° AZ ANGLE: 285° MAG



SNOW ON SAN GORGONIO
 EL ANGLE: 4.8° AZ ANGLE: 285° MAG

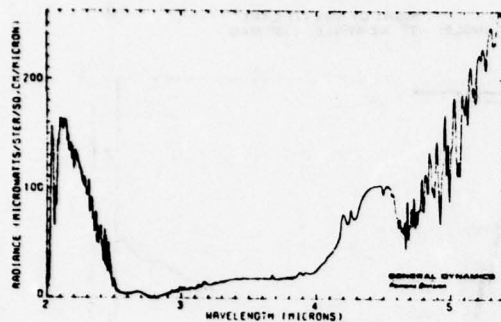


SECOND MT. PEAK
 EL ANGLE: 3.0° AZ ANGLE: 285° MAG

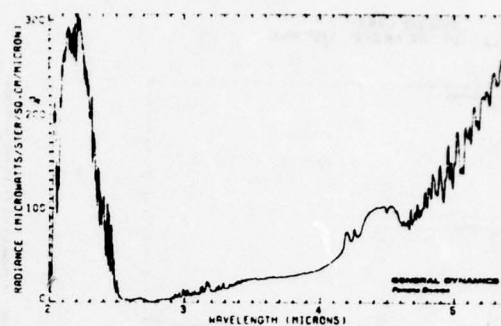


LOCATION: DESERT HOT SPRINGS
 DATE: APRIL 23, 1970
 ELEVATION: 1087 FEET
 TEMPERATURE: 76°F
 RELATIVE HUMIDITY: 9%
 SUN ANGLE: 67.5° EL 178° AZ MAG

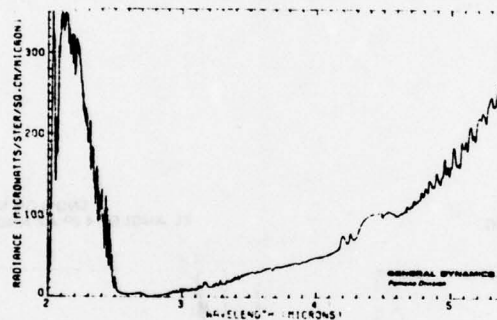
BLUE SKY
 EL ANGLE: 8.5° AZ ANGLE: 210° MAG



SNOW AND ROCKS
 EL ANGLE: 8.2° AZ ANGLE: 210° MAG

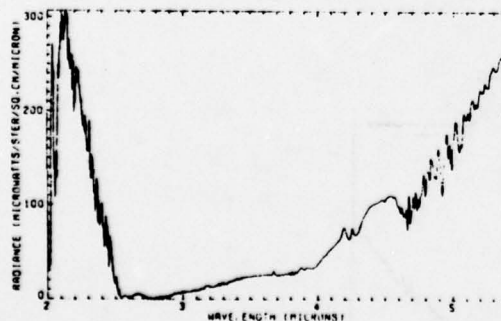


HOT SPOT BELOW PEAK
 EL ANGLE: 7.0° AZ ANGLE: 210° MAG

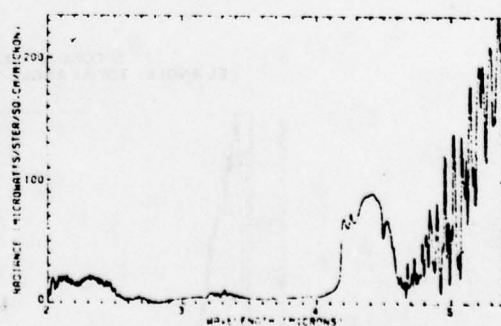


LOCATION: DESERT HOT SPRINGS
 DATE: APRIL 23, 1970
 TIME: 1237 PST
 ELEVATION: 1087 FEET
 TEMPERATURE: 76°F
 RELATIVE HUMIDITY: 9%
 SUN ANGLE: 65.7° EL 192° AZ MAG

BLUE SKY 3°
 EL ANGLE: 3° AZ ANGLE: 345° MAG

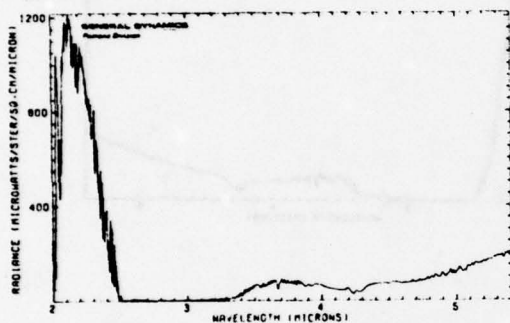


BLUE SKY 44°
 EL ANGLE: 44° AZ ANGLE: 345° MAG

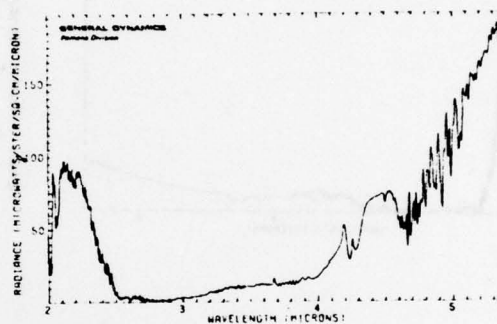


LOCATION: SAN ONOFRE
 DATE: APRIL 28, 1970
 TIME: 1458 PST
 ELEVATION: 110 FEET
 TEMPERATURE: 64°F
 RELATIVE HUMIDITY: 32%
 SUN ANGLE: 39° EL 230° AZ MAG

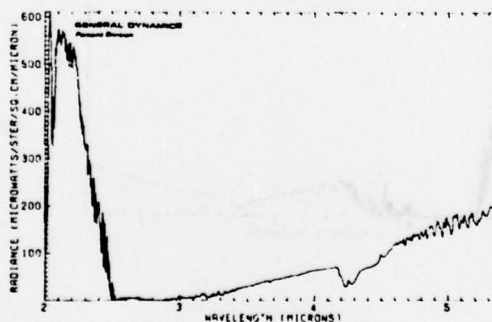
CLOUD
 EL ANGLE: 85° AZ ANGLE: 240° MAG



BLUE SKY ABOVE CLOUD
 EL ANGLE: 90° AZ ANGLE: 240° MAG

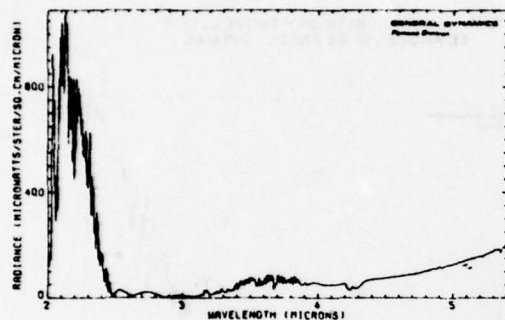


HILLSIDE
 EL ANGLE: 80° AZ ANGLE: 240° MAG

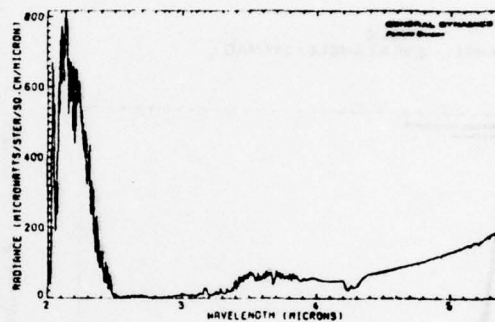


LOCATION: SAN ONOFRE
 DATE: APRIL 28, 1970
 TIME: 1528 PST
 ELEVATION: 110 FEET
 TEMPERATURE: 60°F
 RELATIVE HUMIDITY: 41%
 SUN ANGLE: 31° EL 230° AZ MAG

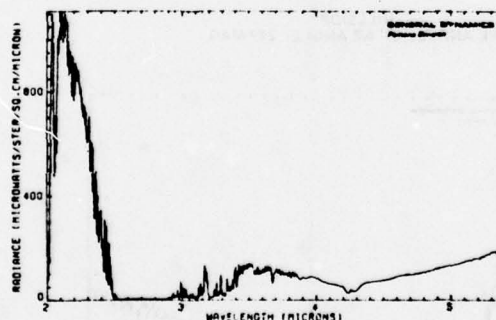
CLOUD OVER CATALINA
 EL ANGLE: +5° AZ ANGLE: 230° MAG



CATALINA ISLAND
 EL ANGLE: +2° AZ ANGLE: 230° MAG

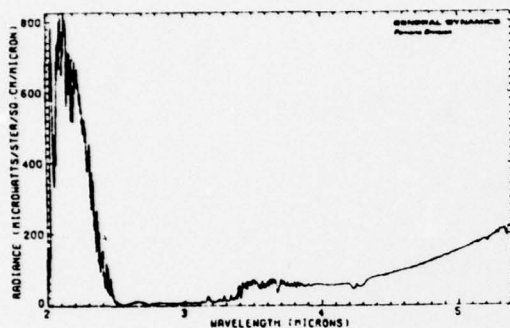


OCEAN BELOW CATALINA
 EL ANGLE: -3° AZ ANGLE: 230° MAG

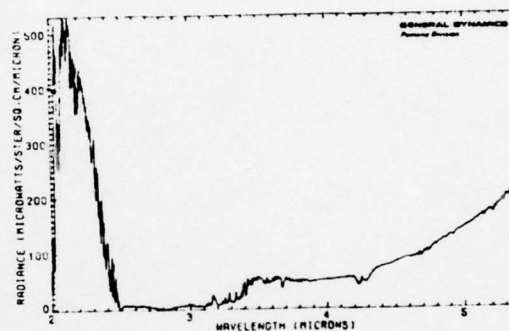


LOCATION: SAN ONOFRE
 DATE: MAY 14, 1970
 TIME: 14:59 PST
 ELEVATION: 110 FEET
 TEMPERATURE: 72°F
 RELATIVE HUMIDITY: 60%
 SUN ANGLE: 39.5° EL 236° AZ MAG

BLUE SKY
 EL ANGLE: +5° AZ ANGLE: 217° MAG



WATER
 EL ANGLE: -5° AZ ANGLE: 217° MAG



BUSH
 EL ANGLE: -10° AZ ANGLE: 217° MAG

